

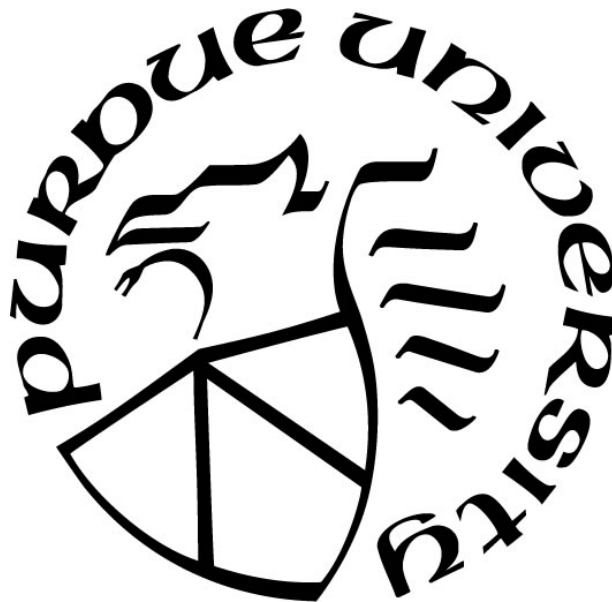
# **SIMULATION AND OPTIMIZATION OF HVAC SYSTEMS WITH INTEGRATED DESICCANT-BASED WHEELS**

by  
**Yu-Wei Hung**

**A Dissertation**

*Submitted to the Faculty of Purdue University  
In Partial Fulfillment of the Requirements for the degree of*

**Doctor of Philosophy**



Lyles School of Civil Engineering  
West Lafayette, Indiana  
August 2021

**THE PURDUE UNIVERSITY GRADUATE SCHOOL**  
**STATEMENT OF COMMITTEE APPROVAL**

**Dr. W. Travis Horton, Chair**

School of Civil Engineering

**Dr. Brandon E. Boor**

School of Civil Engineering

**Dr. Eckhard A. Groll**

School of Mechanical Engineering

**Dr. Ming Qu**

School of Civil Engineering

**Approved by:**

Dr. Dulcy Abraham

Dedicated to my Father

## **ACKNOWLEDGMENTS**

I would like to express my deepest and sincerest gratitude to my academic advisor, Dr. W. Travis Horton, for his continuous support and insightful guidance throughout my Ph.D. career. I really appreciate that he agreed to have me as a part-time student in 2017 while I was working as a full-time engineer at the time; it allows me to accumulate working experience and also make progress in the research. I am grateful to be involved in the Purdue Center for High Performance Buildings project and the World Bank project after I returned to school. This fulfilling and meaningful journey could have never been achieved without his much assistance.

I would like to make special thanks to Dr. Brandon E. Boor, Dr. Eckhard E. Groll, and Dr. Ming Qu (alphabetical order of the last name) for their thoughtful comments and recommendations on this dissertation. They not only offer expertise in the building science and thermal system realm, also being always encouraging.

My heartfelt gratitude is given to my parent and my aunt. They teach me the importance of education and encourage me to pursue higher academic degrees. Their support outside of academia helps me go through difficult times. I would not be where I am today without them. Most of all, I would like to dedicate this research to my father, who passed away in 2019. He was always being supportive of my decisions and encouraged me to pursue a Ph.D. degree. I wish he were here to share this joyful moment with me and my mother. This work is in memory of my father.

# TABLE OF CONTENTS

LIST OF TABLES .....	4
LIST OF FIGURES .....	5
NOMENCLATURE .....	7
ABSTRACT.....	9
1. BACKGROUND AND MOTIVATION.....	10
2. LITERATURE REVIEW .....	14
2.1 Experimental Evaluation Studies.....	15
2.2 Mathematical Model Development Studies.....	18
2.3 Nusselt Number Evaluation Studies .....	24
2.4 Wheel Integrated HVAC System Study .....	26
2.5 Literature Review Conclusion .....	27
3. RESEARCH OBJECTIVES.....	29
4. MATHEMATICAL MODEL DEVELOPMENT .....	31
4.1 Governing Equations .....	31
4.1.1 Energy Balance of Air Stream.....	32
4.1.2 Energy Balance of Matrix.....	33
4.1.3 Moisture Balance of Air Stream .....	33
4.1.4 Moisture Balance of Matrix.....	34
4.1.5 General Adsorption Isotherm .....	34
4.2 Constants and Input Parameters.....	34
4.2.1 Reynolds Number .....	35
4.2.2 Thermal Diffusivity of Air.....	35
4.2.3 Prandtl Number.....	35
4.2.4 Peclet Number .....	36
4.2.5 Nusselt Number .....	36
4.2.6 Lewis Number .....	37
4.2.7 Biot Number .....	38
4.2.8 Hydraulic Diameter .....	38
4.3 Control Volume .....	39

4.4	Finite Difference Method.....	40
4.4.1	FDM of Air Stream Energy Balance .....	41
4.4.2	FDM of Matrix Energy Balance .....	42
4.4.3	FDM of Air Stream Mass Balance .....	44
4.4.4	FDM of Matrix Mass Balance .....	45
4.5	Solution Method.....	47
4.6	Simulation Setup .....	48
4.7	Simulation Results and Validation.....	48
4.7.1	Energy Recovery Wheel Simulation Results and Validation .....	48
4.7.2	Desiccant Wheel Simulation Results and Validation .....	54
4.7.3	Fourier Number .....	56
5.	ENERGY RECOVERY WHEEL MAPPING METHOD DEVELOPMENT .....	57
5.1	Buckingham's Pi Theorem .....	57
5.2	Energy Recovery Wheel Mapping Method Development.....	59
5.2.1	Operating Range and Training Data Selection .....	67
5.3	Validation with FDM Energy Recovery Wheel Model .....	68
5.3.1	Validation with Other Literature .....	70
5.4	Conclusion of the Energy Recovery Wheel Mapping Method .....	72
6.	DESICCANT WHEEL MAPPING METHOD DEVELOPMENT .....	74
6.1	Original Wheel Mapping Method Form Extension Study .....	74
6.2	Desiccant Wheel Mapping Method Development.....	76
6.2.1	Operating Range and Training Data Quantity .....	82
6.3	Validation of the Desiccant Wheel Mapping Method .....	84
6.4	Conclusion of the Desiccant Wheel Mapping Method .....	87
7.	ENERGY RECOVERY WHEEL CASE STUDY .....	89
7.1	Building Performance Simulation and Optimization Introduction.....	89
7.2	Small Office Building Model Development .....	91
7.3	Small Office Building Performance Simulation Results .....	97
7.4	Energy Recovery Wheel Optimization Development.....	100
7.4.1	Energy Recovery Wheel Optimization Setups .....	100
7.4.2	Energy Recovery Wheel Initial Guess Value Study .....	101

7.4.3	Sensitivity Study of Energy Recovery Wheel Variables .....	102
7.5	Energy Recovery Wheel Optimization Results .....	108
7.5.1	Variant Air Change Rates Optimization.....	108
7.5.2	Variant Climates Optimization .....	109
7.6	Conclusion of Energy Recovery Wheel Case Study.....	112
8.	DESICCANT WHEEL CASE STUDY .....	113
8.1	Supermarket Introduction .....	113
8.2	Supermarket Building Model Development .....	113
8.3	Supermarket Building Performance Simulation Results .....	115
8.4	Desiccant Wheel Optimization Development.....	119
8.4.1	Desiccant Wheel Optimization Setups .....	119
8.4.2	Desiccant Wheel Initial Guess Value Study .....	120
8.4.3	Sensitivity Study of Desiccant Wheel Variables .....	120
8.5	Desiccant Wheel Optimization Results .....	127
8.5.1	Desiccant Wheel Design Optimization.....	127
8.5.2	Variant Climates Optimization .....	129
8.6	Conclusion of Desiccant Wheel Case Study.....	130
9.	CONCLUSION AND FUTURE WORK .....	131
9.1	Achieved Research Objectives .....	131
9.2	Conclusion .....	132
9.3	Future Work .....	133
APPENDIX A. FINITE DIFFERENCE METHOD DERIVATION FOR GOVERNING EQUATIONS.....		135
APPENDIX B. TRNSYS MODEL DEMONSTRATION .....		145
REFERENCES .....		153
PUBLICATION .....		159

## LIST OF TABLES

Table 1 Nusselt numbers are utilized in papers that study energy recovery wheels.....	25
Table 2 Grid independence study boundary conditions.....	52
Table 3 Operating range of energy recovery wheel mapping method.....	67
Table 4 Effect of training data set selection to mapping method prediction .....	68
Table 5 Range of training data set selected from the literature .....	70
Table 6 Operating range of the desiccant wheel mapping method.....	83
Table 7 Utility rate of the study locations.....	96
Table 8 Initial guess of energy recovery wheel target variables.....	102
Table 9 Input values of energy recovery wheel target variables for sensitivity study.....	104
Table 10 Energy recovery wheel optimal design at different utility rate .....	108
Table 11 Energy recovery wheel optimal design at different wheel price .....	108
Table 12 Optimal energy recovery wheel design at different ACHs.....	109
Table 13 Optimal energy recovery wheel design at different locations .....	111
Table 14 Initial guess of desiccant wheel target variables.....	120
Table 15 Input values of desiccant wheel target variables for sensitivity study.....	122
Table 16 Optimal desiccant wheel design vs. original design.....	128
Table 17 Optimal desiccant wheel design in different locations .....	130



## LIST OF FIGURES

Fig. 1 Woking theory of desiccant based wheels.....	12
Fig. 2 Target variables in a flute of a wheel .....	32
Fig. 3 The cross-sectional area of an isosceles triangular duct [40] .....	37
Fig. 4 Flute of a wheel and its estimated sine wave function .....	39
Fig. 5 The control volume of a wheel .....	40
Fig. 6 Inlet and outlet air temperature difference of experimental data against FDM simulation result.....	50
Fig. 7 Air humidity ratio of experimental data against FDM simulation result .....	51
Fig. 8 $T_{SA}$ with different space and time segment while $T_{OA} = 40^{\circ}\text{C}$ .....	53
Fig. 9 $T_{g,SA}$ with different space and time segment while $T_{g,OA} = 35^{\circ}\text{C}$ .....	53
Fig. 10 $T_{g,SA}$ with different space and time segment while $T_{g,OA} = 30^{\circ}\text{C}$ .....	54
Fig. 11 Air temperature difference between the selection tool data and the FDM prediction.....	55
Fig. 12 Air humidity ratio difference between the selection tool data and the FDM prediction ..	56
Fig. 13 Buckingham's pi prediction and FDM outcome .....	59
Fig. 14 Effect of the traveling time of a flute in one airstream on wheel performance .....	63
Fig. 15 Effect of the air face velocity on wheel performance.....	64
Fig. 16 Effect of the wheel depth on wheel performance .....	65
Fig. 17 $\Delta T_{g,SA}$ between FDM simulation and mapping method prediction, MAPE = 6.33% .....	71
Fig. 18 $W_{g,SA}$ between FDM simulation and mapping method prediction, MAPE = 3.61% .....	72
Fig. 19 $\Delta T_{g,SA}$ between FDM simulation results and original mapping method prediction .....	75
Fig. 20 $\Delta W_{g,SA}$ between data sets and original mapping method prediction .....	76
Fig. 21 Effect of the traveling time of a flute in one airstream on desiccant wheel performance	77
Fig. 22 Effect of the air face velocity in supply stream on desiccant wheel performance .....	78
Fig. 23 Effect of the wheel depth on desiccant wheel performance .....	80
Fig. 24 Effect of the air face velocity in regeneration stream on desiccant wheel performance ..	81
Fig. 25 Frequency distribution of MAPE with different random training data points .....	84
Fig. 26 $\Delta T_{g,SA}$ between data sets and mapping method prediction .....	86
Fig. 27 $\Delta W_{g,SA}$ between data sets and mapping method prediction.....	87

Fig. 28 Schematic of (a) vapor-compression HVAC system (b) energy recovery wheel integrated HVAC system .....	92
Fig. 29 Moisture balance logic.....	95
Fig. 30 Monthly cooling/heating sensible load of a conventional HVAC system.....	98
Fig. 31 Monthly cooling/heating sensible load of a wheel-integrated HVAC system .....	99
Fig. 32 Relative humidity of the conditioned zone.....	100
Fig. 33 Energy recovery wheel variables' sensitivity study on air temperature change.....	105
Fig. 34 Energy recovery wheel variables' sensitivity study on costs .....	106
Fig. 35 Relative humidity of conventional vs. wheel system .....	111
Fig. 36 Schematic of (a) vapor compression system (b) desiccant wheel integrated HVAC system .....	114
Fig. 37 Energy consumptions of conventional vapor-compression HVAC system components	117
Fig. 38 Energy consumptions of desiccant wheel integrated HVAC system components .....	118
Fig. 39 Humidity ratios of evaporator entering air for two systems and supply air condition ...	119
Fig. 40 Desiccant wheel variables' sensitivity study on leaving air humidity ratio .....	122
Fig. 41 Desiccant wheel variables' sensitivity study on costs .....	125
Fig. 42 Energy consumptions of optimized desiccant wheel integrated HVAC system components .....	128

## NOMENCLATURE

Symbol	Description	Units
$A$	Area	$m^2$
$c$	Separation factor	$ul$
$C_p$	Specific heat	$J/kg \cdot K$
$D$	Diffusivity	$m^2/s$
$d_h$	Hydraulic diameter	$m$
$h$	Convective heat transfer coefficient	$W/m^2 \cdot K$
$h_m$	Convective mass transfer coefficient	$kg/m^2 \cdot s$
$H_{evap}$	Heat of evaporation	$J/mol$
$k$	Thermal conductivity of air	$W/m \cdot K$
$L$	Characteristic length or wheel depth	$m$
$\dot{m}$	Air mass flow rate	$kg/s$
$M_v$	Water vapor molar mass	$kg/mol$
$p$	Perimeter length	$m$
$P$	Gas pressure	$Pa$
$R$	Ideal gas constant = 8.315	$J/mol \cdot K$
$t$	time	$sec$
$T$	Temperature	$^{\circ}C$ or $K$
$u$	Air face velocity	$m/s$
$\nu$	Kinematic viscosity	$m^2/s$
$W$	Humidity ratio (water vapor/dry air)	$kg/kg$

### Greek Letters

Symbol	Description	Units
$\gamma_d$	Moisture loading in desiccant composite	$kg/kg$
$\gamma_{max}$	Maximum moisture loading in desiccant composite	$kg/kg$
$\delta$	Thickness	$m$
$\Delta H_{ads}$	Heat of adsorption	$J/kg$

$\rho$	Density	$kg/m^3$
--------	---------	----------

Symbol	Subscript	Description
abs		Absolute temperature
d		Wheel desiccant
g		Wet air
j		Space segment for the finite difference method
m		Wheel matrix
n		Time segment for the finite difference method
RPM		Wheel rotation speed
sat		Saturation pressure
sub		Wheel substrate
v		Water vapor
EA		Exhaust air
OA		Outdoor air
RA		Return air or regeneration air
SA		Supply air

## **ABSTRACT**

Energy recovery ventilation (ERV) systems are designed to decrease the energy consumed by building HVAC systems. ERV's scavenge sensible and latent energy from the exhaust air leaving a building or space and recycle this energy content to pre-condition the entering outdoor air. A few studies found in the open literature are dedicated to developing detailed numerical models to predict or simulate the performance of energy recovery wheels and desiccant wheels. However, the models are often computationally intensive, requiring a lot of time to perform parametric studies. For example, if the physical characteristics of a study target change (e.g., wheel diameter or depth) or if the system runs at different operating conditions (e.g., wheel rotation speed or airflow rate), the model parameters need to be recalculated. Hence, developing a mapping method with better computational efficiency, which will enable the opportunity to conduct extensive parametric or optimal design studies for different wheels is the goal of this research. In this work, finite difference method (FDM) numerical models of energy recovery wheels and desiccant wheels are established and validated with laboratory test results. The FDM models are then used to provide data for the development of performance mapping methods for an energy wheel or a desiccant wheel. After validating these new mapping approaches, they are employed using independent data sets from different laboratories and other sources available in the literature to identify their universality. One significant characteristic of the proposed mapping methods that makes the contribution unique is that once the models are trained, they can be used to predict performance for other wheels with different physical geometries or different operating conditions if the desiccant material is identical. The methods provide a computationally efficient performance prediction tool; therefore, they are ideal to integrate with transient building energy simulation software to conduct performance evaluations or optimizations of energy recovery/ desiccant wheel integrated HVAC systems.

## 1. BACKGROUND AND MOTIVATION

The U.S. Energy Information Administration 2017 Annual Energy Outlook reports that energy use of heating, ventilation, and air conditioning (HVAC) systems represents about 30% of the total building energy consumption among U.S. commercial buildings. Traditional vapor-compression refrigeration systems contribute to environmental impacts in different ways; first of all, the CFC and HCFC refrigerants used in these systems are ozone-depleting substances; next, most refrigerants are considered greenhouse gases and as such, exhibit a strong global warming potential; and lastly, refrigeration systems consume a high portion of the energy that is generated by fossil fuels. As widely acknowledged, fossil fuel combustion releases polluting chemicals, such as Carbon Monoxide (CO), Nitrogen Oxides (NO<sub>x</sub>), and Sulfur Oxides (SO<sub>x</sub>), which have harmful effects on human health, in addition to Carbon Dioxide (CO<sub>2</sub>), which is considered as the baseline measure against which other greenhouse gases are compared. [1]

Energy recovery ventilators (ERV's) are devices that are made for scavenging the energy contained in exhaust air and using it to pre-condition the incoming outdoor air. During the cooling season, an ERV pre-cools and dehumidifies the outdoor air before it enters the cooling coil or space. Vice versa, in the heating season, they will pre-heat and humidify the outdoor air. The benefits of applying ERV's are reducing the energy consumption of air conditioning and heating systems, therefore more outdoor air can be introduced to the space to improve indoor air quality.

The integration of energy recovery ventilators (ERV's) into HVAC systems presents an opportunity to reduce the impact of these systems on their environment. Energy recovery ventilation is a method of harvesting the energy (both sensible and latent) contained in exhaust air leaving a building or space, and recycling its energy content to pre-condition the outdoor air entering the building or space. Therefore, the appropriate application of ERV's has the potential to significantly reduce energy consumed by building HVAC systems. ERV systems can be implemented in residential buildings, commercial buildings, and industrial facilities. ASHRAE 90.1 Energy Standard for Buildings Except Low-Rise Residential Buildings, which are the generally accepted building design and construction standards for energy efficiency, present the appropriate specifications for ERV systems that can assist to achieve those requirements in section 6.5.6- Energy recovery. [2]

ASHRAE 62.1 Ventilation for Acceptable Indoor Air Quality, provides methods for calculating the air change rates required for different types of buildings to achieve an acceptable indoor air quality. [3] The indoor air quality is shown to have an impact on the health and comfort of occupants, and is related to sick building syndrome (SBS) and building related illnesses (BRI). High indoor humidity may lead to more intensive microbial activity (e.g., mold or fungus), which may also lead to a high level of volatile organic compound (VOC) concentration in buildings. The main purpose of ANSI/ASHRAE Standard 62.1-2016 Ventilation for Acceptable Indoor Air Quality, is to specify minimum ventilation rates that will yield an acceptable indoor air quality for occupants and that minimizes negative health impacts. The standard is not only intended for regulating new buildings but also existing buildings. ASHRAE 62.1, gives minimum ventilation rates for different building zones and also recommends an acceptable level of relative humidity in occupied spaces. [3] Meanwhile, introducing more outdoor air means that operating costs will increase. Thus, ERV's are one of the solutions to achieve a balance between energy efficiency and indoor air quality.

Energy recovery wheels and desiccant wheels are types of ERV's. Energy recovery wheels are typically made from materials that exhibit a good balance between thermal conductivity, thermal mass, structural strength, and weight (typically Aluminum), with the addition of a desiccant coating to address latent energy transport. Desiccant wheels are generally made from materials that exhibit a low thermal conductivity and thermal mass (typically fiber paper) to minimize sensible energy transport, with a thick layer of desiccant coating to provide latent energy transport. The physical construction of this type of wheel is similar to that of a long strip of cardboard that has been rolled-up into a wheel, where the corrugated channels form passages that air can travel through. The energy recovery wheel collects energy (both sensible and latent) from the return air and utilizes it to pre-condition the outdoor air. The wheel generally operates by rotating through a supply air stream and an exhaust air stream as shown schematically in Fig. 1. Desiccant wheels behave very similarly to energy recovery wheels, however, desiccant wheels emphasize latent energy transfer and compromise on thermal transfer.

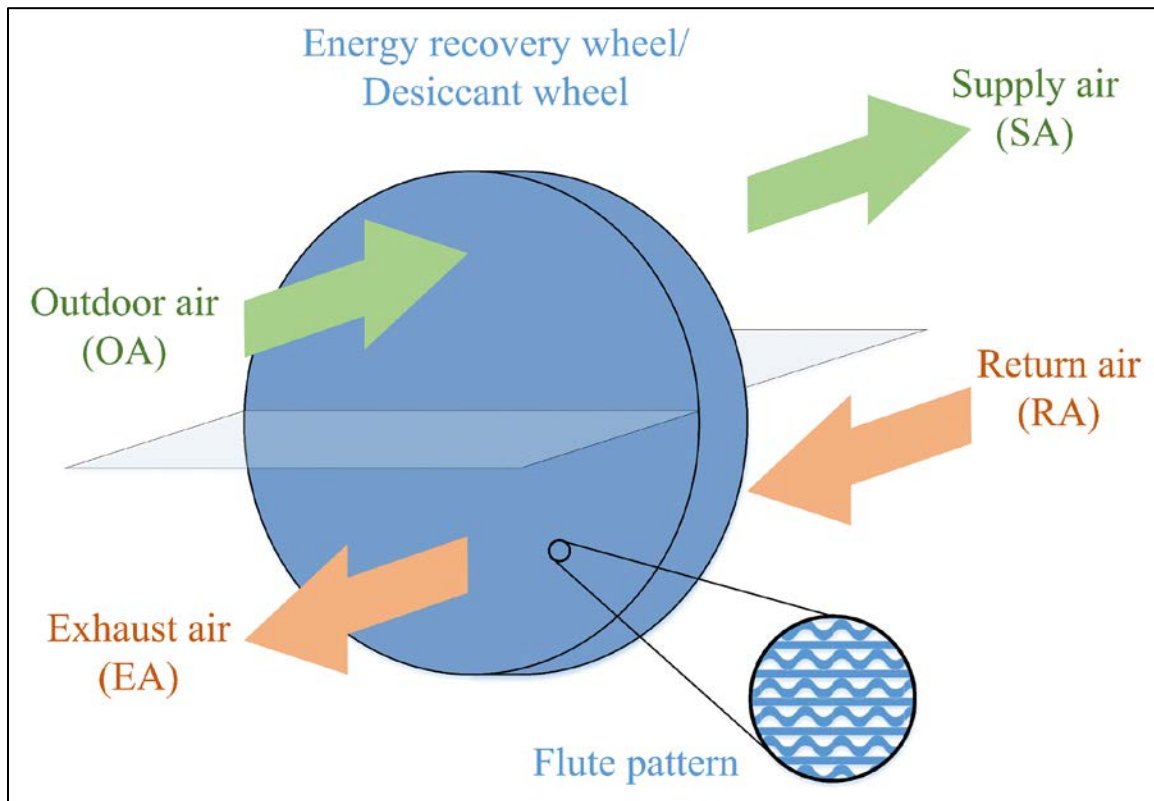


Fig. 1 Working theory of desiccant based wheels

While an energy recovery wheel or a desiccant wheel is rotating, heat and mass transfer takes place between the air, desiccant, and substrate of the wheel. Four governing equations dominate the heat and mass transfer processes, which include mass and energy conservation in both the air and desiccant. The four governing equations will be presented in Chapter 4. A finite difference method (FDM) is commonly applied to solve the governing equations and simulate the heat and mass transfer occurring in a wheel. Even though FDM is a powerful tool, it is time-consuming to complete the computation. If an energy consumption simulation of an energy recovery wheel or a desiccant wheel integrated HVAC system is conducted on an annual basis using hourly load and weather data, it will take a tremendous amount of time to generate the full set of results. Furthermore, an optimization of the parametrized models using FDM would be limited in the application due to its computational time. Hence, current building energy simulation software utilizes an efficiency factor to simulate the performance of wheels, instead of



implementing FDM in a wheel component module in various building energy modeling platforms [4], a typical energy recovery wheel module or a desiccant wheel module uses an efficiency factor to conduct simulations, the efficiency factor is typically provided by wheel manufacturers or obtained from experimental results. If optimizations or parametric studies are conducted in building energy software, different efficiencies of the energy recovery wheel/desiccant wheel need to be input for each iteration according to the control variables. Thus, it is difficult to conduct optimizations or parametric studies of a wheel-integrated HVAC system with the current setup in building energy simulation software. Optimization of the whole HVAC system integrated with a wheel will require a more efficient approach instead of an FDM or an efficiency factor method.

Establishing performance mapping methods of energy recovery wheels and desiccant wheels is a valuable approach for conducting optimizations or parametric studies of an energy recovery ventilator or a desiccant wheel integrated-HVAC system. Typically, studies on energy recovery wheels or desiccant wheels focus on establishing FDM models to predict the performance of a selected wheel, then conduct optimization on one of the physical dimensions (e.g., wheel diameter or depth) or operating settings (e.g., wheel rotation speed or airflow rate). Currently, there is no study in the literature proposing the development of a mapping model controlling all physical dimensions and operating settings at the same time. If a study targets another wheel that has a different physical dimension or runs at a different operating setting, the models need to be retrained. For parametric studies on wheels with different geometries or operating settings, the work of training and validating the models for all the wheels would consume a tremendous amount of time; hence, this characteristic of FDM models is disadvantageous for conducting parametric or optimization studies. If an approach can accurately and quickly predict the performance of energy recovery wheels or desiccant wheels with different geometries or operating conditions, it will be beneficial for academic studies and research and development activities in the industry. For industry, the solution can achieve a more economical design; for academia, the solution can provide an easy approach for studies on different HVAC systems that employ desiccant wheels or energy recovery wheels. Therefore, it is necessary to develop an efficient mapping method for conducting parametric studies or optimization research on desiccant wheel/energy recovery wheel integrated HVAC systems.

## 2. LITERATURE REVIEW

The concept of implementing a thermal wheel was introduced by Fredrik Ljungström in 1920. Abundant research and development activities have been dedicated to understanding thermal wheel physical behavior and analyzing and optimizing their design for nearly a century. Simonson [8] developed a new approach to the governing equations for energy wheels. The governing equations which were dependent on the enthalpy and relative humidity of the air and the desiccant were modified to depend on the temperature and humidity ratio of the air and the desiccant. Furthermore, reasonable assumptions were introduced that allow the governing equations to be uncoupled. Hence, the governing equations can be solved separately, simplifying the finite difference method solving process. Simonson's governing equations have been widely utilized in research ever since.

Ge et. al. [9] compared different mathematical models that have been developed for performance predictions of energy recovery wheels and desiccant wheels. The paper categorizes models based on assumptions, governing equations, and solution methods; and sorts the models into two major types: gas-side resistance (GSR) models and gas and solid-side resistance (GSSR) models. In the GSR model, heat and mass diffusion within the desiccant material itself is not considered, but heat conduction within the substrate is included. The temperature and humidity ratio within the desiccant from the surface layer to the inner layer are assumed identical. The GSR model compromises accuracy for relatively simple governing equations that can be solved more quickly. The GSSR mathematical model includes second-order heat and mass transfer terms within the desiccant in the governing equations, which refines the precision of this model. The heat and mass transports exhibit as diffusion within the desiccant. The GSSR model can be subcategorized into three more types: Pseudo-gas-side (PGS) model, gas & solid-side (GSS) model, and Parabolic concentration profile (PCP) model. The PGS model introduces lumped transfer coefficients to represent heat and mass transfer resistances in the gas side and solid side instead of directly involving the second-order heat and mass transfer terms of the diffusions in the governing equations. Nonetheless, lumped transfer coefficients require considerable experimental data to calculate. The GSS model engages heat and mass transfer coefficients of desiccant and the second-order heat and mass transfer terms. The GSS model's accuracy is improved. However, while the GSS model can offer a more accurate prediction of energy recovery wheel performance, the

computational time is significantly longer. The PCP model proposes a parabolic concentration profile to show the diffusion of heat and mass transfer within the desiccant. The PCP model avoids the shortcomings of PGS and GSS models. On the other hand, the applicable range of the PCP model is limited. Based on the characteristics of the above models, the GSR model will be utilized in the current research effort because of its time-saving advantage, less dependence on extensive experimental data, and acceptable accuracy in performance predictions.

## **2.1 Experimental Evaluation Studies**

Physical experiments have been conducted for the performance evaluation of desiccant wheels or energy recovery wheels. Angrisani et al. [10] designed a poly-generation system consisting of a natural gas-powered CHP and a desiccant wheel integrated HVAC system. They focused on studying the dehumidification capacity of a desiccant wheel. They observed that the outdoor weather (temperature and humidity ratio) condition affects the performance of desiccant wheels significantly. Hence, the system was simulated multiple times based on the weather data of major cities worldwide. The dehumidification efficiency of the desiccant wheel decreases while inlet outdoor air temperature and humidity ratio increase.

Uckan et al. [11] configured a desiccant based evaporative cooling system for HVAC application and tested it under hot and humid climates. Results showed that the effectiveness and the cooling capacity for the system are high even with different outdoor conditions.

Kang and Lee [12] experimentally evaluated the performance of three different thicknesses of desiccant wheels. Various airflow rates and rotation speeds are controlled to observe the dehumidification efficiency of the wheels. Their result showed the effect of the wheel depth, air velocity, and rotation speed on the performance of a wheel.

Eicker et al. [13] conducted experiments on several desiccant wheels available in the market. They measured and calculated parameters listed as follows: specific-heat inputs during regeneration, process air enthalpy change, dehumidification effectiveness, moisture removal (represented by functions of the rotation speed), inlet humidity ratio, volume flow ratio, and regeneration temperature. They discovered that the optimal rotation speed is lower for lithium chloride or compound based wheels than for silica gel wheels. While the regeneration air temperature increases, dehumidification capacity increases also. In addition, dehumidification efficiency increases at an equal rate. The relationship between regeneration specific heat input and

enthalpy changes of the process air were observed and recorded. Then, the influence of the regeneration air humidity was also significant. Lower relative humidity of the regeneration air boosts the dehumidification potential. Finally, the dehumidification efficiency is not affected notably by specific regeneration heat input and latent heat change of the process air. In humid climates, this is an advantage for desiccant cooling applications.

Angrisani et al. [14] conducted experiments on the performance of different parameters under various inlet temperatures and humidity ratios of the process air stream; also, under different inlet temperatures and humidity ratios of the regeneration air stream; and different ratios of airflow rates between the regeneration air stream and process air stream. Comparisons between the results of experiments and the data provided by a manufacturer were demonstrated. The testing results show good agreements with data provided by a manufacturer. Angrisani observed that the dehumidification capacity and efficiency are influenced more by the regeneration temperature than the regeneration air flow rate according to the experiments. The author also mentioned that the experiments could be employed for other academic purposes, and provided a testing method guide for future testing setup in other research.

Enteria et al. [15] conducted experiments evaluating a heat wheel and a desiccant wheel operating separately and together at different regeneration temperatures ranging from 60 to 80 °C. The evaluations were based on moisture removal capacity, moisture removal regeneration, moisture mass balance, total energy balance, sensible coefficient of performance, latent coefficient of performance and, total coefficient of performance. The study identified that moisture removal capacity and moisture removal regeneration these two parameters could not determine the efficiency of the wheels alone. Sensible coefficient of performance, latent coefficient of performance and, total coefficient of performance should be included to fully determine the efficiency of the wheels. The results were shared for benchmarking or validation of other researchers' purposes.

Goldsworthy and White [16] analyzed and optimized the performance of a system consisting of a desiccant wheel and an indirect evaporative cooler. At the regeneration air temperature equals 70°C, a supply airflow rate to regeneration airflow rate ratio of 0.67 generated the best performance. COPs of the system with different wheel depths were evaluated and a correlation of wheel depth, wheel rotation speed, and power consumption of the system was plotted

and discussed. There is not a general a systemized approach that describes the effect of wheel rotation speed, wheel depth, and airflow rates on the wheel performance delivered in the paper.

Angrisani et al. [17] tested the rotational speed on dehumidification effectiveness at low regeneration temperatures (60°C to 70°C) since the rotational speed of desiccant wheels is the most influential to the performance. Furthermore, the author indicated the effect of rotational speed on the thermal performance of the desiccant wheel (e.g., process air outlet temperature or SER). The author explained that thermal performance is important to the analysis since it also influences the dehumidification potential. Among different testing conditions, they observed that the wheels have optimized dehumidification capacity while rotational speeds range from 5–10 RPH depending on the operating environment.

Recently, a new desiccant material was investigated in different studies. Cao et al. [18] experimented with three different depths of new polymer desiccant wheels. The regeneration temperatures were varied to study optimum sensible and latent COP. Additionally, different wheel rotation speeds were tested to locate optimal working conditions. The author pointed out that a 50mm or 70mm polymer desiccant wheel depth can deliver the same or even better performance than the traditional desiccant wheel (150mm depth). Hence, a more compact HVAC system can be expected with the application of a polymer desiccant wheel.

Zendehboudi and Esmaili [19] investigated the potential and the performance of desiccant wheels applied in hot and humid climates. Two desiccant materials, Silica Gel and Molecular Sieve were studied. When the wheel rotation speed increases, that leads to moisture removal decreases for both materials. Furthermore, the sensible heat transfer increases when the wheel rotation speed increases.

Zendehboudi et al. [20] conducted parametric studies on Silica Gel and Molecular Sieve wheels under three different wheel depths. The model was built by a hybrid approach-adaptive neuro-fuzzy inference system (hybrid-ANFIS), and the model was compared with a genetic algorithm-least square support vector machine approach. The hybrid-ANFIS was proven to be a simple and fast tool for wheel simulations, and artificial neural network algorithms are suitable for solving engineering problems and mapping experimental data. Then regeneration temperature, regeneration airflow rate, and wheel rotation speed were targeted for optimization, and the results were plotted.

Tu and Hwang [21] identified the performance of a desiccant and optimized process stream to regeneration stream facial area ratio when the regeneration process utilized three different heat sources (electrical heater, natural gas burner, and vapor compression system). An area ratio = 2:1 is suggested when an electrical heater or a natural gas burner is used; an area ratio = 1:1 is suggested when a vapor compression cycle is used; and an area ratio = 1:1 is suggested when a heat recovery unit is used.

One major application of energy recovery wheels is their use as ventilation air preconditioners in HVAC systems. Several papers in the literature have studied the performance of HVAC systems with integrated energy recovery wheels. Chung [22] develop a comparison between different energy recovery wheel flute geometries, wheel rotation speeds, outdoor air conditions, return air conditions, and adsorption isotherms of desiccants. The paper shows performance variations with the different variables mentioned above and focuses on the optimization of the wheel characteristics to achieve the most efficient COP.

## **2.2 Mathematical Model Development Studies**

Mathematical modeling of an energy recovery wheel is complicated due to the complex physical processes of heat and mass transfer occurring in a wheel. Hence, there are studies devoted to developing a simple approach to simulating the performance of energy recovery wheels. Zhai [7] includes detailed information related to the numerical simulation settings for an energy recovery wheel and an active desiccant wheel. The author intended to develop a numerical model that applies to both types of wheels. The model was established based on the finite difference method (FDM) and the explicit Euler forward approach. The effect of the purge setting and the residual moisture in wheels were considered in this research. In the paper, physical parameters for an energy recovery wheel and adsorption isotherms are stated. This information can be utilized by other researchers to validate their energy recovery wheel or desiccant wheel numerical models. The energy recovery wheel and the desiccant wheel that were studied and presented in this paper are commercially available in the marketplace. The model was validated by experiments. The author observed that the purge reduced the performance of the energy recovery wheel by 5% but the impact on the active desiccant wheel was limited. The author also noticed that a well performing wheel (both energy recovery wheel and desiccant wheel) requires an optimized design

between environmental conditions, airflow rate, and wheel operation strategies. An optimization procedure was neither proposed nor developed in this research.

Van den Bulck and co-workers [23] pointed out that GSSR models consume a lot of computational time, so they proposed a solution to this problem by applying an effectiveness-number of transfer units ( $\epsilon$ -NTU) method to the governing equations. The results of this research demonstrated that an  $\epsilon$ -NTU model can accurately and quickly predict the performance of a desiccant cooling system, which makes it suitable to utilize in long-term energy simulations. The study established a prototypical function to calculate the efficiency of the energy recovery wheel. However, the function is valid for one energy recovery wheel. If there is another wheel planned to be simulated, the function needs to be recomputed for the new wheel. This characteristic makes the model unsuitable for parametric or optimization studies.

Beccali and co-workers [24] believe that the models used to compute heat and mass transfer phenomena inside desiccant based systems are too excessive, and so they proposed a straightforward empirical model that can be used to estimate the performance of a desiccant wheel. An empirical model called “Model 54” was built to predict the outlet air temperature and humidity ratio in a silica gel desiccant wheels based system. Their approach requires the training of 54 coefficients to fully develop the prediction capabilities for an energy recovery wheel. An empirical equation that is further reduced in complexity was later investigated by Beccali et al. [24], which calculates the performance of an energy recovery wheel via only four parameters. The model was formulated by the relative humidity and the enthalpies of the outdoor air stream and return air stream. Results of the simplified model were shown to predict reasonably well the performance of all the wheels included in the study. The model is suitable for predicting the performance of a selected wheel, however, numerous data points are required. Additionally, if wheel geometries change, the model needs to be re-trained. Hence, the model is also not suitable for extensive parametric studies nor optimization.

De Antonellis [25][26] conducted optimization and parametric studies that were focused on maximizing the sensible effectiveness of an ERV while minimizing pressure drop under different inlet air conditions. De Antonellis [26] conducted an optimization of energy recovery wheels. An FDM mathematical model was developed. The model was established on the PDE governing equations and solved by the Euler forward method in MATLAB. Then the model was validated against experimental data. There were five experiments conducted. Two observed outlet

process air humidity ratios versus different angular positions. From these two experiments, the effectiveness of dehumidification was observed. At the very first stage (smaller angular position), the dehumidification process was less effective, since the desiccant is still warm. After the desiccant was warmed up, the dehumidification capacity reaches its maximum. Then the dehumidification capacity gradually decreased, because the desiccant water content increased. The other three experiments emphasized the effect of wheel rotation speed on the dehumidification capacity. The best dehumidification effect ranges from 5 to 10 rev/h under different inlet air humidity ratios. Next, parametric studies were performed with a few sets of combinations of different inlet air temperatures, humidity ratios, airflow rates, and wheel rotation speeds. The study focused on observing the pattern of the energy recovery wheel's effectiveness to each parameter and delivered a graphical comparison. A simplified equation or systematized solution approach, which can be used to predict the performance of an energy recovery wheel was not included.

Parmar [27] implemented an artificial neural network (ANN) method to predict the outlet air temperature and humidity ratio in the process air stream. The artificial neural network method delivers a precise and accurate result. The works completed in the paper includes comparing experimental results versus data published by the manufacturer; the model was trained and validated in a given range, and the ANN simulation results yielded smaller mean square error results than other algorithms; a curve-fitted equation was generated and used for estimation of the outlet air temperature and humidity ratio of the desiccant wheel while designing a desiccant cooling system.

Koronaki et al. [28] developed and trained a black box model via the artificial neural network method. The key parameters of experimental data to predict state conditions of the air in the process and regeneration streams includes process air inlet temperature, humidity ratio, and airflow rate and regenerations air inlet temperature, humidity ratio, and airflow rate. It was shown that the model is capable of predicting outlet air conditions of temperature and humidity ratio and the conditions of the desiccant under different climates. The physical characteristics and operating conditions of the wheel are not considered. This approach is similar to using the efficiency factor of a wheel to predict performance. Hence, the model is not suitable for parametric studies, since whenever physical characteristics and operating conditions of a wheel change, the model has to be retrained.



Jani et al. [29] introduced another artificial neural network-based model for predicting the outlet conditions of temperature and humidity ratio in the process air stream. The model was validated against experimental data. Based on the predictions of the outlet conditions, dehumidification effectiveness and moisture removal capacity are calculated. The model demonstrated good agreement between testing results and model predictions, and the correlation of the two data sets ranges from 0.998 to 0.999. Furthermore, the unique character of the method introduced in the research is the requirement of only a few number of testing data points. The artificial neural network developed by Jani only needs 10 data points for training the model. This reduces excessive time and cost on experiments of desiccant wheels. The model is designed for one single wheel. Once any of the physical dimensions (e.g., wheel diameter or wheel depth) of the wheel changes, the artificial neural network model must be retrained. This behavior makes the model unsuitable for more generalized optimization and parametric studies.

Yamaguchi and Saito [30] designed and conducted experiments then developed and validated a mathematical model of a silica gel desiccant wheel. The experiments controlled different operating conditions listed as follows: regeneration air temperatures, airflow rates, and rotation speeds. In their research, the average relative error of the humidity ratios at the outlet of the supply air stream between the predictions of the mathematical model and the measurements of the experiments is 3.3%; the average relative error of the air temperatures at the outlet of the supply air stream is 10.8%. The experiment and the mathematical model showed good agreement between each other. The authors delivered a graphical illustration of the effects on the dehumidification performance of the desiccant wheel according to different inlet air velocities, temperatures, and wheel depths. The charts showed the effect of each variable on wheel performance (e.g., inlet air velocity to the dehumidification performance, wheel depth to the dehumidification performance). The effect of the combination of two or more control variables was not presented in the paper.

Antonellis et al. [31] proposed efficiency parameters for desiccant wheel performance prediction. The outlet condition was estimated based on the efficiency of a wheel, and the correlation between the model and the experimental data was identified. The relative error between the predictions and measurements is lower than 10% in 82.1% of the studies on humidity ratio and 98.2% of studies on air temperature. In other words, almost 20% of the cases have a relative error prediction that is higher than 10% while implementing their efficiency parameter method. Meanwhile, the relative error of the pressure drop was under 5% in all cases. The calculation of

root-mean-square errors was performed. The RMSE between the predictions and the measurements was  $0.66^{\circ}\text{C}$  for air temperatures and  $0.24\text{ g/kg}$  for humidity ratios. The author mentioned that this method is suitable for building energy simulation since the calculation is less time-consuming. On the other hand, the method may not be ideal for parametric studies nor optimizations. This is because the method needs to be retrained if desiccant wheel physical dimensions change.

Zendehboudi [32] introduced a model via the least square support vector machine and a genetic algorithm to predict the performance of desiccant wheels. The model takes rotation speed, inlet air temperature, and humidity ratio of the process stream as the inputs, and generates outputs of outlet air temperature and humidity ratio of the process stream and regeneration stream, moisture removal capacity, and sensible energy ratio. The sensible energy ratio is dominated by the desiccant material type. The model was examined by three statistical error tests. There were two types of desiccant materials tested (silica gel and molecular sieve); the regressions were 0.994 and 0.996 respectively; the mean square errors were 0.0038 and 0.072; the mean average errors were 0.056 and 0.23. The model delivered a high quality of predictive results. The method is more suitable for building energy simulation comparing to the artificial neural network method since it computes faster, and is more precise and accurate. However, the model doesn't include physical characteristics (e.g., wheel diameter or wheel depth) or operating conditions (e.g., airflow rate) of the wheel. Therefore, the model is not an ideal tool for parametric studies nor optimizations, since the model needs to be retrained whenever the physical characteristics and operating conditions of a wheel change.

Panaras et al. [33] introduced a model of a simplified efficiency factor to represent the performance of desiccant wheels based on Jurinak formulas. The efficiency factors of the model only require few measurements, so the model is easy to train. The model is validated by using experimental data, then the test results were compared with manufacturers' data provided. The results agreed well with each other. The application of temperature ranging from  $30^{\circ}\text{C}$  to  $60^{\circ}\text{C}$ , and humidity ratio ranging from  $0\text{ g/kg}$  to  $12\text{ g/kg}$ . The operating range covers the typically applied environment of desiccant wheels. The model was proven to be applicable for evaluating the efficiency of desiccant wheels. Based on this study, a constant representing the efficiency factor of a desiccant wheel is valid. However, the model needs to be retrained if the physical dimensions

of the desiccant wheel change. Even though the model is easy to train, this characteristic of the model limits its application in parametric studies or optimization.

Zendehboudi [34] proposed a generic algorithm for desiccant wheel optimization. Regeneration temperature, surface area ratio, rotational speed, and diameter are selected as the most influential design variables of the wheels. The response surface method is implemented to form the algorithm formula, then a genetic algorithm is utilized as an optimization tool in this research. In this paper, quadratic equations that consist of four designed variables represent the outlet temperature and humidity ratio for the desiccant wheels. The algorithm was validated and shown to be reliable and accurate. However, the wheel depth is not considered in the algorithm, as well as the inlet air temperature. Both features make the algorithm lack the flexibility necessary for parametric studies.

The optimization of an energy recovery wheel based on an artificial neural network method is proposed by Comino [35]. The author targets to develop a model that gives the prediction of two outputs (air temperature and humidity ratio of the outlet process stream). The input layer contains the inlet air temperature/humidity ratio of the process stream and regeneration stream, airflow rate, and rotational speed. A graphical relationship between each input is demonstrated in the paper. The artificial neural network method is suitable for optimizations, on the contrary, it is not ideal for parametric studies. Furthermore, wheel depth is not considered in the artificial neural network method. This characteristic prevents the method from delivering flexible parametric studies on wheel depth.

Kodama et al. [36] targeted to optimize the wheel rotation to achieve the best dehumidification and cooling performance. The authors investigated the optimized rotational speed and performance of a wheel by plotting experimental data points on a psychrometric chart. The temperature and humidity ratio changes between inlet and outlet conditions have a linear relationship in a desiccant wheel system. This characteristic inspires the development of a more generalized performance mapping method in the research.

Chung et al. [37] investigated numerical functions for the moisture removal capacity of a desiccant wheel represented by the regeneration air temperature, rotational speed, and surface area ratio. The model was validated over a range of air temperatures in the regeneration stream from 60°C to 150°C. Then the numerical functions are utilized in optimizing the moisture removal capacity by varying the rotational speed and the surface area ratio. Two phenomena were observed

in this study. The first one is that the optimum wheel rotation speed decreases then becomes constant while the air temperature of the regeneration stream increases. The other one is that the lower the humidity ratio of the outdoor air, the higher the optimum wheel rotation speed becomes. The study indicated that there is a certain relationship between inlet air conditions and wheel rotation speed to wheel performance. The function brought the idea that wheel performance can be represented as a function of wheel physical characteristics and operating conditions.

Antonellis et al. [38] developed a one-dimensional gas-side resistances desiccant wheel model. The model was examined with experimental data. The Euler forward method is utilized in model development and simulation. With the model, the authors researched the optimized rotational speed and process air stream angular position by considering inlet air temperatures and humidity ratio of the process and regeneration streams. The optimization with FDM is time-consuming, and this is one of the improvements in using a mapping method to conduct optimizations. The researcher presented a trend of performance impacts of each control parameter. However, FDM optimization is not time efficient, hence, it will not be implemented in this research.

Ge et al. [39] established a mathematical model for performance estimation of a silica gel wheel. Gas-side and solid-side resistances are both considered in the model (gas-side resistance model). The new model delivered a more accurate and precise prediction than the author's previous work. The author controlled experimental environments including the angle of regeneration section (from  $100^\circ$  to  $160^\circ$ ), the regeneration temperature (from  $80^\circ\text{C}$  to  $90^\circ\text{C}$ ), and process/regeneration airflow rate (from 2.0 m/s to 3.5 m/s). In the study, there were few conclusions delivered according to the simulation results. First, absolute moisture removal and relative moisture removal capacities increase when the central angle of the regeneration section gets bigger. Next, a lower relative moisture removal capacity was observed when the ambient humidity ratio is higher. Third, higher relative moisture capacity was obtained while the regeneration temperature increases. Last, moisture removal capacity to an optimal rotational speed was observed while approaching maximum moisture removal capacity. The result demonstrated the trends of desiccant wheel performance.

### 2.3 Nusselt Number Evaluation Studies

The Nusselt number, which is defined as the ratio of conductive thermal resistance to convective thermal resistance is an important value in the heat transfer analysis of an energy

recovery wheel. Most energy recovery wheels use sinewave shaped channels in their design and construction. Chung [14] mentions that the Nusselt number of a triangular channel is similar to that of a sine-shaped channel, and so are the hydraulic diameters. Lakshminarayanan [40] states that the actual Nusselt number varies along the airflow axis for different shaped triangular ducts. Haji-Sheikh and co-workers [41] discuss the phenomenon of Nusselt number variation in the developing region of a triangular duct.

There are abundant studies available in the literature that are focused on energy recovery wheels and desiccant wheel; however, most papers assume a constant Nusselt number throughout the wheel in their studies. The following papers listed in Table 1 all consider the Nusselt number as having a constant value along with the flute of the energy recovery wheel. However, Haji-Sheikh et al. [41] noted that the Nusselt number is generally in the developing region while the air is traveling through a flute of an energy recovery wheel.

Table 1 Nusselt numbers are utilized in papers that study energy recovery wheels.

Paper	Nu
Design Optimization of Heat Wheels for Energy Recovery in HVAC system, De Antonellis et al., 2014 [25]	constant
Simulation, performance analysis and optimization of desiccant wheels, De Antonellis et al., 2010 [26]	constant
A non-adiabatic desiccant wheel: Modeling and experimental validation, Narayanan et al., 2013 [42]	3.6
Analysis of Simplifying Assumptions for the Numerical Modeling of the Heat and Mass Transfer in a Porous Desiccant Medium, Ruivo et al., 2006 [43]	constant
Comparative performance of desiccant wheel with effective, Yadav & Yadav, 2014 [44]	constant
Effect of desiccant isotherm on the performance of desiccant wheel, Chung & Lee, 2009 [45]	constant
Mathematical investigation of purge sector angle for clockwise and anticlockwise rotation of desiccant wheel, Yadav & Yadav, 2016 [46]	constant
Modeling analysis of an enthalpy recovery wheel with purge air, Ruan et al, 2012 [47]	3.267
Application of Desiccant Adsorption for Air-Conditioning Cycle, Esfandiari Nia & van Paassen, 2006 [48]	3.63-4.364
Use of compound desiccant to develop high performance desiccant cooling system, Jia et al., 2006 [49]	20

## 2.4 Wheel Integrated HVAC System Study

Nia et al. [50] proposed a correlation method to obtain the efficiency of the desiccant wheel according to the operating conditions (rotational speed, process air dry-bulb temperature/humidity ratio, regeneration air dry-bulb temperature, process airstream face velocity) and the wheel physical measurements (desiccant thickness, hydraulic diameter of flutes). The authors used more than 500 data points generated by a numerical model to train and validate the method. The prediction of the correlation method delivered results of less than 2% error. The author suggested that the correlation can be implemented in studies of annual energy consumption simulations; however, wheel depth- an important wheel design parameter was not included in the correlation method.

Ruivo et al. [51] introduced an efficiency method based on the enthalpies and relative humidity in the process airstream and regeneration stream. The traditional wheel efficiency factor is calculated by dry-bulb temperature and humidity ratio measurement. The authors collected a wide range of experimental data to examine the method, then indicated that the new efficiency method is more accurate than the traditional efficiency factor in predicting outlet air conditions. Ruivo et al. [51] suggested that the efficiency method is beneficial to implement in building energy simulation; nonetheless, the method is designed for a wheel with unchanged geometries and operating conditions. Hence, the method is not ideal for conducting optimizations of a wheel integrated system under transient operating conditions.

De Antonellis et al. [25] took the first step in the design optimization of energy recovery wheel-integrated HVAC Systems. There were two test rigs built, and the inlet air conditions are fixed. One was designed for sensible measurement, and the other was for pressure drop measurement. A parametric study about the relationship between sensible effectiveness and pressure drop was conducted. The most ideal wheel depth in a specific airflow range was identified. Next, parametric studies of flute dimensions took place. Lastly, wheel depth parametric studies were conducted. The study emphasized the evaluations of energy recovery wheels. The optimization results are based on experimental data, and there is no method proposed for integrating with transient building energy performance simulation software.

Comino et al. [52] investigated the performance of a desiccant wheel and indirect evaporative cooler integrated HVAC system (DW-IEC system). The annual energy consumption of the system was compared with a traditional direct expansion conventional system (DX system).

The authors established an empirical function that contains 21 coefficients to represent the performance of a desiccant wheel to predict the outlet air condition from the desiccant wheel. The empirical function was implemented into a building energy simulation software (TRNSYS) to conduct an annual simulation at 15 minute timesteps. The results indicated that the DW-IEC system provided up to 46.8% energy saving over a DX system. Even though the empirical function proposed by Comino et al. [52] can be utilized in a transient building energy simulation, it is limited to one desiccant wheel design. If geometries or operating conditions of the desiccant wheel change, the empirical function needs to be retrained; hence, the function is not suitable for optimizations or parametric studies.

## **2.5 Literature Review Conclusion**

The above studies utilize constant Nusselt numbers while analyzing the performances of energy recovery wheels. This may lead to some information loss on the performance prediction of energy recovery wheels or desiccant wheels. If a dynamic Nusselt number is utilized in a mathematical model of energy recovery wheels, the accuracy of the energy recovery wheel or desiccant wheel simulation would be enhanced.

Previous research presented in the open literature is focused on developing a method to predict the performance of a single energy recovery wheel or a single desiccant wheel without changing the wheel physical dimensions (e.g., wheel diameter or depth), and then applying the model under different working conditions (e.g., air temperature, humidity ratio, or airflow rate). With this approach, if any physical dimensions of the energy recovery wheel or desiccant wheel change, the models in the above studies need to have their approach modified and recalculated to determine the new operating characteristics. This is also true of any case where the operating settings (e.g., wheel rotation speed or airflow rate) change. In addition, the process is time-consuming and requires a set of experimental data. For parametric studies on geometries of energy recovery wheels or desiccant wheels, it will take a significant amount of time to establish and run all of the necessary model perturbations. This makes the use of these models disadvantageous for carrying out parametric or optimization studies for changing wheel physical dimensions.

The complexity of simulating a wheel integrated HVAC system has been noted in previous studies. Several approaches are proposed in order to simplify the simulation procedure; however, the universality of the approaches is limited because they lack the flexibility to change wheel

physical dimensions or operating settings. Thus, the approaches are not ideal for optimizing a wheel design under transient operating conditions.

Since these models are not ideal for parametric studies and optimization research on wheel dimensions or operating settings simultaneously, it is necessary to develop a new method to conduct this type of study. Significant advancements in industrial settings and academic research are possible with the development of a solution procedure that can quickly and accurately predict energy recovery wheel or desiccant wheel performance while design parameters or operating settings change. For industry, the solution can offer a more economical design; for academia, the solution can provide an easy approach for studying HVAC systems with energy recovery wheels or desiccant wheels.



### 3. RESEARCH OBJECTIVES

The objective of this research is to develop simple, robust, and accurate simulation tools to evaluate and optimize the performance of air handling units (AHU) integrated with an energy recovery wheel or a desiccant wheel in different climates across the U.S. Once the tools have been developed, they will be used to find optimized solutions for various cooling technologies that are recently proposed in the literature. The following list indicates the phases of research that will support these objectives.

- Develop a mapping method for energy recovery wheels
  - Develop a detailed FDM numerical model of energy recovery wheels
    - Implement dynamic Nusselt number
  - Validate the numerical model
    - Validate with experimental data
    - Validate with literature data
  - Develop and validate a mapping method for energy recovery wheels
    - Identify the form of the mapping method
    - Conduct validation against the numerical model
    - Conduct validation against literature data
- Develop a mapping method for desiccant wheels
  - Develop a detailed FDM numerical model for desiccant wheels
    - Implement dynamic Nusselt number
  - Validate the numerical model
    - Validate with manufacturer's data
    - Validate with literature data
  - Develop and validate a mapping method of desiccant wheels
    - Identify the form of the mapping method
    - Conduct validation against the numerical model
    - Conduct validation against literature data

- Conduct a performance evaluation and optimization of HVAC systems via implementing a mapping method of energy recovery wheel or desiccant wheels with a transient building energy performance simulation software
  - Evaluate the performance of an HVAC system integrated with an energy recovery wheel
    - Develop a model of the target building and the HVAC system
    - Conduct optimizations of the energy recovery wheel
    - Evaluate the performances and costs of the optimized energy recovery wheel design in different climates
  - Evaluate the performance of an HVAC system integrated with a desiccant wheel
    - Develop a model of the target building and the HVAC system
    - Conduct optimizations of the desiccant wheel
    - Evaluate the performance and costs of the optimized desiccant wheel design in different climates

## **4. MATHEMATICAL MODEL DEVELOPMENT**

The implicit FDM is selected to develop a mathematical method for energy recovery wheels and desiccant wheels in this research. The main reason for using the implicit method is that it reaches convergence faster, and it is widely used for heat and mass transfer analysis. At the beginning of this phase, an explicit method was utilized to develop a mathematical model of an energy recovery wheel. The explicit model functions well for heat transfer analysis, however, once the mass transfer was included, the explicit model delivered a diverged result. Then, the explicit FDM was replaced by the implicit FDM. The implicit method performs well for combined heat and mass transfer analysis. Hence, the implicit method is more applicable to this case. In order to conduct the FDM calculation, the first step is to isolate the target variables, then transform the governing equations to time and space partial differential equations separately.

### **4.1 Governing Equations**

Heat and mass transfer of energy recovery wheels and desiccant wheels are similar; hence, the same set of governing equations can be used to describe the performance prediction of both types of wheels. The target variables are the temperature of the air, the humidity ratio of the air, the temperature of the matrix, and the humidity ratio of the matrix. The matrix is the combination of the desiccant layer, a thin air film on the top of the desiccant, and air in the desiccant layer. The desiccant on wheels is thin (25 to 65 microns typically), hence, the temperature and humidity ratio in the matrix are assumed identical.

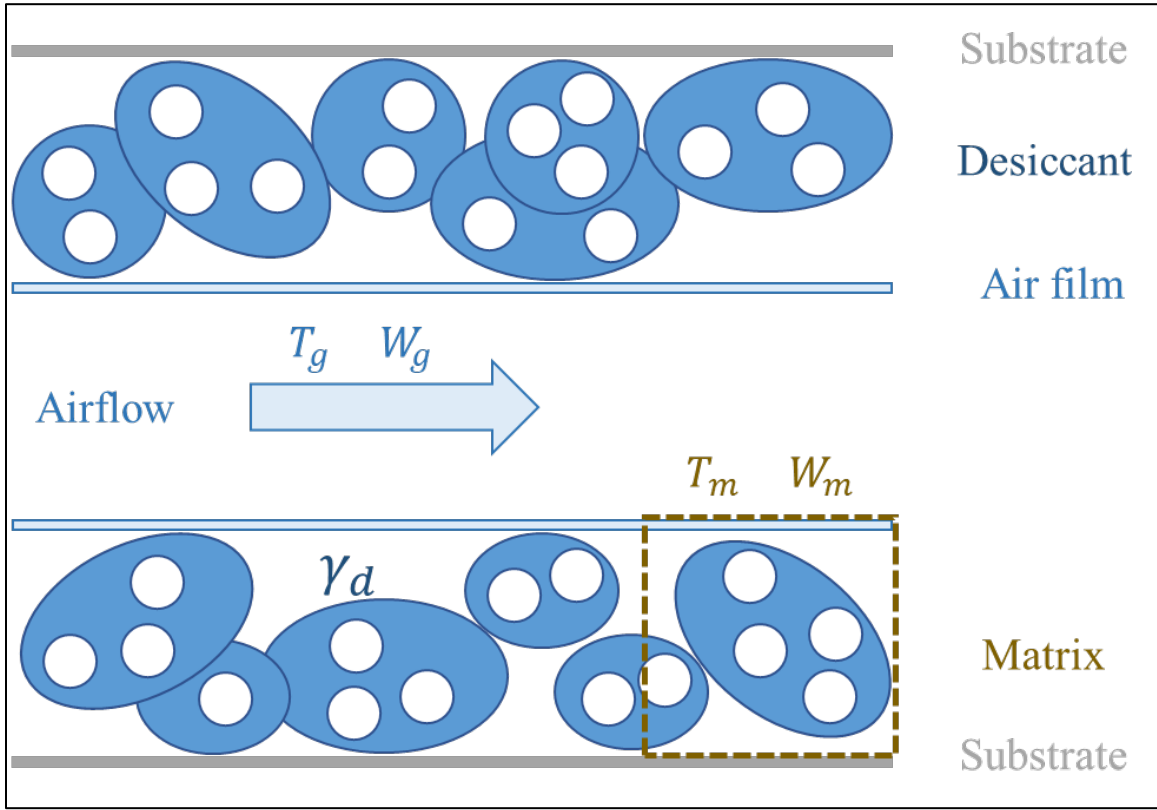


Fig. 2 Target variables in a flute of a wheel

#### 4.1.1 Energy Balance of Air Stream

$$\frac{\partial T_g}{\partial t} = \frac{h}{d_h \rho_g C p_g} (T_m - T_g) - u \frac{\partial T_g}{\partial x} \quad (1)$$

LHS:

1. Rate of energy storage in the air

RHS:

1. Rate of convective heat transfer between the air and the matrix
2. Rate of heat flux by axial airflow

Note: rate of heat conduction in the air is neglected; the rate of sensible heat transfer of the vapor before condensation or the moisture before evaporation are neglected

#### 4.1.2 Energy Balance of Matrix

$$\begin{aligned} \frac{\partial T_m}{\partial t} = & \frac{k_{sub}}{\rho_{sub} C p_{sub}} \frac{\partial^2 T_m}{\partial x^2} \\ & + \frac{h_m \Delta H_{ads}}{\rho_{sub} \delta_{sub} C p_{sub} + \rho_d \delta_d C p_d} (W_g - W_m) \\ & + \frac{h}{\rho_{sub} \delta_{sub} C p_{sub} + \rho_d \delta_d C p_d} (T_g - T_m) \end{aligned} \quad (2)$$

LHS:

1. Rate of energy storage in the matrix

RHS:

1. Rate of conduction heat transfer in the substrate
2. Rate of heat generated by moisture sorption or adsorption
3. Rate of convective heat transfer between the air and the matrix

Note: rate of sensible heat transfer of the condensed vapor or the evaporated moisture is neglected

#### 4.1.3 Moisture Balance of Air Stream

$$\frac{\partial W_g}{\partial t} = \frac{h_m}{d_h \rho_g} (W_m - W_g) - u \frac{\partial W_g}{\partial x} \quad (3)$$

LHS:

1. Rate of moisture storage in the air

RHS:

1. Rate of convective moisture transfer between air and the matrix
2. Rate of moisture flux resulted by axial airflow

#### 4.1.4 Moisture Balance of Matrix

$$\frac{\partial \gamma_d}{\partial t} = \frac{h_m}{\delta_d \rho_d} (W_g - W_m) \quad (4)$$

LHS:

1. Rate of moisture storage in the desiccant

RHS:

1. Rate of convective moisture transfer between the air and the matrix

Note: rate of mass diffusion in desiccant in the axial direction is neglected

#### 4.1.5 General Adsorption Isotherm

$$\frac{\gamma_d}{\gamma_{max}} = \frac{1}{1 - c + \frac{c}{\varphi}} \quad (5)$$

There are five unknown variables which are the temperature of the air  $T_g$ , the temperature of the matrix  $T_m$ , absolute humidity of the air  $W_g$ , absolute humidity of the matrix  $W_m$ , moisture content of desiccant  $\gamma_d$ , but there are only four equations. The variables cannot be solved with insufficient equations. Hence, we introduce one more equation: the adsorption isotherm of the desiccant.

#### 4.2 Constants and Input Parameters

To solve the implicit FDM, a matrix method operation was utilized. The constants of each term in the governing equations were fitted into a matrix and form the operators for the matrix method. Some constants need to be determined before developing the program of the mathematical model of energy recovery wheels and desiccant wheels. Several important constants from thermodynamics and fluid dynamics must first be evaluated before the program development. The constants include the following: Reynolds number, Peclet number, Nusselt number, Lewis number,

Biot number, and Fourier number. In addition, other important parameters like the hydraulic diameter of an energy recovery wheel flute and the control volume used for the mathematical model are also illustrated.

#### 4.2.1 Reynolds Number

$$Re = \frac{uL}{\nu} \quad (6)$$

The typical range of Reynolds number for airflow in the flute of an energy recovery wheel or a desiccant wheel is about 500 to 600, which indicates that the air will ultimately develop into laminar flow in a wheel flute.

#### 4.2.2 Thermal Diffusivity of Air

$$\alpha = \frac{k_g}{\rho_g C p_g} \quad (7)$$

Peclet number can evaluate whether the flow in an energy recovery wheel or desiccant wheel is in the flow domain or the diffusion domain. To calculate the Peclet number, the thermal diffusivity of the air needs to be computed first.

#### 4.2.3 Prandtl Number

$$Pr = \frac{\nu}{\alpha} \quad (8)$$

Once the thermal diffusivity of the air is identified, the Prandtl number can be calculated. Then, the Prandtl number can be used for determining the Peclet number.

#### 4.2.4 Peclet Number

$$Pe = Re \cdot Pr \quad (9)$$

Typically, the range of Peclet numbers is from 400 to 480 for airflow in the flute of an energy recovery wheel or a desiccant wheel. Since the Peclet number is significantly larger than 1, the thermodynamic and physical behaviors in energy recovery wheels or desiccant wheels are dominated by flow considerations and show that neglecting heat and mass conduction and diffusion in the axial direction is a reasonable assumption.

#### 4.2.5 Nusselt Number

The local Nusselt number data of isosceles triangular ducts for various vertex angles are stated in the paper by Lakshminarayanan [40]. The data includes local Nusselt numbers of isosceles triangles for vertex angles ranging from 5 degrees to 170 degrees. Once the hydraulic diameter of the energy recovery wheel flute is obtained it is then converted to an isosceles triangular shape with the same hydraulic diameter. The vertex angles ( $2\beta$ ) of the isosceles triangle shown in Fig. 3 can be determined and the local Nusselt number calculated by interpolation using the information in the paper by Lakshminarayanan [40].

In the work of Lakshminarayanan [40], local Nusselt numbers along the entire length of the duct are presented. Hence, a function of the local Nusselt number developing along the duct can be established by curve-fitting the available data. The Nusselt number as a function of duct depth ( $x_{duct\ depth}$ ) is represented by (10):

$$f_{Nu}(x_{duct\ depth}) = a \cdot x_{duct\ depth}^b \quad (10)$$

For purposes of the study conducted and reported in this paper, the Nusselt number for the target wheel at the entrance is  $Nu=109.7$ , and the local Nusselt number is calculated based on the above function. The local Nusselt number function for the target wheel is implemented into an FDM model to compute local convective heat transfer coefficients.



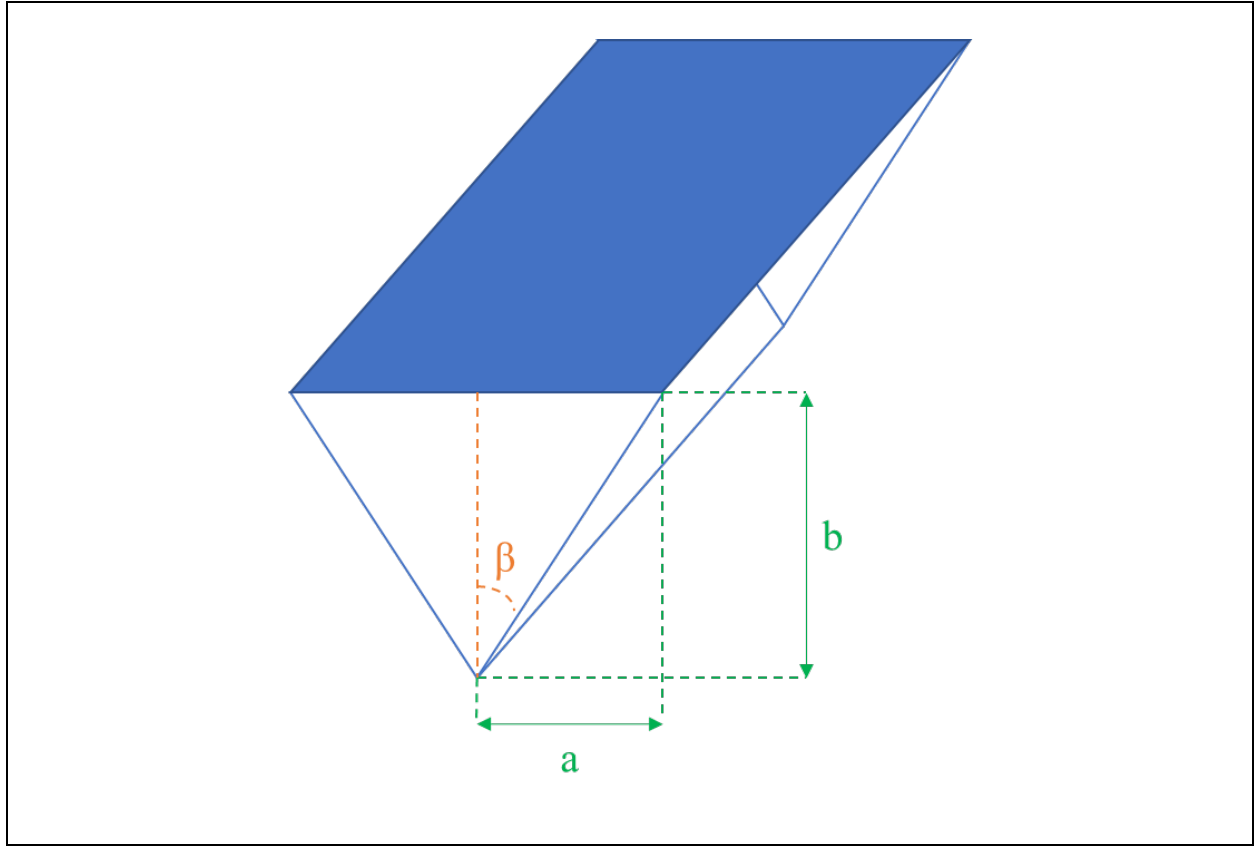


Fig. 3 The cross-sectional area of an isosceles triangular duct [40]

#### 4.2.6 Lewis Number

$$Le = \frac{h}{Cp_g h_m} \quad (11)$$

After the convective heat transfer coefficient is determined, the convective mass transfer coefficient can be calculated via the Lewis number, which is typically assumed as unity. A significant majority of the papers mentioned in the literature review also assume a Lewis number of 1.0, including Zhai [7], Antonellis [26], Chung [45], Narayanan [42], Yadav [46], and Nia [48].

#### 4.2.7 Biot Number

$$Bi_h = \frac{h}{k_d} \delta_d \quad (12)$$

$$Bi_m = \frac{h_m}{D_d} \delta_d \quad (13)$$

The typical thickness of the desiccant layer in energy recovery wheels or desiccant wheels ranges from 25 to 65 microns, hence, the Biot number is much smaller than 0.1. Thus, the temperature and humidity ratio of the matrix (thin air layer on top of the desiccant, and the desiccant can be assumed as identical).

#### 4.2.8 Hydraulic Diameter

The flute of energy recovery wheels or desiccant wheels is a sinewave shaped honeycomb structure as shown in the photograph of Fig. 4, which is a scaling plot that shows a comparison between the flute and a pure sine wave function. The bottom of the flute is twice as long as its height. The following sine wave function of the width of a flute ( $x_{flute}$ ) is used to describe the flute geometry.

$$f(x_{flute}) = 2\sin\left(\frac{\pi x_{flute}}{4}\pi\right) \quad (14)$$

Finally, the hydraulic diameter can be calculated as:

$$d_h = \frac{4A_{flute}}{p_{flute}} = \frac{4 \int_0^4 2\sin\left(\frac{\pi x_{flute}}{4}\pi\right) dx}{\int_0^4 \sqrt{\frac{\pi^2}{4} \cos^2\left(\frac{\pi x_{flute}}{4}\pi\right) + 1} dx} \quad (15)$$

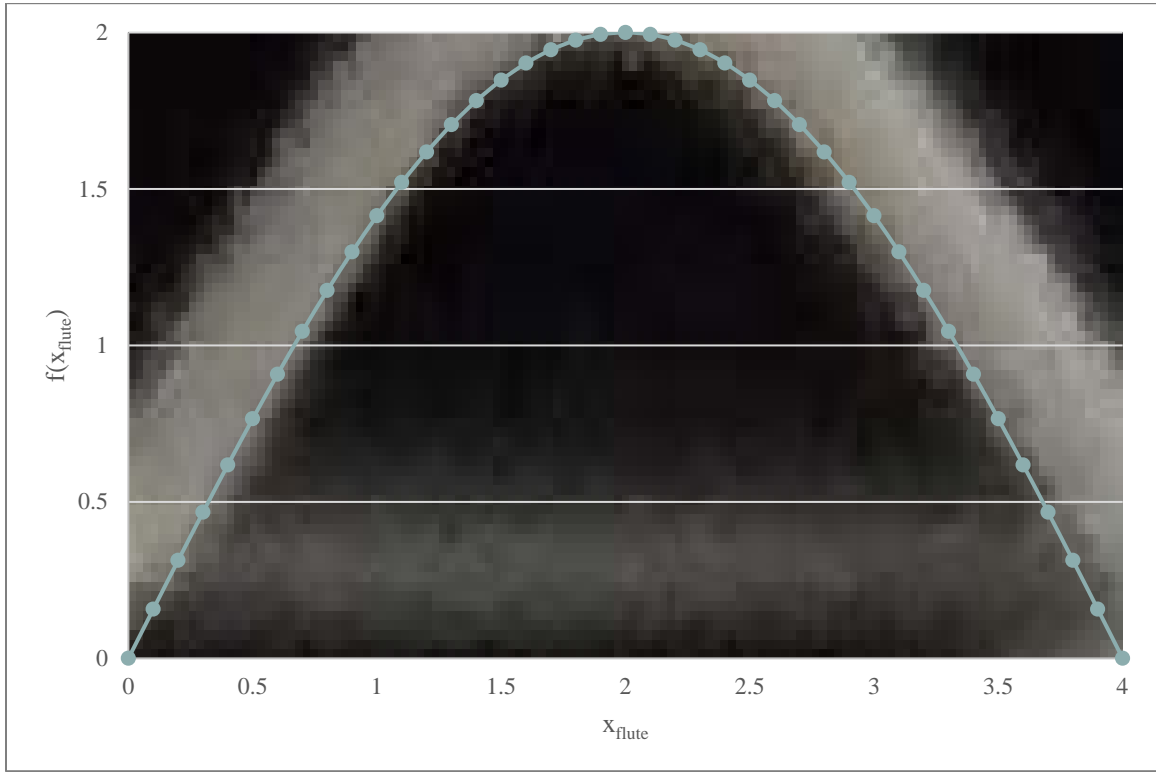


Fig. 4 Flute of a wheel and its estimated sine wave function

### 4.3 Control Volume

A single flute is selected to perform the analysis. The boundary of the control volume is from the center of the substrate. The control volume includes the substrate, desiccant, and air tunnel, then it develops from the inlet to the outlet of an energy recovery wheel or a desiccant wheel, as shown in Fig. 5.

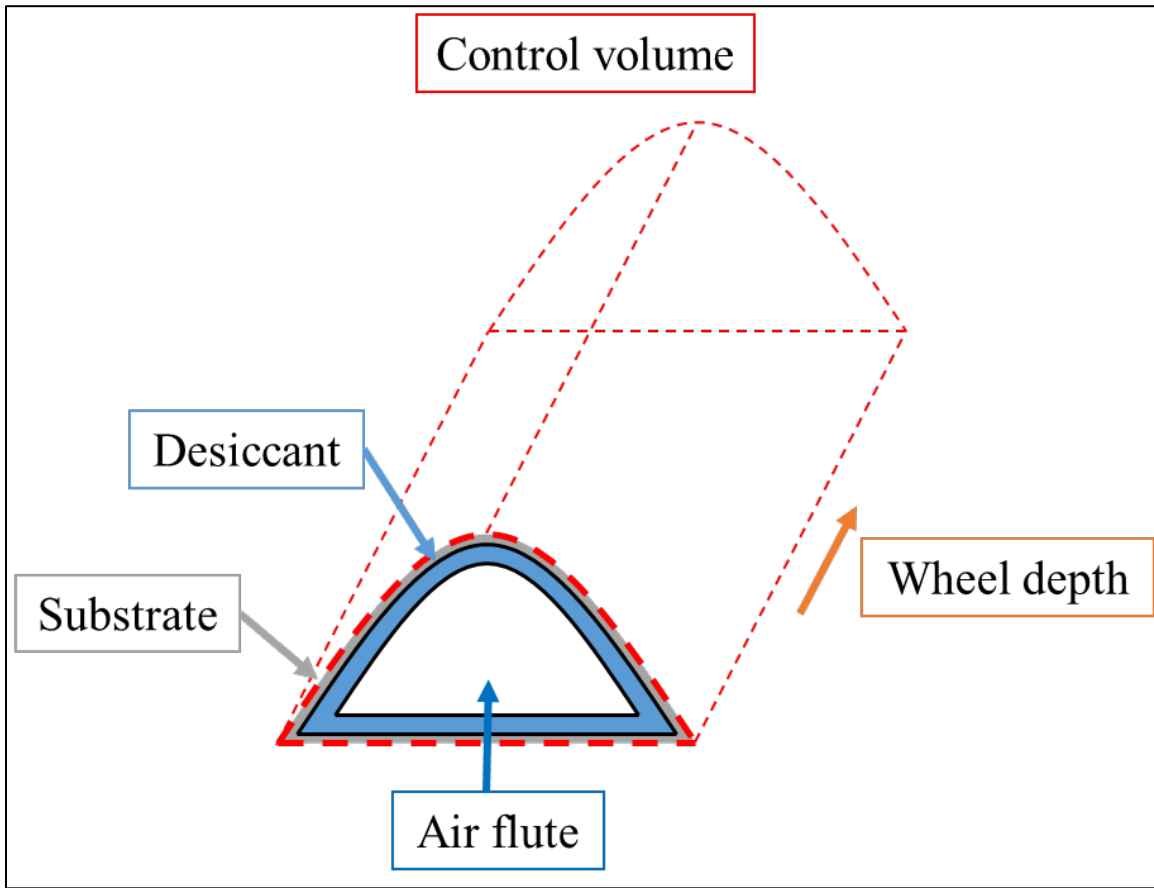


Fig. 5 The control volume of a wheel

#### 4.4 Finite Difference Method

The absolute humidity of the desiccant is dependent on other variables. To simplify the calculation, the absolute humidity of the desiccant would be the last term to compute after all other variables are obtained from the FDM.

For the space domain, a second-order approximation is chosen for application in the FDM. Compared with first-order approximations, the second-order has higher accuracy in predicting the results. The higher order FDM approximations take significantly more computational time. Second-order approximation exhibits a good balance between accuracy and efficiency, so it is selected for use in this research. For the time domain, a first-order approximation is used in the

FDM. For space FDM analysis, forward difference representation is utilized in the beginning two segments; a backward difference representation is utilized in the last two segments; and a central difference representation is utilized for the rest. Typically, a first-order approximation for the time domain delivers relatively accurate predictions while performing heat and mass transfer analysis. Hence, for computational efficiency, forward difference representation and a marching method are applied in the time domain FDM analysis. The FDM approximation form of the governing equations are stated as follow:

#### 4.4.1 FDM of Air Stream Energy Balance

$$\frac{\partial T_g}{\partial t} = \frac{h}{d_h \rho_g C p_g} (T_m - T_g) - u \frac{\partial T_g}{\partial x} \quad (16)$$

The Second-order forward space, first-order backward time FDM approximations for the first two nodes in space (space  $x_j$ ,  $j=0, 1$ ).

$$\begin{aligned} & \left[ \frac{1}{\Delta t} + \frac{h}{D_h \rho_g C p_g} + \frac{-3u}{2\Delta x} \right] T_g(x_j, t_{n+1}) \\ & + \frac{4u}{2\Delta x} T_g(x_{j+1}, t_{n+1}) + \frac{-u}{2\Delta x} T_g(x_{j+2}, t_{n+1}) \\ & = \frac{1}{\Delta t} T_g(x_j, t_n) + \frac{h}{D_h \rho_g C p_g} T_m(x_j, t_n) \end{aligned} \quad (17)$$

The second-order central space, first-order backward time FDM approximations for the nodes in the middle (space  $x_j$ ,  $j=2$  to  $J-2$ ).

$$\begin{aligned} & \frac{u}{12\Delta x} T_g(x_{j-2}, t_{n+1}) + \frac{-8u}{12\Delta x} T_g(x_{j-1}, t_{n+1}) + \frac{1}{\Delta t} T_g(x_j, t_{n+1}) \\ & + \frac{8u}{12\Delta x} T_g(x_{j+1}, t_{n+1}) + \frac{-u}{12\Delta x} T_g(x_{j+2}, t_{n+1}) \\ & = \left[ \frac{1}{\Delta t} + \frac{-h}{D_h \rho_g C p_g} \right] T_g(x_j, t_n) + \frac{h}{D_h \rho_g C p_g} T_m(x_j, t_n) \end{aligned} \quad (18)$$

The second-order backward space, first-order backward time FDM approximations for the last two nodes (space  $x_j$ ,  $j=J-1, J$ ).

$$\begin{aligned} & \frac{u}{2\Delta x} T_g(x_{j-2}, t_{n+1}) + \frac{-4u}{2\Delta x} T_g(x_{j-1}, t_{n+1}) + \left[ \frac{1}{\Delta t} + \frac{3u}{2\Delta x} \right] T_g(x_j, t_{n+1}) \\ &= \left[ \frac{1}{\Delta t} + \frac{-h}{D_h \rho_g C p_g} \right] T_g(x_j, t_n) + \frac{h}{D_h \rho_g C p_g} T_m(x_j, t_n) \end{aligned} \quad (19)$$

#### 4.4.2 FDM of Matrix Energy Balance

The governing equation of the matrix temperature is a second-order differential function. If second-order difference representations are applied, the equations would become very complex, and reduce the calculation efficiency. Thus, a first-order difference representation for space FDM analysis is selected for the governing equation of the matrix temperature to maintain calculation speed.

$$\begin{aligned} \frac{\partial T_m}{\partial t} = & \frac{k_{sub}}{\rho_{sub} C p_{sub}} \frac{\partial^2 T_m}{\partial x^2} + \frac{h_m \Delta H_{ads}}{\rho_{sub} \delta_{sub} C p_{sub} + \rho_d \delta_d C p_d} (W_g - W_m) \\ & + \frac{h}{\rho_{sub} \delta_{sub} C p_{sub} + \rho_d \delta_d C p_d} (T_g - T_m) \end{aligned} \quad (20)$$

The second-order forward space, first-order backward time finite difference approximations for the first two nodes in space (space  $x_j$ ,  $j=0, 1$ ).

$$\begin{aligned}
& \left[ \frac{1}{\Delta t} + \frac{-k_{sub}}{\rho_{sub} C p_{sub} \Delta x^2} \right] T_m(x_j, t_{n+1}) + \frac{2k_{sub}}{\rho_{sub} C p_{sub} \Delta x^2} T_m(x_{j+1}, t_{n+1}) \\
& + \frac{-k_{sub}}{\rho_{sub} C p_{sub} \Delta x^2} T_m(x_{j+2}, t_{n+1}) \\
& = \left[ \frac{1}{\Delta t} + \frac{-h}{\rho_{sub} \delta_{sub} C p_{sub} + \rho_d \delta_d C p_d} \right] T_m(x_j, t_n) \\
& + \frac{h}{\rho_{sub} \delta_{sub} C p_{sub} + \rho_d \delta_d C p_d} T_m(x_j, t_n) \\
& + \frac{h_m \Delta H_{ads}}{\rho_{sub} \delta_{sub} C p_{sub} + \rho_d \delta_d C p_d} W_g(x_j, t_n) \\
& + \frac{-h_m \Delta H_{ads}}{\rho_{sub} \delta_{sub} C p_{sub} + \rho_d \delta_d C p_d} W_m(x_j, t_n)
\end{aligned} \tag{21}$$

The second-order central space, first-order backward time finite difference approximations for the nodes in the middle (space  $x_j$ ,  $j=2$  to  $J-2$ ).

$$\begin{aligned}
& \frac{-k_{sub}}{\rho_{sub} C p_{sub} \Delta x^2} T_m(x_{j-1}, t_{n+1}) + \left[ \frac{2k_{sub}}{\rho_{sub} C p_{sub} \Delta x^2} + \frac{1}{\Delta t} \right] T_m(x_j, t_{n+1}) \\
& + \frac{-k_{sub}}{\rho_{sub} C p_{sub} \Delta x^2} T_m(x_{j+1}, t_{n+1}) \\
& = \left[ \frac{1}{\Delta t} + \frac{h}{\rho_{sub} \delta_{sub} C p_{sub} + \rho_d \delta_d C p_d} \right] T_m(x_j, t_n) \\
& + \frac{h}{\rho_{sub} \delta_{sub} C p_{sub} + \rho_d \delta_d C p_d} T_g(x_j, t_n) \\
& + \frac{h_m \Delta H_{ads}}{\rho_{sub} \delta_{sub} C p_{sub} + \rho_d \delta_d C p_d} W_g(x_j, t_n) \\
& + \frac{-h_m \Delta H_{ads}}{\rho_{sub} \delta_{sub} C p_{sub} + \rho_d \delta_d C p_d} W_m(x_j, t_n)
\end{aligned} \tag{22}$$

The second-order backward space, first-order backward time finite difference approximations for the last two nodes (space  $x_j$ ,  $j=J-1, J$ ).

$$\begin{aligned}
& \frac{-k_{sub}}{\rho_{sub}Cp_{sub}\Delta x^2}T_m(x_{j-2}, t_{n+1}) + \frac{2k_{sub}}{\rho_{sub}Cp_{sub}\Delta x^2}T_m(x_{j-1}, t_{n+1}) \\
& + \left[ \frac{1}{\Delta t} + \frac{-k_{sub}}{\rho_{sub}Cp_{sub}\Delta x^2} \right] T_m(x_j, t_{n+1}) \\
& = \left[ \frac{1}{\Delta t} + \frac{-h}{\rho_{sub}\delta_{sub}Cp_{sub} + \rho_d\delta_dCp_d} \right] T_m(x_j, t_n) \\
& + \frac{h}{\rho_{sub}\delta_{sub}Cp_{sub} + \rho_d\delta_dCp_d} T_g(x_j, t_n) \\
& + \frac{h_m\Delta H_{ads}}{\rho_{sub}\delta_{sub}Cp_{sub} + \rho_d\delta_dCp_d} W_g(x_j, t_n) \\
& + \frac{-h_m\Delta H_{ads}}{\rho_{sub}\delta_{sub}Cp_{sub} + \rho_d\delta_dCp_d} W_m(x_j, t_n)
\end{aligned} \tag{23}$$

#### 4.4.3 FDM of Air Stream Mass Balance

$$\frac{\partial W_g}{\partial t} = \frac{h_d}{d_h\rho_g} (W_m - W_g) - u \frac{\partial W_g}{\partial x} \tag{24}$$

The second-order forward space, first-order backward time finite difference approximations for the first two nodes in space (space  $x_j$ ,  $j=0, 1$ ).

$$\begin{aligned}
& \left[ \frac{1}{\Delta t} + \frac{-3u}{2\Delta x} \right] W_g(x_j, t_{n+1}) + \frac{4u}{2\Delta x} W_g(x_{j+1}, t_{n+1}) + \frac{-u}{2\Delta x} W_g(x_{j+2}, t_{n+1}) \\
& = \left[ \frac{1}{\Delta t} + \frac{-h_m}{d_h\rho_g} \right] W_g(x_j, t_n) + \frac{h_m}{d_h\rho_g} W_m(x_j, t_n)
\end{aligned} \tag{25}$$

The second-order central space, first-order backward time finite difference approximations for the nodes in the middle (space  $x_j$ ,  $j=2$  to  $J-2$ ).



$$\begin{aligned}
& \frac{u}{12\Delta x} W_g(x_{j-2}, t_{n+1}) + \frac{-8u}{12\Delta x} W_g(x_{j-1}, t_{n+1}) + \frac{1}{\Delta t} W_g(x_j, t_{n+1}) \\
& + \frac{8u}{12\Delta x} W_g(x_{j+1}, t_{n+1}) + \frac{-u}{12\Delta x} W_g(x_{j+2}, t_{n+1}) \\
& = \left[ \frac{1}{\Delta t} + \frac{-h_m}{d_h \rho_g} \right] W_g(x_j, t_n) + \frac{h_m}{d_h \rho_g} W_m(x_j, t_n)
\end{aligned} \tag{26}$$

The second-order backward space, first-order backward time finite difference approximations for the last two nodes (space  $x_j$ ,  $j=J-1, J$ ).

$$\begin{aligned}
& \frac{u}{2\Delta x} W_g(x_{j-2}, t_{n+1}) + \frac{-4u}{2\Delta x} W_g(x_{j-1}, t_{n+1}) + \left[ \frac{1}{\Delta t} + \frac{3u}{2\Delta x} \right] W_g(x_j, t_{n+1}) \\
& = \left[ \frac{1}{\Delta t} + \frac{-h_m}{d_h \rho_g} \right] W_g(x_j, t_n) + \frac{h_m}{d_h \rho_g} W_m(x_j, t_n)
\end{aligned} \tag{27}$$

#### 4.4.4 FDM of Matrix Mass Balance

The variation rate of moisture content in the matrix is dependent on the humidity ratio of the air and the matrix. The general adsorption isotherm (29) is introduced to the matrix mass balance governing equation (4) to replace the variation rate of moisture content in the desiccant by the temperature and the humidity ratio of the matrix.

$$\begin{aligned}
\frac{\partial \gamma_d}{\partial t} &= \frac{\partial \gamma_d}{\partial T_{m,abs}} \frac{\partial T_{m,abs}}{\partial t} + \frac{\partial \gamma_d}{\partial W_m} \frac{\partial W_m}{\partial t} \\
&= \frac{\partial \gamma_d}{\partial \varphi} \frac{\partial \varphi}{\partial T_{m,abs}} \frac{\partial T_{m,abs}}{\partial t} + \frac{\partial \gamma_d}{\partial \varphi} \frac{\partial \varphi}{\partial W_m} \frac{\partial W_m}{\partial t} \\
&= \frac{h_m}{\delta_d \rho_d} (W_g - W_m)
\end{aligned} \tag{28}$$

$$\frac{\gamma_d}{\gamma_{max}} = \frac{\varphi}{\varphi - c\varphi + c} \quad (29)$$

$$\varphi = \frac{P_v}{P_{v,sat}} \quad (30)$$

The partial pressure of the water vapor in the matrix can be represented as the absolute temperature and the humidity ratio of the matrix based on the ideal gas law.

$$P_v = \rho_v \frac{R}{M_v} T_{m,abs} = W_m \rho_g \frac{8.314}{0.018} T_{m,abs} = 461.89 W_m \rho_g T_{m,abs} \quad (31)$$

The saturated vapor pressure at a specific temperature can be determined by the Clausius-Clapeyron relation (32), and take the water boiling point at the standard atmospheric pressure as  $P_1$ .

$$\ln\left(\frac{P_1}{P_2}\right) = \frac{h_{fg}}{R} \left(\frac{1}{T_2} - \frac{1}{T_1}\right) \quad (32)$$

$$P_2 = 101325 \times e^{-\frac{40660}{8.314} \left(\frac{1}{T_2} - \frac{1}{373.15}\right)} \quad (33)$$

$$P_{v,sat} = 101325 \times e^{-\frac{40660}{8.314} \left(\frac{1}{T_{m,abs}} - \frac{1}{373.15}\right)} = 4.98 \times 10^{10} e^{-\frac{4890.55}{T_{m,abs}}} \quad (34)$$

$$\varphi = \frac{P_v}{P_{v,sat}} = \frac{461.89 W_m \rho_g T_{m,abs}}{4.98 \times 10^{10} e^{-\frac{4890.55}{T_{m,abs}}}} = 9.28 \times 10^{-9} W_m \rho_g T_{m,abs} e^{\frac{4890.55}{T_{m,abs}}} \quad (35)$$

$$\begin{aligned}
& \left\{ \frac{c\gamma_{max}}{(\varphi - c\varphi + c)^2} \left[ 9.28 \times 10^{-9} T_{m,abs}(x_j, t_n) \rho_g e^{\frac{4890.55}{T_{m,abs}(x_j, t_n)}} \right] \frac{1}{\Delta t} \right\} W_m(x_j, t_{n+1}) \\
&= \left\{ \frac{c\gamma_{max}}{(\varphi - c\varphi + c)^2} \left[ 9.28 \times 10^{-9} T_{m,abs}(x_j, t_n) \rho_g e^{\frac{4890.55}{T_{m,abs}(x_j, t_n)}} \right] \frac{1}{\Delta t} + \frac{-h_m}{\delta_d \rho_d} \right\} \\
&\times W_m(x_j, t_n) \\
&+ \left\{ \frac{c\gamma_{max}}{(\varphi - c\varphi + c)^2} \left[ \frac{9.28 \times 10^{-9} W_m(x_j, t_n) \rho_g e^{\frac{4890.55}{T_{m,abs}(x_j, t_n)}}}{- \frac{4.54 \times 10^{-5} W_m(x_j, t_n) \rho_g e^{\frac{4890.55}{T_{m,abs}(x_j, t_n)}}}{T_{m,abs}(x_j, t_n)}} \right] \frac{1}{\Delta t} \right\} \\
&\times T_{m,abs}(x_j, t_n) \\
&+ \left\{ \frac{c\gamma_{max}}{(\varphi - c\varphi + c)^2} \left[ \frac{9.28 \times 10^{-9} W_m(x_j, t_n) \rho_g e^{\frac{4890.55}{T_{m,abs}(x_j, t_n)}}}{- \frac{4.54 \times 10^{-5} W_m(x_j, t_n) \rho_g e^{\frac{4890.55}{T_{m,abs}(x_j, t_n)}}}{T_{m,abs}(x_j, t_n)}} \right] \frac{-1}{\Delta t} \right\} \\
&\times T_{m,abs}(x_j, t_{n+1}) \\
&+ \frac{h_m}{\delta_d \rho_d} W_g(x_j, t_n)
\end{aligned} \tag{36}$$

#### 4.5 Solution Method

An implicit FDM is selected for solving the differential equations that model the performance of an energy recovery wheel or a desiccant wheel in this research. The primary reason for using an implicit method is that it is more stable, and more inclined to converge for the heat and mass transfer analysis.

There are five unknown variables, which include the air temperature  $T_g$ , the matrix temperature  $T_m$ , absolute humidity of the air  $W_g$ , absolute humidity of the matrix  $W_m$ , and the moisture loading of the desiccant  $\gamma_d$ ; however, there are only four equations. Therefore, one additional equation is introduced to close the problem formulation. Eq. 4.4-14 is the adsorption isotherm of the desiccant.

As observed, the absolute humidity of the desiccant is dependent on other variables. To simplify the calculation, the absolute humidity of the desiccant is the last term to be computed after all other variables are obtained from the FDM.

To discretize the space domain, a second-order approximation is chosen in the FDM. As compared with a first-order approximation, a second order is less sensitive to grid size and more likely to converge even with coarse grid size. A second-order approximation exhibits a good balance between accuracy and computational efficiency, so it is selected for use in this research. For the time domain, a first-order approximation is used in the FDM. For space FDM analysis, a forward difference representation is utilized in the beginning segments; a backward difference representation is utilized in the final segments; a central difference representation is utilized for the remaining segments. Generally, a first-order approximation is sufficient for the time domain.

## **4.6 Simulation Setup**

In numerical analysis, relaxation methods are commonly utilized to aid in the stability and/or speed of the solution process. The under-relaxation method takes a portion of the step change between the last iteration and the current iteration to dampen the simulation. This can reduce step oscillations and help the solution to converge more reliably. An under-relaxation factor of 0.9 has been found useful in the current research to aid in convergence without significantly impacting simulation speed.

## **4.7 Simulation Results and Validation**

### **4.7.1 Energy Recovery Wheel Simulation Results and Validation**

Energy recovery wheel test data have been obtained from two separate laboratories whose test facilities are both constructed according to the AHRI 1060 [6] standard. At one laboratory, the temperature sensors have  $\pm 0.75\%$  of error; the relative humidity sensors have  $\pm 3\%$  of error; the airflow rate sensors have  $\pm 2\%$  of error. The uncertainty percentage of sensible measurements is 3%; the uncertainty percentage of latent measurements is 6%; the uncertainty percentage of airflow rate measurements is 4%. At the other laboratory, the uncertainty percentage of sensible measurements ranges from 0.43% to 0.73%; the uncertainty percentage of latent measurements ranges from 1.33% to 1.53%; the uncertainty percentage of airflow rate measurements ranges from 0.23% to 0.42%.

Measurement uncertainty in an experimental apparatus can propagate in some test cases to cause unrealistic performance values of experimental data. The enthalpy of the inlet air and the

enthalpy of the outlet air of an ERV should be equal in theory, so an energy balance calculation was conducted on the available experimental data prior to model validation to ensure that low-quality data points are not influencing the study. Most of the data points used for validation were found to have an acceptable energy balance. However, those data points with an enthalpy difference between inlet air and outlet air larger than 5% of the total enthalpy of inlet air to the total enthalpy of the outlet air are marked as orange in Fig. 6 and Fig. 7, which show temperature and humidity parity plots between model-predicted values and the experimental measurements. It is noticeable that the drift between simulation results and testing data is larger when the enthalpy difference between inlet air and outlet air is larger. Typically, the airflow rate of the supply air stream and the airflow rate of the return air stream are equal or only slightly different (within 10%), so the impact from pressure differential between the two streams is insignificant. Thus, the effect of pressure differential is neglected in the FDM model since this circumstance is not typical in an energy recovery wheel application. However, some of the available test data were conducted with high airflow rate differences for other research purposes. Those data points with high airflow rate differences are marked as orange in Fig. 6 and Fig. 7. With exception of the above two conditions that were discussed, the simulation results correspond with the experimental test data to within  $\pm 10\%$ ; indicating that the energy recovery wheel model can deliver reasonable results that agree with actual performance.

Fig. 6 is a parity plot drawn to visualize the accuracy of the output temperature results between the simulations and the experimental data. The x-axis represents the temperature difference between the outdoor air temperature and the supply air temperature from the experimental data, while the y-axis represents the corresponding simulation results.

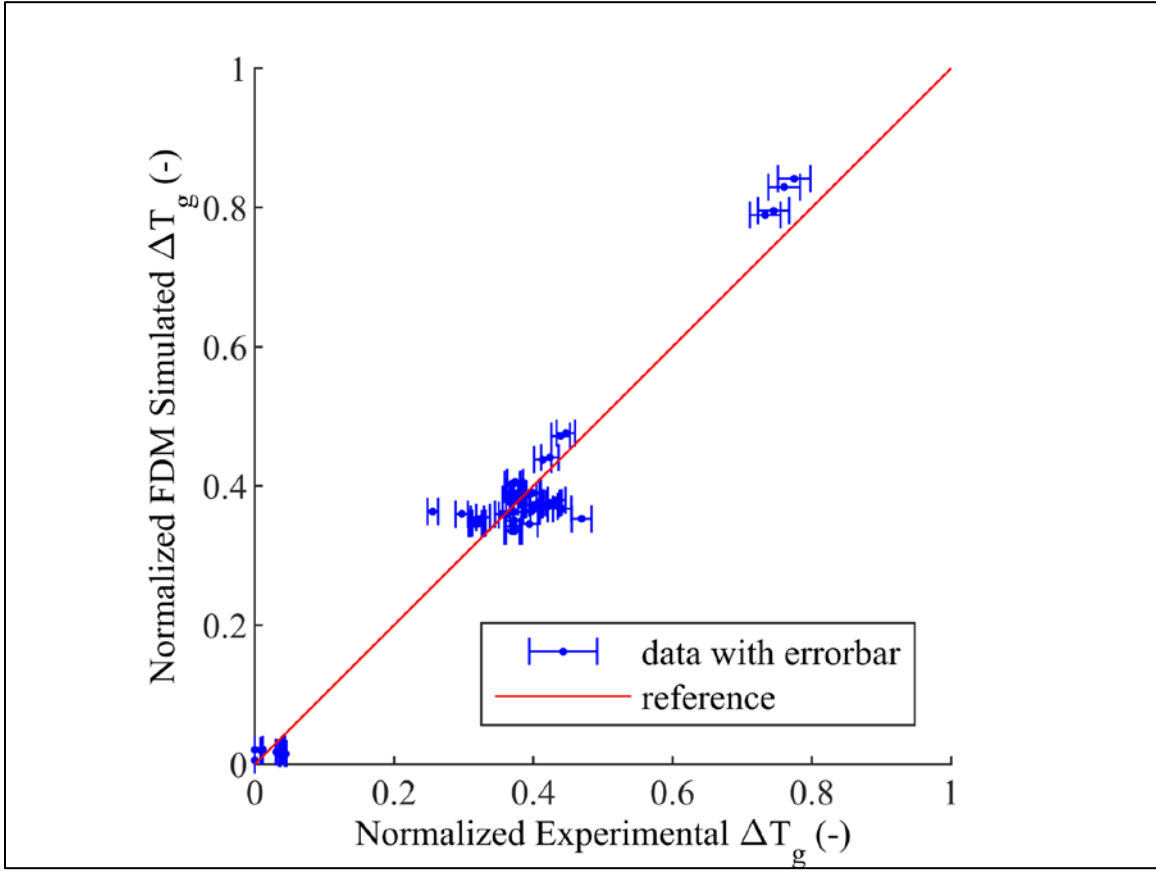


Fig. 6 Inlet and outlet air temperature difference of experimental data against FDM simulation result

Fig. 7 is a parity plot drawn to visualize the accuracy of the output absolute humidity between the simulations and the experimental data. The x-axis represents the absolute humidity of the supply air leaving the energy recovery wheel from the experimental data, while the y-axis represents the corresponding simulation results.

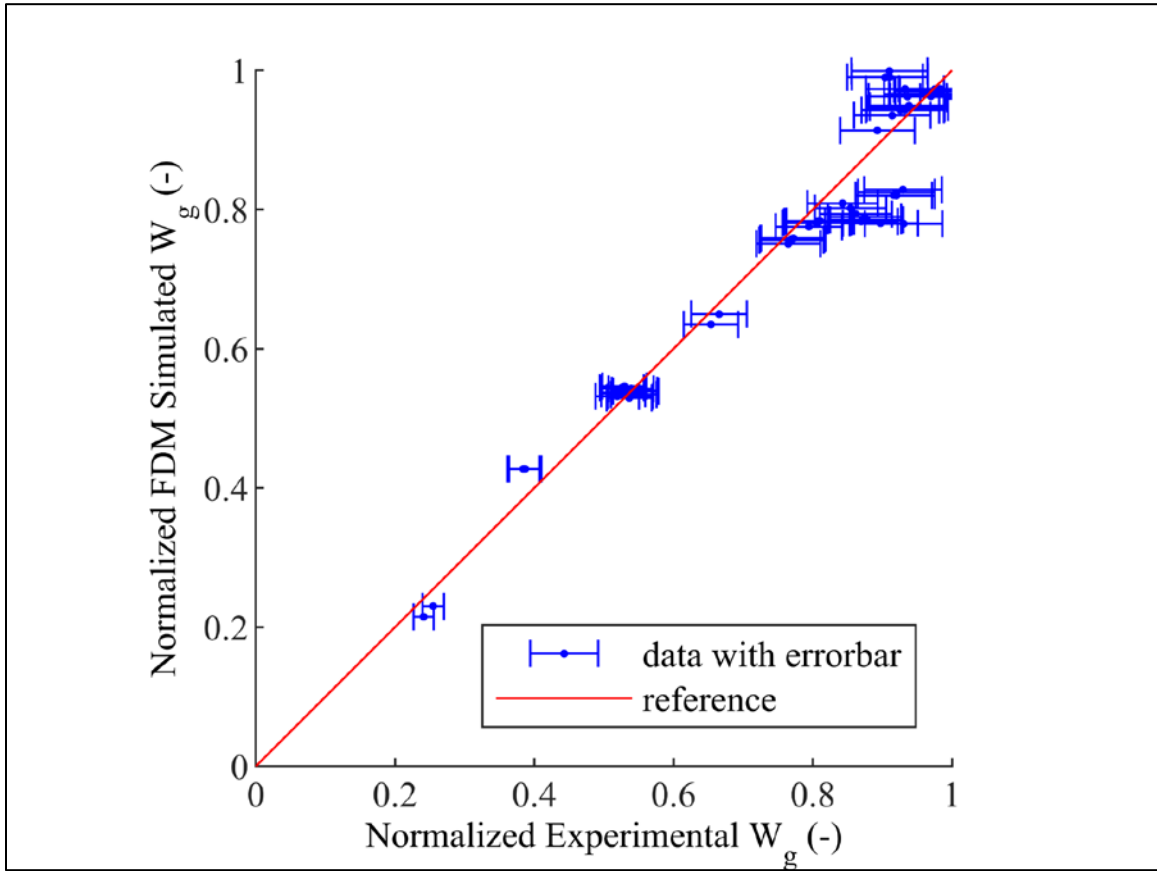


Fig. 7 Air humidity ratio of experimental data against FDM simulation result

A Nusselt number correction factor has been implemented in the code to adjust the convective heat transfer coefficient to improve the solution accuracy. A correction factor of 0.9 has been found to give satisfactory results across all of the simulations used in this research.

After the model was validated, a grid independence study was conducted. In theory, the simulation results should converge to similar results under the same input conditions with different grid sizes. A grid independence study was conducted on the FDM to ensure that the grid size is not influencing the simulation result. Hence, several simulations were performed using different time and space grid sizes with different inlet air temperatures to see whether the results converge to the same value. Table 2 shows the inputs for the grid independence study, while Fig. 8, Fig. 9, and Fig. 10 present the results under the same boundary conditions with different grid sizes (space segment quantity  $x=10, 20, 30$ , and  $x$ -axis is time segment quantity). The simulation results start

to converge at 8 time segments; therefore, the mathematical model and simulation program are established correctly so the results are independent of space and time grid size.

Table 2 Grid independence study boundary conditions

Input parameters	Input value
Wheel Diameter (m)	1
Wheel Depth (m)	0.2
Outdoor Airflow Rate (CFM)	3000
Return Airflow Rate (CFM)	3000
Time Traveling through Wheel (s)	0.053
Outdoor Air Temperature (°C)	30-40
Return Air Temperature (°C)	25
Outdoor Air Humidity Ratio (kg/kg)	0.018
Return Air Humidity Ratio (kg/kg)	0.009
Wheel Rotation Speed (RPM)	20
Hydraulic Diameter (m)	0.002



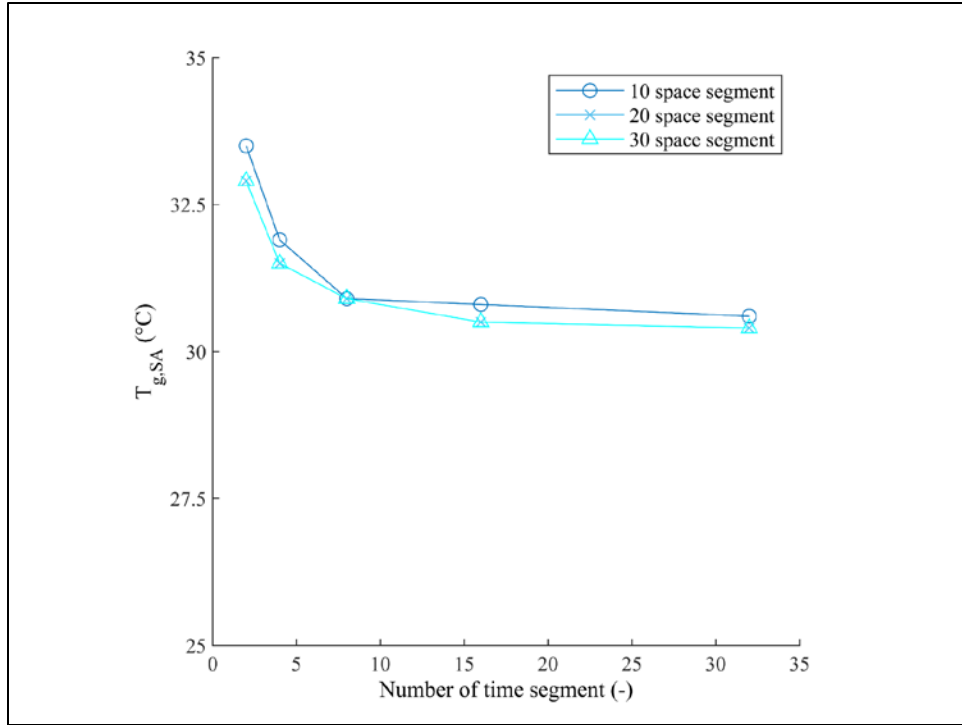


Fig. 8  $T_{SA}$  with different space and time segment while  $T_{OA} = 40^{\circ}\text{C}$

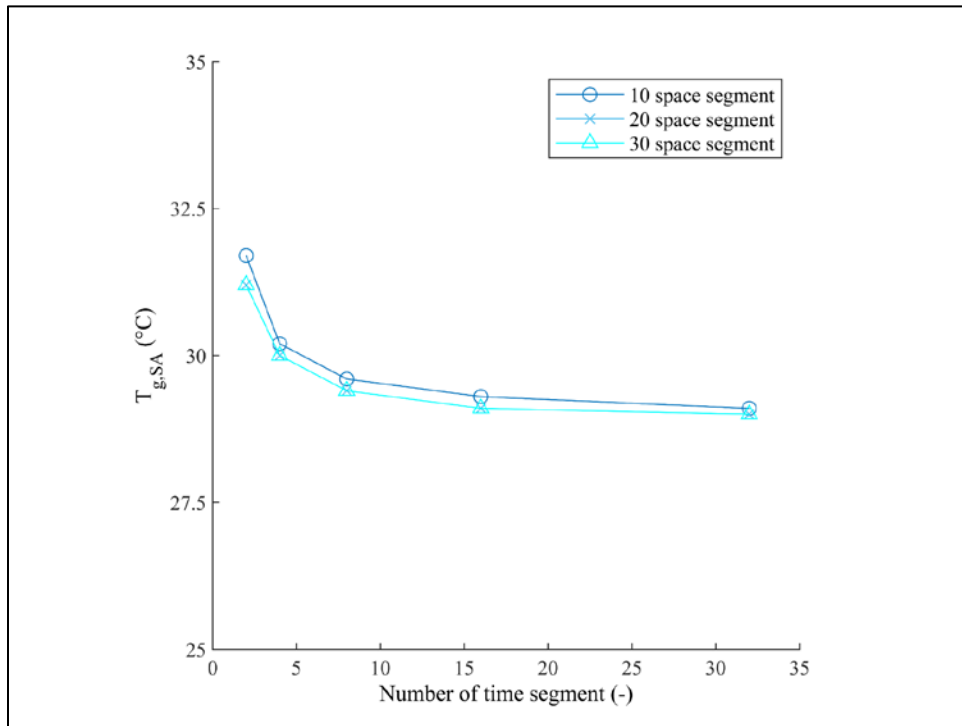


Fig. 9  $T_{g,SA}$  with different space and time segment while  $T_{g,OA} = 35^{\circ}\text{C}$

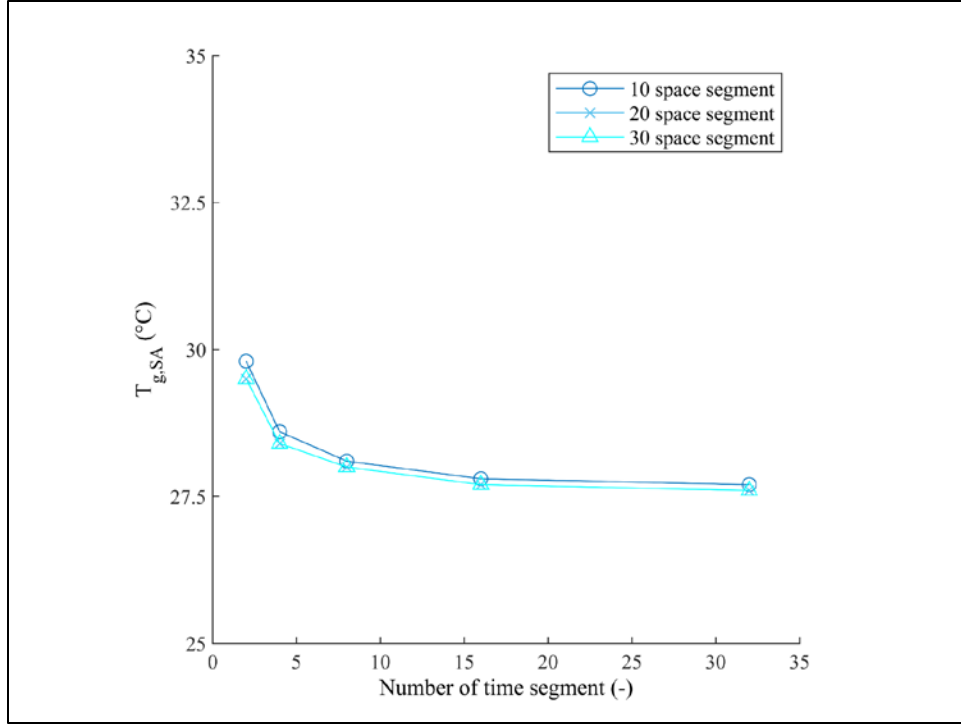


Fig. 10  $T_{g,SA}$  with different space and time segment while  $T_{g,OA} = 30^{\circ}\text{C}$

#### 4.7.2 Desiccant Wheel Simulation Results and Validation

The FDM model was validated and shown that it is accurate in energy recovery wheel applications, then the model was extended to the desiccant wheel performance prediction. The data sets utilized to valid the FDM model are generated by a selection tool from desiccant wheel Manufacturer B. The selection tool is constructed, trained, and validated using experimental data that is collected from a laboratory compliant with the AHRI 1060 standard [6]. The uncertainty of sensible energy measurements is specified to be lower than 0.73%; the uncertainty of latent measurements is specified to be lower than 1.53%; the uncertainty of airflow measurements is specified to be lower than 0.42%. The data sets are generated according to the following wheel dimensions and operating conditions: eight different sizes of wheels (four diameter sizes: 370mm, 545mm, 1090mm, 1530mm; two wheel depth sizes: 200mm, 400mm) are selected to generate data; six cities (Seattle, WA, Flagstaff, AZ, Phoenix, AZ, Columbus, OH, Jacksonville, FL, New York, NY) in a dry season and a humid season; two regeneration inlet air temperatures ( $93.3^{\circ}\text{C}$  and  $140.6^{\circ}\text{C}$ ).

Fig. 11 and Fig. 12, parity plots, visualize the accuracy of the supply air temperature and humidity ratio between the prediction of the FDM model and the data set generated by the selection tool from desiccant wheel manufacturer B. The x-axis of Fig. 11 shows the temperature difference between the outdoor air entering and leaving the wheel from the selection tool data sets; Fig. 12 represents the humidity ratio difference. The y-axes in Fig. 11 and Fig. 12 exhibit the corresponding predictions of temperature difference and humidity ratio difference from the FDM model. A Nusselt number correction factor of 0.8 has been employed to tune the convective heat transfer coefficient in order to refine the accuracy of the FDM model. The FDM predictions agree with the selection tool data to within  $\pm 10\%$ ; indicating that the desiccant wheel FDM model delivers reasonable predictions against the actual wheel performance.

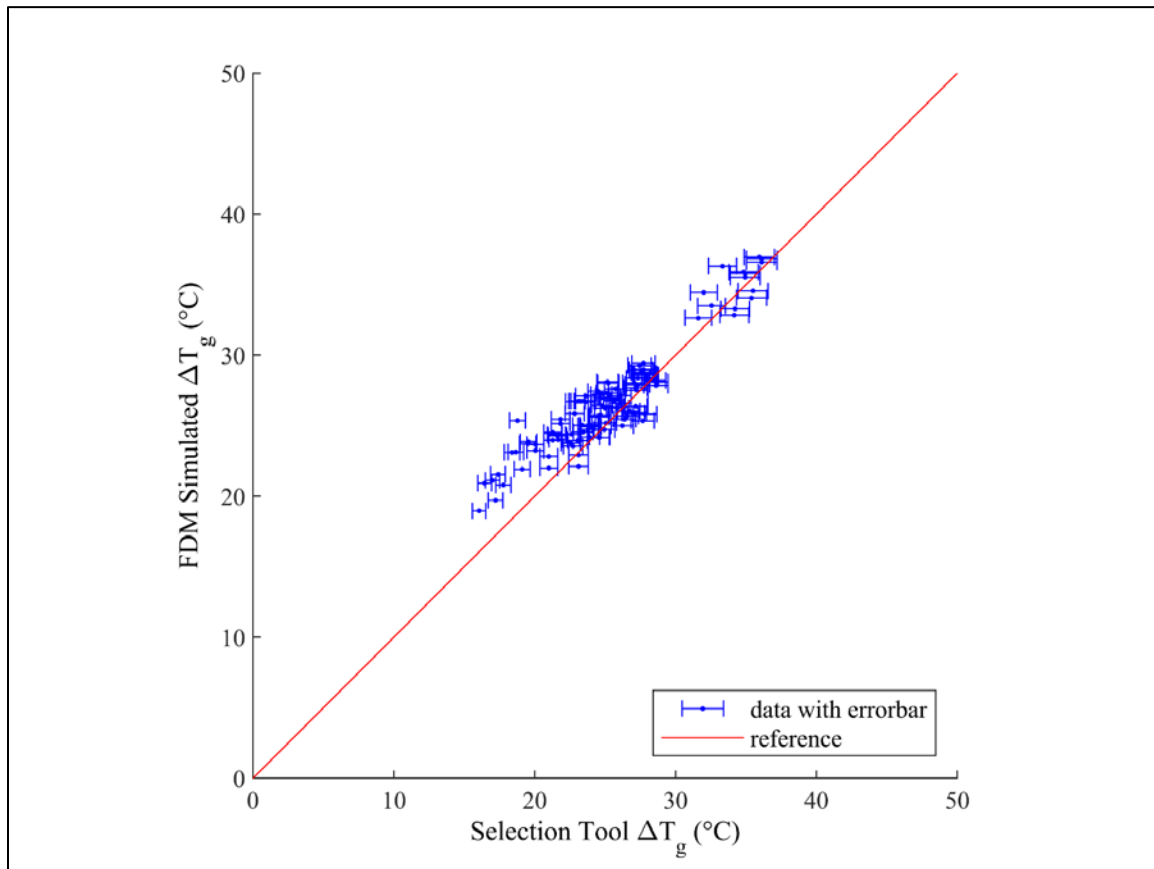


Fig. 11 Air temperature difference between the selection tool data and the FDM prediction

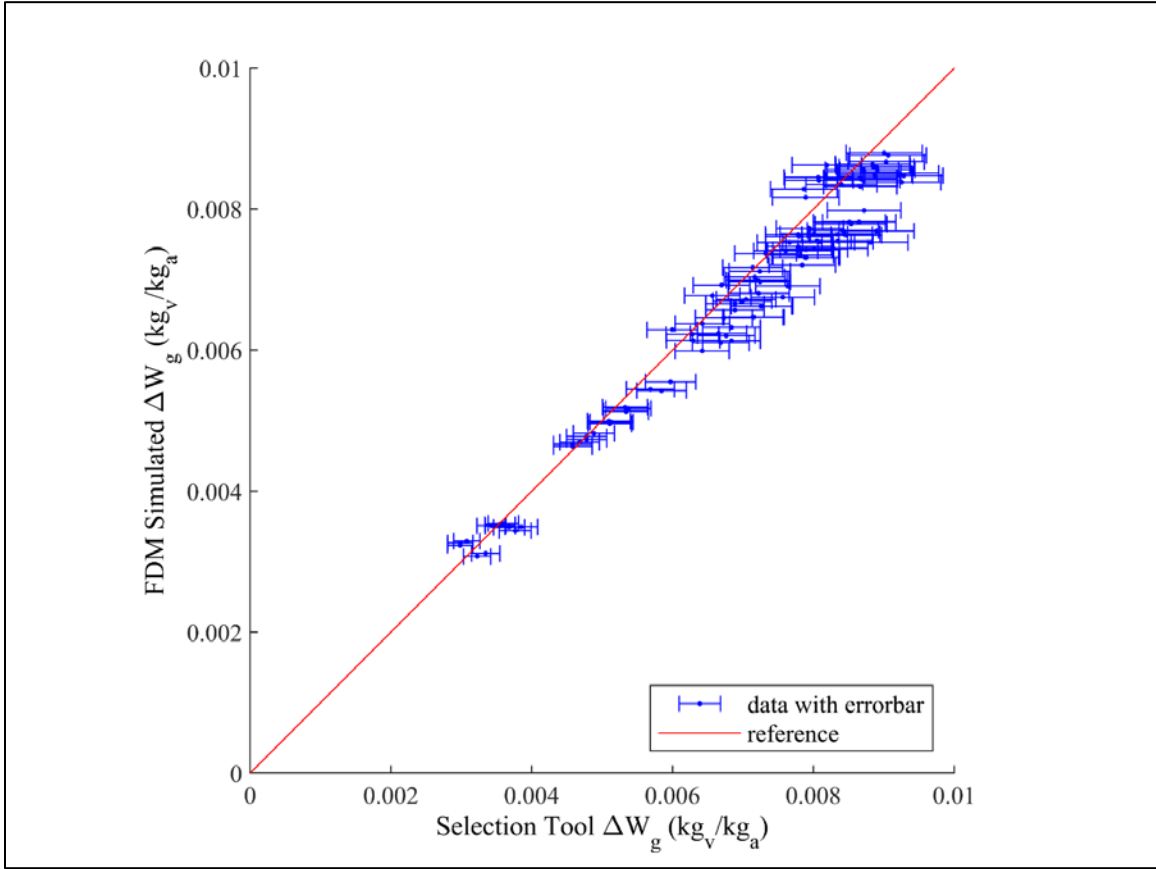


Fig. 12 Air humidity ratio difference between the selection tool data and the FDM prediction

### 4.7.3 Fourier Number

$$Fo = \frac{\alpha \Delta t}{L^2} \quad (37)$$

Typically, the Fourier number is set to be smaller than 0.45 in FDMs, which means that the characteristic time should be less than 0.066 seconds in this case to ensure the stability of the solution. Hence, the simulation time should be segmented into more than two grids to satisfy the typical setting of the Fourier number. In the previous simulations, the time domain is segmented by 15 and the space domain is 25, which satisfies the Fourier number stability requirement.

## **5. ENERGY RECOVERY WHEEL MAPPING METHOD DEVELOPMENT**

This chapter has been extracted and published in the International Journal of Refrigeration in October 2020 by Hung and Horton. The publication is attached in the Appendix - Publication.

Many studies discussed in the literature review section are devoted to establishing FDM models to predict the performance of a selected energy recovery wheel geometry. Nonetheless, if a study targets another energy recovery wheel that has a different physical dimension (e.g., diameter or depth), or runs at different operating settings (e.g., wheel rotation speed or airflow rate), the models need to be recalculated. For parametric studies on energy recovery wheels with different geometries or operating settings, the work of training and validating the models for all of the wheels will consume a tremendous amount of time. Taking the FDM model developed in this study as an example, it takes around 3 minutes to generate a result for one condition of energy recovery wheel operation with the FDM model. If a study is conducted on an annual basis using hourly load and weather data, it will take more than four hundred hours to generate the full set of results. Furthermore, if two or three different wheel configurations are to be compared the simulation time will grow considerably. This characteristic of FDM models is disadvantageous for conducting parametric or optimization studies. If another approach can accurately and quickly predict the performance of energy recovery wheels with different geometries or operating conditions, it will be beneficial for academic studies and research and development activities in the industry. For industry, the solution can offer a more economical design; for academia, the solution can provide an easy approach for studies on different HVAC systems that employ energy recovery wheels. Hence, it is necessary to develop a more efficient method for conducting parametric studies or optimization research on different energy recovery wheels.

### **5.1 Buckingham's Pi Theorem**

In this research, a mapping method introduces simple empirical relationships to predict complicated physical phenomena occurring in an energy recovery wheel. The physical processes in an energy recovery wheel involve complex phenomena of heat and mass transfer, so using FDM

to simulate energy recovery wheel operation is complicated and time-consuming. Hence, it will be more efficient if an empirical relationship can be developed to predict the performance of an energy recovery wheel. Currently, the appropriate terms and dimensions for a mapping method to analyze the performance of an energy recovery wheel are unknown. Buckingham's pi theorem is potentially a useful tool to identify dimensionless terms of an unknown equation. Hence, this approach was first selected to develop a general solution for energy recovery wheel performance prediction. The main purpose is to establish a solution for predicting supply air temperature and absolute humidity from an energy recovery wheel. The equations (38) & (39) that result from implementing Buckingham's pi theorem are shown as follows, and the validation results are given in Fig. 11; however, the validation of this approach was not successful. As Fig. 11 illustrates, Buckingham's pi theorem was not capable of accurately representing the performance over a wide range of operating conditions and wheel geometries, but there is a pattern showing a general relationship exists between the FDM simulation results and Buckingham's pi predictions. Therefore, the terms and dimensions from Buckingham's pi theorem may be useful in the further development of a mapping method.

$$\begin{aligned}
& T_{g,SA} \\
& = k_0 T_{g,OA} \left( \frac{T_{g,RA}}{T_{g,OA}} \right)^{k_1} \left( \frac{h/\rho_g C p_g t_{RPM}}{L} \right)^{k_2} \left( \frac{d_h}{L} \right)^{k_3} \left( \frac{u_{OA} t_{RPM}}{L} \right)^{k_4} \left( \frac{u_{RA} t_{RPM}}{L} \right)^{k_5}
\end{aligned} \tag{38}$$

$$\begin{aligned}
& W_{g,SA} \\
& = k_6 (W_{g,OA})^{k_7} (W_{g,RA})^{k_8} \left( \frac{h_m/\rho_g t_{RPM}}{L} \right)^{k_9} \left( \frac{d_h}{L} \right)^{k_{10}} \left( \frac{u_{OA} t_{RPM}}{L} \right)^{k_{11}} \left( \frac{u_{RA} t_{RPM}}{L} \right)^{k_{12}}
\end{aligned} \tag{39}$$

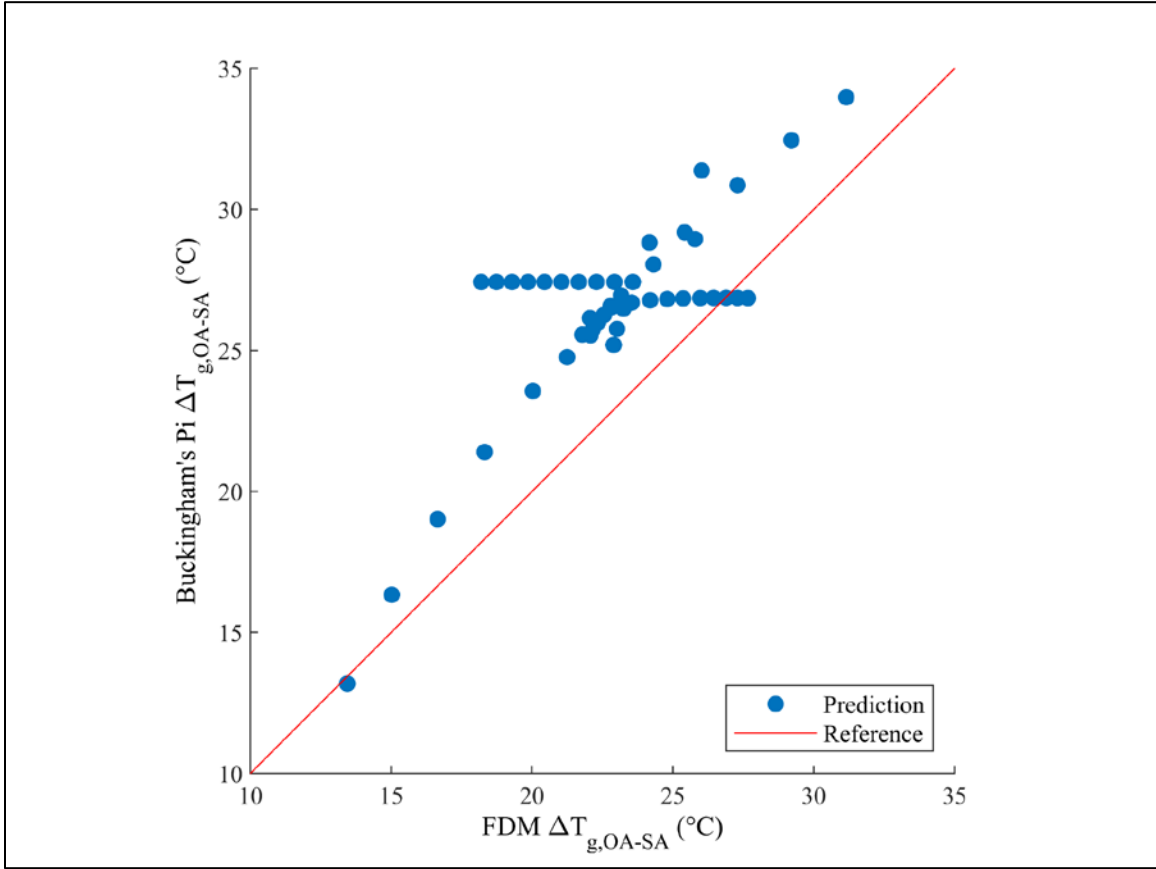


Fig. 13 Buckingham's pi prediction and FDM outcome

## 5.2 Energy Recovery Wheel Mapping Method Development

In AHRI 1060 “Performance Rating of Air-to-Air Exchangers for Energy Recovery Ventilation Equipment” [6], (38) representing the efficiency of an energy recovery wheel is stated as follows, with the return air stream flow rate is assumed always equal or smaller than the outdoor air stream flow rate. This equation will be used as a preliminary form to establish the mapping method.

$$\varepsilon = \frac{c_{OA}(X_{OA} - X_{SA})}{c_{RA}(X_{OA} - X_{RA})} \quad (40)$$

$$X = T_g \text{ or } W_g$$

$$c = Cp_g \dot{m}_g$$

In AHRI 1060, c represents the capacity rate for the airstreams. Thus, the efficiency equation in AHRI 1060 can be written as (41) and (42).

AHRI 1060 efficiency equation of supply air temperature:

$$T_{g,SA} = T_{g,OA} - \varepsilon_g \frac{\dot{m}_{RA} Cp_g}{\dot{m}_{OA} Cp_g} (T_{g,OA} - T_{g,RA}) \quad (41)$$

AHRI 1060 efficiency equation of supply air humidity ratio:

$$W_{g,SA} = W_{g,OA} - \varepsilon_w \frac{\dot{m}_{RA} \Delta H_{ads}}{\dot{m}_{OA} \Delta H_{ads}} (W_{g,OA} - W_{g,RA}) \quad (42)$$

The form of the efficiency equations is similar to the air temperature and humidity governing equations as shown in the following relationships. Hence, the efficiency factor should be similar to the red colored terms in the governing equations.

Energy balance governing equation of the airstream:

$$\frac{\partial T_g}{\partial t} = \frac{h}{d_h \rho_g Cp_g} (T_m - T_g) - u \frac{\partial T_g}{\partial x} \quad (43)$$

Mass balance governing equation of the airstream:

$$\frac{\partial W_g}{\partial t} = \frac{h_d}{d_h \rho_g} (W_m - W_g) - u \frac{\partial W_g}{\partial x} \quad (44)$$

Before finalizing the form of the mapping method, wheel rotation speed and wheel depth should be included also. While developing an energy recovery wheel, it is common to change the



wheel rotational speed and the wheel depth to design a product that fits the application requirements; therefore, these two variables are also included. Additionally, the hydraulic diameter of the flutes affects convective heat and mass transfer coefficients, so these coefficients will be represented in the mapping method by hydraulic diameter. Finally, observations from Buckingham's pi theorem show that the outdoor airflow rate should be considered in the efficiency factor. If the energy wheel efficiency equation is combined in part with Buckingham's pi theorem, the AHRI 1060 efficiency equations (41) & (42), and the physical governing equations (43) & (44), the following general equations (45) & (46) are obtained.

Supply air temperature:

$$T_{g,SA} = T_{g,OA} - \frac{h}{\rho_g C p_g} f(t_{RPM}) f(u_{OA}) f(L) \frac{u_{RA}}{u_{OA}} (T_{g,OA} - T_{g,RA}) \quad (45)$$

Supply air humidity ratio:

$$W_{g,SA} = W_{g,OA} - \frac{h_m}{\rho_g} f(t_{RPM}) f(u_{OA}) f(L) \frac{u_{RA}}{u_{OA}} (W_{g,OA} - W_{g,RA}) \quad (46)$$

The convective heat transfer coefficient can be calculated using the Nusselt number, thermal conductivity, and characteristic length (hydraulic diameter), and expressed in the following form. Then the Nusselt number can be expressed as an integral of the wheel depth.

$$h = \frac{Nu \cdot k_g}{d_h} = \frac{0.59L^{0.624}}{d_h} \quad (47)$$

The functions relating wheel performance to rotational speed,  $f(t_{RPM})$ , airflow rate,  $f(u_{OA})$ , and wheel depth,  $f(L)$ , need to be developed. By running the energy recovery wheel FDM model it is possible to isolate each variable and its effect on the performance results. Using this approach, one input variable is changed at a time while all other inputs remain fixed. The trend of

influence on the changing variable is observed and the results are used to identify the form of an empirical function for that variable.

Fig. 12, Fig. 13, and Fig. 14 show the results of changing the different variables, including traveling time of a flute in one airstream (which is a surrogate for rpm), outdoor air face velocity, and wheel depth. By observing its pattern, a general function format can be developed. First, the traveling time of a flute in one air stream is isolated. For easier observation, the traveling time of a flute in one air stream is moved to the left-hand side of the equation, and the rest of the terms are moved to the right-hand side. Then, the function was divided by the conditions at the maximum traveling time. Thus, the traveling was isolated. Three trials were conducted. Non-isolated variables (e.g.  $T_g$ ,  $W_g$ ,  $u$ ,  $d_h$ , etc.) were controlled as constant in each trial, and non-isolated variables were different in each trial. This variable isolation process would be performed for outdoor air face velocity and wheel depth also.

The effect of the traveling time of a flute in one airstream to the supply air temperature is linear, and the regression  $R^2$ -value is 0.8607, 0.9951, and 0.9671. The function of the traveling time of a flute in one airstream is shown as (49).

$$\begin{aligned}
 & \frac{f(t_{RPM})}{f(t_{RPM})_{max}} \\
 &= \frac{\frac{T_{g,OA} - T_{g,SA}}{T_{g,OA} - T_{g,RA}} \frac{u_{OA}}{u_{RA}} \frac{\rho_g C p_g}{h} \frac{1}{f(u_{OA}) f(L)}}{\frac{(T_{g,OA} - T_{g,SA})_{max}}{(T_{g,OA} - T_{g,RA})_{max}} \frac{u_{OA}}{u_{RA}} \frac{\rho_g C p_g}{h} \frac{1}{f(u_{OA}) f(L)}} \\
 &= \frac{T_{g,OA} - T_{g,SA}}{(T_{g,OA} - T_{g,SA})_{max}}
 \end{aligned} \tag{48}$$

$$f(t_{RPM}) = a_1 t_{RPM} + b_1 \tag{49}$$

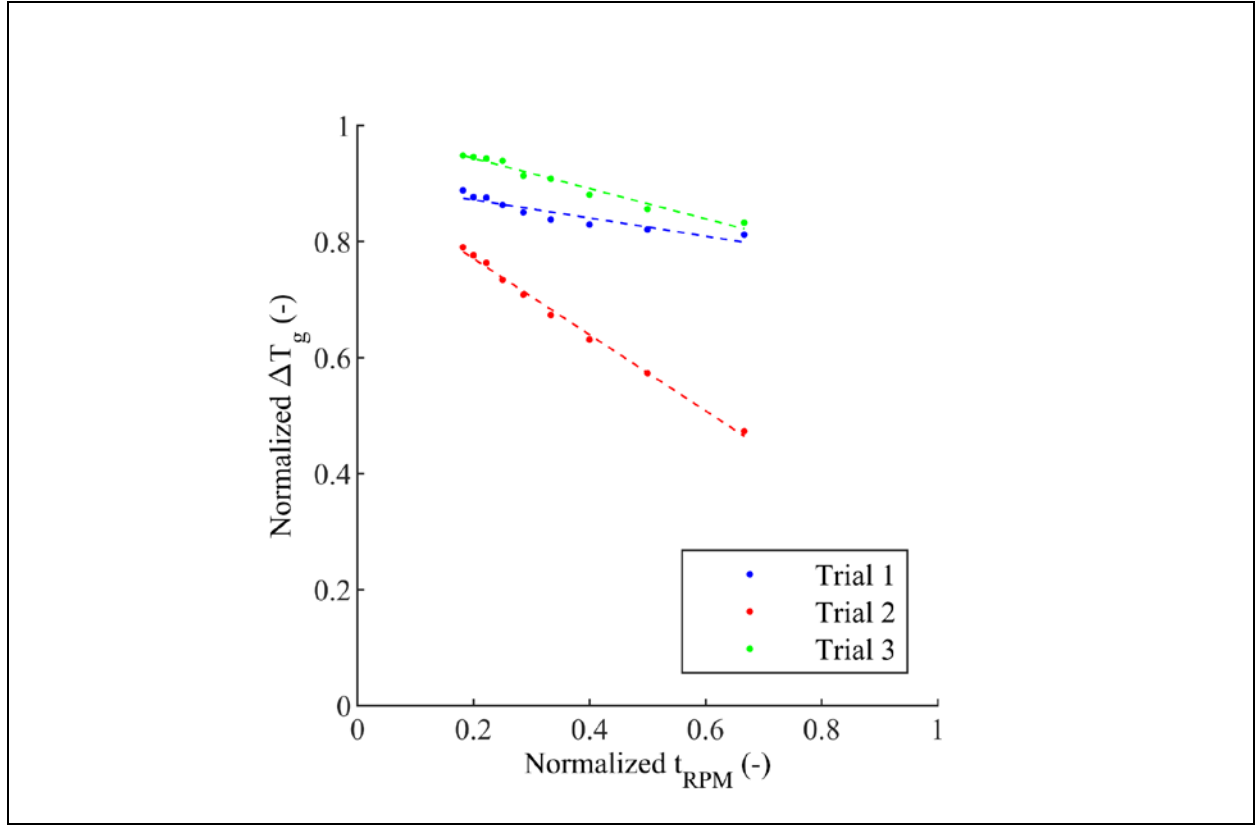


Fig. 14 Effect of the traveling time of a flute in one airstream on wheel performance

Next, the air face velocity is isolated. The effect of the air face velocity on the supply air temperature is linear, and the regression  $R^2$ -value is 0.9757, 0.9985, and 0.9925. The function of the air face velocity is shown as (51).

$$\begin{aligned}
 & \frac{f(u_{OA})}{f(u_{OA})_{max}} \\
 &= \frac{\frac{T_{g,OA} - T_{g,SA}}{T_{g,OA} - T_{g,RA}} \frac{u_{OA}}{u_{RA}} \frac{\rho_g C p_g}{h} \frac{1}{f(t_{RPM}) f(L)}}{\frac{(T_{g,OA} - T_{g,SA})_{max}}{(T_{g,OA} - T_{g,RA})_{max}} \frac{u_{OA}}{u_{RA}} \frac{\rho_g C p_g}{h} \frac{1}{f(t_{RPM}) f(L)}}} \\
 &= \frac{T_{g,OA} - T_{g,SA}}{(T_{g,OA} - T_{g,SA})_{max}}
 \end{aligned} \tag{50}$$

$$f(u_{OA}) = a_2 u_{OA} + b_2 \quad (51)$$

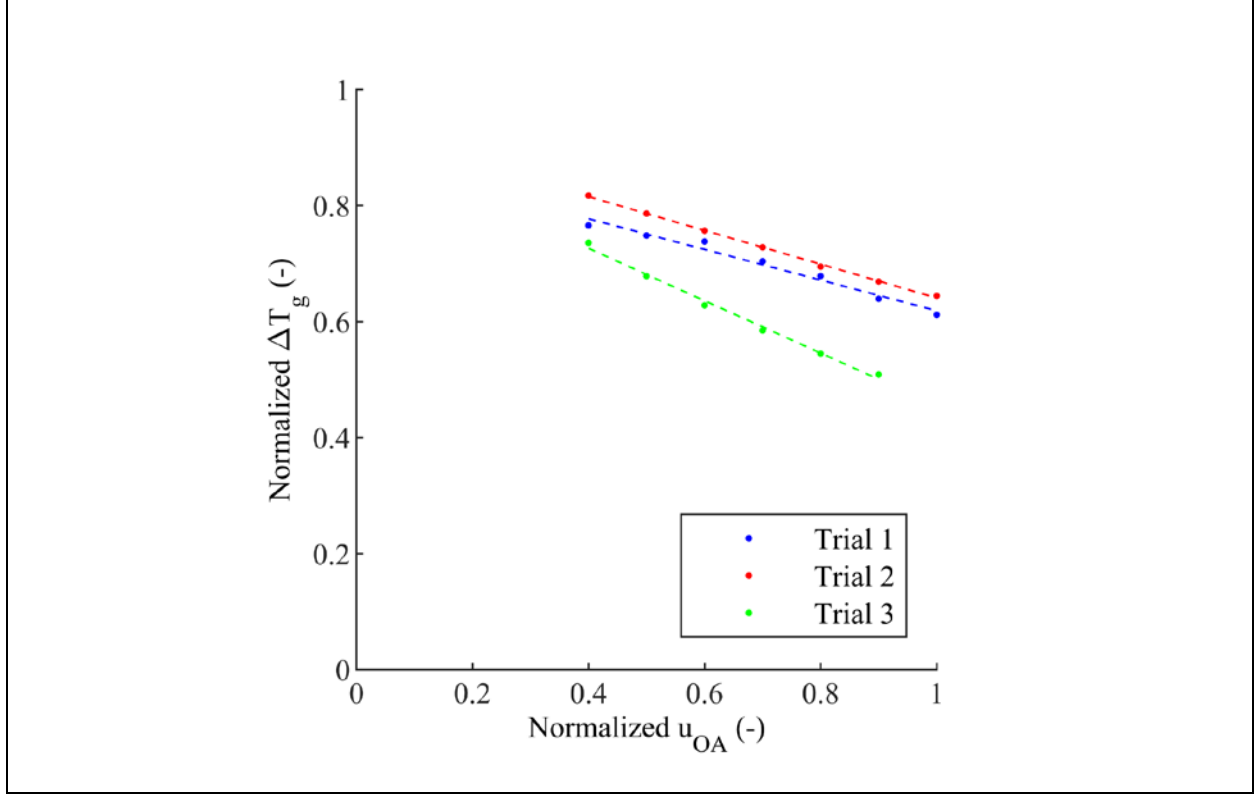


Fig. 15 Effect of the air face velocity on wheel performance

Last, the wheel depth is isolated. The effect of the wheel depth on the supply air temperature is linear, and the regression  $R^2$ -value is 0.9956, 0.9990, and 0.9914. The function of the wheel depth is shown as the following (53):

$$\begin{aligned}
& \frac{f(L)}{f(L)_{max}} \\
&= \frac{\frac{T_{g,OA} - T_{g,SA}}{T_{g,OA} - T_{g,RA}} \frac{u_{OA}}{u_{RA}} \frac{\rho_g C p_g}{h} \frac{1}{f(u_{OA}) f(t_{RPM})}}{\frac{(T_{g,OA} - T_{g,SA})_{max}}{(T_{g,OA} - T_{g,RA})_{max}} \frac{u_{OA}}{u_{RA}} \frac{\rho_g C p_g}{h} \frac{1}{(u_{OA}) f(t_{RPM})}} \\
&= \frac{T_{g,OA} - T_{g,SA}}{(T_{g,OA} - T_{g,SA})_{max}}
\end{aligned} \tag{52}$$

$$f(L) = a_3 e^{b_3 L} + c_3 e^{d_3 L} \tag{53}$$

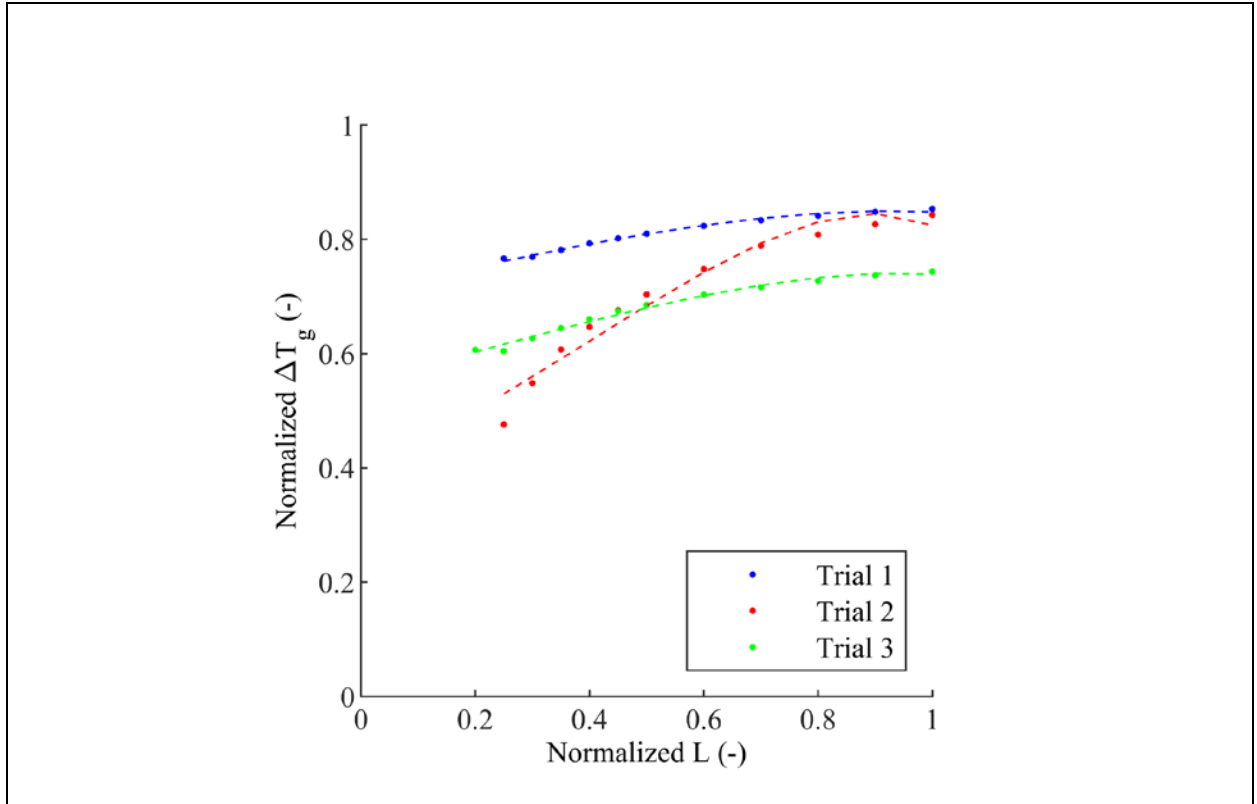


Fig. 16 Effect of the wheel depth on wheel performance

All the selected regressions have an indicated  $R^2$  value that is high, so the relationships capture the results well. Among the mapping method of air temperature and humidity ratio prediction, the function of the wheel rotation speed, the function of airflow rate, and the function of wheel depth are identical for the two prediction methods. This is because the heat and mass transfer processes of an energy recovery wheel are linear processes on a psychrometric chart. Hence, the form of the temperature and humidity ratio mapping methods share the same equation format. Finally, the format of the mapping method for supply air temperature and supply air humidity ratio can be identified as follow.

Supply air temperature:

$$T_{g,SA} = T_{g,OA} - \frac{0.59L^{0.624}}{d_h \rho_g C p_g} (a_1 t_{RPM} + b_1)(a_2 u_{OA} + b_2)(a_3 e^{b_3 L} + c_3 e^{d_3 L}) \times \frac{u_{RA}}{u_{OA}} (T_{g,OA} - T_{g,RA}) \quad (54)$$

Supply air humidity ratio:

$$W_{g,SA} = W_{g,OA} - \frac{0.59L^{0.624}}{d_h \rho_g} (a_1 t_{RPM} + b_1)(a_2 u_{OA} + b_2)(a_3 e^{b_3 L} + c_3 e^{d_3 L}) \times \frac{u_{RA}}{u_{OA}} (W_{g,OA} - W_{g,RA}) \quad (55)$$

This mapping method was developed based on the efficiency definition in AHRI 1060 and the governing equations of energy recovery wheel heat and mass transfer. This characteristic leads the mapping method to a semi-empirical approach. The ANN approach proposed by Jani [29] requires 10 data points for training. This mapping method requires only 8 data points for training, so the work of generating data points for training is further reduced. Solving for all of the unknown constants simultaneously in the equations of the mapping method can be challenging; however, a feasible approach is to determine the coefficients for the functions of each influence variable separately. To achieve that, it is necessary to generate data points that only change one variable

while fixing all other variables. For instance, if the function of the airflow rate is selected, boundary conditions for the FDM simulation should be all the same other than the airflow rate. The effect of the airflow rate can then be distinguished. Results of the FDM simulation eliminate the effect of variables other than airflow rate, and the results can be used as training data points for the mapping method. The same procedure will be repeated for determining constants of the wheel rotation speed function, and the wheel depth function. The functions of wheel rotation speed and airflow rate are linear. It is easier to solve these two functions first. Then the function of wheel depth is more complex to solve. Thus, it is more feasible to solve this function by curve-fitting after the functions of the airflow rate and wheel depth are first solved.

### 5.2.1 Operating Range and Training Data Selection

Next, the application range of the mapping method can be identified. Boundary conditions of extreme cases are input into the FDM model, then the results of the mapping method with the same boundary conditions are compared with the FDM simulation results. If the results agree with each other, then the application range of the mapping method is valid. The application range of the mapping method is listed in Table 3.

Table 3 Operating range of energy recovery wheel mapping method

Variables	Value
Temperature (°C)	-10 to 60
Humidity Ratio (kg/kg)	0.001 to 0.03
Airflow Face Velocity (m/s)	2- 6
Rotation Speed (RPM)	15-60
Wheel Depth (m)	0.1-0.5

Before determining the constants of the mapping method, there is one characteristic that needs to be clarified, which is the independence of the mapping method to the training data points. Theoretically, even if the training data sets are different, they should lead to similar constants for the mapping method and should not affect its typical prediction performance. Therefore, several

different sets of training data points are applied to train the mapping method to evaluate its applicability and robustness. There are a few notes on the data points that were used in the training procedure: (1) The training data points can be randomly selected if only one variable is changing. (2) The temperature prediction of the supply air was computed via the FDM simulation. The predictions of the mapping method are compared with the FDM model simulation result. To quantify the difference between the mapping method and the FDM simulation, mean square errors of temperature differences between the two outputs were calculated.

As Table 4 study results for the effect of training data set to mapping prediction shows, the mean square errors are small, so the mapping method and the FDM simulation agree with each other. The error percentage is defined as the supply air temperature difference between the mapping method and the FDM model over the temperature change across the wheel (from outdoor air to the supply air). The error percentages are all smaller than 10%. Hence, with random training data points, the mapping method still deliveries precise and accurate results.

Table 4 Effect of training data set selection to mapping method prediction

Trial	Equations coefficients								MSE of $\Delta T_{g, OA-SA}$ (°C)	Error Percentage (%)
	a1	b1	a2	b2	a3	b3	c3	d3		
1	-2.28	10.93	-0.76	11.17	0.16	-1.25	-0.62	-38.13	0.93	5.17%
2	-2.84	11.53	-1.35	13.65	0.15	-1.25	-0.60	-38.13	1.06	6.71%
3	-2.72	11.53	-0.94	11.91	0.15	-1.25	-0.60	-38.13	0.95	5.46%
4	-2.90	11.60	-0.89	11.92	0.15	-1.25	-0.60	-38.13	1.42	9.83%
5	-2.64	11.47	-1.73	13.89	0.17	-1.25	-0.68	-38.13	1.05	8.86%

### 5.3 Validation with FDM Energy Recovery Wheel Model

Since the energy recovery wheel FDM model has been validated, the mapping method can be trained and validated using FDM simulation results. The boundary conditions that are utilized in training and validation are the same as those used to validate the FDM model. The inputs are based on laboratory test measurements, which is the same as the FDM model simulation, then the predictions of the mapping method are compared with FDM model simulation results. The mapping method results after training are shown as (56) & (57), then parity plots are shown in Fig.



15 and Fig. 16. For supply air temperature and humidity validation, a total of 136 data points from one independent laboratory and a total of 4 data points from another independent laboratory were simulated using the FDM. 8 were selected for training the empirical equations, and the rest of the data points are used for validation. Among those 8 data points, extreme conditions are selected first, then the rest are randomly selected. To visualize the resulting difference between the mapping method and the FDM, a parity plot for temperature and humidity is generated and shown as Group 1 and Group 2 in Fig. 15 and Fig. 16. As the figures show, the results of prediction from the mapping method and the energy recovery wheel program (FDM) agree very well with each other, and the mean absolute percentage errors (MAPE) are listed for each figure. In addition, a total of 20 data points generated by the selection tool from manufacturer B is utilized to validate the model also. The temperature and humidity prediction is plotted as Group 3 in Fig. 15 and Fig. 16.

Temperature:

$$\begin{aligned}
 T_{g,SA} = & \\
 & T_{g,OA} - \frac{0.59L^{0.624}}{d_h \rho_g C p_g} (-0.2523t_{RPM} + 1.1584) \times \\
 & (-0.2163u_{OA} + 2.644)(6.866e^{-1.26L} - 27.42e^{-38.4L}) \\
 & \times \frac{u_{RA}}{u_{OA}} (T_{g,OA} - T_{g,RA})
 \end{aligned} \tag{56}$$

Absolute humidity:

$$\begin{aligned}
 W_{g,SA} = & \\
 & W_{g,OA} - \frac{0.59L^{0.624}}{d_h \rho_g} (-0.2523t_{RPM} + 1.1584) \times \\
 & (-0.2163u_{OA} + 2.644)(6.866e^{-1.26L} - 27.42e^{-38.4L}) \\
 & \times \frac{u_{RA}}{u_{OA}} (W_{g,OA} - W_{g,RA})
 \end{aligned} \tag{57}$$

### 5.3.1 Validation with Other Literature

Now the mapping method will be examined for its universality. The data and boundary conditions from De Antonellis [25][26] are utilized as another data source to validate the usefulness of the empirical model, and Table 5 lists the range of the data points. There are a total of 18 data points included in this paper. 8 data points are used for training, and 10 data points are used for validation. A temperature difference parity plot (Fig. 17, Group 4), and humidity ratio parity plot (Fig. 18, Group 4) are shown to compare the prediction differences. As observed, the result from the mapping method agrees well with the data in the paper. The application of the mapping method is not limited to one specific type of energy recovery wheel and operating environment.

Table 5 Range of training data set selected from the literature

Input Parameters	Input Value
Outdoor air temperature (°C)	20-35
Return air temperature (°C)	15-35
Outdoor air humidity ratio (kg/kg)	0.018
Return air humidity ratio (kg/kg)	0.009

Temperature:

$$\begin{aligned}
 T_{g,SA} = & \\
 T_{g,OA} - & \frac{0.59L^{0.624}}{d_h\rho_g C p_g} (-0.02297t_{RPM} + 0.889667) \times \\
 & (-0.616u_{OA} + 12.9072)(0.7745e^{0.2691L} - 0.588e^{-9.574L}) \\
 & \times \frac{u_{RA}}{u_{OA}} (T_{g,OA} - T_{g,RA})
 \end{aligned} \tag{58}$$

Humidity:

$$\begin{aligned}
 W_{g,SA} = & \\
 W_{g,OA} - & \frac{0.59L^{0.624}}{d_h\rho_g}(-0.02297t_{RPM} + 0.889667) \times \\
 & (-0.616\dot{m}_{OA} + 12.9072)(0.7745e^{0.2691L} - 0.588e^{-9.574L}) \\
 & \times \frac{u_{RA}}{u_{OA}}(W_{g,OA} - W_{g,RA})
 \end{aligned} \tag{59}$$

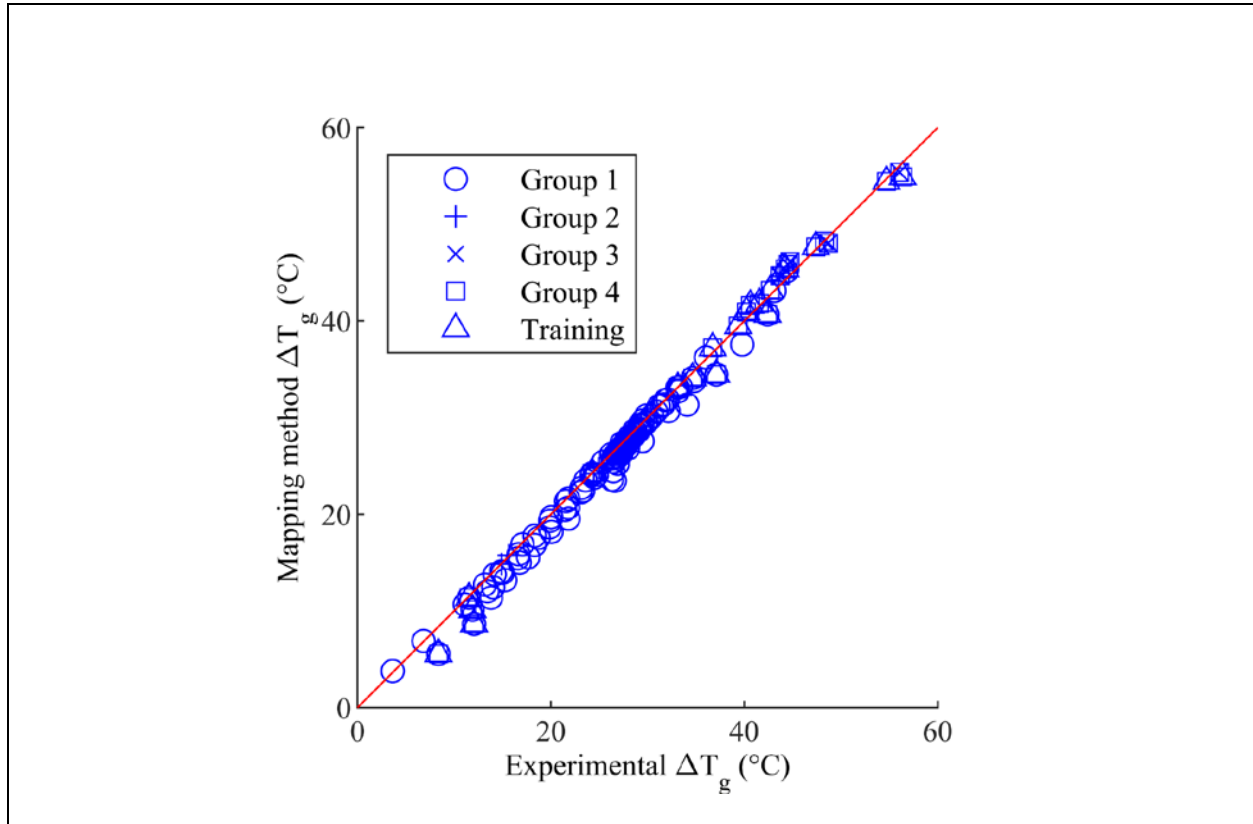


Fig. 17  $\Delta T_{g,SA}$  between FDM simulation and mapping method prediction, MAPE = 6.33%

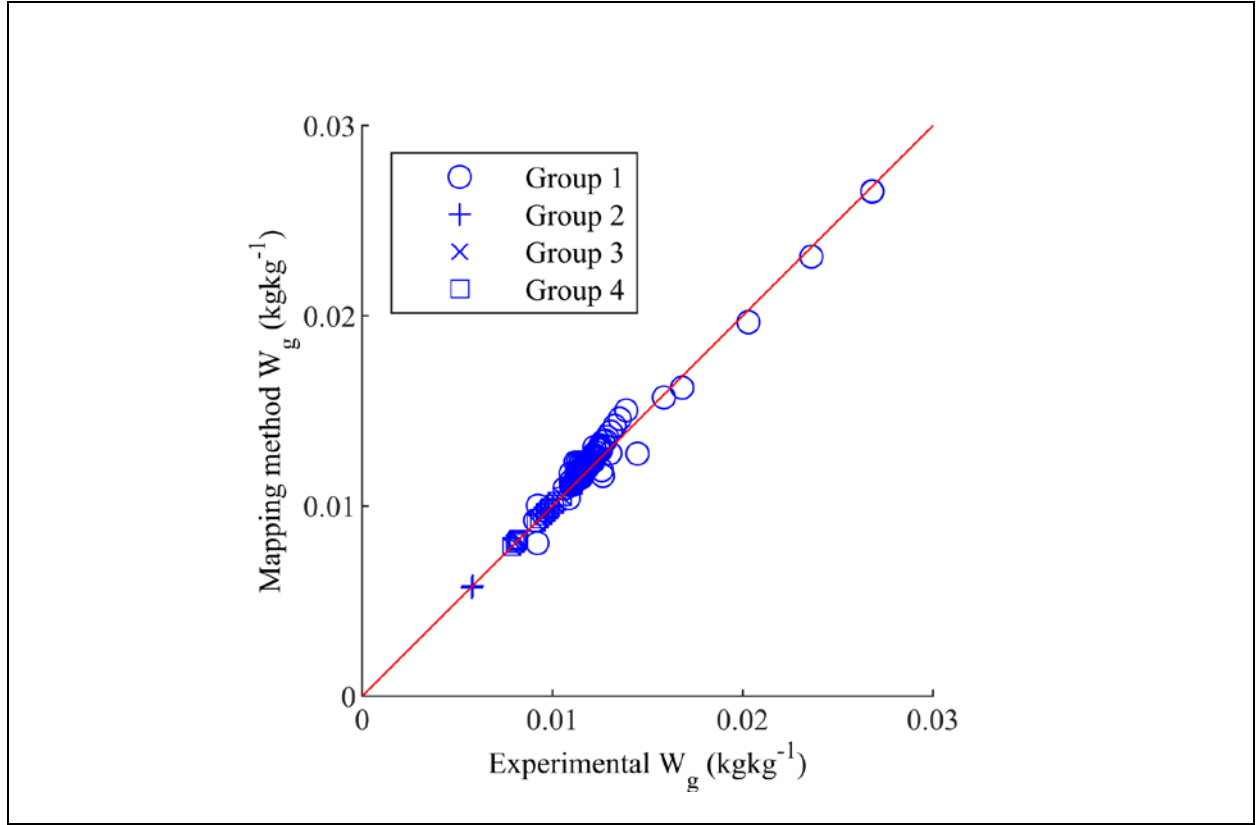


Fig. 18  $W_{g,SA}$  between FDM simulation and mapping method prediction, MAPE = 3.61%

#### 5.4 Conclusion of the Energy Recovery Wheel Mapping Method

In this stage, a mathematical model of energy recovery wheels to predict performance is constructed. Additionally, a mapping method for performance estimation of energy recovery is also established. The model and the mapping method both are applicable for the analysis and optimization of an energy recovery wheel. Input boundary conditions include outdoor air conditions, return air conditions, the geometry of an energy recovery wheel (diameter and depth of the wheel), and operating conditions (wheel rotation speed), and the applicable range is defined. This feature of flexible inputs makes the mathematical model and mapping method ideal for commercial usage (e.g., selection tool), and for academic research (e.g., optimization analysis).

The validation is carried out using experimental results as well as data published in other papers. The experimental data were collected from two different laboratories. The mathematical

model and mapping method can be applied for at least two types of energy recovery wheels which were studied in Zhai [7] and Antonellis [25][26].

The mapping method is more efficient in predicting the performance of wheel geometries and operating conditions than other energy recovery wheel models developed in other papers. The proposed mapping method for energy recovery wheel performance prediction contributes to the establishment of a time-efficient and user-friendly tool for the design, analysis, and optimization of an energy recovery wheel integrated HVAC system.

## 6. DESICCANT WHEEL MAPPING METHOD DEVELOPMENT

A semi-empirical mapping method for the performance prediction of energy recovery wheels was developed and validated in Chapter 5. The next objective is to develop a semi-empirical mapping method for desiccant wheels. The mapping method proposed in Chapter 5 is designed for predicting the performance of energy recovery wheels; nonetheless, desiccant wheels share similar working principles and physical phenomena with energy recovery wheels. Hence, the process of configuring the energy recovery wheel semi-empirical mapping method is implemented to develop a semi-empirical mapping method for desiccant wheels. The new mapping method is expected to exhibit the same benefits as the energy recovery wheel mapping method, e.g., the method requires only a small number of data points to train, which significantly reduces the time and the cost of experimental testing. The characteristics of the method can be beneficial to the research and development activities of desiccant wheels.

### 6.1 Original Wheel Mapping Method Form Extension Study

The proposed semi-empirical mapping method for energy recovery wheels is designed for predicting the outlet air temperature and humidity ratio in the supply stream. The mapping method consists of the inlet air conditions of the supply stream and the regeneration stream, and the characteristics of the target wheel including rotational speed, the air face velocities, and wheel depth to estimate the performance of a wheel. The coefficients of the wheel characteristics need to be trained separately, e.g., to obtain  $a_1$  and  $a_2$  in (54) the wheel rotational speed is the only variable changed while fixing all other variables. The finite difference method (FDM) desiccant wheel model developed previously was utilized in this section to generate the training data sets. After the mapping method is trained and all coefficients are obtained, the mapping method was employed to predict the performance of the desiccant wheel from manufacturer B. The predictions of the mapping method against the FDM simulation results are based on the boundary conditions from the selection tools.

As Fig. 21 and Fig. 22 show, the mapping method predictions do not agree with the FDM simulation results very well. The outlet air temperature prediction in the supply stream delivered a 20.7% mean absolute percentage error (MAPE), and the outlet air humidity ratio prediction

exhibited constant over-predicted results. For the temperature prediction, the potential issue could be that there is a missed variable in the semi-empirical mapping method. For the humidity prediction, humidity ratio may not be a suitable variable to utilize in the mapping method. In desiccant wheel applications, regeneration air would be heated up to decrease the relative humidity. The humidity ratio of the regeneration air may be equal to or less than the outdoor air, and this characteristic makes the humidity ratio unsuitable for desiccant wheel performance mapping. Hence, the original form of the energy recovery wheel semi-empirical mapping method is not completely suitable for the desiccant wheel performance prediction; hence, it is necessary to investigate a new form of the semi-empirical method for desiccant wheels in order to utilize the method for the performance prediction of desiccant wheels.

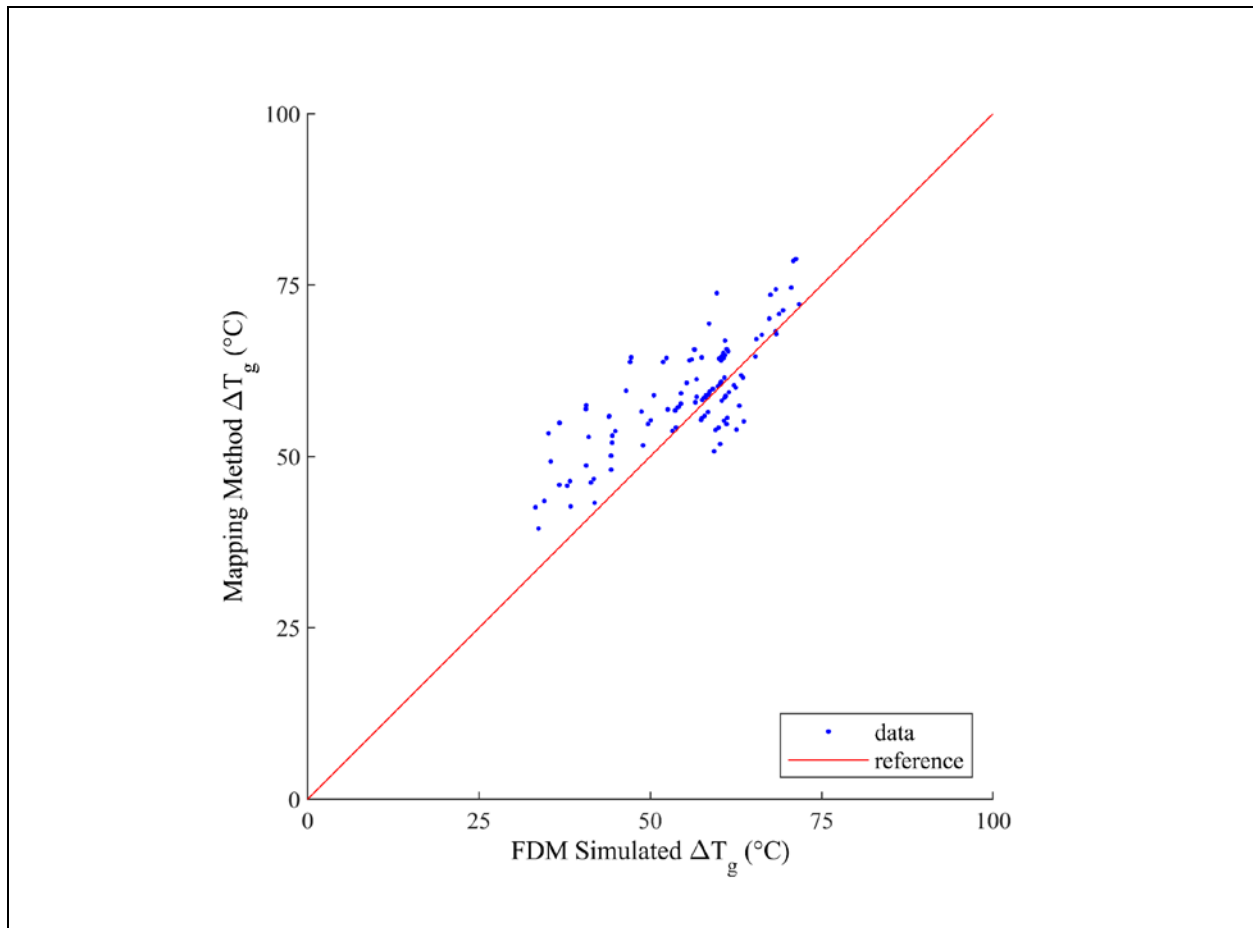


Fig. 19  $\Delta T_{g, SA}$  between FDM simulation results and original mapping method prediction

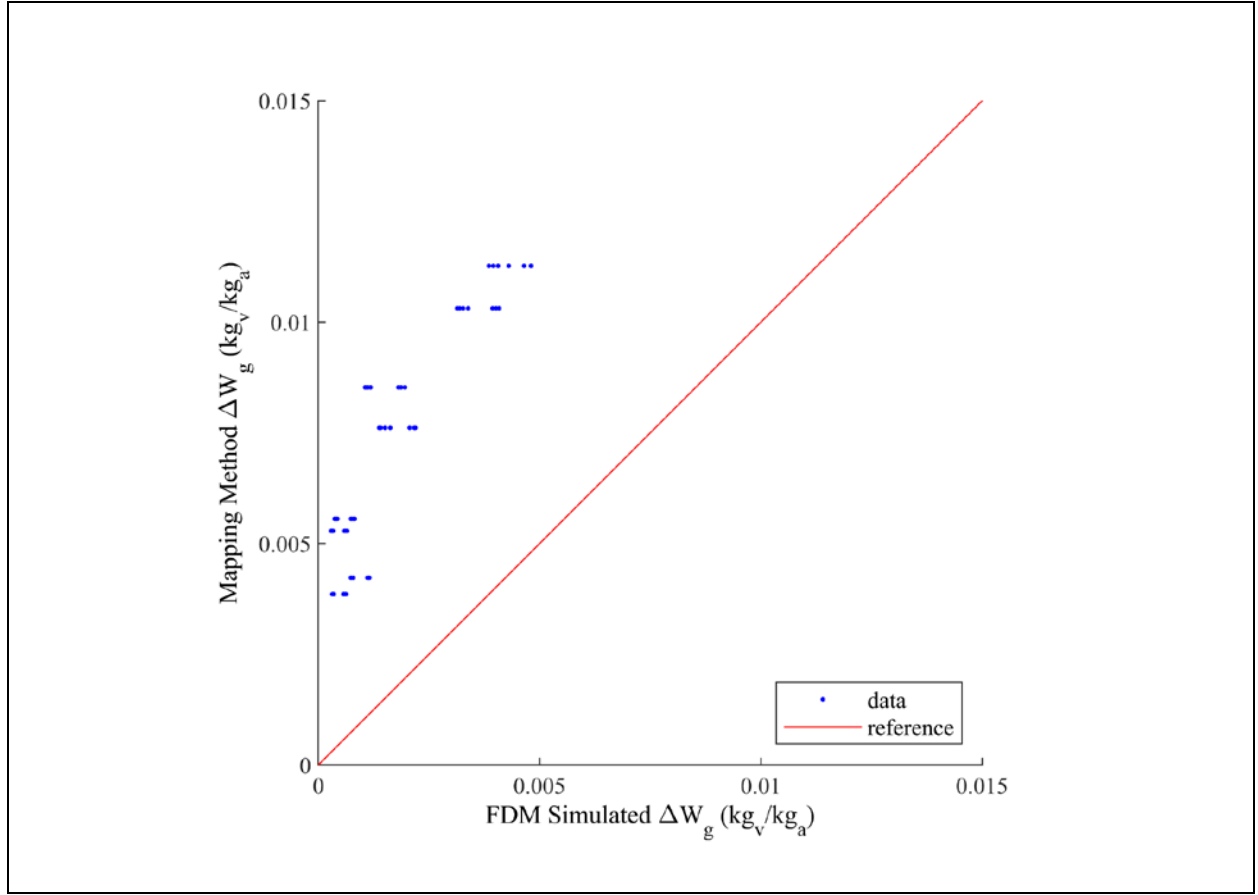


Fig. 20  $\Delta W_{g, SA}$  between data sets and original mapping method prediction

## 6.2 Desiccant Wheel Mapping Method Development

The procedure of developing the semi-empirical mapping method of energy recovery wheels is illustrated in Chapter 5.2. This procedure will be utilized to develop a semi-empirical mapping method for desiccant wheels. The following elements form the semi-empirical mapping method for an energy recovery wheel: a representation of the traveling time for a wheel rotating through an airstream is a linear function; the representation of the air face velocity in the supply stream is a linear function; the representation of the wheel depth is a second-order exponential function; the regeneration air face velocity is represented by a ratio of the air face velocity in the regeneration stream to the air face velocity in the supply stream. The first step for investigating the new form of the semi-empirical mapping method is identifying the representation form of each



parameter (rotational speed, outdoor/regeneration air face velocity, wheel depth). With the desiccant wheel FDM model developed in Chapter 4.7.2, it is possible to isolate each parameter and its effect on the supply air condition. To observe the impact of each parameter on the prediction, one input parameter is varied at a time, while all other inputs keep unchanged. The trend of influence on the changing parameter can be detected, then used to formulate a function of the semi-empirical mapping method for that parameter.

The relationship between the traveling time of a flute in one airstream and the supply air temperature was identified to be linear for desiccant wheels. Three trials were conducted and each of the trials delivered a high regression to a linear function ( $R^2$ -values of 0.9983, 0.9990, and 0.9521) as shown in Fig. 21 that is drawn based on (60). A linear function was selected to build the functional form between the traveling time of a flute in one airstream and the supply air condition; hence, the function is represented as shown in (61).

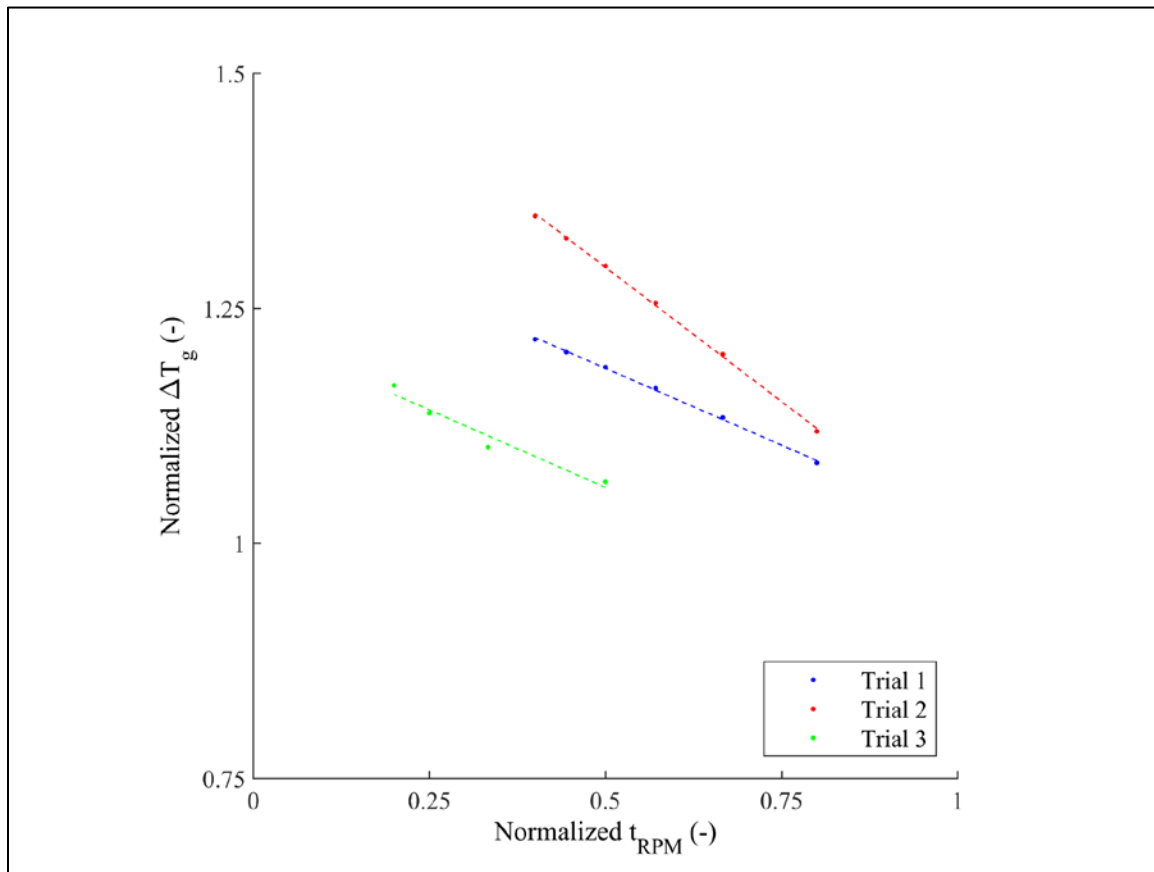


Fig. 21 Effect of the traveling time of a flute in one airstream on desiccant wheel performance

$$\frac{f(t_{RPM})}{f(t_{RPM})_{max}} = \frac{T_{g,OA} - T_{g,SA}}{(T_{g,OA} - T_{g,SA})_{max}} \quad (60)$$

$$f(t_{RPM}) = a_1 t_{RPM} + b_1 \quad (61)$$

Then, the air face velocity in the supply stream was isolated for the next investigation, and the effect of the supply air face velocity on the supply air condition was plotted in Fig. 22 that is plotted according to (62). In each trial, the relationship is substantially linear, with regression  $R^2$ -values of 0.9992, 0.9999, and 0.9996. Therefore, the form of the air face velocity function in the supply stream was also decided to be a linear function as presented in (63).

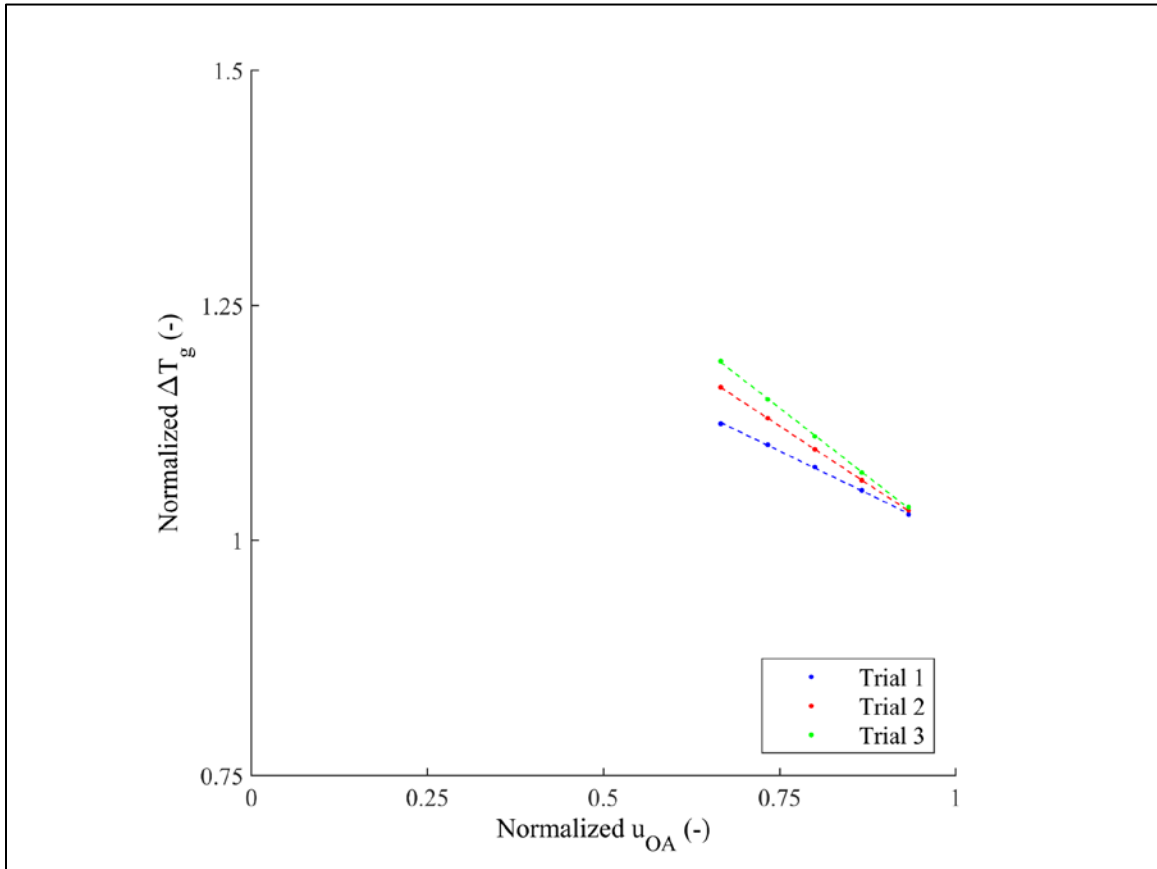


Fig. 22 Effect of the air face velocity in supply stream on desiccant wheel performance

$$\frac{f(u_{OA})}{f(u_{OA})_{max}} = \frac{T_{g,OA} - T_{g,SA}}{(T_{g,OA} - T_{g,SA})_{max}} \quad (62)$$

$$f(u_{OA}) = a_2 u_{OA} + b_2 \quad (63)$$

Last, the wheel depth influence function was isolated Fig. 23, composed of (64), shows that the influence of the wheel depth on the supply air condition is not linear in all trial cases. To capture the relationship between wheel depth and wheel performance, different approaches (polynomial, power, and exponential) were utilized to generate the most appropriate functional form. A two term exponential regression provides the best approximation consistently, and  $R^2$ -values are 0.999, 0.9998, and 0.9999. Accordingly, this exponential form is used for representing the wheel depth effect, shown as (65).

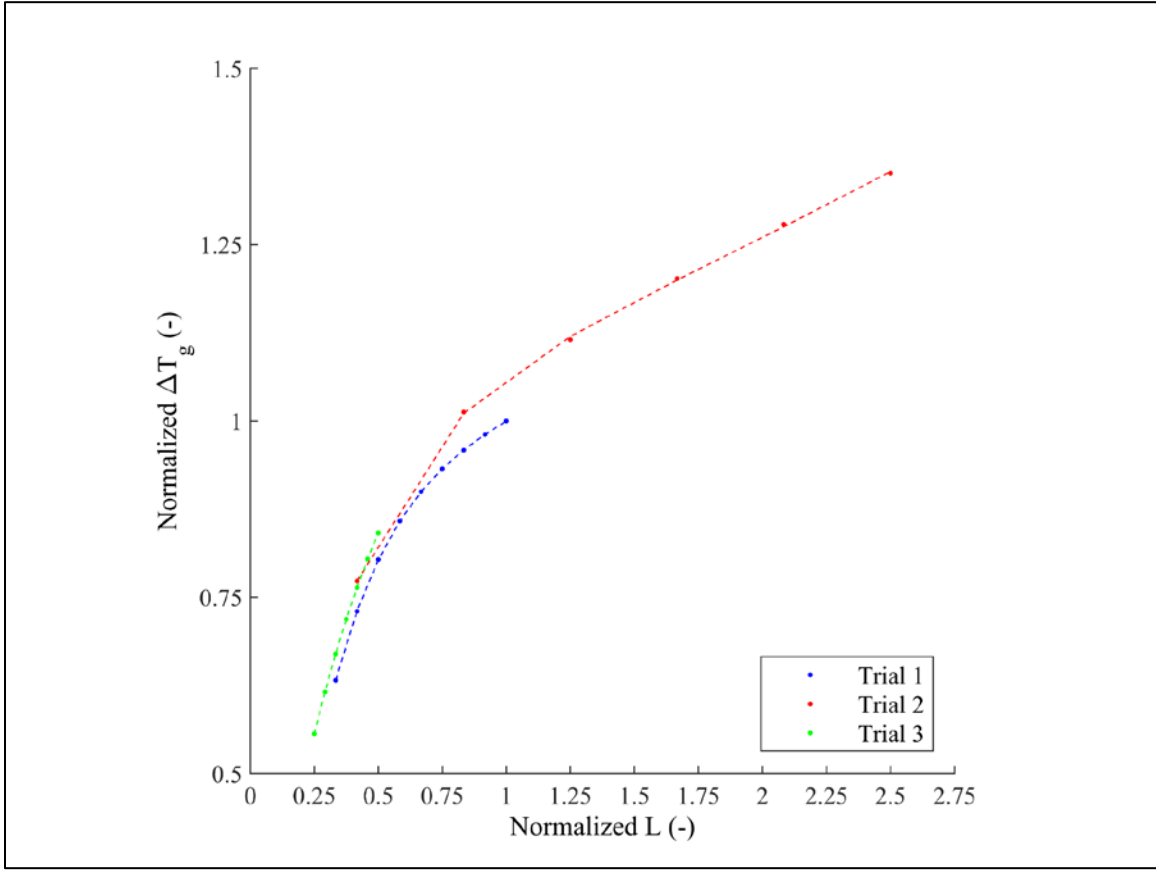


Fig. 23 Effect of the wheel depth on desiccant wheel performance

$$\frac{f(L)}{f(L)_{max}} = \frac{T_{g,OA} - T_{g,SA}}{(T_{g,OA} - T_{g,SA})_{max}} \quad (64)$$

$$f(L) = a_3 e^{b_3 L} + c_3 e^{d_3 L} \quad (65)$$

Furthermore, the influence of air face velocity in the regeneration stream on the supply air condition is investigated. The semi-empirical energy recovery wheel mapping method uses a ratio of the air face velocity in the regeneration stream to the air face velocity in the supply stream to include the regeneration airflow rate. Desiccant wheels typically operate at a significantly slower rotational speed (< 0.5 RPM) compared to energy recovery wheels (20 RPM – 40 RPM); hence,

the influence of the air face velocity in the regeneration stream could be more influential in the desiccant wheel application. The isolation process was conducted to identify the functional form according to (66), and the effect of the air face velocity in the regeneration stream on the supply air condition, shown in Fig. 24, to be linear, with regression of 0.9999, 0.9999, and 0.9998. Therefore, the functional form of the air face velocity in the regeneration stream was also selected to be a linear function as (67) shown.

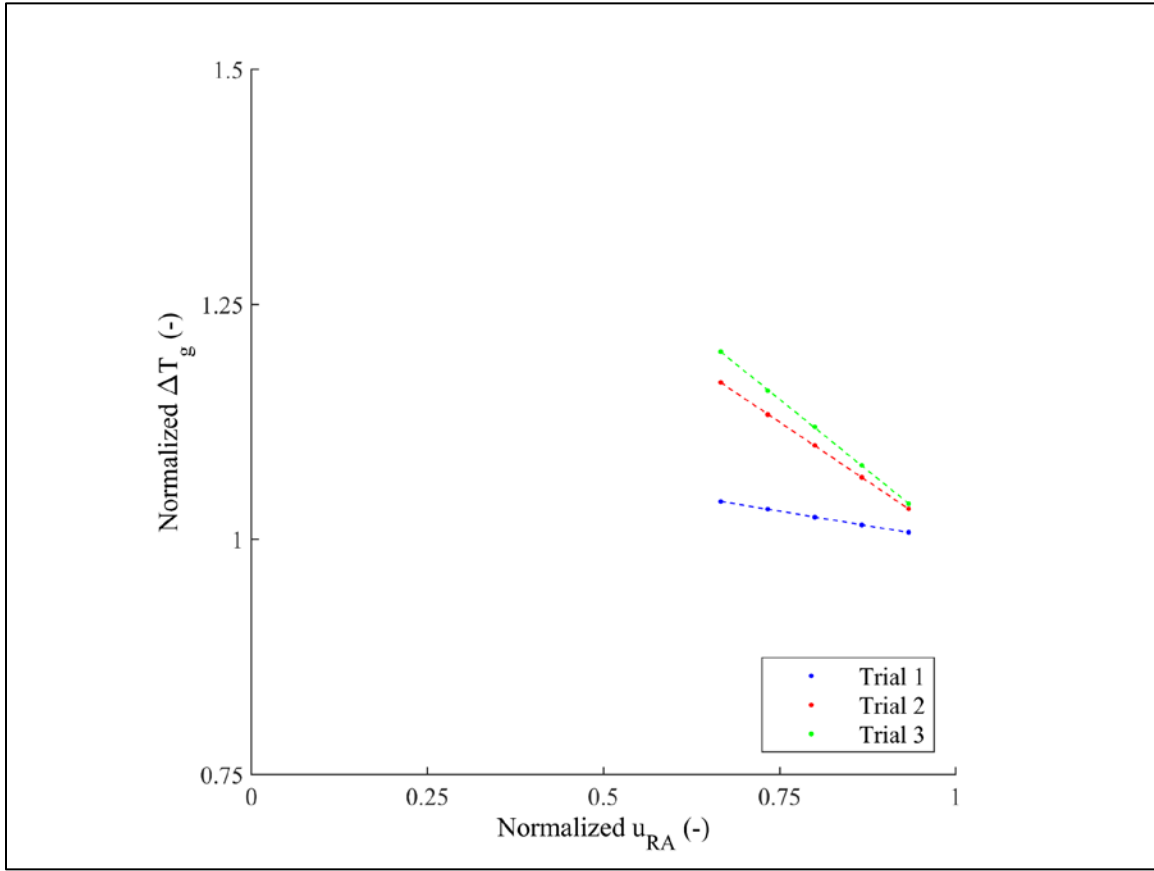


Fig. 24 Effect of the air face velocity in regeneration stream on desiccant wheel performance

$$\frac{f(u_{RA})}{f(u_{RA})_{max}} = \frac{T_{g,OA} - T_{g,SA}}{(T_{g,OA} - T_{g,SA})_{max}} \quad (66)$$

$$f(u_{RA}) = a_2 u_{RA} + b_2 \quad (67)$$

In addition, the humidity ratio is utilized in the semi-empirical mapping method for energy recovery wheels; however, the humidity ratio of the regeneration air may sometimes be equal to or less than the outdoor air. The regeneration air would typically be heated up to provide a higher moisture removal capacity; thus, the saturation vapor pressure of the regeneration air is increased, and the relative humidity is decreased. This characteristic leads to the result that the humidity ratio is not an ideal parameter to be utilized in the performance mapping of desiccant wheels. Another representative form of humidity has been investigated including relative humidity, wet-bulb temperature, and dew point temperature. Relative humidity shows a good capability to predict the performance of desiccant wheels. Therefore, the forms of semi-empirical mapping method for desiccant wheels are presented as (68) for supply air dry-bulb temperature and (69) for supply air relative humidity.

$$T_{g,SA,out} = T_{g,SA,in} - \frac{0.59L^{a_0}}{d_h \rho_g C p_g} (a_1 t_{RPM} + b_1)(a_2 u_{SA} + b_2)(a_3 u_{RA} + b_3)(a_4 e^{b_4 L} + c_4 e^{d_4 L})(T_{g,SA,in} - T_{g,RA,in}) \quad (68)$$

$$\phi_{g,SA,out} = \phi_{g,SA,in} - \frac{0.59L^{m_0}}{d_h \rho_g C p_g} (m_1 t_{RPM} + n_1)(m_2 u_{SA} + n_2)(m_3 u_{RA} + n_3)(m_4 e^{n_4 L} + o_4 e^{p_4 L})(\phi_{g,SA,in} - \phi_{g,RA,in}) \quad (69)$$

### 6.2.1 Operating Range and Training Data Quantity

The typical application ranges for desiccant wheels are investigated and used as extreme cases employed in this study. The extreme cases were set as the boundary conditions to the FDM model and the mapping method, then the results from the two methods were compared against

each other. The application condition was considered valid, if the error is less than 10%. The application range of the mapping method is stated in Table 6.

Table 6 Operating range of the desiccant wheel mapping method

<b>Variables</b>	<b>Value</b>
SA Temperature (°C)	20 to 50
RA Temperature (°C)	60 to 150
SA/RA Humidity Ratio (kgkg <sup>-1</sup> )	0.001 to 0.025
Airflow Face Velocity (ms <sup>-1</sup> )	1.8 to 5
Rotation Speed (RPH)	4 to 40
Wheel Depth (m)	0.2 to 1.0

The quantity of supplementary training data points is investigated. The data set that was utilized in the development of the variables' characteristic functions is subsequently implemented in this investigation. The data set covers a wide range of wheel geometries and operating conditions; hence, it is suitable for this investigation. Excluding the boundary conditions (8 data points), 6 of the supplementary training data points are randomly selected, and a set of coefficients for the mapping method is generated. Then, the mean absolute percentage error (MAPE) between the mapping method prediction and the data set is calculated. This procedure is repeated 1000 times to evaluate the influence of the supplementary training data points. Figure 25 shows the occurring frequency of MAPEs in the 0% to 10% error region. The pattern of MAPEs is similar to a normal distribution, the mean of MAPEs is 4.28%, the standard deviation of MAPEs is 0.44%; hence, a 95% confidence interval would be observed to fall within 10%.

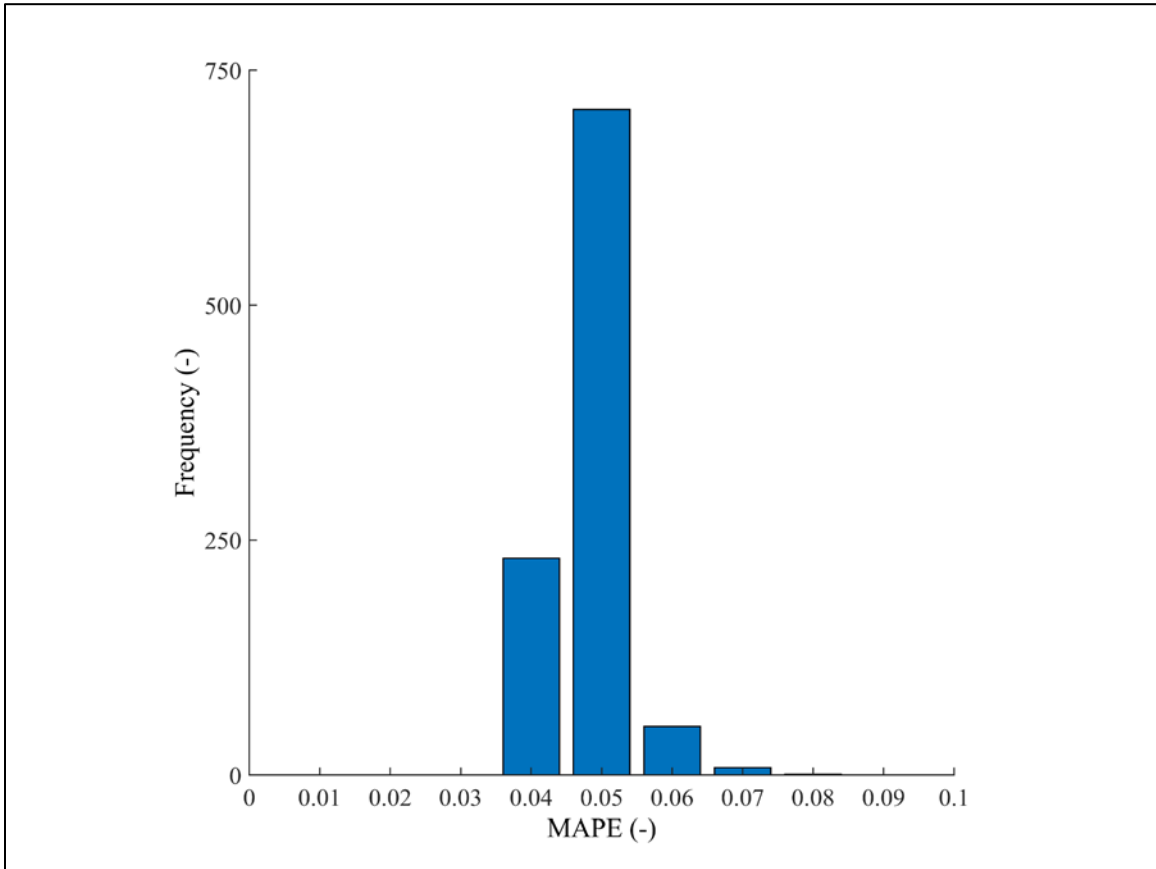


Fig. 25 Frequency distribution of MAPE with different random training data points

### 6.3 Validation of the Desiccant Wheel Mapping Method

The mapping method was trained and validated by employing three separate sets of data to examine the universality of this approach in the desiccant wheel application. The first data set is generated from a selection tool provided by manufacturer B, including eight different sizes of desiccant wheels. The second data set was collected from the published work of Enteria et al. [15], who studied a desiccant wheel under a wide range of operating conditions. The third data set was obtained from the published work of Kang and Lee [12], who conducted experimental testing on two types of desiccant wheels to determine their performance.

Parity plots are drawn for the supply air temperature changes (shown as Fig. 26) and the humidity ratio changes (shown as Fig. 27) to visualize the comparisons between the performance



predictions of the mapping method and the values from the data sets. Even though the desiccant wheel mapping method utilizes relative humidity for performance prediction, relative humidity is not an ideal parameter to represent the humidity change across the desiccant wheel in the supply airstream. Thus, the relative humidity prediction results generated by the mapping method were converted to humidity ratio after the computation. The validation study for the desiccant wheels from the selection tool consists of a total of 203 data points; a total of 60 data points from Enteria et al. [15]; and a total of 43 data points from Kang and Lee [12]. For each data group, the training data points are selected in two ways. The manually selected training data points consist of extreme cases of supply/regeneration airstream face velocity, rotational speed, and depth (total of 8 points); the extra training data points are selected randomly (total of 6 points). As Fig. 26 and Fig. 27 exhibit, the prediction results from the mapping method and the data sets agree with each other, and the mean absolute prediction errors (MAPE) are 4.7% for supply air temperature changes and 0.1% for supply air humidity ratio changes. The desiccant wheel delivered significant moisture removal, and the leaving air humidity ratio is typically low (under 0.005 kg/kg); hence, low MAPE of the supply air humidity ratio changes is obtained. The coefficients of the mapping method for each group of the data sets were obtained through an optimization process. As Chapter 5 mentioned, the optimization approach that is used to train the coefficients could be trapped in a local minimum when the initial guess values are far away from the true value. Therefore, identifying starting values for the coefficients by isolating variables as suggested in the previous chapter is preferable. Furthermore, unlike the semi-empirical mapping method for energy recovery wheels, the coefficients set of the semi-empirical mapping method for desiccant wheels for the air temperature prediction and the relative humidity prediction are not identical. The training process would require to be conducted twice, once for air temperature prediction (68) and once for relative humidity prediction (69).

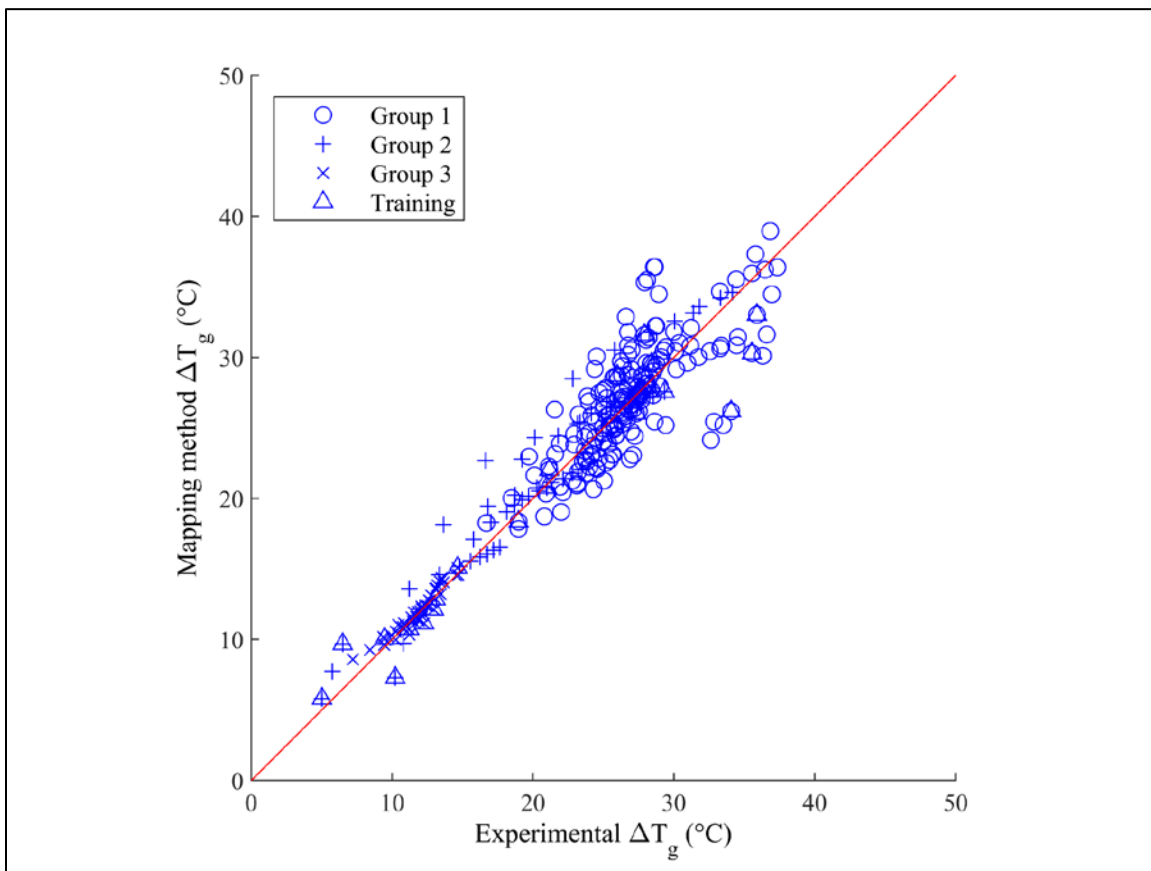


Fig. 26  $\Delta T_{g, SA}$  between data sets and mapping method prediction

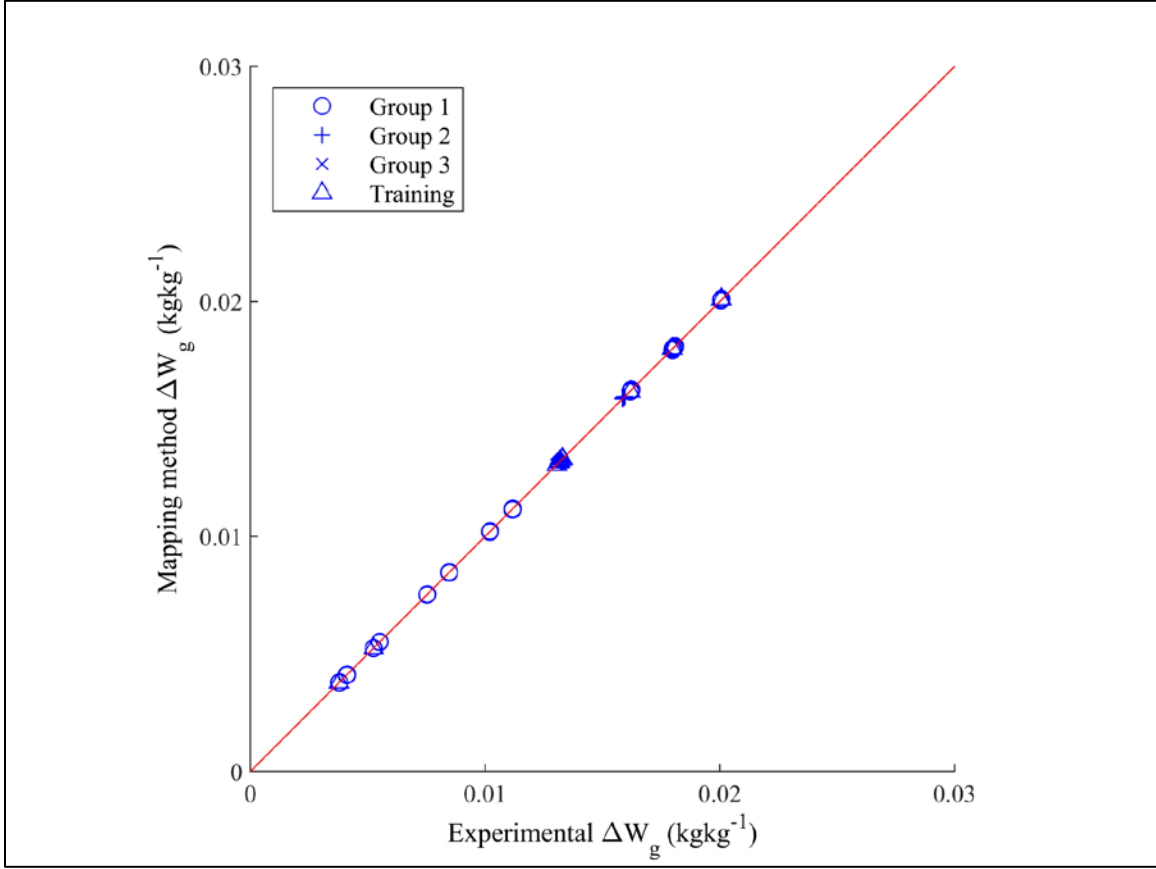


Fig. 27  $\Delta W_{g, SA}$  between data sets and mapping method prediction

#### 6.4 Conclusion of the Desiccant Wheel Mapping Method

A new form for a semi-empirical performance mapping method for desiccant wheels was developed based on the approach implemented for energy recovery wheel mapping found in Chapter 5 and validated based on different data sources in this section. Furthermore, a validated finite difference numerical model for desiccant wheels was also implemented for developing the semi-empirical mapping method. Different data sets are utilized to train and validate the mapping method in order to examine its universality. One data set was generated by the selection tool from manufacturer B, and the other two data sets are collected from published works of literature. Then, the results of the semi-mapping method are validated against the data sets.

The training data points selection and the applicable range of the mapping method are defined. The study in this section extended the application of the semi-empirical performance mapping method to desiccant wheels. Distinct characteristics of the desiccant wheel mapping method are listed as follows: Firstly, the mapping method performs well in the trained range. The boundary of the mapping method should be defined properly, since the mapping method becomes ineffective once the application condition is outside the boundary condition. Secondly, once the boundary conditions are defined, the supplementary random training data points are suggested to improve the accuracy of the predictions. The desiccant wheel semi-empirical mapping method delivers performance prediction with under 5% MAPE for leaving air temperature change and humidity ratio change.

## 7. ENERGY RECOVERY WHEEL CASE STUDY

### 7.1 Building Performance Simulation and Optimization Introduction

An energy recovery wheel is often combined with a conventional vapor compression air conditioner and a heater to condition the supply air in a space to its setpoints. Building energy performance simulation is frequently utilized to evaluate the performance of an HVAC design. Thus, building performance simulation software is selected to construct a model that implements the semi-empirical energy recovery wheel mapping method and conduct performance evaluations and optimizations of the system.

Severe acute respiratory syndrome coronavirus 2 (SARS-CoV-2) is a rapidly emerging disease that has been spread globally since December 2019 [61]. After a series of disease-controlling policies and actions, the Centers for Disease Control and Prevention (CDC) released guidance for the reopening of office buildings for business [62] and building ventilation recommendations [63]. Besides applying proper sanitizing method, CDC indicates that a “high ventilation” rate is recommended for operating an occupied space; however, an absolute value of ventilation rate is not specified. Furthermore, many existing commercial buildings were designed according to ASHRAE 62.1 [3]. This standard only advises the air changes per hour rate (ACH) of a small office building to be higher than around 0.5 ACH, which is considered as a low ventilation rate. Therefore, a series of different ACH rates will be investigated in this case study. Nonetheless, increasing outdoor ACH would result in higher energy consumption for air-conditioning and heating. An energy recovery ventilator is ideal for the application of raising outdoor air intake without tremendously increasing energy consumption on conditioning. Hence, an energy recovery wheel integrated HVAC in a small office building will be studied in this section, and this study will focus on the building energy performance with variant outdoor ACH.

TRNSYS is a transient simulation software package that has been commercialized and available since 1975. It has continued to develop through an international collaboration between the United States (Thermal Energy System Specialists and the University of Wisconsin-Solar Energy Laboratory), France (Centre Scientifique et Technique du Bâtiment), and Germany (TRANSSOLAR Energietechnik). [4] TRNSYS not only maintains flexible energy simulation characteristics, but also implements the addition of mathematical models, available add-on

components, and the ability to communicate with other programs (e.g., MATLAB or Python). TRNSYS has been used extensively in the heating, ventilation, and air-conditioning (HVAC) area, conventional building energy management, and building energy performance prediction. The philosophy behind TRNSYS is conducting a simulation of the design system by breaking it into different components in an individual module. TRNSYS provides open-source code to the public so that users can customize components for their different simulation objectives, or users may select applicable components for their purpose from the TRNSYS standard library such as refrigeration systems, hydrogen systems, mechanical systems, and many others. Above all, TRNSYS is an approved LEED simulation software package (LEED online v3) and ASHRAE Standard 140 approved.

TRNSYS is well known for its flexible graphically based user platform and robust computation ability for transient system simulations. The application includes predicting the performance of thermal and electrical systems. TRNSYS consists of two parts: One part is an engine (called the kernel) that reads the input variables, computes the system setup, and plots results. The kernel also provides utilities that (among other things) determine thermophysical properties of materials, invert matrices, perform linear regressions, and interpolate external data files. The other is an extensive library of component modules, where each module represents one part of the overall system. The library includes most typical HVAC elements (e.g., pumps, coils, coolers, heaters, and fans). Modules are modifiable, so users can change existing components to the target application or simply utilize the default setups. [4] TRNSYS can also import three-dimensional geometrical building models. The simulation engine facilitates the programming with user-adjustable components and an easy-using modifiable graphical interface. The standard model accurately calculates and displays the energy usage and consumption between a building, climate, and the surroundings. All the above features make TRNSYS a powerful building energy simulation software package. As a result, TRNSYS is an ideal tool for this simulation.

GenOpt is an optimization program developed by Lawrence Berkeley National Laboratory, and it is designed for minimizing a target function. GenOpt is widely used to couple with building energy performance simulation programs, e.g., TRNSYS, EnergyPlus, DOE-2, etc. GenOpt can read the output files from external building energy performance simulation software and write input files for external programs to read; hence, GenOpt can conduct optimization of a building and its HVAC system by working with external building energy performance simulation software.

GenOpt is a flexible optimization program, the optimization target variables can be continuous or discrete; the upper bounds and the lower bounds of each variable can be defined individually; several optimization algorithms are built-in and ready to be used, e.g., Hooke-Jeeves algorithm, golden-section search, particle swarm optimization, etc.

TRNOPT is a TRNSYS module developed by Thermal Energy System Specialists (TESS) in order to provide a user-friendly coupling tool between TRNSYS and GENOPT. TRNOPT serves as an interface program between two programs and guides users step-by-step to establish the optimization process. TRNOPT connects TRNSYS and GenOpt well, and delivers reliable results; hence, it is selected to perform this case study.

## **7.2 Small Office Building Model Development**

A building energy simulation model was constructed based on the small office reference building developed and published by the United States Department of Energy (U.S. DOE) [64]. The small office is a one-story building with an attic; the area is 511 m<sup>2</sup> (28 m length x 18 m width); the ceiling height is 3.05 m. The main entrance door (2.13 m height x 1.83 m length) is located on the south wall. The dimension of the windows is 1.52 m height x 1.83 m width, and there are six windows on the south/north wall and four windows on the east/west wall. The occupied conditioned space is cut into five simulation zones, since multi-zone simulation is capable of delivering a more accurate prediction for the building energy performance evaluation. The building is divided into four zones on the perimeter and one zone in the center. The exterior walls are set as the mass wall type, which has continuous insulation. The U-value of the exterior walls is 0.51 W/m<sup>2</sup>K; the U-value of the exterior roof is 0.316 W/m<sup>2</sup>K. These settings satisfy the requirements listed in the U.S. DOE commercial reference building models code [64]. Since the building model is constructed based on the reference building, and a standard building energy simulation software (TRNSYS) is used, this approach delivers reliable results even without validation of the model. Figure 28 (a) exhibits the layout of a typical conventional vapor-compression HVAC system in a small office building that requires fresh outdoor air introduced to the occupied space, and (b) shows the layout of an energy recovery wheel integrated HVAC system.

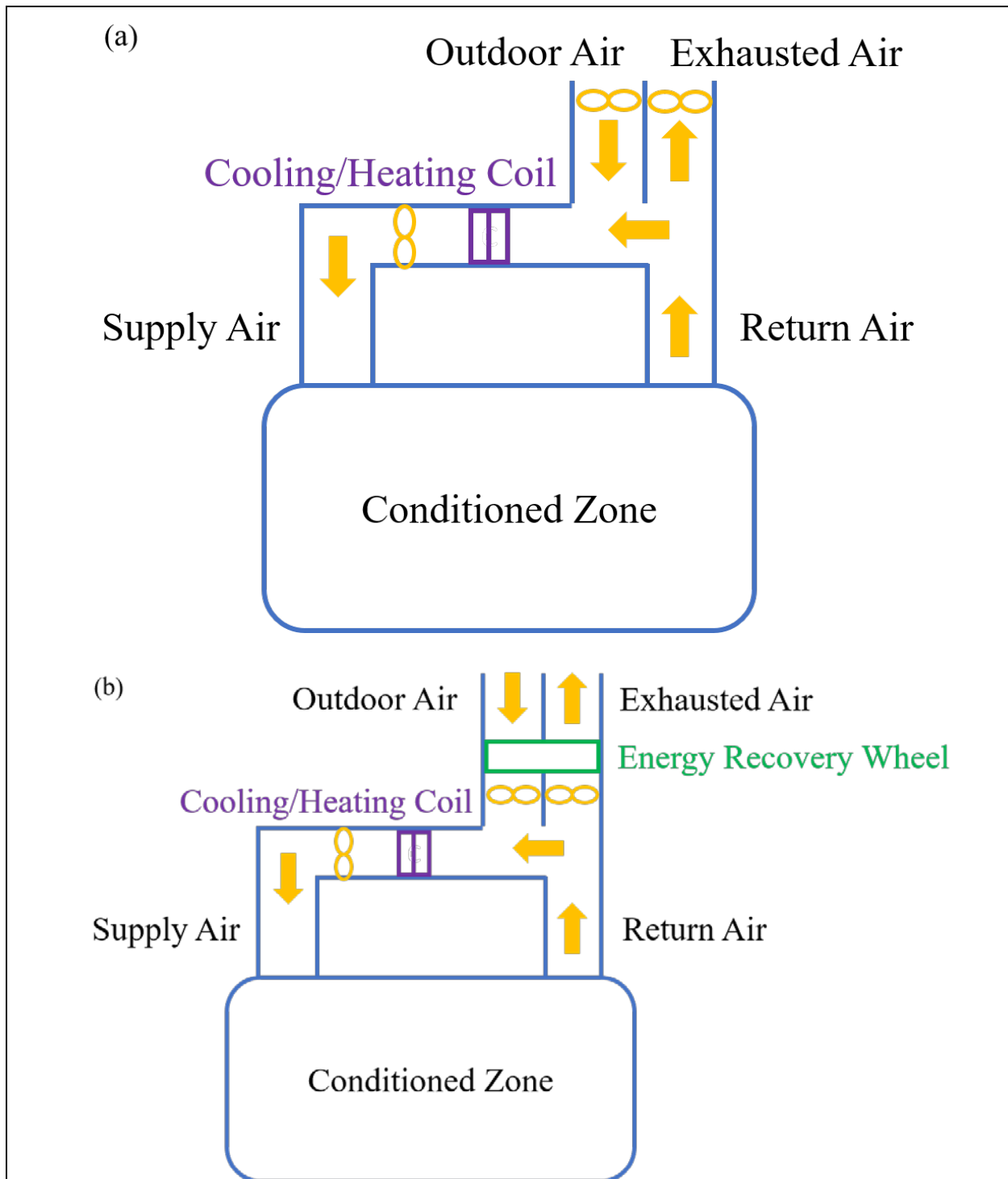


Fig. 28 Schematic of (a) vapor-compression HVAC system (b) energy recovery wheel integrated HVAC system



The weather data utilized in the simulation is typical meteorological year 3 (TMY3) data. TMY is a weather file format that includes hourly data of solar and meteorological information for one year, and the data sets are collected and compiled by the U.S. DOE. The first generation TMY weather data sets were released in the 1980s, then they were updated in the 2000s and renamed TMY3 [65]. TMY3 weather data sets are widely used in building energy performance simulations and evaluations for different HVAC system designs or different climates. Since office buildings are typically open year-round, the study period is from January 1st 0:00 to December 31<sup>st</sup> 23:59. The occupancy schedule and internal load schedule are set to be the same as the schedule specified in the DOE reference building.

The HVAC system is a constant air volume design and operates 24/7 annually. The airflow rate is determined by the maximum sensible load of the space and the air change rate. In this study, the cooling is provided by a single-speed air conditioner, and the cooling setpoint temperature is 23.89°C. TRNSYS built-in component library includes a single-speed air-conditioner (A/C) unit (Type 921), that is utilized to simulate the cooling process. Then, the power consumption of the A/C ( $P_{AC}$ ) is calculated proportionally according to the instant A/C power consumption output from Type 921 ( $P_{921}$ ), the sensible load of the space ( $\dot{Q}_{sen}$ ), and sensible heat removal provided by Type 921 ( $\dot{Q}_{sen,921}$ ). The ratio function is shown as (70). The heating is supplied by an electric heating coil, and the heating setpoint temperature is 20°C. Since the efficiency of the electric heating coil is almost 100%, the energy input to the heating coil is assumed to be equal to the heating sensible load of the space. The conventional vapor-compression HVAC system layout and wheel-integrated HVAC system layout are shown in Fig. 28 (a) and (b) respectively. The main duct air flow rate is calculated based on the maximum cooling demand of the space and a rule-of-thumb: 680 m<sup>3</sup>/h per 3.5 kW (400 ft<sup>3</sup>/min per 1 refrigeration ton).

$$P_{AC} = P_{921} \frac{\dot{Q}_{sen}}{\dot{Q}_{sen,921}} \quad (70)$$

The fan power consumption,  $P_{fan}$  [kJ/h], is calculated based on the air volumetric flow rate,  $\dot{V}$  [m<sup>3</sup>/s] air pressure drop,  $\Delta P$  [pa], and fan efficiency,  $\epsilon$  [-]. The fan efficiency is assumed as 70% in this study. The total pressure drop of the entire circulation is assumed to be 498 pa (2 in-H<sub>2</sub>O). The air pressure drop across the wheel,  $\Delta P_{wheel}$  [pa], is calculated based on the work of De Antonellis et al. [26]. In the equation, Fanning friction factor,  $f$  is determined by the Reynolds

number. The Reynolds number,  $Re$  [-], is related to air density, air face velocity, wheel flute hydraulic diameter, and dynamic viscosity of air. The Sutherland model (73) is utilized to calculate the dynamic viscosity of air,  $\mu$  [kg/ms], and the reference dynamic viscosity of air is  $1.78E^{-5}$  kg/ms at 288.13K (14.98°C).

$$P_{fan} = \frac{3.5937 \dot{V} \Delta P}{\varepsilon} \quad (71)$$

$$\Delta P_{wheel} = 4f \frac{L}{D_h} \frac{1}{2} \rho u^2 \quad (72)$$

$$f = \frac{13}{Re}$$

$$Re = \frac{\rho u D_h}{\mu}$$

$$\mu = \mu' \left( \frac{T}{T'} \right)^{1.5} \frac{T'}{T + 113} \quad (73)$$

$$\mu' = 1.78E^{-5} \text{ kg/ms @ } T' = 288.13K$$

The moisture balance is achieved by calculating the moisture removal rate provided by the A/C shown as (74), then the moisture removal rate is fed to the space as a negative moisture gain. Type 921 can output the humidity ratio of the leaving air ( $W_{921}$ ); the mix air humidity ratio ( $W_{MA}$ ) can be calculated from return air condition ( $W_{RA}$ ) and outdoor air condition ( $W_{OA}$ ) based on outdoor ACH; hence, the moisture removal rate ( $\dot{m}_{AC}$ ) can be obtained. The logic of the moisture balance of the HVAC system and the conditioned zone is visualized as Fig. 29.

$$\begin{aligned} \dot{m}_{AC} &= \dot{m}_a (W_{out} - W_{in}) \\ &= \dot{m}_a (W_{921} - W_{MA}) \end{aligned} \quad (74)$$

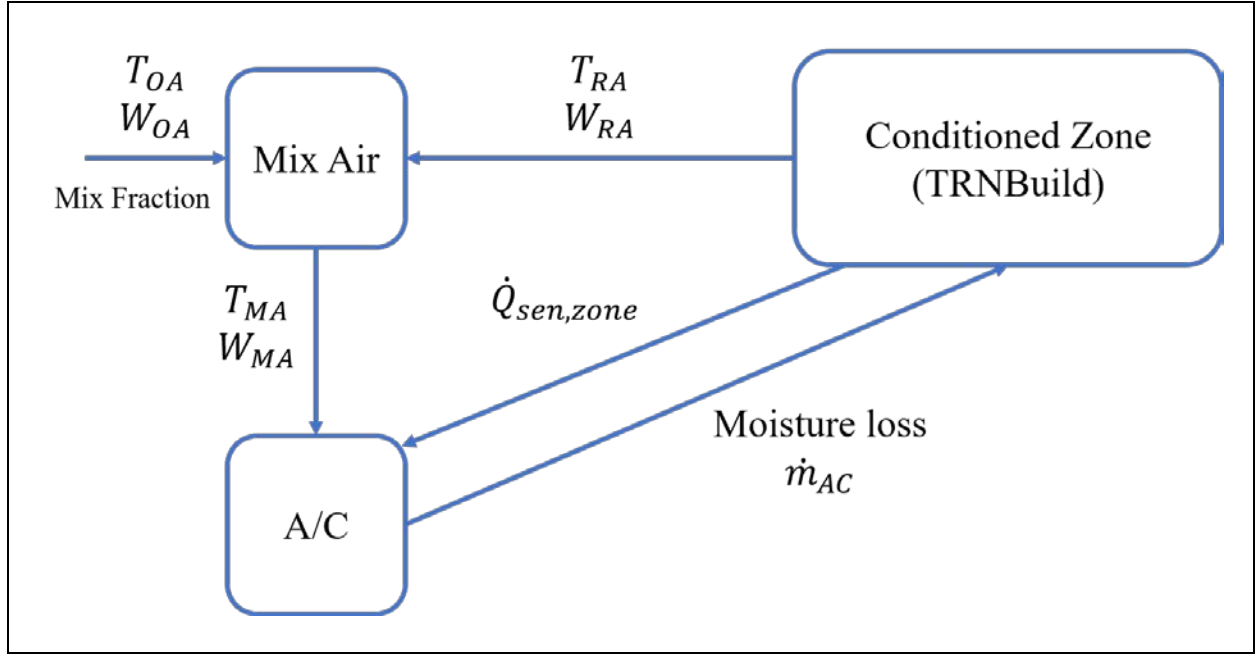


Fig. 29 Moisture balance logic

The wheel-integrated HVAC system model includes a set of functions constructed in TRNSYS to utilize the energy recovery wheel mapping method in order to predict the performance of energy recovery wheels, and then the outcomes are fed to the building energy simulation platform. The components include an input module that receives energy recovery configurations (wheel depth, rotational speed, outdoor air face velocity, and exhaust air face velocity); a computation module that consists of (54) for leaving air temperature prediction in the supply stream and (55) for leaving air humidity ratio estimation in the supply stream. As Fig. 28 (b) shows, the inlet air of the wheel in the supply airstream is from the ambient, which can be collected from TMY3; the regeneration air is part of the return air from the conditioned zone, which can be obtained from TRNSYS. The power consumption of the wheel motor is assumed to be 0.1864 kW (0.25 HP). Last, the purge section is determined by the outdoor air face velocity and the wheel rotational speed. The percentage of the wheel section is calculated based on (75).

$$Percentage_{purge} = \frac{L/u_{OA}}{t_{RPM}} \quad (75)$$

The price of energy recovery wheels is difficult to obtain, since limited information is available in the public domain. Wheel manufacturers are protective of this sensitive information, since the benefits of the companies may be hurt if the price information is leaked to their competitors. Lewis [66] included the prices of a series of wheels in different dimensions from a wheel manufacturer. Even though the price Lewis [66] presented is not obtained from the same wheel manufacturer with the energy recovery wheel selected for this study, the information is utilized in this study to approximate the wheel initial cost for the optimization study. The price approximation is generated by interpolation and extrapolation of the prices in the work of Lewis [66], and (76) is the price approximation function. The price is determined by the wheel diameter and depth, and the calculation outcome represents the wheel price at the unit depth (1 mm). Once the unit depth of the wheel is obtained by inputting the wheel diameter, the final wheel price can be calculated by multiplying the wheel depth in mm. Hence, the price for different sizes of energy recovery wheels can be approximated by this method. The utility rates of the study locations are collected from the U.S. Energy Information Administration [67]. The average retail electricity prices (cents/kWh) of each state are listed on the website; hence, the utility rate of the studied locations is selected based on their state. Table 7 shows the utility rate of the study cities and their state.

$$price_{wheel} = 19.464d^2 - 3.1162d + 6.9463 \quad (76)$$

Table 7 Utility rate of the study locations

City	State	Utility Rate
Phoenix	Arizona	\$ 0.1052
San Francisco	California	\$ 0.1689
Miami	Florida	\$ 0.1044
West Lafayette	Indiana	\$ 0.0991
Minneapolis	Minnesota	\$ 0.1033
Houston	Texas	\$ 0.0860

### 7.3 Small Office Building Performance Simulation Results

After the small office building model was constructed in TRNSYS, an annual dynamic building energy performance simulation was conducted under TMY3 weather conditions of West Lafayette, IN. Fig. 30 shows the monthly cooling sensible load and the monthly heating sensible load (summary of five thermal zones) of the conditioned space that utilizes conventional vapor-compression cooling and electric heating HVAC systems over a typical meteorological year.

An energy recovery wheel is integrated with the HVAC system of the small office building based on the schematic shown in Fig. 28 (b). According to the wheel sizing guidelines from Manufacturer A, a 0.25 m depth and 0.39 m diameter energy recovery wheel that operates at 20 RPM, and 3 m/s face velocity in the outdoor airstream is recommended for the application of the small office building in West Lafayette, IN. The geometries and operating conditions of the recommended wheel are input to the energy recovery wheel mapping method in TRNSYS, and the TRNSYS model delivers the performance simulation results. The bar plot of the monthly cooling sensible load and the monthly heating sensible load of the wheel integrated HVAC system is presented in Fig. 31.

Fig. 30 and Fig. 31 indicate that cooling sensible loads are observed during the summertime (May to September), and the peak monthly cooling sensible load occurs in July. The heating sensible loads appear for the rest of the year (October to April), and the peak monthly heating sensible load is noticed in December. After applying the energy recovery wheel into the HVAC system, both the cooling and heating sensible loads are reduced; however, the reduction of the heating sensible load is more notable than the reduction of the cooling sensible load. The annual cooling sensible load decreases 3.2% from the original conventional system, and the annual heating sensible load decreases 21.6% from the original. The annual heating sensible load is greater than the annual cooling sensible load, and the summer ambient conditions are relatively mild; thus, West Lafayette is a heating-dominated climate, and the sensible load reduction during summertime is less significant than the wintertime.

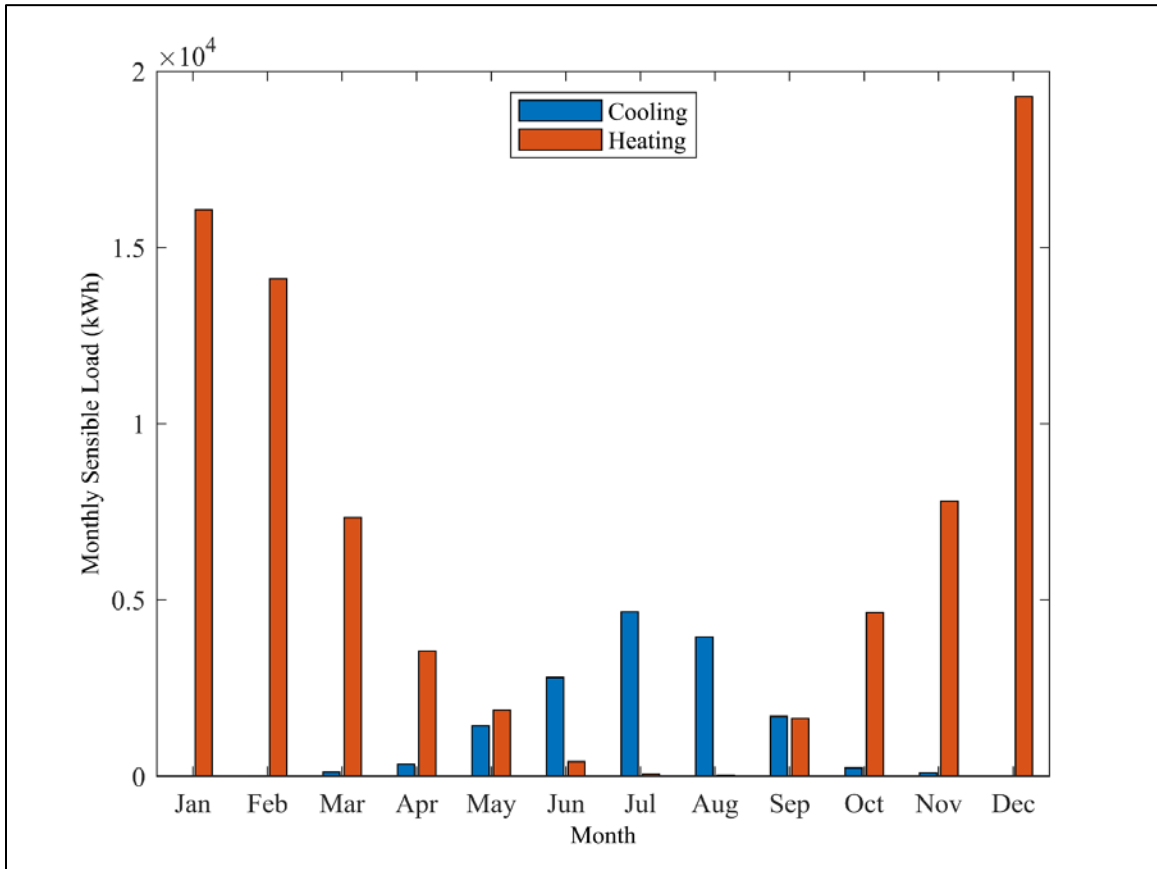


Fig. 30 Monthly cooling/heating sensible load of a conventional HVAC system

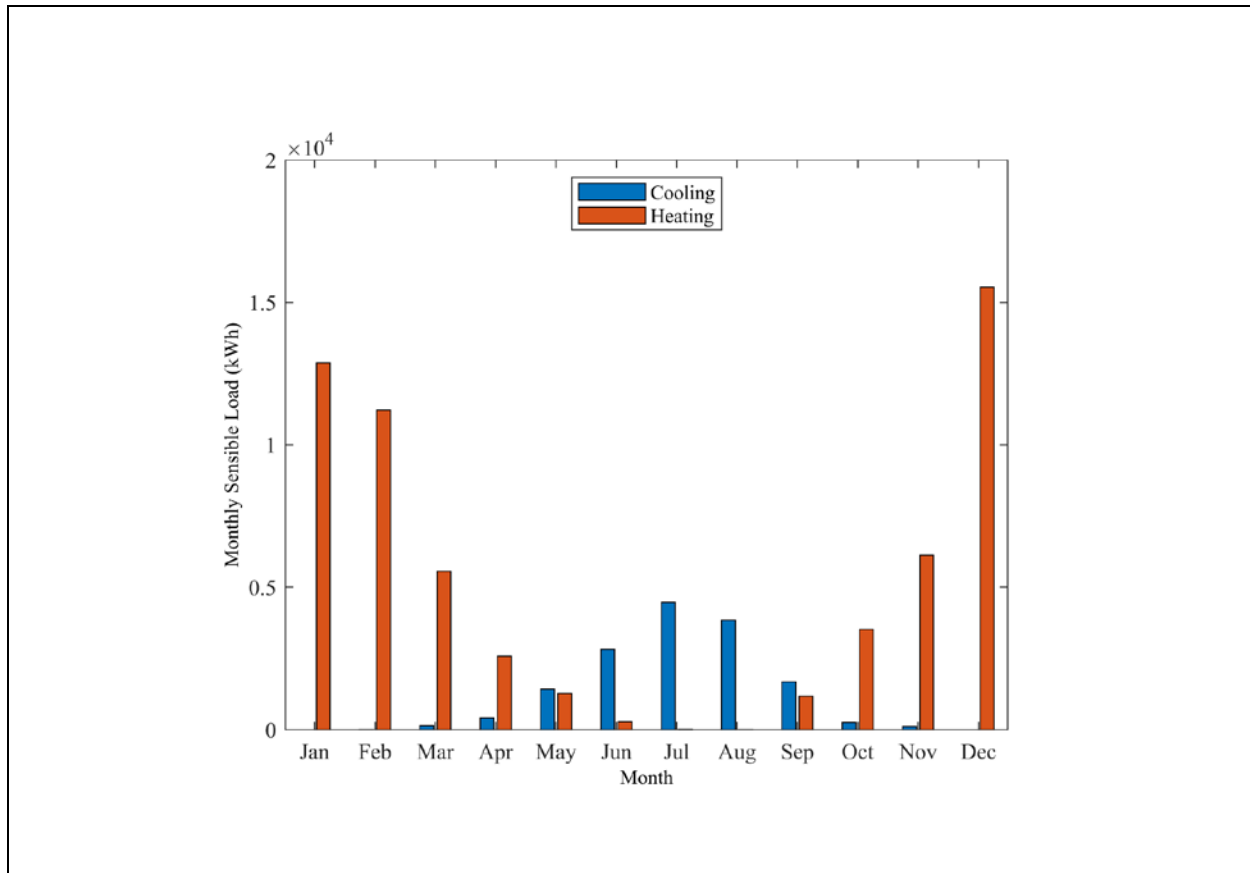


Fig. 31 Monthly cooling/heating sensible load of a wheel-integrated HVAC system

The air relative humidity of the conditioned zone is investigated to evaluate the impact of an energy recovery wheel on indoor environmental comfort. Fig. 32 shows the indoor air relative humidity of the conventional system case, and the wheel system case. The two cases share a similar pattern, higher relative humidity during summer and lower relative humidity during winter. Nonetheless, during the cooling season, the indoor relative humidity of the wheel system case is lower than the conventional system. The energy recovery wheel removes a portion of the moisture in the incoming outdoor air; hence, the relative humidity drops during the cooling season. Oppositely, during the heating season, the indoor relative humidity of the wheel system case is slightly higher than the conventional system. The energy recovery wheel harvests some moisture in the exhaust airstream, and dumps it in the supply air stream, so the relative humidity increases a little in the heating season. Therefore, the energy recovery wheel moderately improves indoor environmental humidity and comfort.

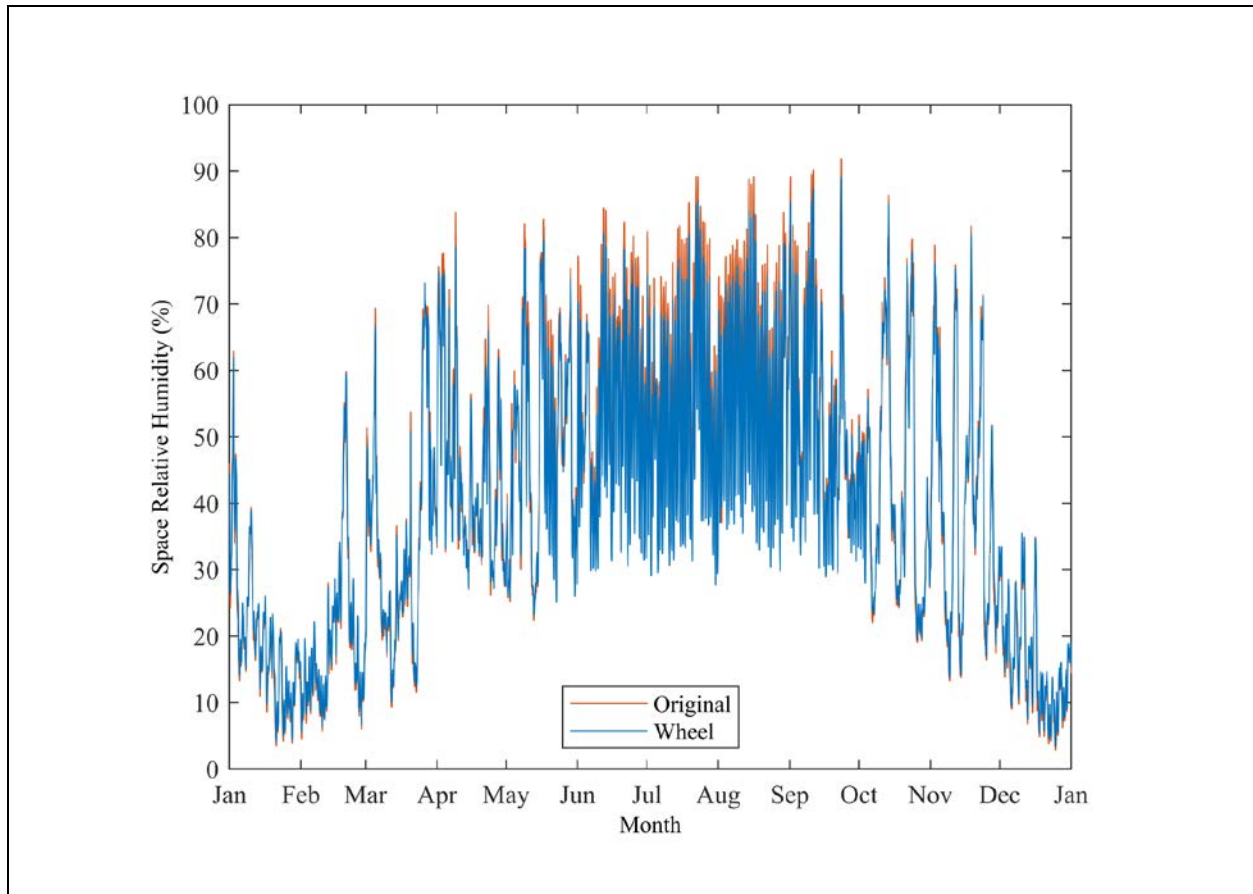


Fig. 32 Relative humidity of the conditioned zone

## 7.4 Energy Recovery Wheel Optimization Development

### 7.4.1 Energy Recovery Wheel Optimization Setups

As Chapter 7.1 mentioned, the Centers for Disease Control and Prevention (CDC) released guidelines for reopening office buildings [62] and building ventilation recommendations [63]; however, CDC does not specify absolute values of ventilation rate. According to ASHRAE 62.1 [3], the air changes per hour rate (ACH) of a small office building should be at least 0.5 ACH. In addition, the CDC specified 6 outdoor ACH for hospital buildings. Thus, different outdoor ACHs are investigated in this study to identify the impact of different ACHs on the energy consumption of the HVAC system; the outdoor ACHs of the study cases are set to be 0.5, 1, 2, ..., 6 ACH.



The operating ranges of target variables are listed in Table 3, the rotational speed ranges from 15 RPM to 60 RPM; the air face velocity ranges from 2 m/s to 6 m/s; the wheel depth ranges from 0.1 m to 0.5 m. In order to have the mapping method covering a wider applicable range of the energy recovery wheel, more wheel geometries, and more operating conditions are generated by finite difference method energy recovery wheel model based on Manufacturer A's wheel design and desiccant material. The outcomes are fed to the mapping method and used to train a new map to extend the operating range. As the result, the lower bound of wheel depth is expanded to 0.025 m, and the upper bound is extended to 1 m. The target variables (rotational speed, outdoor air face velocity, and wheel depth) are set to be continuous in the operating range of the energy recovery wheel mapping method.

Several optimization algorithms are provided by GenOpt, Hooke-Jeeves algorithm, and particle swarm optimization are selected to conduct the optimization in this study. However, an issue occurred while particle swarm optimization was utilized. TRNSYS and TRNBuild (building module in TRNSYS) ran into errors while parallel simulation executing. According to a clarification from the TESS specialist, it is the nature of TRNSYS and TRNBuild. TRNSYS and TRNBuild do not support parallel simulation well due to how they are programmed. Particle swarm optimization uses multiple particles (different combinations of variable values) simultaneously to compute, and this procedure requires parallel simulation. Thus, particle swarm optimization may not be suitable in this situation; on the other hand, the Hooke-Jeeves algorithm works smoothly with TRNSYS. Thus, it is selected for this case study instead of particle swarm optimization.

#### **7.4.2 Energy Recovery Wheel Initial Guess Value Study**

Before initiating the optimization, the impact of the initial guess for each variable was investigated. Three trials were conducted for each variable, and three initial guesses represent the lower range, middle range, and higher range of the variables. The initial guesses of each variable are listed in Table 8. Besides the study variable, other variables remain constant. For instance, while the wheel depth is studied, three optimizations are conducted at the different initial guesses of wheel depth (e.g., 0.3 m, 0.6 m, 0.9 m). Besides the wheel depth, other variables (rotational speed and outdoor air face velocity) are set as constant across three trials. Thus, the influence of the initial guess for the study variable can be identified. The optimization results of the nine trials

converged to the same value. This phenomenon indicates that the initial guess of the target variables has no impact on the final optimization result. The optimization would not be trapped at a local minimum with the Hooke-Jeeves algorithm.

Table 8 Initial guess of energy recovery wheel target variables

Trial	1	2	3
Rotational Speed (RPM)	37.5	25	18.75
OA Face Velocity (m/s)	3	4	5
Wheel Depth (m)	0.3	0.6	0.9

#### 7.4.3 Sensitivity Study of Energy Recovery Wheel Variables

The sensitivity study of each target variable was conducted to determine their influence on the optimization results. Each target variable was cut into several segments, and the segment sizes are listed in Table 8. Similar to the process of the study for initial guess, all other variables remain constant besides the study variable. For instance, while the wheel rotational speed is investigated, four rotational speeds (15, 30, 40, 60 RPM) were input and run an annual simulation individually for a small office building in West Lafayette with 1 ACH via TRNSYS, while other variables (outdoor air face velocity and wheel depth) stays unchanged. Hence, the influence of each target variable can be observed. For each variable, the annual energy consumption (summary of air-conditioning, heating, fan, wheel operating), and annual total cost (operating cost and averaged wheel cost) are plotted to observe the influence of each variable.

Fig. 33 exhibits the sensitivity study of each target variable against the average temperature difference across the wheel in the supply air stream over the whole study period; Fig. 34 presents the sensitivity study of each variable against the total cost (average initial wheel cost and annual operating cost). For Fig. 33 and Fig. 34, the target variable is traveling time (rotational speed) in (a); the target variable is outdoor air face velocity in (b); the target variable is wheel depth in (c). According to Fig. 33, and Fig. 34, rotational speed and outdoor air face velocity are less influential on the wheel performance than wheel depth. In addition, the influence of rotational speed and outdoor airstream face velocity on the wheel performance is linear; the influence of wheel depth is second-order exponential. The patterns of the influences are the same as each variable's

relationship functions in the mapping method. Thus, the mapping method delivers a corresponding influence on the wheel performance in the building energy performance simulation.

Fig. 33 (a) indicates that the temperature difference is higher while the traveling time is shorter (higher rotational speed); this is because more enthalpy recovery is achieved when the wheel rotates faster. Fig. 33 (b) exhibits that more temperature changes for slower outdoor air face velocity due to more time for heat and mass transfer occurring between air and the desiccant. An optimal wheel depth is noticed in Fig. 33 (c). This phenomenon is observed in the works of Uckan et al. [11], De Antonellis et al. [25][26], and Yamaguchi & Saito [30].

Fig. 34 possesses the opposite behavior pattern comparing with the results in Fig. 33, due to the fact that the operating cost is inversely proportional to the temperature change across the wheel; more temperature change of the incoming outdoor air and less heating/cooling energy would be required. Fig. 34 (a) illustrates that the operating cost is lower while the traveling time is shorter (e.g., higher rotational speed). Fig. 34 (b) shows a lower operating cost with slower outdoor air face velocity. An optimal wheel depth is seen also in Fig. 34 (c). Fig. 34 (a) and (b) show a higher initial wheel cost for a faster rotational speed and slower outdoor air face velocity. A faster rotational speed would lead to a larger purge section, then more outdoor air needs to be introduced to meet the fresh air demand and results in a larger size wheel. A slower outdoor air face velocity requires a larger wheel face area to achieve; thus, bigger wheel diameter is expected.

Different utility rates and wheel prices were analyzed comparing with the local utility rate and the original wheel price, and the study segments are listed in Table 8. Table 9 shows the optimal wheel geometries and operating conditions at different utility rates; Table 10 lists the optimal wheel designs while the wheel initial price varies. According to Table 9, while the utility rate grows, the optimal wheel depth increases in order to achieve more enthalpy exchange between the supply airstream and the exhaust airstream; hence, the increasing cost of the energy consumption can be compensated. On the other hand, Table 10 indicates that the optimal wheel depth is inverse proportional to the wheel initial price. In the utility rate and wheel initial price sensitivity study, rotational speed and outdoor airstream face velocity remain in a similar range between all cases since these two variables are less influential than the wheel depth.

Table 9 Input values of energy recovery wheel target variables for sensitivity study

Target Variable	Segments						
Rotational Speed (RPM)	15	30	40	60			
OA Face Velocity (m/s)	2	3	4	5	6		
Wheel Depth (m)	0.025	0.05	0.1	0.25	0.5	0.75	1
Utility Rate (\$)	50%	75%	100%	125%	150%		
Wheel Price (\$)	10%	50%	100%	150%	200%		

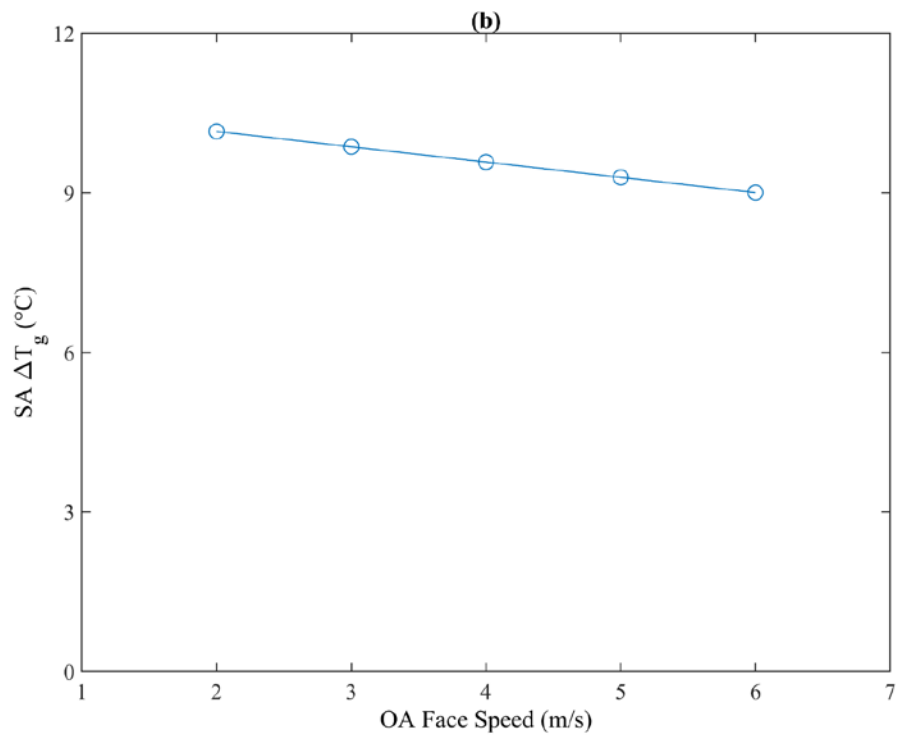
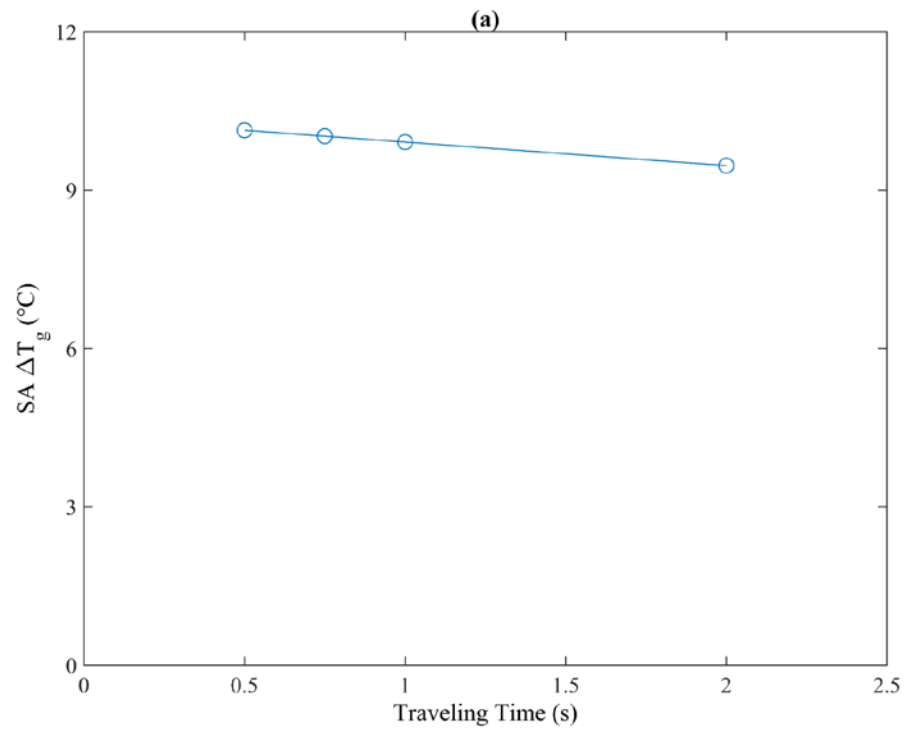


Fig. 33 Energy recovery wheel variables' sensitivity study on air temperature change

Fig. 33 continued

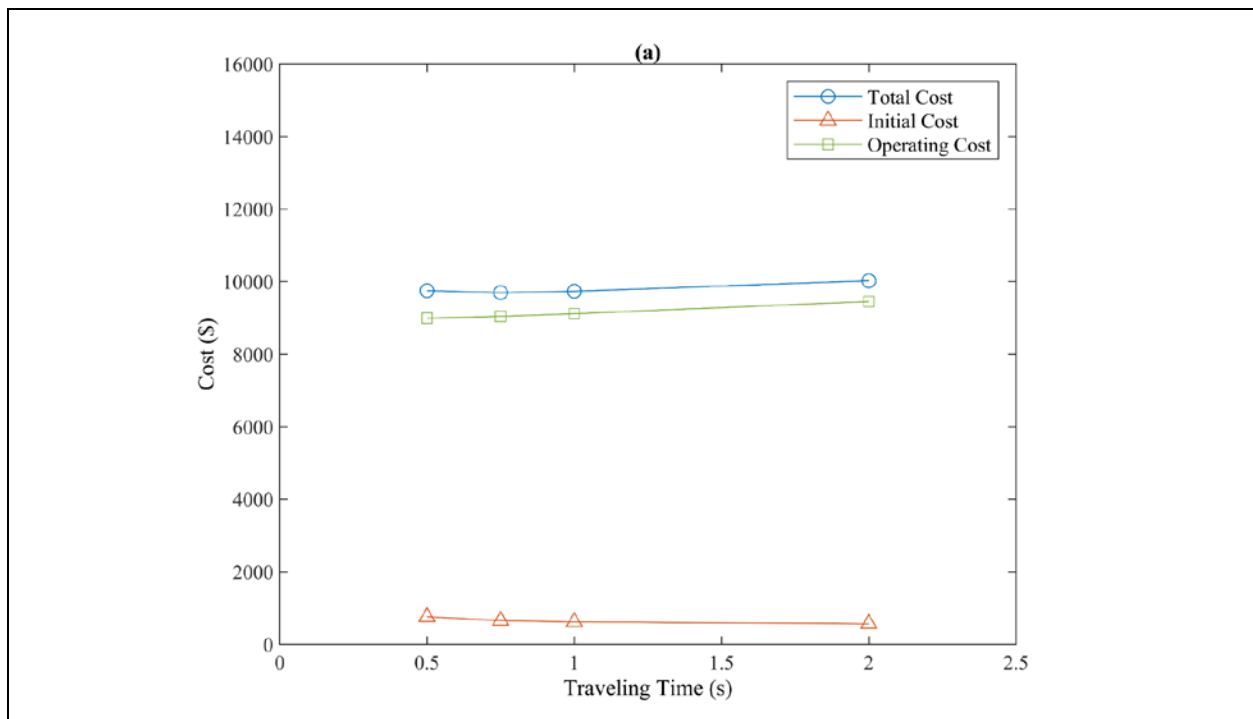
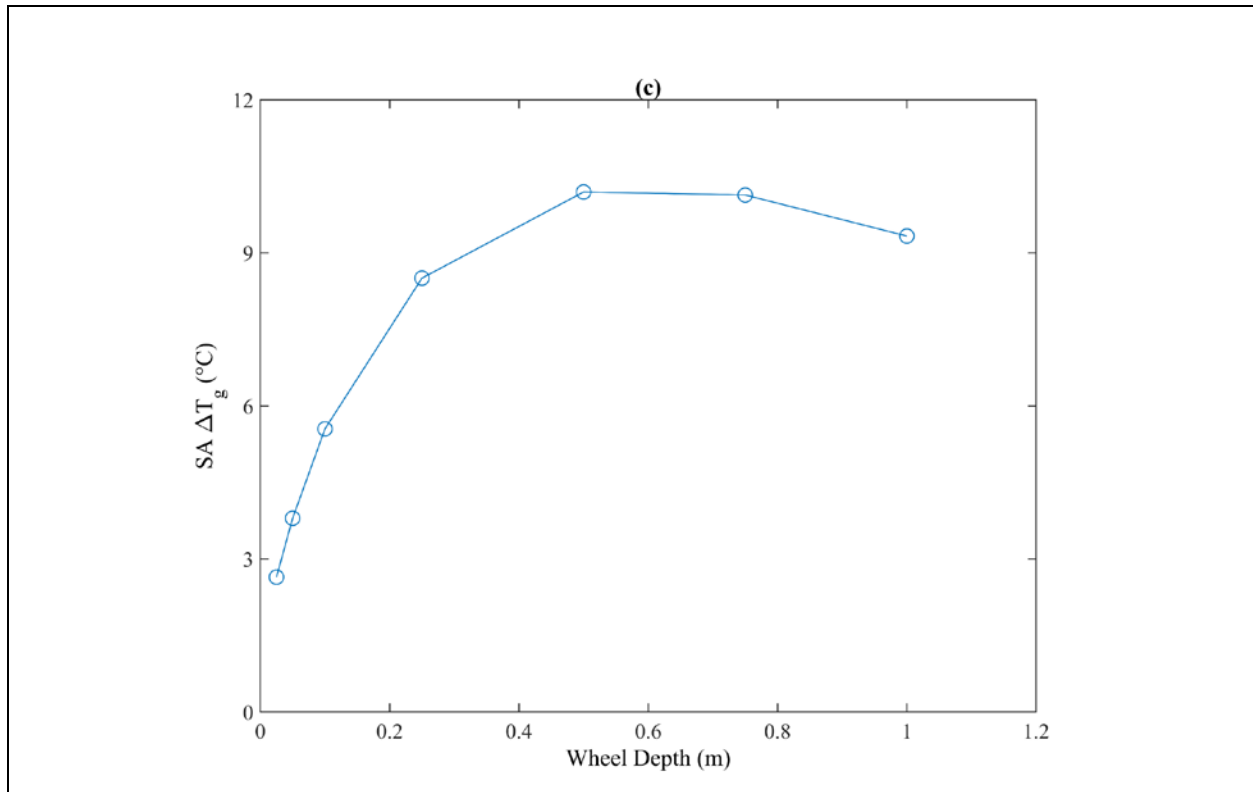


Fig. 34 Energy recovery wheel variables' sensitivity study on costs

Fig. 34 continued

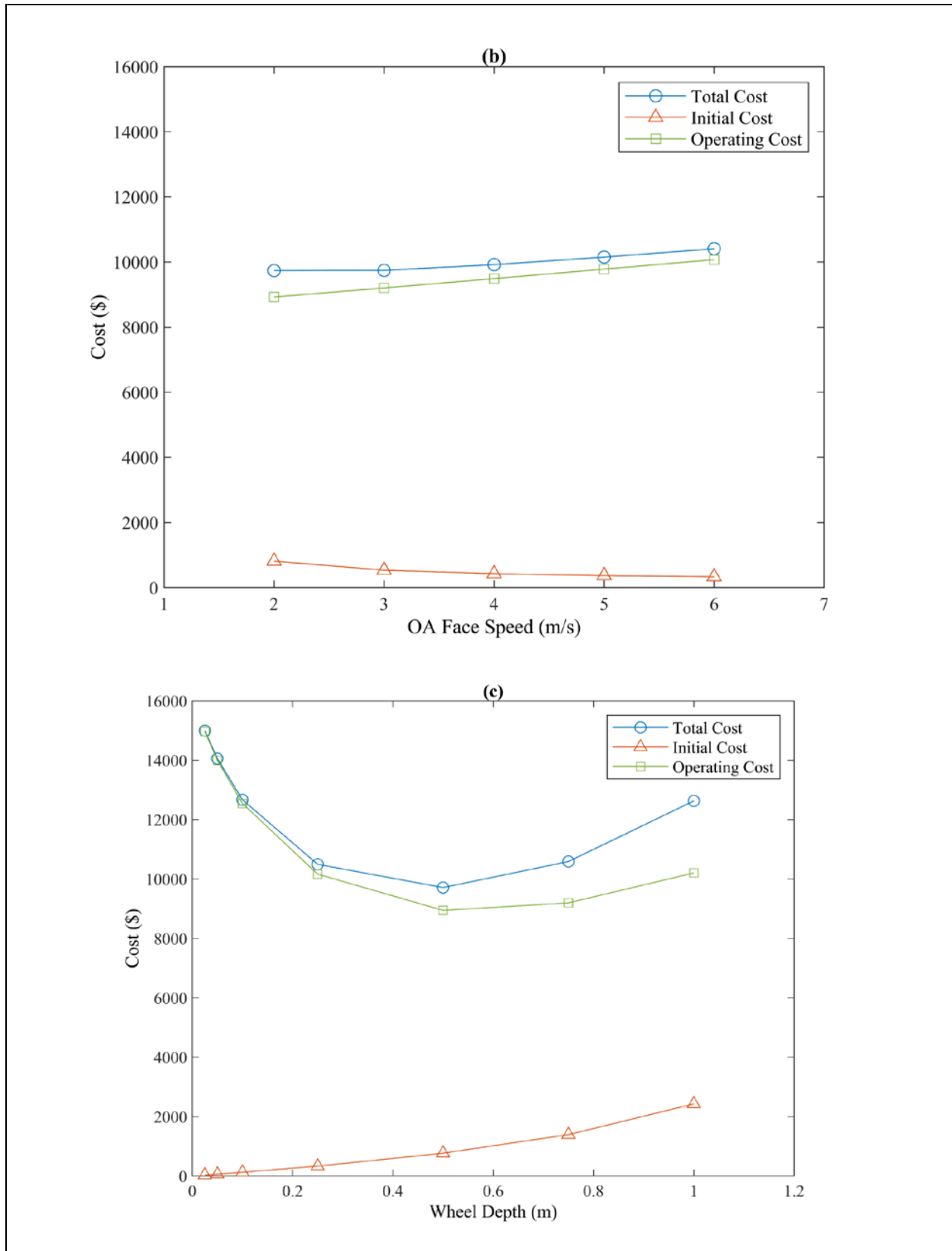


Table 10 Energy recovery wheel optimal design at different utility rate

Utility Price	50%	75%	100%	125%	150%
Depth (m)	0.399	0.440	0.450	0.464	0.474
RPM	46.2	42.9	42.5	41.4	40.0
OA Face Velocity (m/s)	2.95	2.60	2.38	2.24	2.05

Table 11 Energy recovery wheel optimal design at different wheel price

Wheel Price	10%	50%	100%	150%	200%
Wheel Depth (m)	0.540	0.491	0.450	0.425	0.399
Rotational Speed (RPM)	47.1	40.0	42.5	44.0	46.2
OA Face Velocity (m/s)	2.00	2.00	2.38	2.69	2.95

## 7.5 Energy Recovery Wheel Optimization Results

### 7.5.1 Variant Air Change Rates Optimization

A small office building located in West Lafayette, IN is selected to perform the optimization study. As the last section mentioned, outdoor ACHs of the cases are set to be 0.5, 1, 2, ..., 6 ACH; thus, the impact of ACH on the wheel selection can be identified. Table 11 exhibits the optimal wheel geometries and operating conditions with different outdoor ACHs. The optimal wheel depth increases while ACH grows. Since higher ACH leads to more energy required to cool or heat the incoming outdoor air, a wheel depth that is closer to the optimal depth provides more enthalpy exchange to reduce energy consumption for air conditioning and heating. Rotational speed and outdoor airstream face velocity remain in a similar range between all cases, because wheel depth is more dominant on wheel performance. Low rotational speed contributes less enthalpy exchange between two airstreams; however, higher rotational speed results in more purge section required to eliminate carry-over, so more outdoor air is sent to the exhaust stream and wasted. Thus, the optimal rotational speed is observed around the middle of the rotational speed range (15 RPM to 60 RPM). Fast outdoor face velocity shortens the time of the air in a wheel flute, so the heat and mass transfer between the air and desiccant are compromised. As the result, the optimal outdoor air face velocity appears in the lower end of the range (between 2 m/s to 6 m/s).



Oppositely, a lower face velocity means a larger wheel diameter is required; hence, the optimal face velocity depends on the wheel initial price; thus, a different optimal speed can be observed with different initial wheel prices. Finally, the last row of Table 11 lists the operating cost savings between the conventional vapor-compression system and the wheel-integrated system. More cost reduction is expected with higher ACH, since high ACH means more incoming outdoor air to condition. Hence, applying an energy recovery wheel is more beneficial under high ACH conditions.

Table 12 Optimal energy recovery wheel design at different ACHs

ACH	0.5	1	2	3	4	5	6
Wheel Depth (m)	0.417	0.450	0.470	0.480	0.480	0.480	0.483
Rotational Speed (RPM)	44.4	42.5	41.4	40.7	40.7	40.7	42.9
OA Face Velocity (m/s)	2.28	2.38	2.46	2.44	2.46	2.49	2.50
Operating Cost Reduction (%)	17.4	28.8	41.6	48.5	52.8	55.7	57.8

### 7.5.2 Variant Climates Optimization

The next optimization study is to investigate the trend of optimal energy recovery wheel designs in different climates. Four locations are chosen to conduct the study, and each of them represents a typical climate zone in the U.S. The four locations are Miami, FL for hot and humid climate; Phoenix, AZ for hot and dry climate; San Francisco, CA for mild climate; and Minneapolis, MN for cold climate. As Table 11 indicates, the 7 optimal wheel configurations for different values of ACH do not show significant variation from 2 to 6 ACH; hence, the optimization study for these different locations will be performed only at 0.5, 2, 6 ACH to simplify the simulation, and still represent the influence of different ACHs. The utility rate of each location is based on the averaged state electricity rate collect from the U.S. EIA website [67].

Table 12 exhibits that optimal wheel geometries and operating conditions for four locations under three ACHs. The optimal wheel depth increases when the ACH increases in all locations. The optimal rotational speed remains in the middle range other than for the lowest ACH in Miami, FL. This may be caused by the energy and utility cost savings, which are not sufficient to compensate for the price of a deeper wheel, and a cheaper approach is by increasing the rotational

speed to harvest more energy; thus, the rotational speed is high in the 0.5 ACH Miami, FL case. The optimal outdoor air face velocity stays in the low range among all cases. Thinner optimal wheel depth is noticed in hot climates. In hot climates, the ambient temperature is closer to the room setpoint temperature during the winter, and less heating is required; thus, the benefit of using an energy recovery wheel becomes less. This phenomenon results in thinner wheels in hot climates.

Fig. 35 shows the indoor relative humidity of the vapor-compression conventional HVAC system and wheel-integrated HVAC system for a small office building with 2 ACH in Miami, FL. As the figure indicates, lower indoor relative humidity is observed in the wheel-integrated case compared to the conventional system. Even though the energy recovery wheel may not be advantageous from an energy-savings aspect, the indoor relative humidity decreases, and the indoor comfort can be improved by applying an energy recovery wheel. In a mild climate, less demand for heating and cooling is observed. However, a requirement for energy recovery wheels is still noticed due to the high utility rate like San Francisco. In a cold climate, the requirement of an energy recovery wheel is considerable. The energy recovery wheel pre-cools incoming outdoor air during summer; furthermore, it can collect waste heat in the exhaust airstream during winter. The heating energy requirement is reduced, then significant energy saving is achieved especially for the HVAC system utilizing an electric heating coil.

Table 13 Optimal energy recovery wheel design at different locations

	Miami			Phoenix		
ACH	0.5	2	6	0.5	2	6
Depth (m)	0.065	0.157	0.197	0.284	0.357	0.394
Rotational Speed (RPM)	60	45.7	40	44.4	37.8	36.9
OA Face Velocity (m/s)	2.9	3.03	3.18	2.5	2.76	2.81
	San Francisco			Minneapolis		
ACH	0.5	2	6	0.5	2	6
Depth (m)	0.404	0.455	0.463	0.445	0.495	0.498
Rotational Speed (RPM)	40	43.6	37.5	42.9	33.3	40
OA Face Velocity (m/s)	2.13	2.3	2.25	2.1	2.3	2.35

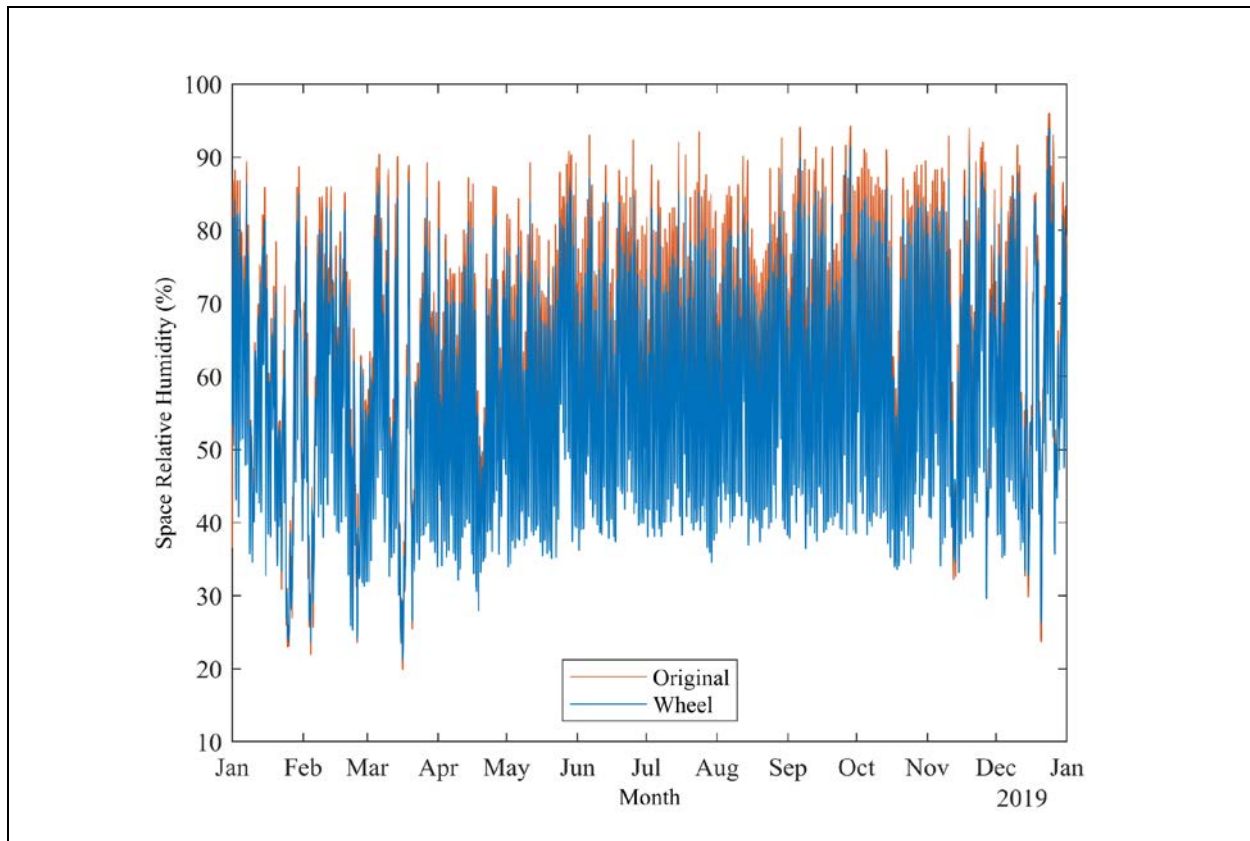


Fig. 35 Relative humidity of conventional vs. wheel system

## **7.6 Conclusion of Energy Recovery Wheel Case Study**

The semi-empirical energy recovery wheel performance mapping method is utilized in building performance simulations and optimizations. The mapping method is easy to implement; communicates with building performance simulation software well; provides reasonable predictions. The trends of optimal energy recovery wheel geometries and operating conditions are identified based on the transient building performance simulation results. The energy recovery wheel is beneficial while the ACH requirement is high; also, the wheel is more favorable in cold climate zones and mild climate zones than in hot climate zones. Furthermore, the energy recovery wheel integrated system provides better indoor comfort than the traditional conventional system. Hence, the semi-empirical energy recovery wheel mapping method is an ideal tool for conducting performance evaluations and optimizations of wheel-integrated HVAC systems.

## **8. DESICCANT WHEEL CASE STUDY**

### **8.1 Supermarket Introduction**

In Chapter 7, a case study implemented with the semi-empirical energy recovery wheel mapping method is investigated, and the simulation outcomes indicate that the mapping method is an ideal tool for energy recovery wheel simulations and optimizations. In this chapter, the semi-empirical desiccant wheel mapping method is evaluated for its utilization in performance evaluations and optimizations. The selected application is the dry storage area in a supermarket building. According to the United States Department of Agriculture (USDA) Commodities [68], the dry-bulb temperature should be maintained between 50°F to 70°F based on the requirement of goods; the relative humidity should be controlled to no higher than 50%. The typical dehumidification process of a traditional vapor-compression system is overcooling the supply air until reaching the humidity setpoint, and then reheating the air to the temperature setpoint. This process is energy-intensive, and a tremendous amount of energy is wasted during overcooling and reheating. Thus, a desiccant wheel is implemented in this application to provide moisture removal capacity, and investigate potential energy reduction by avoiding the overcooling and reheating processes.

### **8.2 Supermarket Building Model Development**

The building model was established based on the supermarket reference building developed and released by the U.S. DOE [64]. The model is divided into six zones: sales, bakery, deli, office, product, and dry storage. The study target is dry storage since it requires humidity control to maintain the quality of goods. The supermarket is a one-story building; the total area is 4182 m<sup>2</sup> (79.2 m length x 52.8 m width); the area of the dry storage is 622 m<sup>2</sup>; the height is 6.10 m. The exterior walls are set as the mass wall type, which has continuous insulation. The U-value of the exterior walls is 0.748 W/m<sup>2</sup>K; the U-value of the exterior roof is 0.382 W/m<sup>2</sup>K. These settings follow the U.S. DOE commercial reference building models code [64]. Same with the small office building, the validation of the model is not required due to the universality of the reference building and the simulation software. Fig. 36 (a) demonstrates the layout of a typical conventional vapor-compression HVAC system that provides cooling and dehumidification to the

dry storage space of a supermarket with fresh outdoor air, and (b) shows the layout of a desiccant wheel integrated version. The outlet air temperature prediction is provided by the temperature function of the energy recovery wheel mapping method (54). In order to reduce the complexity of the simulation, the design of the heat wheel is set constant, with 0.6 m depth, 60 RPM, and 2 m/s air face velocity, which is close to the general optimal heat wheel design across different climate zones. A detailed description of the heat wheel optimization will be presented in Section 8.4. The weather data implemented in the study is typical meteorological year 3 (TMY3) data. Since dehumidification is often required only in the summertime, the study period is from May 1<sup>st</sup>, 0:00 AM to September 30<sup>th</sup>, midnight. For the dry storage, the air temperature setpoint is 20°C, and the humidity ratio is maintained at 0.00225 kg<sub>w</sub>/kg<sub>a</sub>. The rest of the conditioned zones in the supermarket are set to be at 24°C and 50% relative humidity. The following simulation inputs follow the configurations implemented in the energy recovery wheel study: the power consumption of the air conditioner is simulated by a TRNSYS type 921 module and calculated proportionally by (70); the heating elements are 100% efficiency electric heating coil; the power consumption of the wheel motor is assumed to be 0.1864 kW (0.25 HP); the price approximation function (75) is generated by interpolation and extrapolation from the work of Lewis [66].

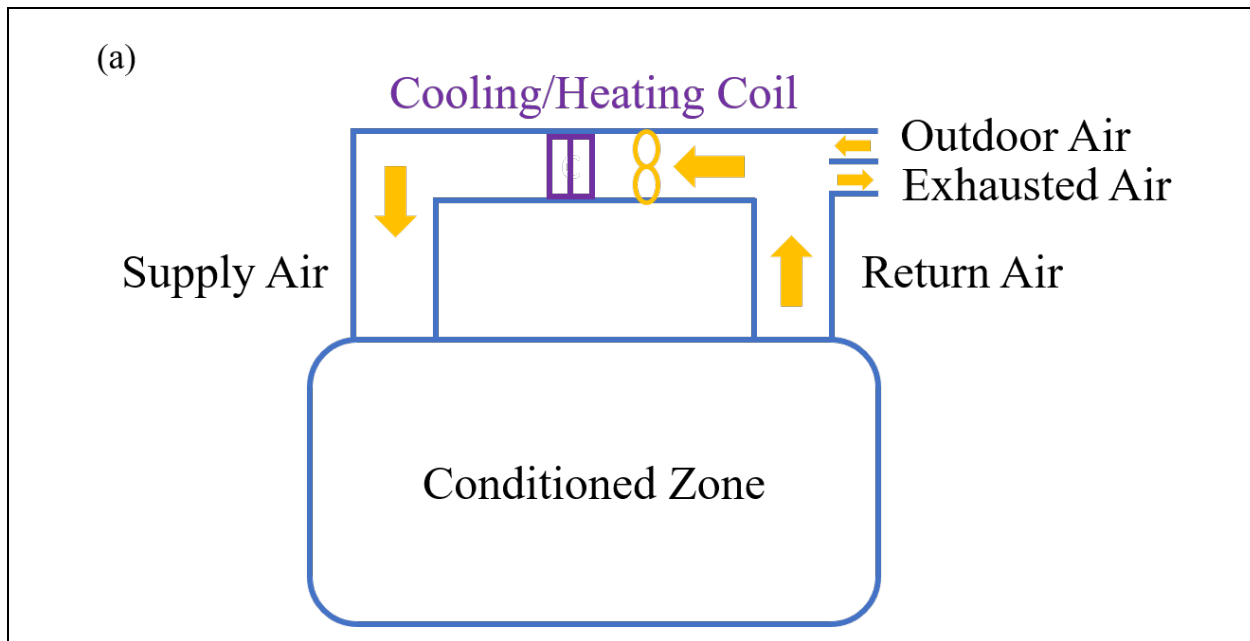
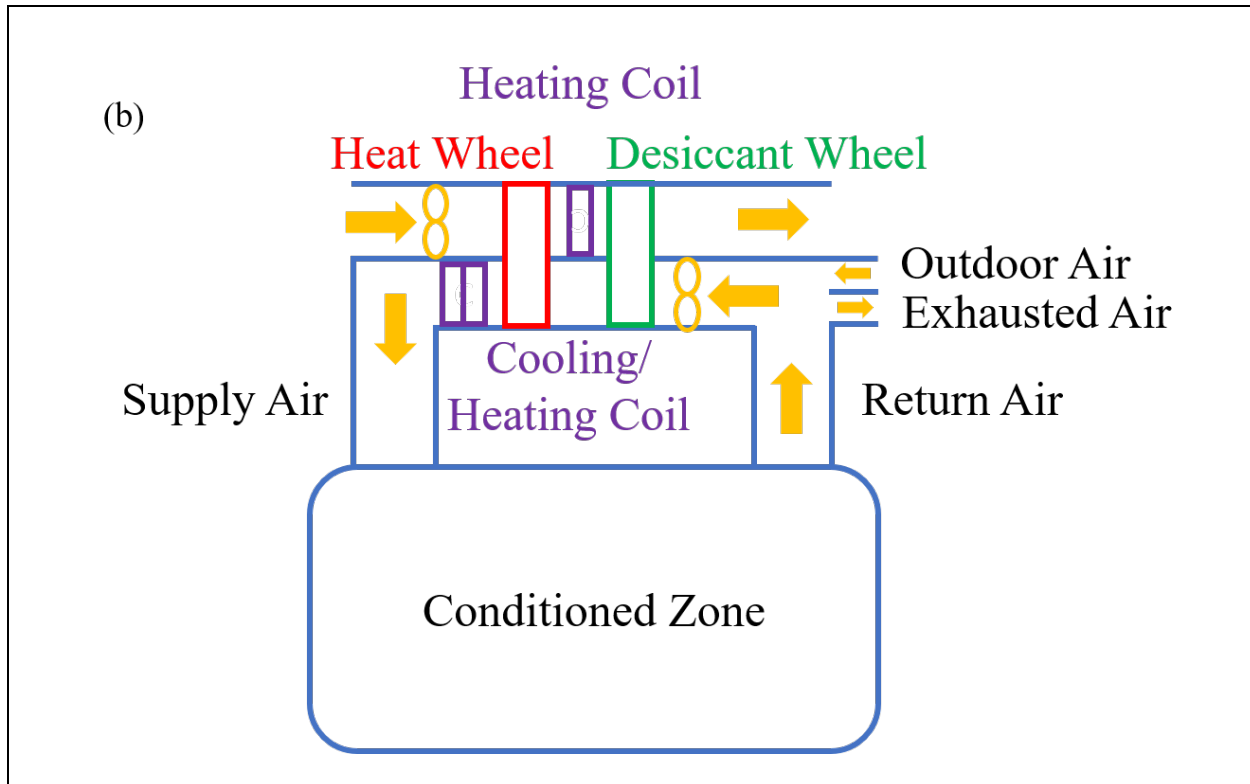


Fig. 36 Schematic of (a) vapor compression system (b) desiccant wheel integrated HVAC system

Fig 36 continued



### 8.3 Supermarket Building Performance Simulation Results

The supermarket building model was established in TRNSYS, and an annual transient building energy performance simulation was conducted to investigate the influence of the desiccant wheel on the supermarket dry storage energy performance located in Miami, FL. A desiccant wheel and heat wheel are integrated into the HVAC system of the supermarket dry storage according to the design shown in Fig. 36 (b). A 0.3 m depth and 1.96 m diameter desiccant wheel that operates at 0.15 RPM (9 RPH), 140°C regeneration temperature, and 3 m/s face velocity in the supply and regeneration airstream are recommended by Manufacturer B. The geometries and operating conditions of the selected wheel are set in the desiccant wheel mapping method, and the TRNSYS model is utilized to conduct the performance simulation by using the mapping method. Fig. 37 shows the hourly energy consumption of the different components (A/C, electric reheating coil, and fan) in a conventional vapor compression HVAC system during the summer. The line plot of the hourly energy consumption of the wheel integrated HVAC system is drawn as Fig. 38.

Fig. 37 and Fig. 38 indicate that the total energy consumption of the desiccant wheel-integrated system is lower by about 66.1% over the traditional conventional HVAC system in the supermarket dry storage application; the A/C power consumption decreases by around 73.8%. Fig. 39 exhibits the entering air humidity ratio of the two systems and supply air condition. As the figure shows, the dehumidification requirement is achieved by the desiccant wheel; thus, the overcooling process is not necessary for the wheel system to remove the moisture in the air, so the A/C power consumption drops. The wheel system employs a significant amount of energy on preheating the inlet regeneration air to reach low relative humidity; however, the vapor-compression system also consumes a tremendous amount of energy on reheating the overcooled supply air. The wheel system consists of not only a desiccant wheel but also a heat wheel. The heat wheel scavenges heat from the air leaving the desiccant wheel before it enters the evaporator and dumps the heat to the regeneration airstream; hence, the air temperature decreases prior to entering the evaporator, so less A/C power consumption is required; also, the preheating energy is reduced, since the incoming ambient air is heated by the heat wheel before entering the preheating coil. As a result, the preheating energy of the wheel system is about 65.3% less than the reheating energy of the vapor-compression system. Hence, the desiccant wheel integrated HVAC system consumes less energy than the conventional vapor-compression system in this case.



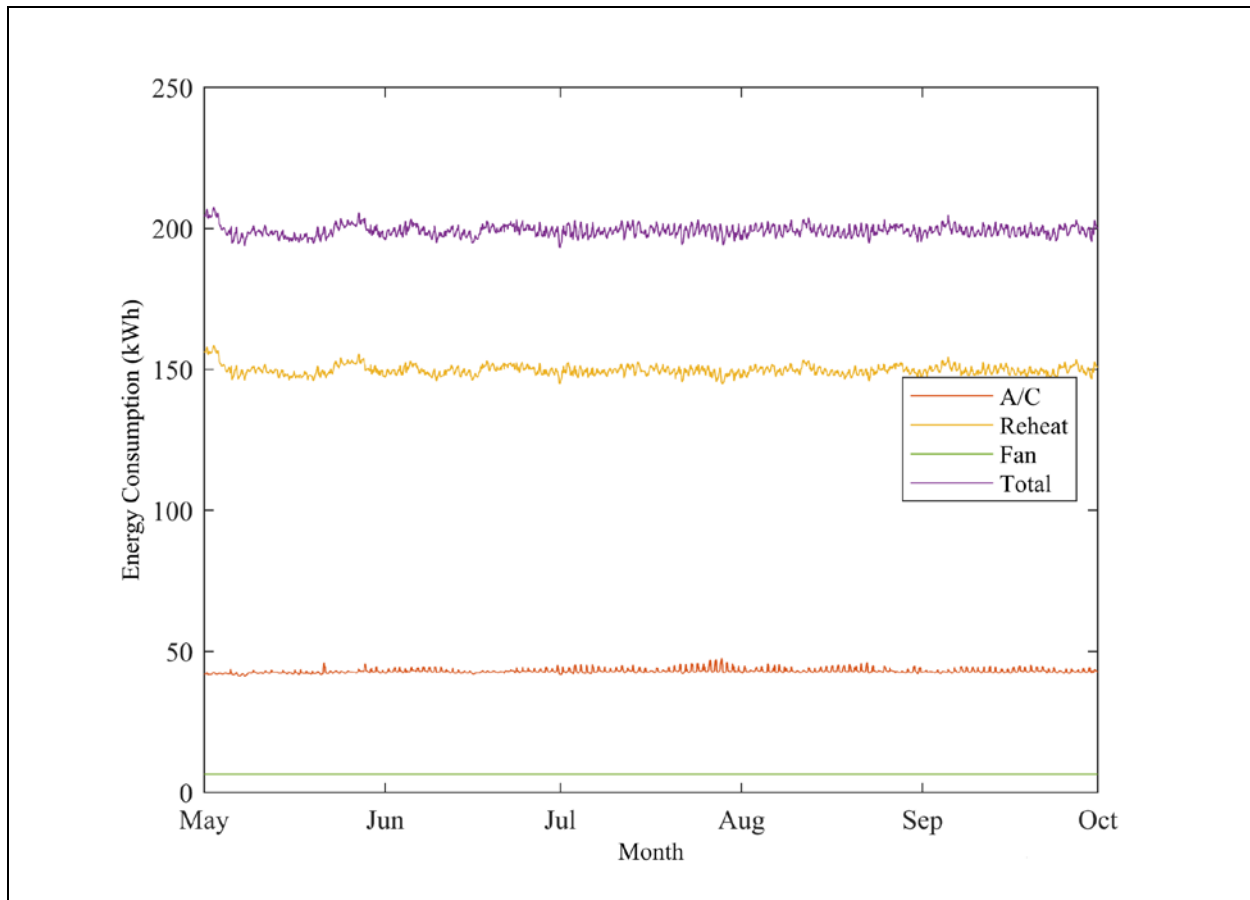


Fig. 37 Energy consumptions of conventional vapor-compression HVAC system components

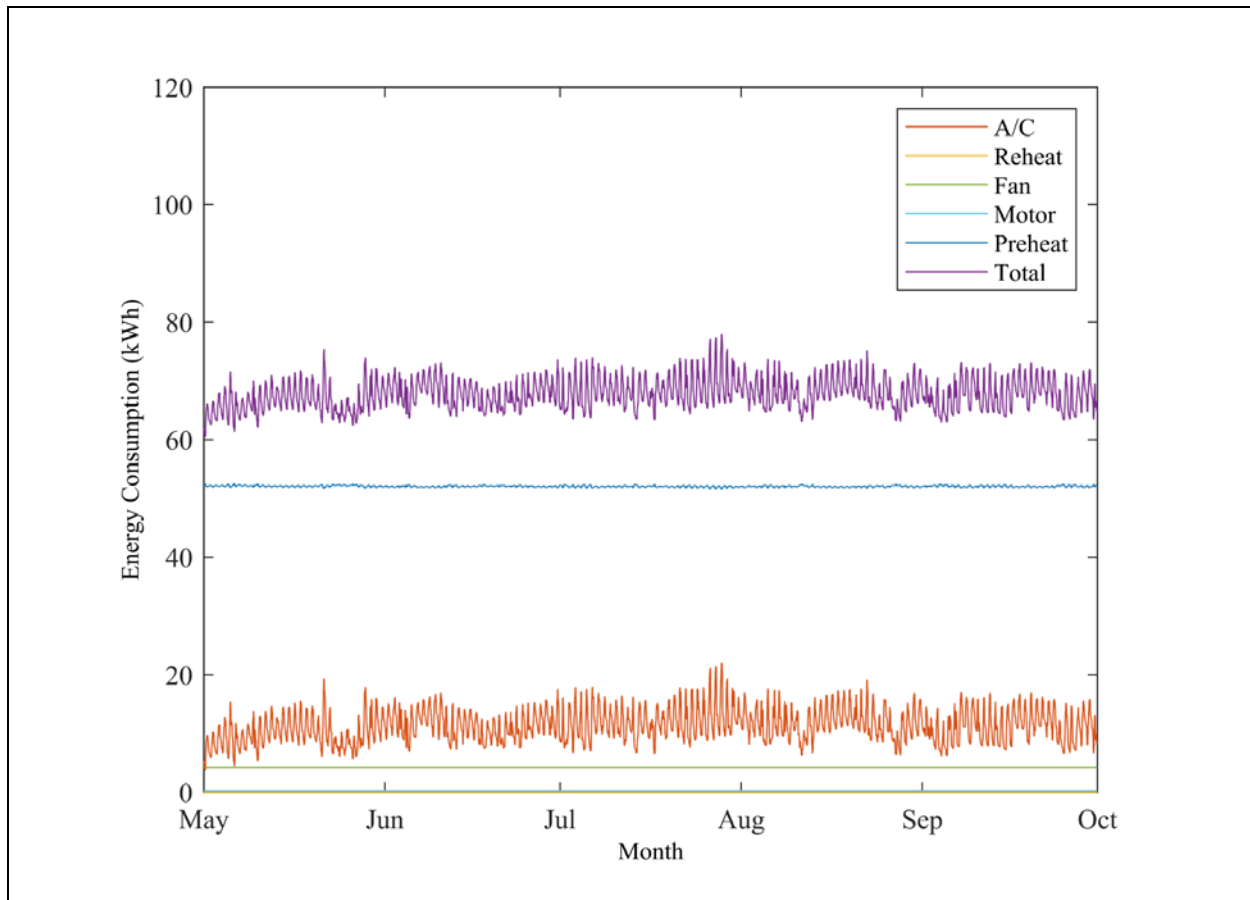


Fig. 38 Energy consumptions of desiccant wheel integrated HVAC system components

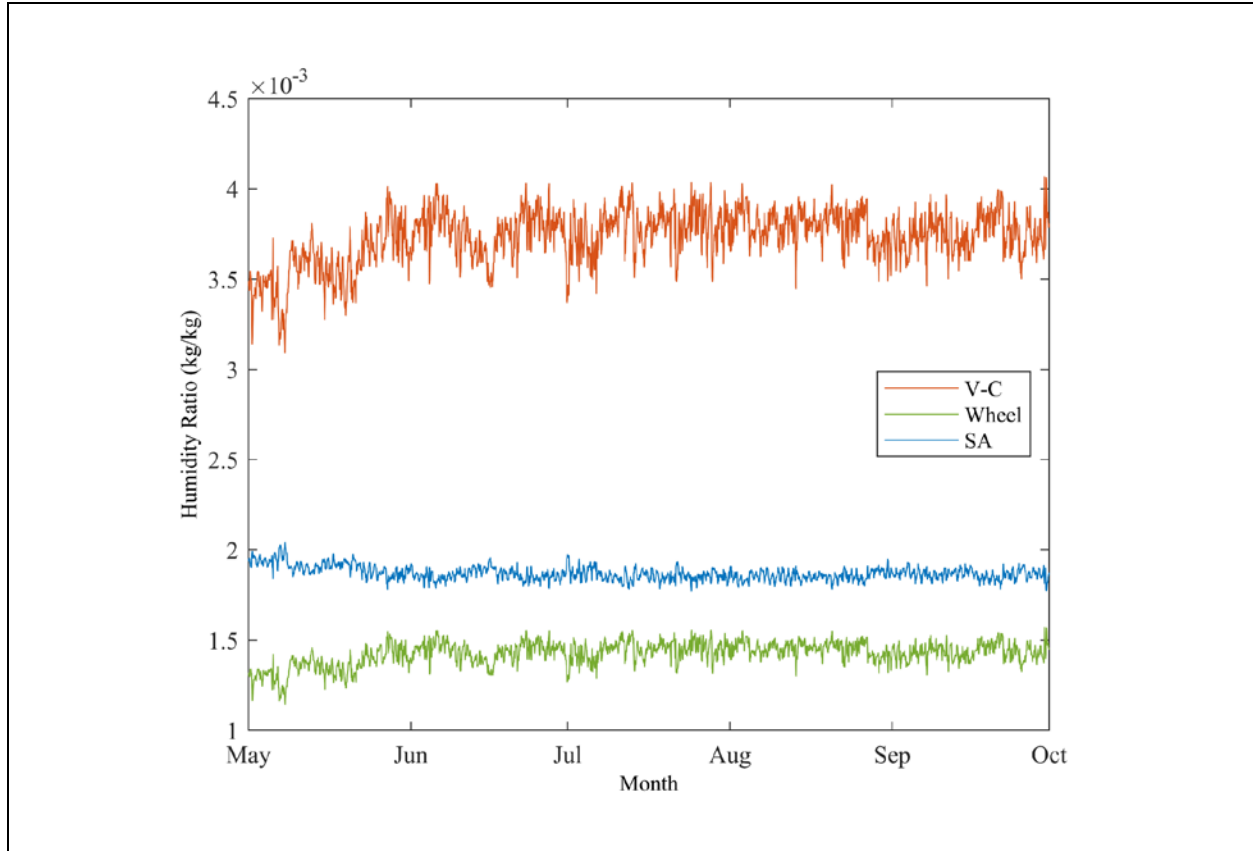


Fig. 39 Humidity ratios of evaporator entering air for two systems and supply air condition

## 8.4 Desiccant Wheel Optimization Development

### 8.4.1 Desiccant Wheel Optimization Setups

In order to have the mapping method covering a wider application, the operating ranges of target variables are extended via the desiccant wheel FDM model based on Manufacturer B's wheel design and desiccant material; the rotational speed ranges from 4 RPH to 40 RPH; the air face velocities of supply airstream and regeneration airstream range from 1.8 m/s to 5 m/s; the wheel depth ranges from 0.1 m to 1 m. The target variables are continuous in the operating range of the desiccant wheel mapping method. Same with the energy recovery wheel optimization, the Hooke-Jeeves algorithm is selected to conduct this study for TRNSYS operating stability.

#### 8.4.2 Desiccant Wheel Initial Guess Value Study

The influence of the initial guess for each target variable was identified. Three trials were conducted for each target variable that covers the lower range, middle range, and higher range, and the initial guesses are given in Table 13. The approach of the initial guess study stated in Section 7.4 is utilized to conduct this investigation. The optimization outcomes of the twelve trials converged to a similar result in a small range. This phenomenon illustrates that the initial guess of the target variables has limited influence on the final result. Hooke-Jeeves algorithm is suitable in this case study.

Table 14 Initial guess of desiccant wheel target variables

Trial	1	2	3
Rotational Speed (RPH)	6.75	9	13.5
SA Face Velocity (m/s)	2	3	4
RA Face Velocity (m/s)	2	3	4
Wheel Depth (m)	0.1	0.4	0.8

#### 8.4.3 Sensitivity Study of Desiccant Wheel Variables

The sensitivity study of impact from desiccant wheel target variables on the optimization results was investigated. The segments of each variable are stated in Table 14. The same sensitivity study process for the energy recovery wheel is utilized, and the influence of each target variable is identified and visualized. Fig. 40 and Fig. 41 presents the sensitivity study of each variable on the leaving air humidity ratio and total cost (operating cost and average initial cost) of the system respectively, in (a) the target variable is a flute traveling time in the air stream (i.e. rotational speed); in (b) the target variable is the supply air face velocity; in (c) the target variable is regeneration air face velocity; in (d) the target variable is wheel depth. For Fig. 40 and Fig. 41, rotational speed, supply airstream face velocity, and regeneration airstream face velocity are less dominant on the wheel dehumidification capacity than wheel depth. Furthermore, the influence of rotational speed, supply airstream face velocity, and regeneration airstream face velocity on the wheel performance is linear; the influence of wheel depth is second-order exponential. The influence patterns of each

variable correspond to their relationship functions in the mapping method, and the pattern is delivered to the building energy simulation program correctly.

Fig. 40 (a) demonstrates that better dehumidification is seen while the traveling time is shorter (higher rotational speed); since more moisture is removed from the supply airstream and dumped into the regeneration airstream, when the wheel rotates faster. Fig. 40 (b) indicates that more moisture is collected from the supply airstream with slower supply air face velocity, since there is more time for mass transfer to occur between air and the desiccant. On the other hand, Fig. 40 (c) shows a higher dehumidification capacity with higher regeneration air face velocity, because more moisture can be carried away to the exhaust air. Last, an optimal wheel depth is observed in Fig. 40 (d). In the works of Uckan et al. [11], De Antonellis et al. [25][26], and Yamaguchi & Saito [30], an optimal wheel depth possesses the best moisture removal capacity, and the relationships between wheel depth and moisture removal capacity are similar with a polynomial relationship in the works of literature.

Fig. 41 (a) possesses a similar behavior pattern comparing with Fig. 40 (a) in the range of traveling time from around 400 s to 500 s (around 5.4 RPH to 6.75 RPH), due to leaving air humidity corresponds to the demand of overcooling-reheating dehumidification process. However, once the wheel rotates faster than around 6.75 RPH, the desiccant wheel provides sufficient dehumidification capacity, no overcooling-reheating dehumidification process, which is where the dominant energy consumption occurs; thus, the operating cost becomes stable. Yet, the desiccant wheel cannot offer sufficient dehumidification capacity when the rotational speed is slower than 5.4 RPH. The overcooling-reheating processes remove all the moisture; hence, a flat operating cost is observed. The phenomenon is noticed in the supply air face velocity sensitivity study also. Fig. 41 (b) indicates that the wheel can provide sufficient dehumidification capacity if operating lower than 3 m/s; nonetheless, dehumidification capacity is fully offered by the overcooling-reheating process if the air face velocity runs faster than 4 m/s. Fig. 41 (c) illustrates that regeneration air cannot carry away the moisture on the desiccant material efficiently while the face velocity is too low. Fig. 41 (d) expresses that a similar pattern of optimal wheel depth is noticed as Fig. 40 (d) showing.

Table 15 Input values of desiccant wheel target variables for sensitivity study

Target Variable	Segments						
Rotational Speed (RPH)	4	4.5	5.4	6.75	9	13.5	40
SA Face Velocity (m/s)	1.8	2	3	4	5		
RA Face Velocity (m/s)	1.8	2	3	4	5		
Wheel Depth (m)	0.1	0.25	0.5	0.75	1		

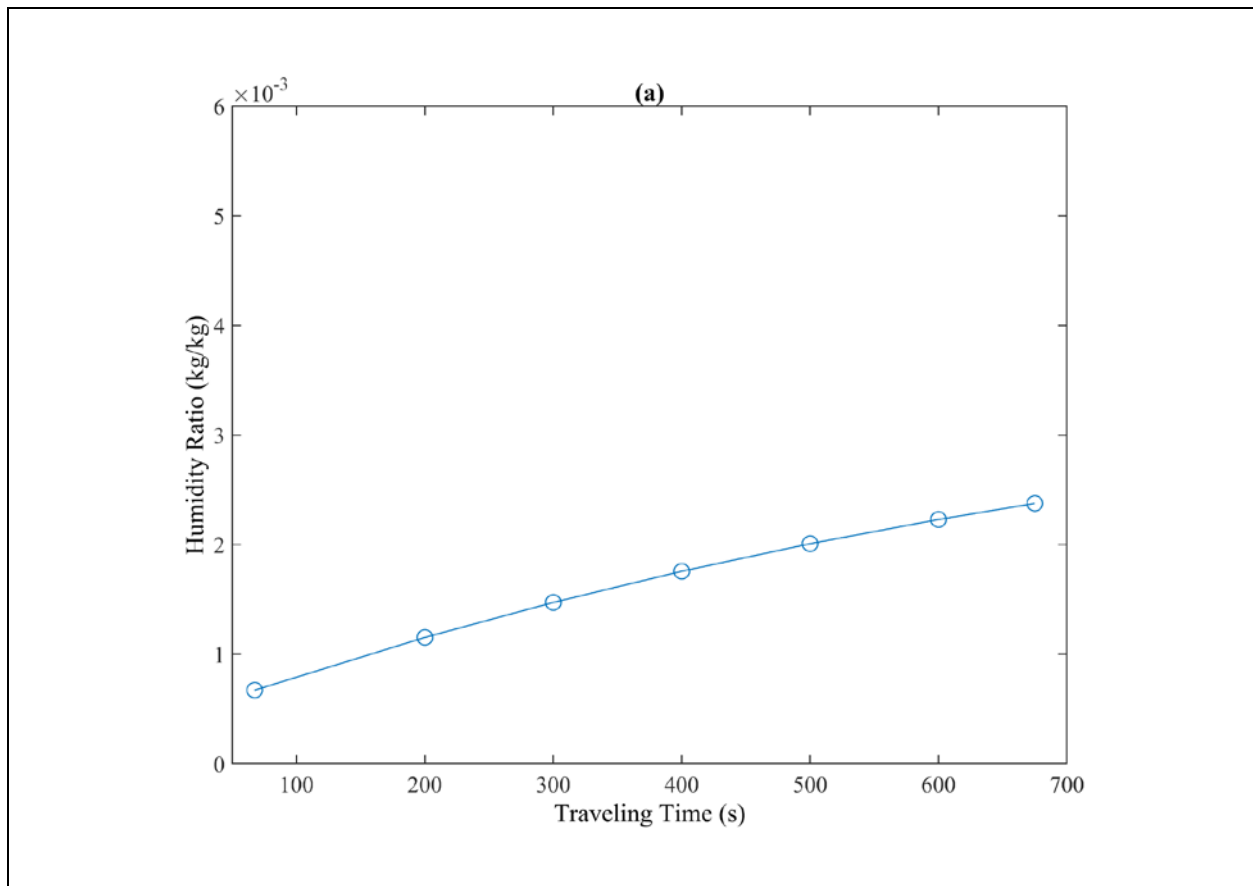


Fig. 40 Desiccant wheel variables' sensitivity study on leaving air humidity ratio

Fig. 40 continued

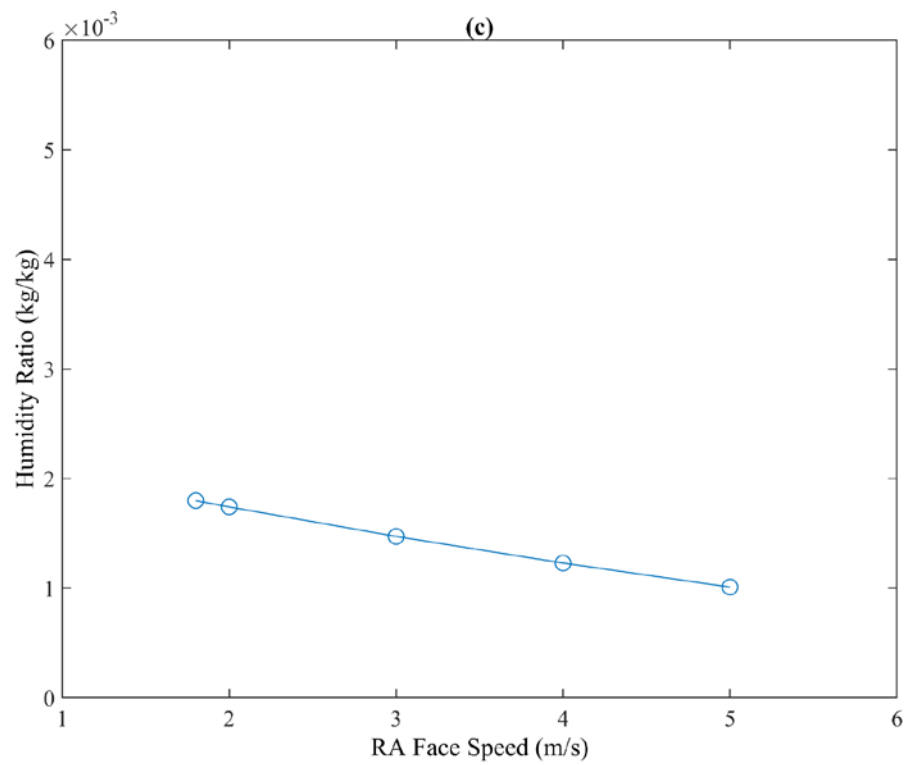
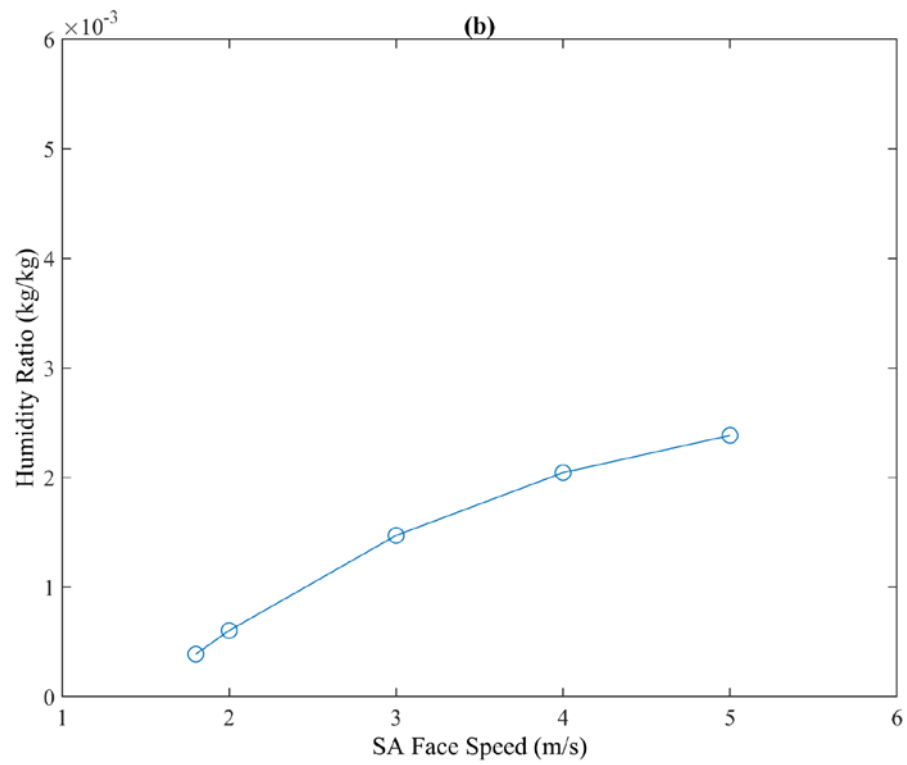
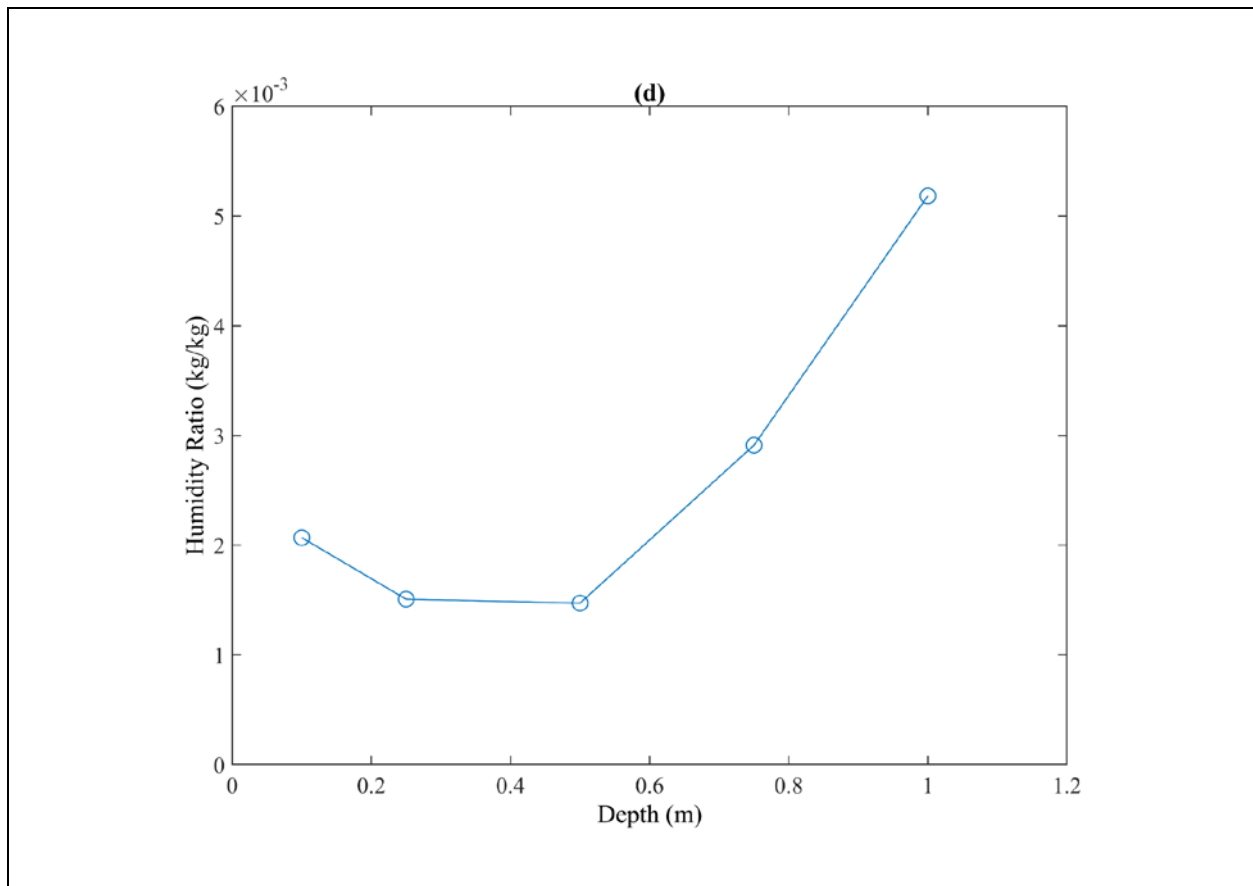


Fig. 40 continued





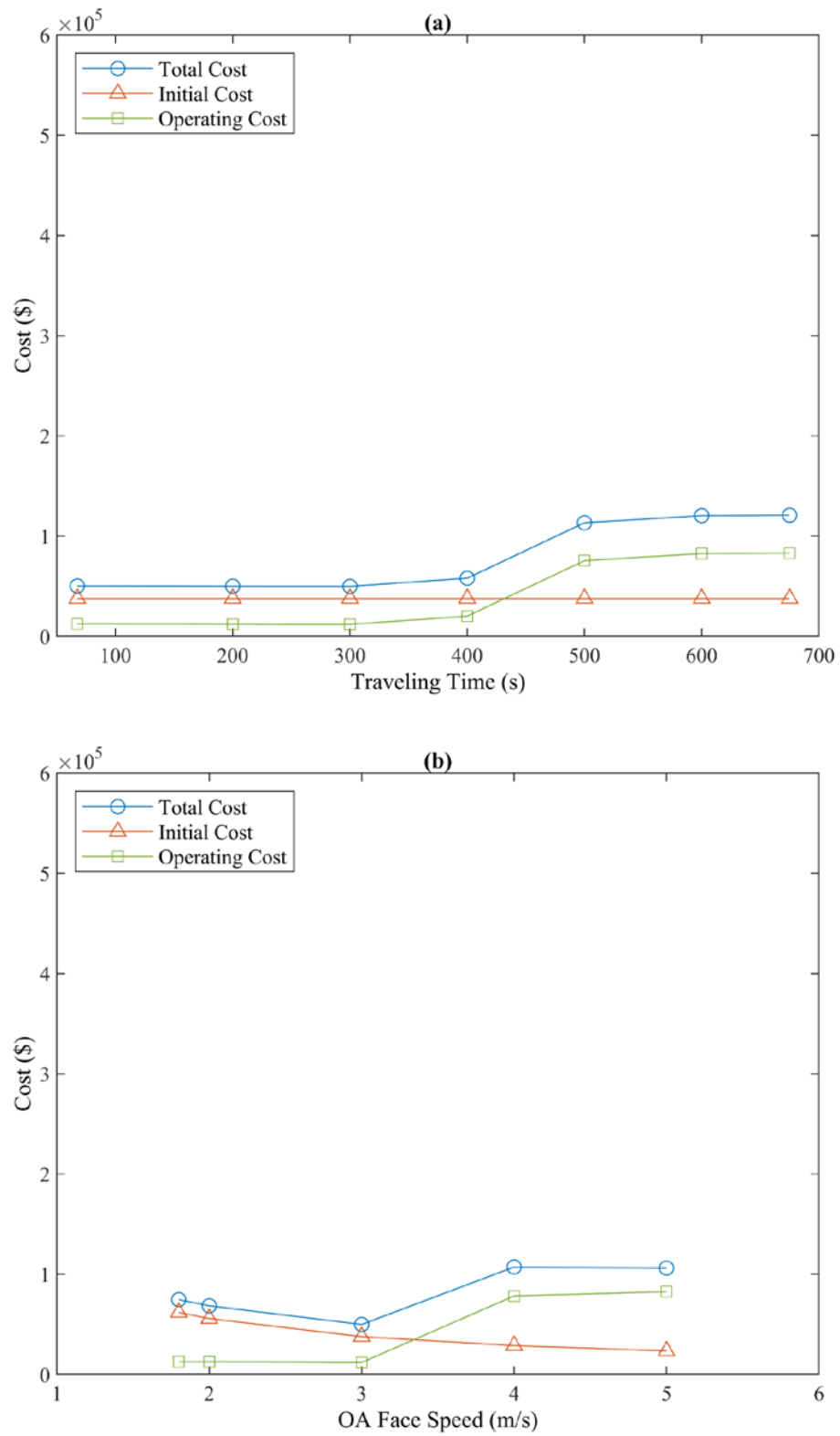
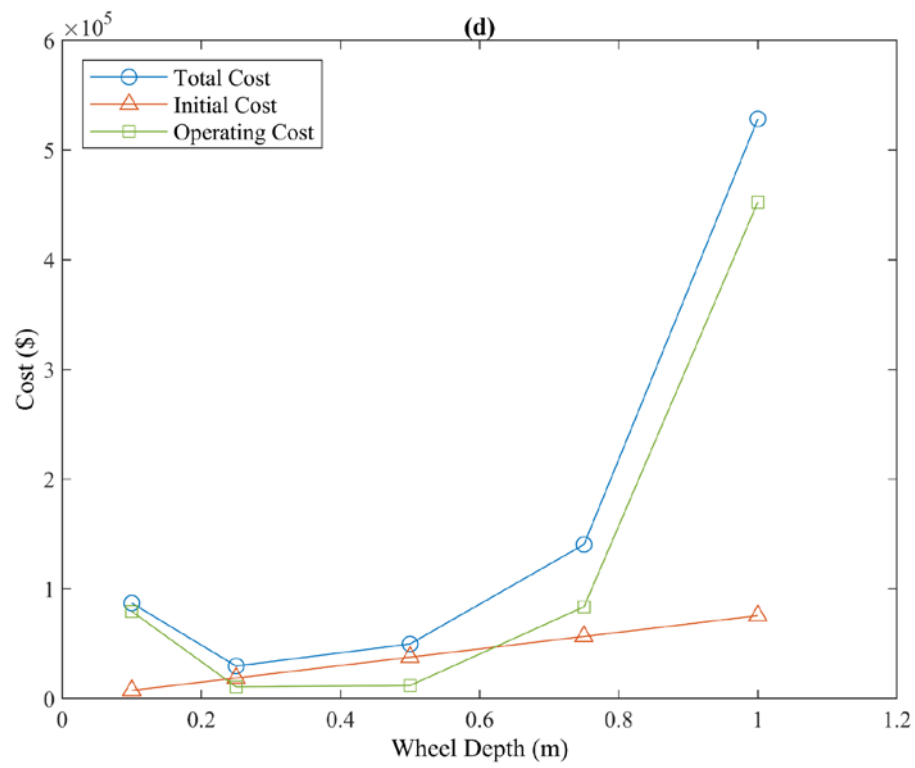
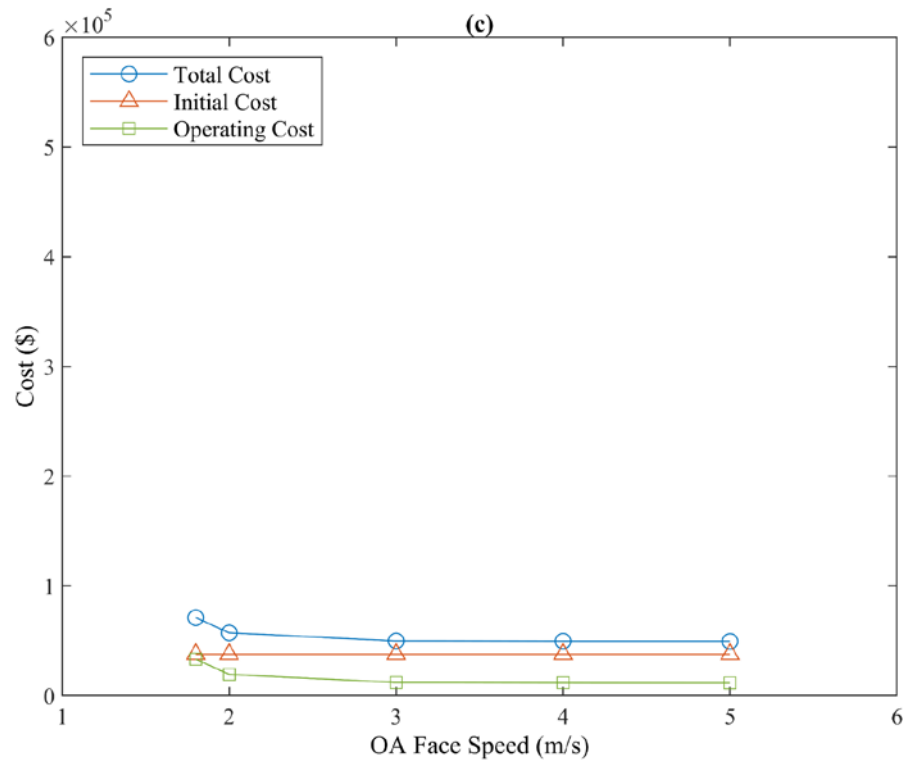


Fig. 41 Desiccant wheel variables' sensitivity study on costs

Fig 41 continued



## **8.5 Desiccant Wheel Optimization Results**

### **8.5.1 Desiccant Wheel Design Optimization**

One optimization is performed with both the desiccant wheel and the heat wheel target variables (rotational speed, SA/RA face velocity, depth of desiccant wheel; rotational speed, SA face velocity, depth of heat wheel). Optimized desiccant wheel and heat wheel designs are delivered by TRNOPT. The optimization outputs for desiccant wheel design is shown in Table 16; wheel depth is thicker for more dehumidification capacity; rotational speed is faster for more mass exchange between supply airstream and regeneration airstream; supply air face velocity and regeneration air face velocity fall in lower end to yield more time for mass transfer between air and desiccant. The optimal heat wheel design is wheel depth at 0.60 m, rotational speed at 60 RPM, supply air face velocity at 2 m/s. The optimal heat wheel design is close to the design with maximum sensible energy recovery according to the sensitivity study conducted in Section 7.4. For the heat wheel, the maximum heat exchange between the regeneration airstream and supply airstream is desired to decrease the air temperature entering the evaporator and to increase the air temperature entering the preheating coil; thus, the power consumptions of the A/C and the preheating coil can be reduced. This phenomenon is anticipated in different climate zones, and similar optimization outcomes are expected. To simplify the optimization, the heat wheel is set to be the optimal design across different locations.

To compare with the results presented in Section 8.2, the supermarket model developed in the previous section is utilized to conduct the optimization study, and the Miami, FL. TMY3 weather data is utilized in the building model. The optimized wheel depth is close to the optimal wheel depth for the best moisture removal capacity. The rotational speed approaches the upper bound of the operating range for more mass exchange between the supply airstream and the regeneration airstream. Supply air face velocity and regeneration air face velocity stay in the lower bound of the operating condition to achieve more mass transfer between air and the desiccant material. Fig. 41 demonstrates the energy consumption of the wheel-integrated system with an optimized desiccant wheel. The total energy consumption of the optimized wheel system is reduced by 8.1% compared with the wheel system recommended by Manufacturer B. The preheating energy consumption decreases 12.3%; though, the A/C energy consumption increases 8.4%. Preheating consumes the most energy among the different components, and it is twice that

of the A/C energy consumption- the second highest energy consumption; hence, the optimization algorithm tends to reduce preheating energy consumption.

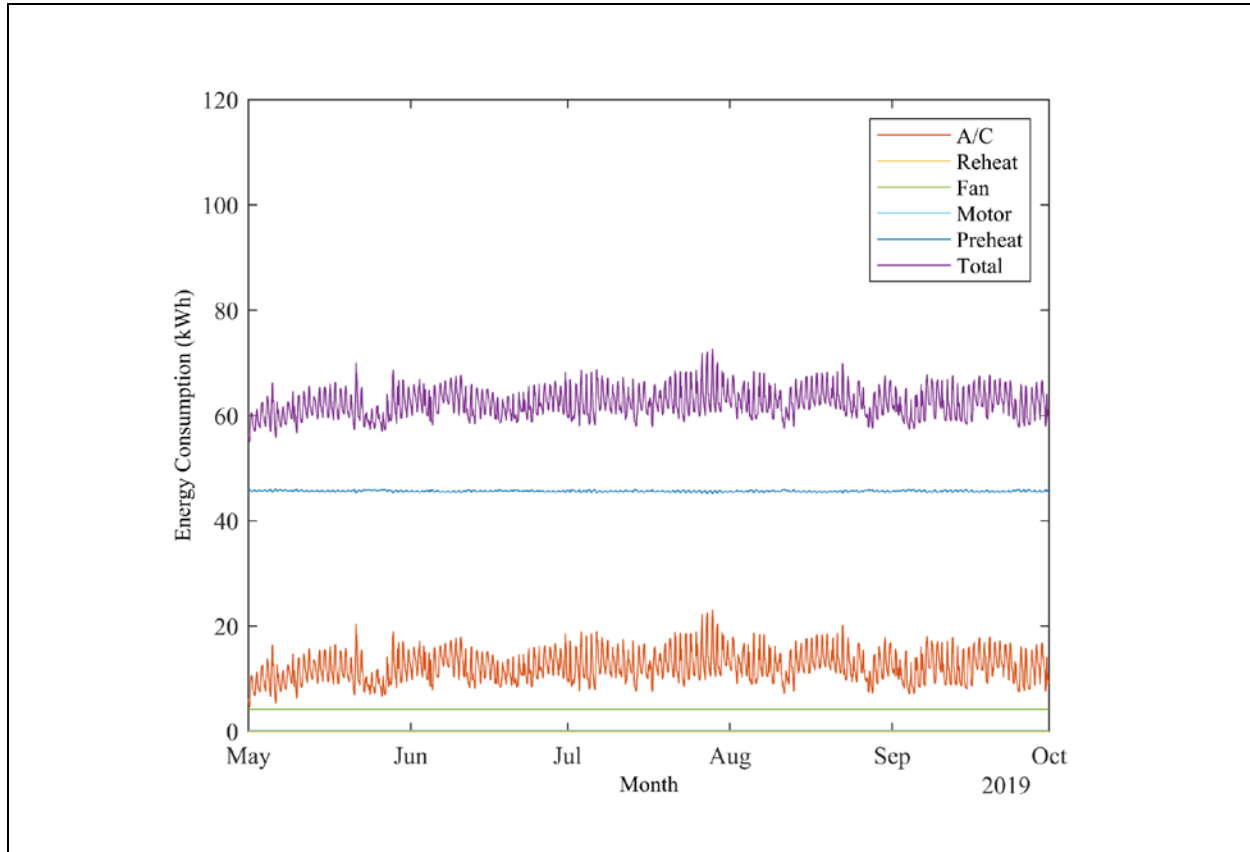


Fig. 42 Energy consumptions of optimized desiccant wheel integrated HVAC system components

Table 16 Optimal desiccant wheel design vs. original design

Variable	Original	Optimization Output
Depth (m)	0.3	0.54
Rotational Speed (RPH)	9	39
SA Face Velocity (m/s)	3	2.64
RA Face Velocity (m/s)	3	1.8

### 8.5.2 Variant Climates Optimization

The final optimization study is to investigate the trend of optimal desiccant wheel designs in different climates. Five locations are chosen to make the comparison, including Miami, FL, and Houston, TX for hot and humid climates; Phoenix, AZ for hot and dry climate; San Francisco, CA for mild climate; and Minneapolis, MN for cold climate. Table 15 illustrates optimal designs for desiccant wheels in different climate zones. The optimal rotational speeds are observed near the upper bound of the operating range. The optimization result indicates that the desiccant wheel tends to reach more mass exchange between the supply airstream and the regeneration airstream. The supply air and regeneration air face velocity appear in the lower end of the range. High face velocity shortens the time of air staying in the wheel flute, so the mass transfers between air and desiccant are decreased. Hence, low air face velocities are preferred for optimal results. The optimization output for regeneration air face velocity tends to move toward the lower boundary, since the moisture removal capacity is more than sufficient in the regeneration airstream. Thus, the optimization output delivers a design with as little regeneration airflow as possible. The optimal wheel depths are generally in the middle of the range besides the result for San Francisco. San Francisco has the highest utility rate among all locations, and a deeper wheel is found as the optimization result in order to provide more moisture removal capacity. An extra optimization study is conducted based on a comparable utility rate with other cities (50% of the original utility rate in San Francisco), and the outcome shows a wheel depth in a similar range with the other locations. Last, the optimization results fall into a small range among different locations. The regeneration inlet air temperature is constant, and the return air is mixed with a small portion of the outdoor fresh air. Hence, the desiccant wheel operates in a fairly constant condition; thus, the optimization conveys similar outcomes.

Table 17 Optimal desiccant wheel design in different locations

	Depth (m)	Rotational Speed (RPH)	SA Face Velocity (m/s)	RA Face Velocity (m/s)
Miami, FL	0.54	39	2.64	1.8
Houston, TX	0.47	39	2.78	1.8
Phoenix, AZ	0.53	39	2.63	1.8
Minneapolis, MN	0.55	39	2.61	1.8
San Francisco, CA	0.71	36	2.25	1.8
San Francisco, CA (50% utility rate)	0.51	39	2.76	1.8

### 8.6 Conclusion of Desiccant Wheel Case Study

Reasonable simulation and optimization outcomes are delivered by integrating the semi-empirical desiccant wheel mapping method and building performance software. The energy consumption of the supermarket dry storage is significantly reduced by employing a desiccant wheel to the HVAC system; the moisture removal is provided by the desiccant wheel, and no overcooling-reheating process is required. The optimization can generate an optimal desiccant wheel design with moderately better energy efficiency than the manufacturer's recommendation. The optimization results appear in a similar range across different climate zones due to a relatively constant operating condition. Hence, the semi-empirical desiccant wheel mapping method is a good approach for simulating and optimizing desiccant wheel-integrated HVAC systems.

## 9. CONCLUSION AND FUTURE WORK

### 9.1 Achieved Research Objectives

The following tasks have been completed to achieve this research objective, and research objectives that have been done are listed and the completed portions are checked.

- ✓ Develop a mapping method for energy recovery wheels
  - ✓ Develop a detailed FDM numerical model of energy recovery wheels
    - ✓ Implement dynamic Nusselt number
  - ✓ Validate the numerical model
    - ✓ Validate with experimental data
    - ✓ Validate with literature data
  - ✓ Develop and validate a mapping method for energy recovery wheels
    - ✓ Identify the form of the mapping method
    - ✓ Conduct validation against the numerical model
    - ✓ Conduct validation against literature data
- ✓ Develop a mapping method for desiccant wheels
  - ✓ Develop a detailed FDM numerical model for desiccant wheels
    - ✓ Implement dynamic Nusselt number
  - ✓ Validate the numerical model
    - ✓ Validate with manufacturer's data
    - ✓ Validate with literature data
  - ✓ Develop and validate a mapping method of desiccant wheels
    - ✓ Identify the form of the mapping method
    - ✓ Conduct validation against the numerical model
    - ✓ Conduct validation against literature data
- ✓ Conduct the performance evaluation and optimization of HVAC systems via implementing the mapping method of the energy recovery wheel or desiccant wheels with transient building energy performance simulation software

- ✓ Analyze an HVAC system integrated with an energy recovery wheel
  - ✓ Develop a model of the target building and the HVAC system
  - ✓ Conduct optimizations of the energy recovery wheel
  - ✓ Evaluate the performances and costs of the optimized energy recovery wheel design in different climates
- ✓ Analyze an HVAC system integrated with a desiccant wheel
  - ✓ Develop a model of the target building and the HVAC system
  - ✓ Conduct optimizations of the desiccant wheel
  - ✓ Evaluate the performances and costs of the optimized desiccant wheel design in different climates

## **9.2 Conclusion**

This research is dedicated to developing numerically efficient and robust performance evaluation methods for energy recovery wheels and desiccant wheels, and utilizing them for building energy simulations and optimizations.

An energy recovery wheel performance mapping method was established in the first phase, and the mapping method has been proven to be capable of capturing the performance of energy recovery wheels accurately and rapidly. An FDM model was built via Python, and the mapping method was trained and validated based on the testing results from a wheel manufacturer and experimental data from the works of open literature. The research in this phase was submitted to the International Journal of Refrigeration. The FDM model and the mapping method are extended to the performance prediction of desiccant wheels. A new form of the mapping method is developed for desiccant wheels, and it has been trained and validated based on the data from another wheel manufacturer and experimental results collected from the open literature.

The semi-empirical wheel mapping methods deliver performance predictions accurately and precisely. Furthermore, the computational efficiency and the flexibility of varying wheel design variables make the mapping methods suitable in building energy performance simulations and optimizations. Several wheel performance prediction methods were proposed in other literature; however, those methods tend to take excessive computational time; lack flexibility in changing design variables of wheels (e.g., rotational speed, air face velocity, wheel depth) simultaneously. Those characteristics make them not the most ideal approach for optimization.



A reliable commercial building energy model in the TRNSYS software platform has been built for simulating and predicting the performance of an energy recovery wheel/desiccant wheel by using the mapping methods, then various case studies have been conducted to observe the trend of optimal wheel designs in different climate zones. The energy consumptions of different components (fans, wheel motors, heating, cooling, etc.) in the HVAC system are considered, and wheel initial costs are estimated. Optimization outputs deliver economical designs of the wheels' physical dimensions and operating conditions under representative climate zones in the U.S. with dynamic weather simulation. The optimal energy recovery wheel and desiccant wheel designs in different climates are identified, and analyzed also.

The performance mapping methods for energy recovery wheels and desiccant wheels are proven to be applicable, and capable to deliver reliable outcomes expeditiously in dynamic building energy simulation and optimization. The trend of optimal designs for energy recovery wheels and desiccant wheels is observed among the optimization outcomes in different operating conditions. The mapping method is an innovative and suitable tool for academic studies and research and development activities in the industry on wheels and whole HVAC systems.

### **9.3 Future Work**

The performance mapping methods for energy recovery wheels and desiccant wheels are suitable tools for building energy simulation and optimization; however, further research may be improved in the following directions.

The approach of the wheel purchase cost in the optimization approach can be improved. The current cost model is developed via interpolation and extrapolation based on the work of Lewis [66]; thus, the model may not be able to reflect the most accurate cost of a wheel, much less for a different wheel manufacturer.

Since this research focuses on the application and optimization of the wheel, the model only considers the wheel initial cost; other initial costs (e.g., ducts, air-conditioner, heating coil, fan, etc) are not considered. According to the sensitivity study conducted in Section 7.4.3, the optimization result is influenced by the initial cost and operating cost significantly. In addition, simple payback analysis is utilized in the study as the optimization target; thus, maintenance cost, inflation, and depreciation are not considered. A more accurate wheel initial cost model and a more

detailed life-cycle analysis for future studies are recommended in order to obtain optimization outcomes closer to reality.

The regeneration air temperature is set as constant in the desiccant wheel case study; however, the regeneration air temperature can be one of the optimization variables, with more diverse data sets (e.g., different regeneration temperatures) to train the mapping method; a more optimal result may be obtained. The optimization algorithm can identify a lower regeneration temperature, and the wheel is still capable to provide sufficient dehumidification capacity; thus, the heating energy consumption can be further reduced. Moreover, if there is waste heat or “free heating” (e.g., solar heat, geothermal, etc.) available, the desiccant wheel system would be a more economically appealing option for dehumidification purposes.

Besides the above stated directions, more potential applications of the performance mapping methods for energy recovery wheels and desiccant wheels can be explored with researchers’ own interest.

## APPENDIX A. FINITE DIFFERENCE METHOD DERIVATION FOR GOVERNING EQUATIONS

### FDM of the air stream energy balance

$$\frac{\partial T_g}{\partial t} = \frac{h}{d_h \rho_g C p_g} (T_m - T_g) - u \frac{\partial T_g}{\partial x}$$

1<sup>st</sup> order backward finite difference approximation for  $\frac{\partial T_g}{\partial t}$

$$\frac{\partial T_g}{\partial t} = \frac{-T_g(x_j, t_n) + T_g(x_j, t_{n+1})}{\Delta t}$$

2<sup>nd</sup> order forward finite difference approximation for  $\frac{\partial T_g}{\partial x}$

$$\frac{\partial T_g}{\partial x} = \frac{-3T_g(x_j, t_{n+1}) + 4T_g(x_{j+1}, t_{n+1}) - T_g(x_{j+2}, t_{n+1})}{2\Delta x}$$

$$\begin{aligned} & \frac{-T_g(x_j, t_n) + T_g(x_j, t_{n+1})}{\Delta t} \\ &= \frac{h}{D_h \rho_g C p_g} [T_m(x_j, t_n) - T_g(x_j, t_n)] \\ & - u \left[ \frac{-3T_g(x_j, t_{n+1}) + 4T_g(x_{j+1}, t_{n+1}) - T_g(x_{j+2}, t_{n+1})}{2\Delta x} \right] \end{aligned}$$

$$\begin{aligned} & \left[ \frac{1}{\Delta t} + \frac{h}{D_h \rho_g C p_g} + \frac{-3u}{2\Delta x} \right] T_g(x_j, t_{n+1}) \\ & + \frac{4u}{2\Delta x} T_g(x_{j+1}, t_{n+1}) + \frac{-u}{2\Delta x} T_g(x_{j+2}, t_{n+1}) \\ &= \frac{1}{\Delta t} T_g(x_j, t_n) + \frac{h}{D_h \rho_g C p_g} T_m(x_j, t_n) \end{aligned}$$

1<sup>st</sup> order backward finite difference approximation for  $\frac{\partial T_g}{\partial t}$

$$\frac{\partial T_g}{\partial t} = \frac{-T_g(x_j, t_n) + T_g(x_j, t_{n+1})}{\Delta t}$$

2<sup>nd</sup> order central finite difference approximation for  $\frac{\partial T_g}{\partial x}$

$$\frac{\partial T_g}{\partial x} = \frac{T_g(x_{j-2}, t_{n+1}) - 8T_g(x_{j-1}, t_{n+1}) + 8T_g(x_{j+1}, t_{n+1}) - T_g(x_{j+2}, t_{n+1})}{12\Delta x}$$

$$\begin{aligned} & \frac{-T_g(x_j, t_n) + T_g(x_j, t_{n+1})}{\Delta t} \\ &= \frac{h}{D_h \rho_g C p_g} [T_m(x_j, t_n) - T_g(x_j, t_n)] \\ & - u \left[ \frac{T_g(x_{j-2}, t_{n+1}) - 8T_g(x_{j-1}, t_{n+1}) + 8T_g(x_{j+1}, t_{n+1}) - T_g(x_{j+2}, t_{n+1})}{12\Delta x} \right] \\ & \frac{u}{12\Delta x} T_g(x_{j-2}, t_{n+1}) + \frac{-8u}{12\Delta x} T_g(x_{j-1}, t_{n+1}) + \frac{1}{\Delta t} T_g(x_j, t_{n+1}) \\ & + \frac{8u}{12\Delta x} T_g(x_{j+1}, t_{n+1}) + \frac{-u}{12\Delta x} T_g(x_{j+2}, t_{n+1}) \\ &= \left[ \frac{1}{\Delta t} + \frac{-h}{D_h \rho_g C p_g} \right] T_g(x_j, t_n) + \frac{h}{D_h \rho_g C p_g} T_m(x_j, t_n) \end{aligned}$$

1<sup>st</sup> order backward finite difference approximation for  $\frac{\partial T_g}{\partial t}$

$$\frac{\partial T_g}{\partial t} = \frac{-T_g(x_j, t_n) + T_g(x_j, t_{n+1})}{\Delta t}$$

2<sup>nd</sup> order backward finite difference approximation for  $\frac{\partial T_g}{\partial x}$

$$\frac{\partial T_g}{\partial x} = \frac{T_g(x_{j-2}, t_{n+1}) - 4T_g(x_{j-1}, t_{n+1}) + 3T_g(x_j, t_{n+1})}{2\Delta x}$$

$$\begin{aligned}
& \frac{-T_g(x_j, t_n) + T_g(x_j, t_{n+1})}{\Delta t} \\
&= \frac{h}{D_h \rho_g C p_g} [T_m(x_j, t_n) - T_g(x_j, t_n)] \\
& - u \left[ \frac{T_g(x_{j-2}, t_{n+1}) - 4T_g(x_{j-1}, t_{n+1}) + 3T_g(x_j, t_{n+1})}{2\Delta x} \right]
\end{aligned}$$

$$\begin{aligned}
& \frac{u}{2\Delta x} T_g(x_{j-2}, t_{n+1}) + \frac{-4u}{2\Delta x} T_g(x_{j-1}, t_{n+1}) + \left[ \frac{1}{\Delta t} + \frac{3u}{2\Delta x} \right] T_g(x_j, t_{n+1}) \\
&= \left[ \frac{1}{\Delta t} + \frac{-h}{D_h \rho_g C p_g} \right] T_g(x_j, t_n) + \frac{h}{D_h \rho_g C p_g} T_m(x_j, t_n)
\end{aligned}$$

### FDM of the matrix energy balance

$$\begin{aligned}
\frac{\partial T_m}{\partial t} &= \frac{k_{sub}}{\rho_{sub} C p_{sub}} \frac{\partial^2 T_m}{\partial x^2} + \frac{h_m \Delta H_{ads}}{\rho_{sub} \delta_{sub} C p_{sub} + \rho_d \delta_d C p_d} (W_g - W_m) \\
&+ \frac{h}{\rho_{sub} \delta_{sub} C p_{sub} + \rho_d \delta_d C p_d} (T_g - T_m)
\end{aligned}$$

1<sup>st</sup> order backward finite difference approximation for  $\frac{\partial T_m}{\partial t}$

$$\frac{\partial T_m}{\partial t} = \frac{-T_m(x_j, t_n) + T_m(x_j, t_{n+1})}{\Delta t}$$

1<sup>st</sup> order forward finite difference approximation for  $\frac{\partial^2 T_m}{\partial x^2}$

$$\frac{\partial^2 T_m}{\partial x^2} = \frac{T_m(x_j, t_{n+1}) - 2T_m(x_{j+1}, t_{n+1}) + T_m(x_{j+2}, t_{n+1})}{\Delta x^2}$$

$$\begin{aligned}
& \frac{-T_m(x_j, t_n) + T_m(x_j, t_{n+1})}{\Delta t} \\
&= \frac{k_{sub}}{\rho_{sub} C p_{sub}} \left[ \frac{T_m(x_j, t_{n+1}) - 2T_m(x_{j+1}, t_{n+1}) + T_m(x_{j+2}, t_{n+1})}{\Delta x^2} \right] \\
&+ \frac{h}{\rho_{sub} \delta_{sub} C p_{sub} + \rho_d \delta_d C p_d} [T_g(x_j, t_n) - T_m(x_j, t_n)] \\
&+ \frac{h_m \Delta H_{ads}}{\rho_{sub} \delta_{sub} C p_{sub} + \rho_d \delta_d C p_d} [W_g(x_j, t_n) - W_m(x_j, t_n)] \\
&\left[ \frac{1}{\Delta t} + \frac{-k_{sub}}{\rho_{sub} C p_{sub} \Delta x^2} \right] T_m(x_j, t_{n+1}) + \frac{2k_{sub}}{\rho_{sub} C p_{sub} \Delta x^2} T_m(x_{j+1}, t_{n+1}) \\
&+ \frac{-k_{sub}}{\rho_{sub} C p_{sub} \Delta x^2} T_m(x_{j+2}, t_{n+1}) \\
&= \left[ \frac{1}{\Delta t} + \frac{-h}{\rho_{sub} \delta_{sub} C p_{sub} + \rho_d \delta_d C p_d} \right] T_m(x_j, t_n) \\
&+ \frac{h}{\rho_{sub} \delta_{sub} C p_{sub} + \rho_d \delta_d C p_d} T_m(x_j, t_n) \\
&+ \frac{h_m \Delta H_{ads}}{\rho_{sub} \delta_{sub} C p_{sub} + \rho_d \delta_d C p_d} W_g(x_j, t_n) \\
&+ \frac{-h_m \Delta H_{ads}}{\rho_{sub} \delta_{sub} C p_{sub} + \rho_d \delta_d C p_d} W_m(x_j, t_n)
\end{aligned}$$

1<sup>st</sup> order backward finite difference approximation for  $\frac{\partial T_m}{\partial t}$

$$\frac{\partial T_m}{\partial t} = \frac{-T_m(x_j, t_n) + T_m(x_j, t_{n+1})}{\Delta t}$$

2<sup>nd</sup> order central finite difference approximation for  $\frac{\partial^2 T_m}{\partial x^2}$

$$\frac{\partial^2 T_m}{\partial x^2} = \frac{T_m(x_{j-1}, t_{n+1}) - 2T_m(x_j, t_{n+1}) + T_m(x_{j+1}, t_{n+1})}{\Delta x^2}$$

$$\begin{aligned}
& \frac{-T_m(x_j, t_n) + T_m(x_j, t_{n+1})}{\Delta t} \\
&= \frac{k_{sub}}{\rho_{sub} C p_{sub}} \left[ \frac{T_m(x_{j-1}, t_{n+1}) - 2T_m(x_j, t_{n+1}) + T_m(x_{j+1}, t_{n+1})}{\Delta x^2} \right] \\
&+ \frac{h}{\rho_{sub} \delta_{sub} C p_{sub} + \rho_d \delta_d C p_d} [T_g(x_j, t_n) - T_m(x_j, t_n)] \\
&+ \frac{h_m \Delta H_{ads}}{\rho_{sub} \delta_{sub} C p_{sub} + \rho_d \delta_d C p_d} [W_g(x_j, t_n) - W_m(x_j, t_n)]
\end{aligned}$$

$$\begin{aligned}
& \frac{-k_{sub}}{\rho_{sub} C p_{sub} \Delta x^2} T_m(x_{j-1}, t_{n+1}) + \left[ \frac{2k_{sub}}{\rho_{sub} C p_{sub} \Delta x^2} + \frac{1}{\Delta t} \right] T_m(x_j, t_{n+1}) \\
&+ \frac{-k_{sub}}{\rho_{sub} C p_{sub} \Delta x^2} T_m(x_{j+1}, t_{n+1}) \\
&= \left[ \frac{1}{\Delta t} + \frac{h}{\rho_{sub} \delta_{sub} C p_{sub} + \rho_d \delta_d C p_d} \right] T_m(x_j, t_n) \\
&+ \frac{h}{\rho_{sub} \delta_{sub} C p_{sub} + \rho_d \delta_d C p_d} T_g(x_j, t_n) \\
&+ \frac{h_m \Delta H_{ads}}{\rho_{sub} \delta_{sub} C p_{sub} + \rho_d \delta_d C p_d} W_g(x_j, t_n) \\
&+ \frac{-h_m \Delta H_{ads}}{\rho_{sub} \delta_{sub} C p_{sub} + \rho_d \delta_d C p_d} W_m(x_j, t_n)
\end{aligned}$$

1<sup>st</sup> order backward finite difference approximation for  $\frac{\partial T_m}{\partial t}$

$$\frac{\partial T_m}{\partial t} = \frac{-T_m(x_j, t_n) + T_m(x_j, t_{n+1})}{\Delta t}$$

2<sup>nd</sup> order backward finite difference approximation for  $\frac{\partial^2 T_m}{\partial x^2}$

$$\frac{\partial^2 T_m}{\partial x^2} = \frac{T_m(x_{j-2}, t_{n+1}) - 2T_m(x_{j-1}, t_{n+1}) + T_m(x_j, t_{n+1})}{\Delta x^2}$$

$$\begin{aligned}
& \frac{-T_m(x_j, t_n) + T_m(x_j, t_{n+1})}{\Delta t} \\
&= \frac{k_{sub}}{\rho_{sub} C p_{sub}} \left[ \frac{T_m(x_{j-2}, t_{n+1}) - 2T_m(x_{j-1}, t_{n+1}) + T_m(x_j, t_{n+1})}{\Delta x^2} \right] \\
&+ \frac{h}{\rho_{sub} \delta_{sub} C p_{sub} + \rho_d \delta_d C p_d} [T_g(x_j, t_n) - T_m(x_j, t_n)] \\
&+ \frac{h_m \Delta H_{ads}}{\rho_{sub} \delta_{sub} C p_{sub} + \rho_d \delta_d C p_d} [W_g(x_j, t_n) - W_m(x_j, t_n)] \\
& \frac{-k_{sub}}{\rho_{sub} C p_{sub} \Delta x^2} T_m(x_{j-2}, t_{n+1}) + \frac{2k_{sub}}{\rho_{sub} C p_{sub} \Delta x^2} T_m(x_{j-1}, t_{n+1}) \\
&+ \left[ \frac{1}{\Delta t} + \frac{-k_{sub}}{\rho_{sub} C p_{sub} \Delta x^2} \right] T_m(x_j, t_{n+1}) \\
&= \left[ \frac{1}{\Delta t} + \frac{-h}{\rho_{sub} \delta_{sub} C p_{sub} + \rho_d \delta_d C p_d} \right] T_m(x_j, t_n) \\
&+ \frac{h}{\rho_{sub} \delta_{sub} C p_{sub} + \rho_d \delta_d C p_d} T_g(x_j, t_n) \\
&+ \frac{h_m \Delta H_{ads}}{\rho_{sub} \delta_{sub} C p_{sub} + \rho_d \delta_d C p_d} W_g(x_j, t_n) \\
&+ \frac{-h_m \Delta H_{ads}}{\rho_{sub} \delta_{sub} C p_{sub} + \rho_d \delta_d C p_d} W_m(x_j, t_n)
\end{aligned}$$

### FDM of the air stream mass balance

$$\frac{\partial W_g}{\partial t} = \frac{h_d}{d_h \rho_g} (W_m - W_g) - u \frac{\partial W_g}{\partial x}$$

1<sup>st</sup> order backward finite difference approximation for  $\frac{\partial W_g}{\partial t}$

$$\frac{\partial W_g}{\partial t} = \frac{-W_g(x_j, t_n) + W_g(x_j, t_{n+1})}{\Delta t}$$



2<sup>nd</sup> order forward finite difference approximation for  $\frac{\partial W_g}{\partial x}$

$$\begin{aligned}
\frac{\partial W_g}{\partial x} &= \frac{-3W_g(x_j, t_{n+1}) + 4W_g(x_{j+1}, t_{n+1}) - W_g(x_{j+2}, t_{n+1})}{2\Delta x} \\
&\quad - \frac{W_g(x_j, t_n) + W_g(x_j, t_{n+1})}{\Delta t} \\
&= \frac{h_m}{d_h \rho_g} [W_m(x_j, t_n) - W_g(x_j, t_n)] \\
&\quad - u \left[ \frac{-3W_g(x_j, t_{n+1}) + 4W_g(x_{j+1}, t_{n+1}) - W_g(x_{j+2}, t_{n+1})}{2\Delta x} \right] \\
&= \left[ \frac{1}{\Delta t} + \frac{-3u}{2\Delta x} \right] W_g(x_j, t_{n+1}) + \frac{4u}{2\Delta x} W_g(x_{j+1}, t_{n+1}) + \frac{-u}{2\Delta x} W_g(x_{j+2}, t_{n+1}) \\
&= \left[ \frac{1}{\Delta t} + \frac{-h_m}{d_h \rho_g} \right] W_g(x_j, t_n) + \frac{h_m}{d_h \rho_g} W_m(x_j, t_n) \\
&\quad a_{31}W_g(x_j, t_{n+1}) + b_{31}W_g(x_{j+1}, t_{n+1}) + c_{31}W_g(x_{j+2}, t_{n+1}) \\
&\quad = d_{31}W_g(x_j, t_n) + e_{31}W_m(x_j, t_n)
\end{aligned}$$

1<sup>st</sup> order backward finite difference approximation for  $\frac{\partial W_g}{\partial t}$

$$\frac{\partial W_g}{\partial t} = \frac{-W_g(x_j, t_n) + W_g(x_j, t_{n+1})}{\Delta t}$$

2<sup>nd</sup> order central finite difference approximation for  $\frac{\partial W_g}{\partial x}$

$$\begin{aligned}
&\frac{\partial W_g}{\partial x} \\
&= \frac{W_g(x_{j-2}, t_{n+1}) - 8W_g(x_{j-1}, t_{n+1}) + 8W_g(x_{j+1}, t_{n+1}) - W_g(x_{j+2}, t_{n+1})}{12\Delta x}
\end{aligned}$$

$$\begin{aligned}
& \frac{-W_g(x_j, t_n) + W_g(x_j, t_{n+1})}{\Delta t} \\
&= \frac{h_m}{d_h \rho_g} [W_m(x_j, t_n) - W_g(x_j, t_n)] \\
& - u \left[ \frac{W_g(x_{j-2}, t_{n+1}) - 8W_g(x_{j-1}, t_{n+1}) + 8W_g(x_{j+1}, t_{n+1}) - W_g(x_{j+2}, t_{n+1})}{12\Delta x} \right]
\end{aligned}$$

$$\begin{aligned}
& \frac{u}{12\Delta x} W_g(x_{j-2}, t_{n+1}) + \frac{-8u}{12\Delta x} W_g(x_{j-1}, t_{n+1}) + \frac{1}{\Delta t} W_g(x_j, t_{n+1}) \\
& + \frac{8u}{12\Delta x} W_g(x_{j+1}, t_{n+1}) + \frac{-u}{12\Delta x} W_g(x_{j+2}, t_{n+1}) \\
&= \left[ \frac{1}{\Delta t} + \frac{-h_m}{d_h \rho_g} \right] W_g(x_j, t_n) + \frac{h_m}{d_h \rho_g} W_m(x_j, t_n)
\end{aligned}$$

1<sup>st</sup> order backward finite difference approximation for  $\frac{\partial W_g}{\partial t}$

$$\frac{\partial W_g}{\partial t} = \frac{-W_g(x_j, t_n) + W_g(x_j, t_{n+1})}{\Delta t}$$

2<sup>nd</sup> order backward finite difference approximation for  $\frac{\partial W_g}{\partial x}$

$$\frac{\partial W_g}{\partial x} = \frac{W_g(x_{j-2}, t_{n+1}) - 4W_g(x_{j-1}, t_{n+1}) + 3W_g(x_j, t_{n+1})}{2\Delta x}$$

$$\begin{aligned}
& \frac{-W_g(x_j, t_n) + W_g(x_j, t_{n+1})}{\Delta t} \\
&= \frac{h_m}{d_h \rho_g} [W_m(x_j, t_n) - W_g(x_j, t_n)] \\
& - u \left[ \frac{W_g(x_{j-2}, t_{n+1}) - 4W_g(x_{j-1}, t_{n+1}) + 3W_g(x_j, t_{n+1})}{2\Delta x} \right]
\end{aligned}$$

$$\begin{aligned}
& \frac{u}{2\Delta x} W_g(x_{j-2}, t_{n+1}) + \frac{-4u}{2\Delta x} W_g(x_{j-1}, t_{n+1}) + \left[ \frac{1}{\Delta t} + \frac{3u}{2\Delta x} \right] W_g(x_j, t_{n+1}) \\
&= \left[ \frac{1}{\Delta t} + \frac{-h_m}{d_h \rho_g} \right] W_g(x_j, t_n) + \frac{h_m}{d_h \rho_g} W_m(x_j, t_n)
\end{aligned}$$

### FDM of the matrix mass balance

$$\begin{aligned}
 \frac{\partial \gamma_d}{\partial t} &= \frac{\partial \gamma_d}{\partial T_{m,abs}} \frac{\partial T_{m,abs}}{\partial t} + \frac{\partial \gamma_d}{\partial W_m} \frac{\partial W_m}{\partial t} \\
 &= \frac{\partial \gamma_d}{\partial \varphi} \frac{\partial \varphi}{\partial T_{m,abs}} \frac{\partial T_{m,abs}}{\partial t} + \frac{\partial \gamma_d}{\partial \varphi} \frac{\partial \varphi}{\partial W_m} \frac{\partial W_m}{\partial t} \\
 &= \frac{h_m}{\delta_d \rho_d} (W_g - W_m)
 \end{aligned}$$

$$\frac{\gamma_d}{\gamma_{max}} = \frac{\varphi}{\varphi - c\varphi + c}$$

$$\varphi = \frac{P_v}{P_{v,sat}} = \frac{461.89 W_m \rho_g T_{m,abs}}{4.98 \times 10^{10} e^{\frac{4890.55}{T_{m,abs}}}} = 9.28 \times 10^{-9} W_m \rho_g T_{m,abs} e^{\frac{4890.55}{T_{m,abs}}}$$

1<sup>st</sup> order backward finite difference approximation for  $\frac{\partial T_{m,abs}}{\partial t}$

$$\frac{\partial T_{m,abs}}{\partial t} = \frac{-T_{m,abs}(x_j, t_n) + T_{m,abs}(x_j, t_{n+1})}{\Delta t}$$

1<sup>st</sup> order backward finite difference approximation for  $\frac{\partial W_m}{\partial x}$

$$\frac{\partial W_m}{\partial t} = \frac{-W_m(x_j, t_n) + W_m(x_j, t_{n+1})}{\Delta t}$$

$$\begin{aligned}
 \frac{\partial \gamma_d}{\partial T_{m,abs}} &= \frac{\partial \gamma_d}{\partial \varphi} \frac{\partial \varphi}{\partial T_{m,abs}} \\
 &= \left[ \frac{c\gamma_{max}}{(\varphi - c\varphi + c)^2} \right] \left[ 9.28 \times 10^{-9} W_m \rho_g e^{\frac{4890.55}{T_{m,abs}}} \right. \\
 &\quad \left. - 4.54 \times 10^{-5} W_m \rho_g e^{\frac{4890.55}{T_{m,abs}}} \times \frac{1}{T_{m,abs}} \right]
 \end{aligned}$$

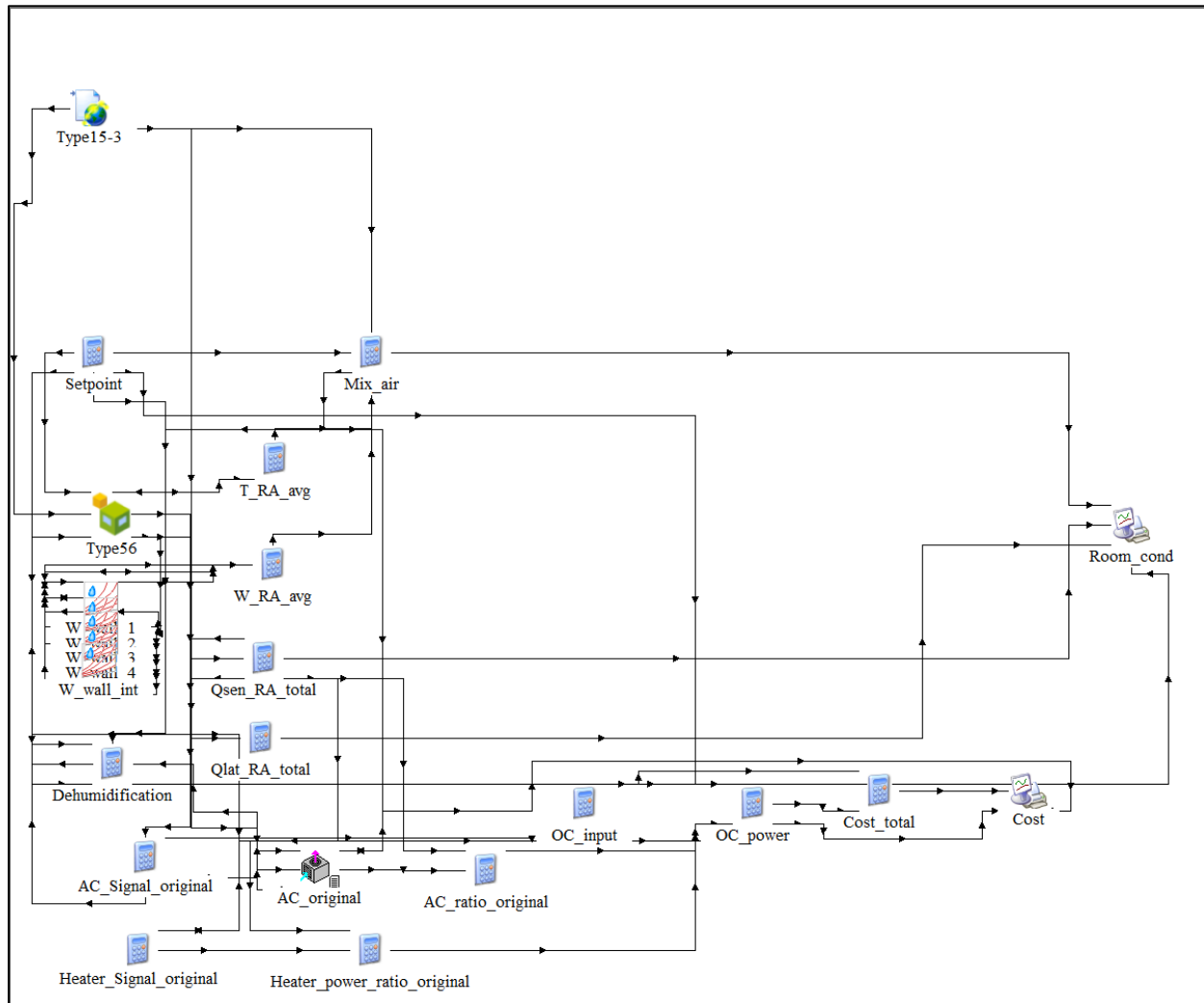
$$\frac{\partial \gamma_d}{\partial W_m} = \frac{\partial \gamma_d}{\partial \varphi} \frac{\partial \varphi}{\partial W_m} = \left[ \frac{c\gamma_{max}}{(\varphi - c\varphi + c)^2} \right] \left[ 9.28 \times 10^{-9} T_{m,abs} \rho_g e^{\frac{4890.55}{T_{m,abs}}} \right]$$

$$\begin{aligned}
& \frac{c\gamma_{max}}{(\varphi - c\varphi + c)^2} \left[ \frac{9.28 \times 10^{-9} W_m(x_j, t_n) \rho_g e^{\frac{4890.55}{T_{m,abs}(x_j, t_n)}}}{4.54 \times 10^{-5} W_m(x_j, t_n) \rho_g e^{\frac{4890.55}{T_{m,abs}(x_j, t_n)}}} \right] \\
& \times \left[ \frac{-T_{m,abs}(x_j, t_n) + T_{m,abs}(x_j, t_{n+1})}{\Delta t} \right] \\
& + \frac{c\gamma_{max}}{(\varphi - c\varphi + c)^2} \left[ 9.28 \times 10^{-9} T_{m,abs}(x_j, t_n) \rho_g e^{\frac{4890.55}{T_{m,abs}(x_j, t_n)}} \right] \\
& \times \left[ \frac{-W_m(x_j, t_n) + W_m(x_j, t_{n+1})}{\Delta t} \right] \\
& = \frac{h_m}{\delta_d \rho_d} [W_g(x_j, t_n) - W_m(x_j, t_n)]
\end{aligned}$$

$$\begin{aligned}
& \left\{ \frac{c\gamma_{max}}{(\varphi - c\varphi + c)^2} \left[ 9.28 \times 10^{-9} T_{m,abs}(x_j, t_n) \rho_g e^{\frac{4890.55}{T_{m,abs}(x_j, t_n)}} \right] \frac{1}{\Delta t} \right\} W_m(x_j, t_{n+1}) \\
& = \left\{ \frac{c\gamma_{max}}{(\varphi - c\varphi + c)^2} \left[ 9.28 \times 10^{-9} T_{m,abs}(x_j, t_n) \rho_g e^{\frac{4890.55}{T_{m,abs}(x_j, t_n)}} \right] \frac{1}{\Delta t} + \frac{-h_m}{\delta_d \rho_d} \right\} \\
& \times W_m(x_j, t_n) \\
& + \left\{ \frac{c\gamma_{max}}{(\varphi - c\varphi + c)^2} \left[ \frac{9.28 \times 10^{-9} W_m(x_j, t_n) \rho_g e^{\frac{4890.55}{T_{m,abs}(x_j, t_n)}}}{4.54 \times 10^{-5} W_m(x_j, t_n) \rho_g e^{\frac{4890.55}{T_{m,abs}(x_j, t_n)}}} \right] \frac{1}{\Delta t} \right\} \\
& \times T_{m,abs}(x_j, t_n) \\
& + \left\{ \frac{c\gamma_{max}}{(\varphi - c\varphi + c)^2} \left[ \frac{9.28 \times 10^{-9} W_m(x_j, t_n) \rho_g e^{\frac{4890.55}{T_{m,abs}(x_j, t_n)}}}{4.54 \times 10^{-5} W_m(x_j, t_n) \rho_g e^{\frac{4890.55}{T_{m,abs}(x_j, t_n)}}} \right] \frac{-1}{\Delta t} \right\} \\
& \times T_{m,abs}(x_j, t_{n+1}) \\
& + \frac{h_m}{\delta_d \rho_d} W_g(x_j, t_n)
\end{aligned}$$

## APPENDIX B. TRNSYS MODEL DEMONSTRATION

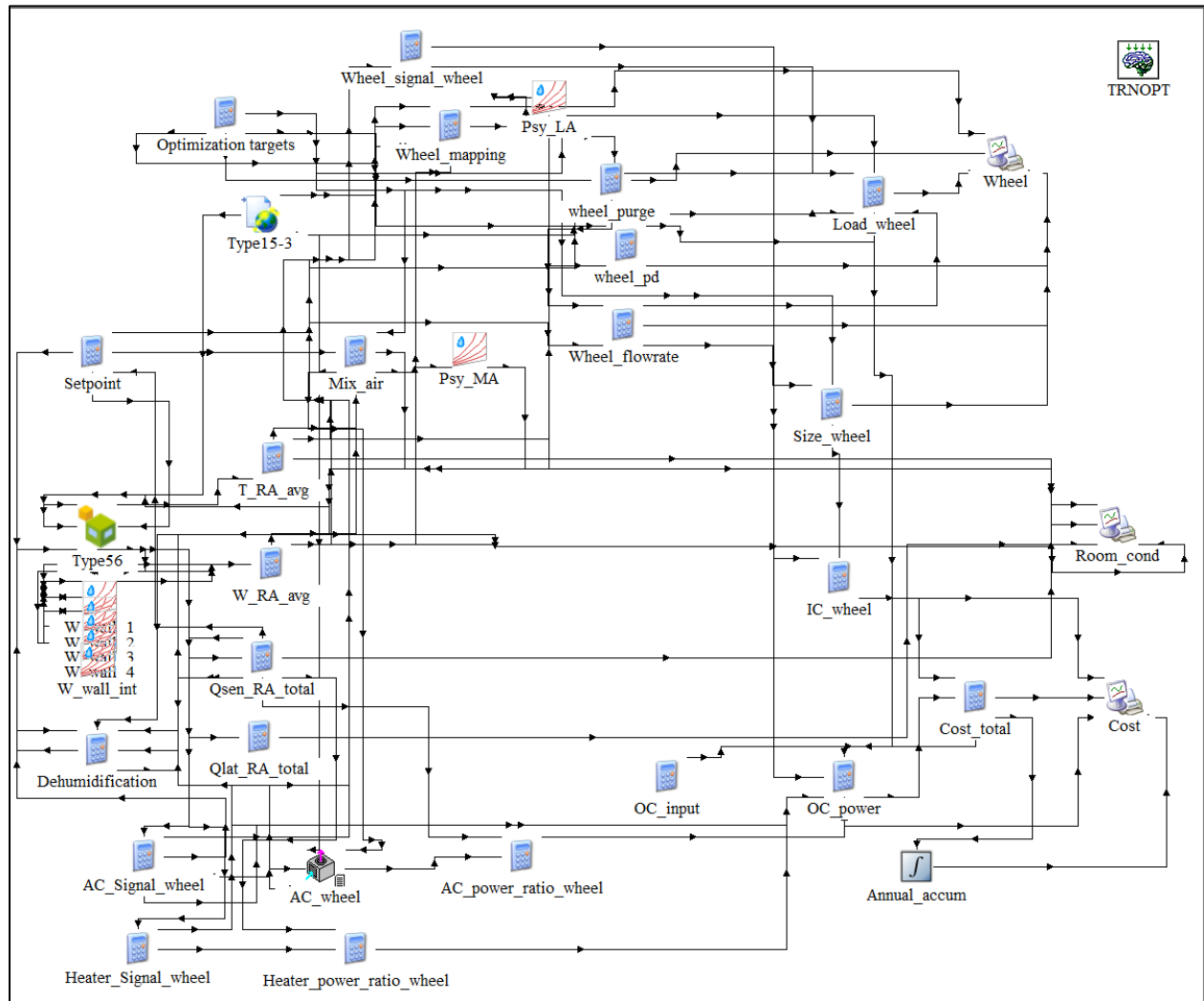
The following figure shows the TRNSYS model for the small office reference building with the conventional vapor-compression HVAC system for the baseline case study.



The following table illustrates the key modules and their functions in the small office reference building baseline HVAC model.

Module Name	Function Description
Type 15-3	Read weather data
Type 56	Communicate with building model
W_wall_1, 2, 3, 4, int	Calculate air conditions of each thermal zone
Mix_air	Calculate mix air conditions
T_RA_avg	Calculate overall return air temperature
W_RA_avg	Calculate overall return air humidity ratio
Qsen_RA_total	Calculate total sensible load of five thermal zones
Qlat_RA_total	Calculate total latent load of five thermal zones
AC_original (Type 921)	Simulate a signal speed A/C
AC_ratio_original	Ratio A/C power consumption
Heater_power_ratio_original	Ratio heater power consumption
Dehumidification	Calculate the dehumidification capacity provided by A/C
OC_power	Calculate operating power consumptions
Cost_total	Calculate operating costs

The following figure shows the TRNSYS model for the small office reference building with the wheel integrated HVAC system for the energy recovery wheel case study.



The following table illustrates the key modules and their functions in the small office reference building wheel integrated HVAC model.

Module Name	Function Description
Type 15-3	Read weather data
Type 56	Communicate with building model
W_wall_1, 2, 3, 4, int	Calculate air conditions of each thermal zone
Mix_air	Calculate mix air conditions
T_RA_avg	Calculate overall return air temperature
W_RA_avg	Calculate overall return air humidity ratio
Qsen_RA_total	Calculate total sensible load of five thermal zones
Qlat_RA_total	Calculate total latent load of five thermal zones
AC_wheel (Type 921)	Simulate a signal speed A/C
AC_ratio_wheel	Ratio A/C power consumption
Heater_power_ratio_wheel	Ratio heater power consumption
Dehumidification	Calculate the dehumidification capacity provided by A/C
OC_power	Calculate operating power consumptions
Cost_total	Calculate total cost (operating cost & initial cost)
Optimization_targets	Input wheel information
Wheel_mapping	Simulate wheel performance by the mapping method
Wheel_purge	Calculate wheel purge section
Wheel_pd	Calculate air pressure drop across the wheel
Wheel_flowrate	Calculate supply airflow rate for the wheel
Size_wheel	Calculate equivalent wheel diameter
IC_wheel	Calculate the initial cost of the wheel
Annual_accum	Calculate accumulated operating cost and averaged initial cost over the study period (1 year)
TRNOPT	Communicate between TRNSYS and GenOpt

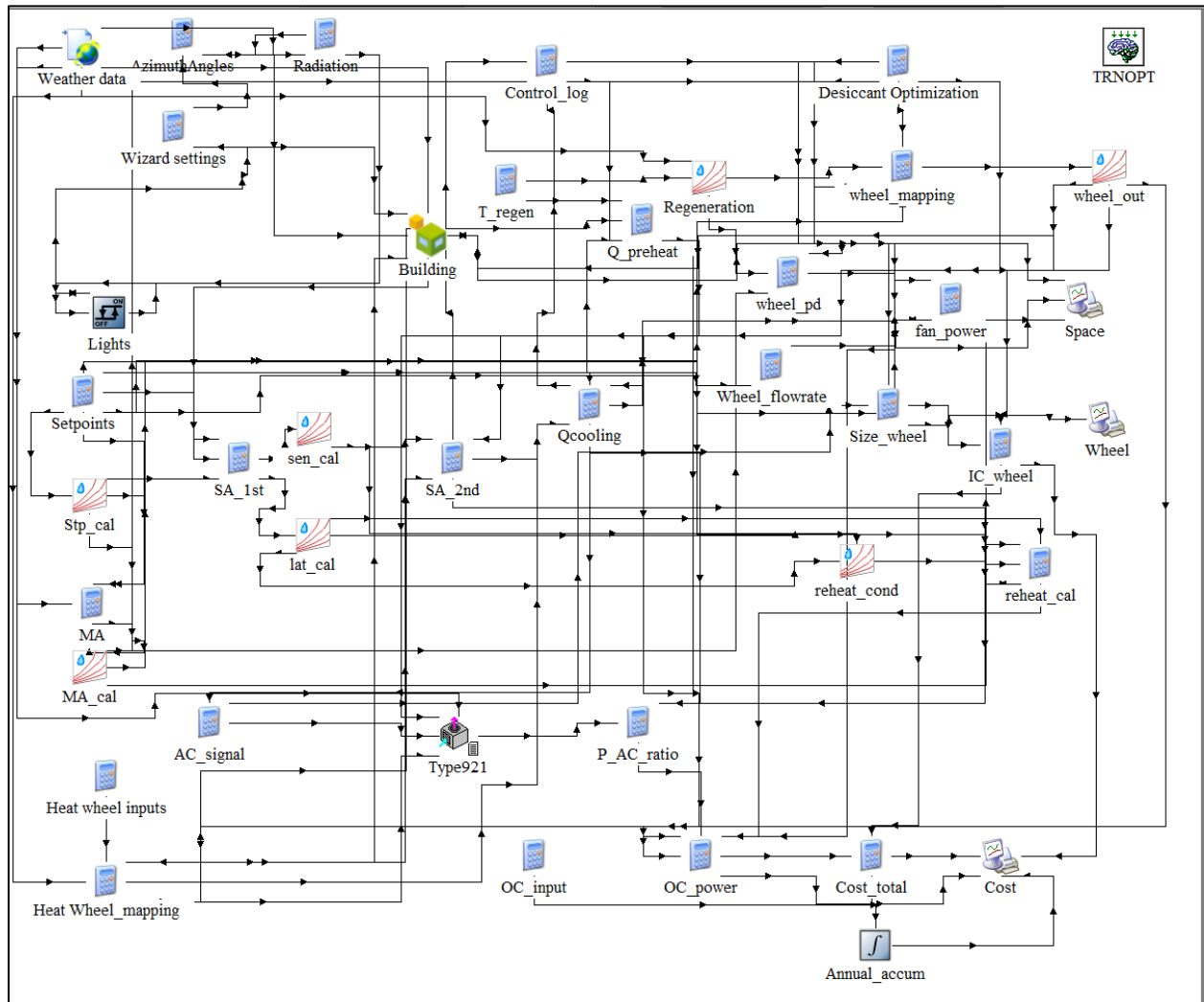




The following table illustrates the key modules and their functions in the dry storage of supermarket reference building baseline HVAC model.

Module Name	Function Description
Weather data	Read weather data
Building	Communicate with building model
SA	Calculate required supply air condition
MA	Calculate mix air conditions
sen_cal	Calculate required supply air condition for sensible load
lat_cal	Calculate required supply air condition for latent load
Qcooling_determine	Determine if overcooling-reheating process required
Reheat_cal	Calculate reheating power consumption
Type 921	Simulate a signal speed A/C
P_AC_ratio	Ratio A/C power consumption
OC_power	Calculate operating power consumptions
Cost_total	Calculate operating costs

The following figure shows the TRNSYS model for the supermarket reference building with the wheel integrated HVAC system for the desiccant wheel case study.



The following table illustrates the key modules and their functions in the dry storage of supermarket reference building with the wheel integrated HVAC system for the desiccant wheel case study.

Module Name	Function Description
Weather data	Read weather data
Building	Communicate with building model
SA_1st	Calculate required supply air condition
SA_2nd	Calculate required supply air condition with wheel outlet condition
MA	Calculate mix air conditions
sen_cal	Calculate required supply air condition for sensible load
lat_cal	Calculate required supply air condition for latent load
Qcooling_determine	Determine if overcooling-reheating process required
Q_preheat	Calculate preheating power consumption
Reheat_cal	Calculate reheating power consumption
Type 921	Simulate a signal speed A/C
P_AC_ratio	Ratio A/C power consumption
OC_power	Calculate operating power consumptions
Cost_total	Calculate operating costs
Desiccant_optimization	Input wheel information
wheel_mapping	Simulate desiccant wheel performance by the mapping method
wheel_pd	Calculate air pressure drop across the wheel
wheel_flowrate	Calculate supply airflow rate for the wheel
Size_wheel	Calculate equivalent wheel diameter
IC_wheel	Calculate the initial cost of the wheel
Heat Wheel_mapping	Simulate heat wheel performance by the mapping method
Annual_accum	Calculate accumulated operating cost and averaged initial cost over the study period (1 year)
TRNOPT	Communicate between TRNSYS and GenOpt

## REFERENCES

- [1] U.S. Energy Information Administration (2017), Annual Energy Outlook 2017, 101-114.
- [2] ANSI/ASHRAE/IES Standard (2016), 90.1-2016 Energy Standard for Buildings Except Low-Rise Residential Buildings, 101-103.
- [3] ANSI/ASHRAE Standard (2016), 62.1-2016 The Standards for Ventilation and Indoor Air Quality, 13-16.
- [4] Resources, e-M. (n.d.). Retrieved from <http://www.trnsys.com/index.html>
- [5] Peoples, J., Hung, Y., Horton, W. T., Ruan, X. (2020), Novel radiative Cooling, prepared to publish
- [6] AHRI Standard (2013), 1060 Performance Rating of Air-to-Air Exchangers for Energy Recovery Ventilation Equipment, 1-3, 9.
- [7] Zhai, C., Archer, D. H., & Fischer, J. C. (2008). Performance Modeling of Desiccant Wheels: 1 — Model Development. ASME 2008 2nd International Conference on Energy Sustainability, 18-53. doi:10.1115/es2008-54185
- [8] Simonson, C. J., & Besant, R. W. (1998). Heat and Moisture Transfer in Energy Wheels During Sorption, Condensation, and Frosting Conditions. *Journal of Heat Transfer*, 120(3), 699–708. doi: 10.1115/1.2824339
- [9] Ge, T. S., Li, Y., Wang, R. Z., & Dai, Y. J. (2008). A review of the mathematical models for predicting rotary desiccant wheel. *Renewable and Sustainable Energy Reviews*, 12(6), 1485–1528. doi:10.1016/j.rser.2007.01.012
- [10] Angrisani, G., Minichiello, F., Roselli, C., & Sasso, M. (2011). Experimental investigation to optimise a desiccant HVAC system coupled to a small size cogenerator. *Applied Thermal Engineering*, 31(4), 506–512. doi: 10.1016/j.applthermaleng.2010.10.006
- [11] Uçkan, I., Yılmaz, T., Hürdoğan, E., & Büyükalaca, O. (2013). Experimental investigation of a novel configuration of desiccant based evaporative air conditioning system. *Energy Conversion and Management*, 65, 606–615. doi: 10.1016/j.enconman.2012.09.014
- [12] Kang, H., & Lee, D.-Y. (2017). Experimental investigation and introduction of a similarity parameter for characterizing the heat and mass transfer in polymer desiccant wheels. *Energy*, 120, 705–717. doi: 10.1016/j.energy.2016.11.122

- [13] Eicker, U., Schürger, U., Köhler, M., Ge, T., Dai, Y., Li, H., & Wang, R. (2012). Experimental investigations on desiccant wheels. *Applied Thermal Engineering*, 42, 71–80. doi: 10.1016/j.applthermaleng.2012.03.005
- [14] Angrisani, G., Minichiello, F., Roselli, C., & Sasso, M. (2012). Experimental analysis on the dehumidification and thermal performance of a desiccant wheel. *Applied Energy*, 92, 563–572. doi: 10.1016/j.apenergy.2011.11.071
- [15] Enteria, N., Yoshino, H., Satake, A., Mochida, A., Takaki, R., Yoshie, R., ... Baba, S. (2010). Experimental heat and mass transfer of the separated and coupled rotating desiccant wheel and heat wheel. *Experimental Thermal and Fluid Science*, 34(5), 603–615. doi: 10.1016/j.expthermflusci.2009.12.001
- [16] Goldsworthy, M., & White, S. (2011). Optimisation of a desiccant cooling system design with indirect evaporative cooler. *International Journal of Refrigeration*, 34(1), 148–158. doi: 10.1016/j.ijrefrig.2010.07.005
- [17] Angrisani, G., Roselli, C., & Sasso, M. (2013). Effect of rotational speed on the performances of a desiccant wheel. *Applied Energy*, 104, 268–275. doi: 10.1016/j.apenergy.2012.10.051
- [18] Cao, T., Lee, H., Hwang, Y., Radermacher, R., & Chun, H.-H. (2014). Experimental investigations on thin polymer desiccant wheel performance. *International Journal of Refrigeration*, 44, 1–11. doi: 10.1016/j.ijrefrig.2014.05.004
- [19] Zendehboudi, A., & Esmaeili, H. (2015). Effect of supply/regeneration section area ratio on the performance of desiccant wheels in hot and humid climates: an experimental investigation. *Heat and Mass Transfer*, 52(6), 1175–1181. doi: 10.1007/s00231-015-1620-5
- [20] Zendehboudi, A., Angrisani, G., & Li, X. (2018). Parametric studies of silica gel and molecular sieve desiccant wheels: Experimental and modeling approaches. *International Communications in Heat and Mass Transfer*, 91, 176–186. doi: 10.1016/j.icheatmasstransfer.2017.12.002
- [21] Tu, R., & Hwang, Y. (2018). Efficient configurations for desiccant wheel cooling systems using different heat sources for regeneration. *International Journal of Refrigeration*, 86, 14–27. doi: 10.1016/j.ijrefrig.2017.12.001
- [22] Chung, J. D. (2016). Modeling and Analysis of Desiccant Wheel. *Desiccant Heating, Ventilating, and Air-Conditioning Systems*, 11–62. doi:10.1007/978-981-10-3047-5\_2
- [23] Van Den Bulck, E., Mitchell, J. W., & Klein, S. A. (1985). Design theory for rotary heat and mass exchangers—I. Wave analysis of rotary heat and mass exchangers with infinite transfer coefficients. *International Journal of Heat and Mass Transfer*, 28(8), 1575–1586. doi:10.1016/0017-9310(85)90259-5

- [24] Beccali, M., Butera, F., Guanella, R., & Adhikari, R. S. (2002). Simplified models for the performance evaluation of desiccant wheel dehumidification. *International Journal of Energy Research*, 27(1), 17–29. doi:10.1002/er.856
- [25] De Antonellis, S., Intini, M., Joppolo, C., & Leone, C. (2014). Design Optimization of Heat Wheels for Energy Recovery in HVAC Systems. *Energies*, 7(11), 7348–7367. doi:10.3390/en7117348
- [26] De Antonellis, S., Joppolo, C. M., & Molinaroli, L. (2010). Simulation, performance analysis and optimization of desiccant wheels. *Energy and Buildings*, 42(9), 1386–1393. doi:10.1016/j.enbuild.2010.03.007
- [27] Parmar, H., & Hindoliya, D. (2011). Artificial neural network based modelling of desiccant wheel. *Energy and Buildings*, 43(12), 3505–3513. doi: 10.1016/j.enbuild.2011.09.016
- [28] Koronaki, I., Rogdakis, E., & Kakatsiou, T. (2012). Thermodynamic analysis of an open cycle solid desiccant cooling system using Artificial Neural Network. *Energy Conversion and Management*, 60, 152–160. doi: 10.1016/j.enconman.2012.01.022
- [29] Jani, D., Mishra, M., & Sahoo, P. (2016). Performance prediction of rotary solid desiccant dehumidifier in hybrid air-conditioning system using artificial neural network. *Applied Thermal Engineering*, 98, 1091–1103. doi: 10.1016/j.applthermaleng.2015.12.112
- [30] Yamaguchi, S., & Saito, K. (2013). Numerical and experimental performance analysis of rotary desiccant wheels. *International Journal of Heat and Mass Transfer*, 60, 51–60. doi: 10.1016/j.ijheatmasstransfer.2012.12.036
- [31] Antonellis, S. D., Intini, M., & Joppolo, C. M. (2015). Desiccant wheels effectiveness parameters: Correlations based on experimental data. *Energy and Buildings*, 103, 296–306. doi: 10.1016/j.enbuild.2015.06.041
- [32] Zendehboudi, A. (2016). Implementation of GA-LSSVM modelling approach for estimating the performance of solid desiccant wheels. *Energy Conversion and Management*, 127, 245–255. doi: 10.1016/j.enconman.2016.08.070
- [33] Panaras, G., Mathioulakis, E., Belessiotis, V., & Kyriakis, N. (2010). Experimental validation of a simplified approach for a desiccant wheel model. *Energy and Buildings*, 42(10), 1719–1725. doi: 10.1016/j.enbuild.2010.05.006
- [34] Zendehboudi, A., & Li, X. (2018). Desiccant-wheel optimization via response surface methodology and multi-objective genetic algorithm. *Energy Conversion and Management*, 174, 649–660. doi: 10.1016/j.enconman.2018.07.078

- [35] Comino, F., Guijo-Rubio, D., Adana, M. R. D., & Hervás-Martínez, C. (2019). Validation of multitask artificial neural networks to model desiccant wheels activated at low temperature. *International Journal of Refrigeration*, 100, 434–442. doi: 10.1016/j.ijrefrig.2019.02.002
- [36] Kodama, A., Hirayama, T., Goto, M., Hirose, T., & Critoph, R. (2001). The use of psychrometric charts for the optimisation of a thermal swing desiccant wheel. *Applied Thermal Engineering*, 21(16), 1657–1674. doi: 10.1016/s1359-4311(01)00032-1
- [37] Chung, J. D., Lee, D.-Y., & Yoon, S. M. (2009). Optimization of desiccant wheel speed and area ratio of regeneration to dehumidification as a function of regeneration temperature. *Solar Energy*, 83(5), 625–635. doi: 10.1016/j.solener.2008.10.011
- [38] Antonellis, S. D., Joppolo, C. M., & Molinaroli, L. (2010). Simulation, performance analysis and optimization of desiccant wheels. *Energy and Buildings*, 42(9), 1386–1393. doi: 10.1016/j.enbuild.2010.03.007
- [39] Ge, T., Ziegler, F., & Wang, R. (2010). A mathematical model for predicting the performance of a compound desiccant wheel (A model of compound desiccant wheel). *Applied Thermal Engineering*, 30(8-9), 1005–1015. doi: 10.1016/j.applthermaleng.2010.01.012
- [40] LAKSHMINARAYANAN, R., & HAJI-SHEIKH, A. (1992). Entrance heat transfer in isosceles and right triangular ducts. *Journal of Thermophysics and Heat Transfer*, 6(1), 167–171. doi:10.2514/3.336
- [41] Haji-Sheikh, A. (2009). Determination of Heat Transfer in Ducts With Axial Conduction by Variational Calculus. *Journal of Heat Transfer*, 131(9), 091702. doi:10.1115/1.3122776
- [42] Narayanan, R., Saman, W. Y., & White, S. D. (2013). A non-adiabatic desiccant wheel: Modeling and experimental validation. *Applied Thermal Engineering*, 61(2), 178–185. doi:10.1016/j.applthermaleng.2013.07.007
- [43] Ruivo, C. R., Costa, J. J., & Figueiredo, A. R. (2006). Analysis of Simplifying Assumptions for the Numerical Modeling of the Heat and Mass Transfer in a Porous Desiccant Medium. *Numerical Heat Transfer, Part A: Applications*, 49(9), 851–872. doi:10.1080/10407780500483552
- [44] Yadav, A., & Yadav, L. (2014). Comparative performance of desiccant wheel with effective and ordinary regeneration sector using mathematical model. *Heat and Mass Transfer*, 50(10), 1465–1478. doi:10.1007/s00231-014-1349-6
- [45] Chung, J. D., & Lee, D.-Y. (2009). Effect of desiccant isotherm on the performance of desiccant wheel. *International Journal of Refrigeration*, 32(4), 720–726. doi:10.1016/j.ijrefrig.2009.01.003



- [46] Yadav, L., & Yadav, A. (2016). Mathematical investigation of purge sector angle for clockwise and anticlockwise rotation of desiccant wheel. *Applied Thermal Engineering*, 93, 839–848. doi:10.1016/j.applthermaleng.2015.10.062
- [47] Ruan, W., Qu, M., & Horton, W. T. (2012). Modeling analysis of an enthalpy recovery wheel with purge air. *International Journal of Heat and Mass Transfer*, 55(17-18), 4665–4672. doi: 10.1016/j.ijheatmasstransfer.2012.04.025
- [48] Esfandiari Nia, F., & van Paassen, D. (2006). Application of Desiccant Adsorption for Air-Conditioning Cycle. 4th International Energy Conversion Engineering Conference and Exhibit (IECEC). doi:10.2514/6.2006-4159
- [49] Jia, C. X., Dai, Y. J., Wu, J. Y., & Wang, R. Z. (2007). Use of compound desiccant to develop high performance desiccant cooling system. *International Journal of Refrigeration*, 30(2), 345–353. doi:10.1016/j.ijrefrig.2006.04.001
- [50] Nia, F. E., van Paassen, D., & Saidi, M. H. (2006). Modeling and simulation of desiccant wheel for air conditioning. *Energy and Buildings*, 38(10), 1230–1239. <https://doi.org/10.1016/j.enbuild.2006.03.020>
- [51] Ruivo, C. R., Carrillo-Andrés, A., Costa, J. J., & Domínguez-Muñoz, F. (2013). A new approach to the effectiveness method for the simulation of desiccant wheels with variable inlet states and airflows rates. *Applied Thermal Engineering*, 58(1-2), 670–678. <https://doi.org/10.1016/j.applthermaleng.2011.12.052>
- [52] Comino, F, Ruiz de Adana, M, & Peci, F. (2018). Energy saving potential of a hybrid HVAC system with a desiccant wheel activated at low temperatures and an indirect evaporative cooler in handling air in buildings with high latent loads. *Applied Thermal Engineering*, 131, 412-427. <https://doi.org/10.1016/j.applthermaleng.2017.12.004>
- [53] Aili, A., Zhao, D., Lu, J., Zhai, Y., Yin, X., Tan, G., & Yang, R. (2019). A kW-scale, 24-hour continuously operational, radiative sky cooling system: Experimental demonstration and predictive modeling. *Energy Conversion and Management*, 186, 586–596. doi: 10.1016/j.enconman.2019.03.006
- [54] Ali, A. H. H. (2013). Desiccant enhanced nocturnal radiative cooling-solar collector system for air comfort application in hot arid areas. *Sustainable Energy Technologies and Assessments*, 1, 54–62. doi: 10.1016/j.seta.2013.01.003
- [55] Eicker, U., & Dalibard, A. (2011). Photovoltaic–thermal collectors for night radiative cooling of buildings. *Solar Energy*, 85(7), 1322–1335. doi: 10.1016/j.solener.2011.03.015
- [56] Goldstein, E. A., Raman, A. P., & Fan, S. (2017). Sub-ambient non-evaporative fluid cooling with the sky. *Nature Energy*, 2(9). doi: 10.1038/nenergy.2017.143
- [57] Hanif, M., Mahlia, T., Zare, A., Saksahdan, T., & Metselaar, H. (2014). Potential energy savings by radiative cooling system for a building in tropical climate. *Renewable and Sustainable Energy Reviews*, 32, 642–650. doi: 10.1016/j.rser.2014.01.053

- [58] Wang, W., Fernandez, N., Katipamula, S., & Alvine, K. (2018). Performance assessment of a photonic radiative cooling system for office buildings. *Renewable Energy*, 118, 265–277. doi: 10.1016/j.renene.2017.10.062
- [59] Zhang, K., Zhao, D., Yin, X., Yang, R., & Tan, G. (2018). Energy saving and economic analysis of a new hybrid radiative cooling system for single-family houses in the USA. *Applied Energy*, 224, 371–381. doi: 10.1016/j.apenergy.2018.04.115
- [60] Commercial Reference Buildings. (n.d.). Retrieved from <https://www.energy.gov/eere/buildings/commercial-reference-buildings>
- [61] Wikimedia Foundation. (2021, April 21). COVID-19. Wikipedia. <https://en.wikipedia.org/wiki/COVID-19>.
- [62] Centers for Disease Control and Prevention. (n.d.). *Workplaces and Businesses*. Centers for Disease Control and Prevention. <https://www.cdc.gov/coronavirus/2019-ncov/community/workplaces-businesses/index.html>.
- [63] Centers for Disease Control and Prevention. (n.d.). *Ventilation in Buildings*. Centers for Disease Control and Prevention. <https://www.cdc.gov/coronavirus/2019-ncov/community/ventilation.html>.
- [64] National Renewable Energy Laboratory. (2011). U.S. Department of Energy commercial reference building models of the national building stock (NREL/TP ; 5500-46861). Golden, CO: National Renewable Energy Laboratory.
- [65] Wilcox, S., Marion, W., & National Renewable Energy Laboratory. (2008). Users manual for TMY3 data sets (Rev. May 2008. ed., NREL/TP ; 581-43156). Golden, Colo.: National Renewable Energy Laboratory.
- [66] Lewis, L.D. (2005). The Florida State University Ringling Conservation Center [Senior Thesis, Pennsylvania State University]. [https://www.engr.psu.edu/ae/thesis/portfolios/2005/ldl127/ldl127FinalReport\\_files/Full%20Report.pdf](https://www.engr.psu.edu/ae/thesis/portfolios/2005/ldl127/ldl127FinalReport_files/Full%20Report.pdf)
- [67] U.S. Energy Information Administration - EIA - Independent Statistics and Analysis. State Electricity Profiles - Energy Information Administration. (n.d.). <https://www.eia.gov/electricity/state/>.
- [68] U.S. Department of Agriculture Food - Safety and Inspection Service. Home | Food Safety and Inspection Service. (n.d.). <https://www.fsis.usda.gov/>

# PUBLICATION

## Semi-empirical mapping method for energy recovery wheel performance simulation

<https://doi.org/10.1016/j.ijrefrig.2020.10.018>

International Journal of Refrigeration 123 (2021) 102–110



Contents lists available at ScienceDirect

International Journal of Refrigeration

journal homepage: [www.elsevier.com/locate/ijrefrig](http://www.elsevier.com/locate/ijrefrig)



## Semi-empirical mapping method for energy recovery wheel performance simulation



Yu-Wei Hung, W. Travis Horton\*

Lyles School of Civil Engineering, Purdue University, 550 Stadium Mall Drive, West Lafayette, IN 47907-2029, USA

### ARTICLE INFO

**Article history:**  
Received 8 May 2020  
Revised 9 October 2020  
Accepted 10 October 2020  
Available online 14 October 2020

**Keywords:**  
Energy recovery wheel  
Finite difference model  
Empirical equation  
Heat and mass transfer

### ABSTRACT

Energy recovery ventilators are often employed in buildings to decrease the energy consumed by their HVAC systems, and to improve overall indoor air quality. Several studies in the open literature have developed physical or empirical models to simulate the performance of energy recovery wheels. However, these models are often computationally intensive, time-consuming, or require numerous experimental data points to train and execute the performance predictions. These models also tend to lack flexibility for varying all of the available wheel design parameters. Hence, developing a mapping method with better computational efficiency and flexibility is the goal of this research. A finite difference numerical model for simulating the performance of an energy wheel has been developed and validated using experimental test results from independent laboratories. This model was then employed to provide an extensive data set for the development of an energy wheel performance mapping method. After validating this new mapping approach, the method predictions were compared against independent data sets from two different laboratories, and additional sources available in the literature, to identify its universality. The mapping method delivers good agreement between the predictions and validation data, and requires only a small number of data points to train, which is one of its novel contributions. Another unique contribution of the proposed mapping method is that once the model is trained it can predict the performance characteristics for other wheels with different physical design geometries and operating conditions, provided only that the desiccant material is the same.

© 2020 Elsevier Ltd and IIR. All rights reserved.

## Méthode de cartographie semi-empirique pour la simulation des performances des roues de récupération d'énergie

**Mots-clés:** Roue de récupération d'énergie; Modèle des différences finies; Équation empirique; Transferts de chaleur et de masse

### Introduction

#### Background

The U.S. Energy Information Administration 2017 Annual Energy Outlook reports that energy use from heating, ventilation, and air conditioning (HVAC) systems represents about 30% of the total building energy consumption among U.S. commercial buildings. Traditional vapor-compression refrigeration systems contribute to

environmental impacts in different ways; first of all, the HCFC and HFC refrigerants used in these systems are ozone-depleting and/or global warming substances; and lastly, refrigeration systems consume a high portion of the energy that is generated by fossil fuels. As widely acknowledged, fossil fuel combustion releases polluting chemicals, such as Carbon Monoxide (CO), Nitrogen Oxides (NO<sub>x</sub>) and Sulfur Oxides (SO<sub>x</sub>), which have harmful effects on human health, in addition to Carbon Dioxide (CO<sub>2</sub>), which is considered as the baseline measure against which other greenhouse gases are compared (U.S. Energy Information Administration 2017).

The integration of energy recovery ventilators (ERV's) into HVAC systems presents an opportunity to reduce the impact of these systems on the environment. Energy recovery ventilation is a method

\* Corresponding author.  
E-mail address: [whorton@purdue.edu](mailto:whorton@purdue.edu) (W. Travis Horton).

## Nomenclature

$c$	Separation factor, $u1$
$C_p$	Specific heat, $J/kg \cdot K$
$d_h$	Hydraulic diameter, $m$
$h$	Convective heat transfer coefficient, $W/m^2 \cdot K$
$h_m$	Convective mass transfer coefficient, $kg/m^2 \cdot s$
$L$	Wheel depth, $m$
$\dot{m}$	Air mass flow rate, $kg/s$
$t$	Time, $sec$
$T$	Temperature, $^{\circ}C$ or $K$
$u$	Air face velocity, $m/s$
$W$	Humidity ratio (water vapor (dry air) $^{-1}$ ), $kg/kg$

## Greek Letters

$\gamma_d$	Moisture loading in desiccant composite, $kg/kg$
$\gamma_{max}$	Maximum moisture loading in desiccant composite, $kg/kg$
$\Delta H_{ads}$	Heat of adsorption, $J/kg$
$\rho$	Density, $kg/m^3$

## Footnotes

$d$	Wheel desiccant
$g$	Wet air
$m$	Wheel matrix
RPM	Wheel rotation speed
EA	Exhausted air
OA	Outdoor air
RA	Return air
SA	Supply air

of harvesting the energy (both sensible and latent) contained in exhaust air leaving a building or space, and recycling its energy content to pre-condition the outdoor air entering the building or space. Therefore, the appropriate application of ERV's has the potential to significantly reduce the energy consumed by building HVAC systems. ERV systems can be implemented in residential buildings, commercial buildings, and industrial facilities. ASHRAE 90.1, which is the generally accepted building design and construction standard for energy efficiency, presents the appropriate specifications for ERV systems that can assist to achieve those goals (ANSI/ASHRAE/IES Standard 2016).

An energy recovery "wheel" is a type of ERV. Energy recovery wheels are typically made from materials that exhibit a good balance between thermal conductivity, thermal mass, structural strength, and weight (typically Aluminum), with the addition of a desiccant coating to address latent energy transport. The physical construction of a wheel is similar to that of a long strip of cardboard that has been rolled-up into a wheel, where the corrugated channels form passages that air can travel through. The wheel generally operates by rotating through a supply air stream and an exhaust air stream as shown schematically in Fig. 1. The energy recovery wheel collects energy (both sensible and latent) from the return air and utilizes it to pre-condition the incoming outdoor air.

## Literature review

The concept of implementing a thermal wheel was introduced by Fredrik Ljungström in 1920. Abundant research and development activities have been dedicated to understanding thermal wheel physical behavior and analyzing and optimizing their design for nearly a century. Simonson and Besant (1998) developed a new approach to solving the governing equations for energy wheels. The governing equations, which are dependent on the enthalpy and relative humidity of the air and the desiccant, were modified

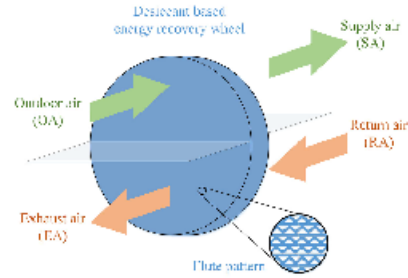


Fig. 1. Desiccant based energy recovery wheel's working theory.

to depend on the temperature and humidity ratio of the air and the desiccant. Furthermore, in Simonson's approach, the governing equations were decoupled; hence, they can be solved separately to simplify the finite difference model solution process. Simonson's governing equations have been widely utilized in research throughout the years.

Ge et al. (2008) compared different mathematical models that have been developed for performance predictions of energy recovery wheels and desiccant wheels. The paper categorizes models based on assumptions, governing equations, and solution methods; and sorts the models into two major types: gas-side resistance (GSR) models and gas and solid-side resistance (GSSR) models. In the GSR model approach, heat and mass diffusion within the desiccant material itself is not considered, but heat conduction within the substrate is included. The temperature and humidity ratio within the desiccant from the surface layer to the inner layer are assumed identical. The GSR model compromises accuracy for relatively simple governing equations that can be solved more quickly. The GSSR mathematical model includes second-order heat and mass transfer terms within the desiccant in the governing equations, which refines the precision of this model. However, while the GSSR model can offer a more accurate prediction of energy recovery wheel performance, the computational time is significantly longer.

Zhai et al. (2008) includes detailed information related to the numerical simulation settings for an energy recovery wheel and a desiccant wheel. Zhai's paper also presents physical parameters for an energy recovery wheel along with adsorption isotherms. This information can be utilized by other researchers to validate their energy recovery wheel or desiccant wheel numerical models.

Due to the complexity and time-consuming nature of solving the governing equations for an energy wheel, several studies in the literature have developed different types of algebraic efficiency factor methods. Van Den Bulck et al. (1985) proposed a solution to this problem by applying an effectiveness-number of transfer units ( $\epsilon$ -NTU) method to the governing equations. Beccali et al. (2002) established a simple and straightforward empirical model that can be used to estimate the performance of a desiccant wheel. Their model is known as "Model 54". An empirical equation which is further reduced in complexity was later invested by Beccali et al. (2002), which calculates the performance of a desiccant wheel via only four parameters, but their approach requires extensive data points for training to fully develop its prediction capabilities for a desiccant wheel. Annonellis et al. (2015) also developed efficiency parameters for desiccant wheel performance prediction. The outlet condition was estimated based on the efficiency of a wheel,

and the correlation between the model and the experimental data was identified. Panaras et al. (2010) introduced a model of a simplified efficiency factor to represent the performance of desiccant wheels based on Jurinak formulas. The efficiency factors developed by Panaras et al. (2010) only require a few measurements, so the model is easy to train.

Zendehboudi (2016) introduced a model via a support vector machine to predict the performance of desiccant wheels, and used a genetic algorithm to decrease simulation time. The model is a function of the following independent variables: wheel rotational speed, inlet air temperature, and inlet air humidity ratio of the process stream; and generates the following outputs: outlet air temperature and humidity ratio of the process stream and regeneration stream, moisture removal capacity, and sensible energy ratio. Other researchers have utilized artificial neural network (ANN) methods to map the performance prediction of energy wheels. Parmar and Hindolija (2011) implemented an ANN method to predict the outlet air temperature and humidity ratio in the process air stream. Koronaki et al. (2012) developed and trained a black box model via the ANN method. The key parameters of experimental data to predict state conditions of the air in the process and regeneration streams include process air inlet temperature, humidity ratio, and airflow rate; and regeneration air inlet temperature, humidity ratio, and airflow rate. Jani et al. (2016) introduced another ANN-based model for predicting the outlet conditions of temperature and humidity ratio in the process air stream. The ANN method approaches deliver accurate results, but require extensive data for the training process.

Different methodologies for performing energy wheel optimization studies have been proposed. De Antonellis et al. (2014 ; 2010) conducted optimization and parametric studies that were focused on maximizing the sensible effectiveness of an ERV while minimizing pressure drop under different inlet air conditions. An optimization of energy recovery wheels based on the artificial neural network (ANN) method was proposed by Comino et al. (2019). The author targets developing a model that predicts two outputs (air temperature and humidity ratio of the outlet process stream). The input layer contains the inlet air temperature/humidity ratio of the process stream and the regeneration stream, airflow rate, and rotational speed. However, the ANN model needs to be trained with a large amount of data that includes the full range of different physical dimensions to be considered. Zendehboudi and Li (2018) proposed a genetic algorithm for desiccant wheel optimization. Regeneration temperature, surface area ratio, rotational speed, and diameter are selected as the most influential design variables. In Zendehboudi's paper, quadratic equations that consist of four design variables represent the outlet temperature and humidity ratio for desiccant wheels. Nonetheless, not all physical dimensions or operating conditions of a wheel (e.g. wheel depth or rotational speed) were considered in this approach.

#### Objectives

Many of the methods outlined in the above studies tend to lack a general level of flexibility because they are not capable of predicting the performance characteristics when one or more of the physical dimensions of a wheel (e.g., wheel diameter, depth, or hydraulic diameter of a flute), or operating conditions (e.g., airflow rate or wheel rotational speed) are changed. If a design parameter or an operating setting of the energy recovery wheel changes, many of the models found in the current literature need to be recalculated or retrained with new experimental data to determine the new performance characteristics. For parametric studies involving different geometries of energy recovery wheels, this approach will take a significant amount of time to establish and run all of the necessary design perturbations, which makes the use of these

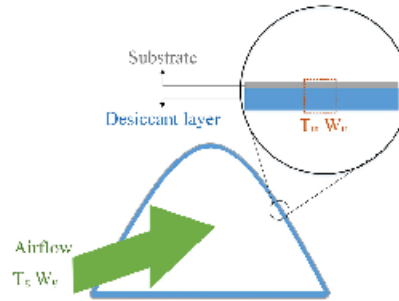


Fig. 2. Target variables in the flute of an energy recovery wheel.

existing models disadvantageous for carrying out extensive optimization studies.

The primary objective of this paper is to present the results of a research effort whose outcome has been the development of a novel algebraic mapping method that can rapidly and accurately predict the performance characteristics of a wide range of energy recovery wheels. Unlike previous mapping approaches, the model form in this paper is sufficiently flexible that it can predict the performance of energy wheels with different physical dimensions, including: wheel depth, wheel diameter, and flute dimensions; and under many different operating conditions, including, rotational speed, and airflow rate. A major benefit of the work presented in this paper is that the algebraic model can be trained with only a small number of data points, which significantly reduces the overhead associated with experimental testing to obtain the necessary data. The efforts spent on developing this mapping method have the potential to provide an effective, economical solution for optimization analyses and parametric studies of ERV's or ERV-integrated air handling units since the computational complexity of the model is significantly reduced.

#### Numerical model development and validation

##### Model development

Fig. 2 shows a close-up view of a single flute in an energy recovery wheel; and is illustrative for identifying the dependent variables of interest in predicting the performance characteristics of the wheel. The five target dependent variables, and their associated governing equations, in the model, are the air temperature  $T_e$ , matrix temperature  $T_m$ , absolute humidity of the air  $W_e$ , absolute humidity of the matrix  $W_m$ , and the moisture loading of the desiccant  $y_d$  (Zhai et al., 2008; Ge et al., 2008). The matrix is a combination of a thin air film on top of the desiccant together with the air in the desiccant layer. The desiccant on energy recovery wheels is thin (25 to 65 microns typically) and the Biot number is significantly smaller than 0.1 (Zhai et al., 2008), hence, a "lumped" temperature and humidity ratio in the matrix are assumed. The assumptions for simplifying the overall analysis are referred to as the gas-side resistance (GSR) model proposed by Zhai et al. (2008) and Ge et al. (2008).

There are four primary governing equations, which include an energy balance on the air Eq. (1); an energy balance on the matrix Eq. (2); a moisture mass balance on the air Eq. (3); and a moisture mass balance on the matrix Eq. (4). There are five un-



**Table 1.**  
Finite difference method representation for derivatives in the governing equations.

Derivative		Finite difference method representation	
1 <sup>st</sup> order time		$\frac{\partial P}{\partial t} = \frac{P(\Delta t, t_j) - P(\Delta t, t_{j-1})}{\Delta t}$	$P = T_p, T_m, W_p, W_m$
1 <sup>st</sup> order space	Entrance	$\frac{\partial Q}{\partial x} = \frac{-3Q(\Delta x, t_j) + 4Q(\Delta x, t_j) - Q(\Delta x, t_j)}{2\Delta x}$	$Q = T_p, W_p, W_m$
	Middle	$\frac{\partial Q}{\partial x} = \frac{Q(\Delta x, t_j) - 8Q(\Delta x, t_j) + 8Q(\Delta x, t_j) - Q(\Delta x, t_j)}{12\Delta x}$	
	Exit	$\frac{\partial Q}{\partial x} = \frac{Q(\Delta x, t_j) - 4Q(\Delta x, t_j) + 3Q(\Delta x, t_j)}{2\Delta x}$	
2 <sup>nd</sup> order space	Entrance	$\frac{\partial^2 R}{\partial x^2} = \frac{R(\Delta x, t_j) - 2R(\Delta x, t_j) + R(\Delta x, t_j)}{\Delta x^2}$	$R = T_m$
	Middle	$\frac{\partial^2 R}{\partial x^2} = \frac{R(\Delta x, t_j) - 2R(\Delta x, t_j) + R(\Delta x, t_j)}{\Delta x^2}$	
	Exit	$\frac{\partial^2 R}{\partial x^2} = \frac{R(\Delta x, t_j) - 2R(\Delta x, t_j) + R(\Delta x, t_j)}{\Delta x^2}$	

known variables in the energy wheel; however, there are only four primary governing equations. Therefore, one additional equation is introduced to close the problem formulation. Eq. (5) represents the general adsorption isotherm of the desiccant.

The finite difference numerical model is developed largely based on the procedures that are outlined in the work of Zhai et al. (2008), with the exception of the approach to calculating the convective heat transfer coefficient, which is described below. The general finite difference approach that is used in this work for converting the governing equations from differential equations to algebraic equations, which can be solved temporally and spatially, is shown in Table 1. According to Chung and Lee (2009), the author mentions that the Nusselt number of a triangular channel is similar to that of a sine-shaped channel. Local Nusselt number data for isosceles triangular ducts with various vertex angles are stated in the paper by Lakshminarayanan and Haji-Sheikh (1992), and the local Nusselt number for the energy wheel model in this current work is interpreted from the work of Lakshminarayanan. After the convective heat transfer coefficient is determined via a Nusselt number correlation, the convective mass transfer coefficient is calculated via the Lewis number, which is typically assumed as unity. A significant majority of the papers mentioned in the literature review also assume a Lewis of 1.0, including Zhai et al. (2008), De Annonellis et al. (2014; 2010), Narayanan et al. (2013), Yadav and Yadav (2016), Esfandiari Nia and van Paassen (2006).

$$\frac{\partial T_k}{\partial t} = \frac{h}{\rho_a \rho_k C_p k} (T_m - T_k) - u \frac{\partial T_k}{\partial x} \quad (1)$$

$$\frac{\partial T_m}{\partial t} = \frac{k_{ab}}{\rho_{ab} \delta_{ab} C_{pab}} \frac{\partial^2 T_m}{\partial x^2} + \frac{h_m \Delta H_{ads}}{\rho_{ab} \delta_{ab} C_{pab} + \rho_d \delta_d C_{pd}} (W_k - W_m) + \frac{h}{\rho_{ab} \delta_{ab} C_{pab} + \rho_d \delta_d C_{pd}} (T_g - T_m) \quad (2)$$

$$\frac{\partial W_k}{\partial t} = \frac{h_m}{\rho_a \rho_k} (W_m - W_k) - u \frac{\partial W_k}{\partial x} \quad (3)$$

$$\frac{\partial W_d}{\partial t} = \frac{h_m}{\rho_d \rho_d} (W_k - W_m) \quad (4)$$

$$\frac{W_d}{W_{max}} = \frac{1}{1 - c + \frac{c}{\varphi}} \quad (5)$$

$$\varphi = \frac{P_p}{P_{p, sat}} = 9.28 \times 10^{-9} W_m \rho_k T_{m, ads} e^{\frac{4890.55}{T_{m, ads}}}$$

Testing data

Experimental test data from energy recovery wheels of three different sizes are listed as the following (diameters: depth)

**Table 2.**  
Experimental conditions for wheels.

	Wheel 1	Wheel 2	Wheel 3
Inlet condition	Summer, winter	Summer	Summer
Air face velocity (ms <sup>-1</sup> )	1.5 - 2.0	1.8 - 2.7	1.8 - 3.4
Rotational speed (RPM)	25	21, 25	35
Sensible uncertainty (K)	0.43 to 0.73	-3 to 3	-3 to 3
Latent uncertainty (K)	1.33 to 1.53	-6 to 6	-6 to 6
Airflow rate uncertainty (%)	0.23 to 0.42	-4 to 4	-4 to 4

1.37:0.2, 1.04:0.1, 0.91:0.095 (m), and have been obtained from two separate laboratories; whose test facilities are both constructed according to the AHRI 1060 (Standard, 2013) testing standard. The experimental conditions that are specified by AHRI 1060 (Standard, 2013) include cooling season tests ( $T_{OA} = 35.0^\circ\text{C}$ ,  $W_{OA} = 0.016 \text{ kg}_{\text{water}}/\text{kg}_{\text{dryair}}$ ;  $T_{RA} = 23.9^\circ\text{C}$ ,  $W_{RA} = 0.009 \text{ kg}_{\text{water}}/\text{kg}_{\text{dryair}}$ ) and heating season tests ( $T_{OA} = 1.7^\circ\text{C}$ ,  $W_{OA} = 0.003 \text{ kg}_{\text{water}}/\text{kg}_{\text{dryair}}$ ;  $T_{RA} = 21.1^\circ\text{C}$ ,  $W_{RA} = 0.007 \text{ kg}_{\text{water}}/\text{kg}_{\text{dryair}}$ ). The experimental conditions for each of the different wheels that were tested are listed in Table 2. At one laboratory, the temperature sensors have  $\pm 0.26^\circ\text{C}$  of error; the relative humidity sensors have  $\pm 3\%$  of error; the airflow rate sensors have  $\pm 2\%$  of error. After propagating the measurement uncertainties through the appropriate performance calculations, the percentage uncertainty in sensible heat transfer measurements, the percentage uncertainty in the latent heat transfer measurements, the percentage uncertainty in airflow rate measurements of two laboratories are listed in Table 2.

Model validation

Fig. 3 presents two parity plots that are drawn to visualize the accuracy of the output temperature and absolute humidity results between the predictions of the finite difference model, developed by the authors, and the experimental data. The x-axis of Fig. 3(a) represents the difference, in the experimental tests, between the outdoor air temperature and the supply air temperature, while that of Fig. 3(b) shows the absolute humidity of the supply air leaving the energy recovery wheel. The y-axes in Fig. 3(a) and 3(b) show the corresponding predictions in the values of the temperature difference and absolute humidity, respectively, from the finite difference model. Each of the axes in Fig. 3 has been normalized by the maximum inlet and outlet air temperature difference, and maximum outlet air humidity ratio. A Nusselt number correction factor has been implemented in the code to adjust the convective heat transfer coefficient to improve the solution accuracy. A correction factor of 0.9 has been found to give satisfactory results across all of the simulations used in this research. The simulation results agree with the experimental test data to within  $\pm 10\%$ ; indicating that the energy recovery wheel model can deliver reasonable results that agree with actual performance.

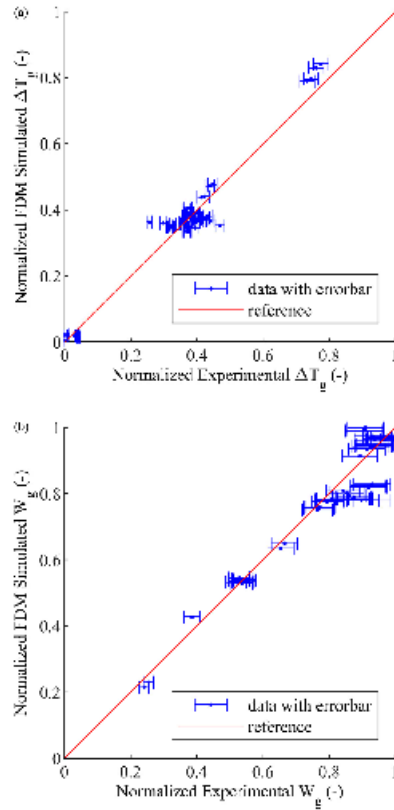


Fig. 3. (a) (b) Parity plots between laboratory data (x-axis) and FDM simulation results (y-axis).

#### Development of a mapping method

##### Mapping method form identification

Many studies discussed in the literature review section are devoted to establishing finite difference models (FDM) to predict the performance of a selected energy recovery wheel within a limited range of geometric parameters, such as, wheel diameter, wheel depth, or flute size; or operating conditions, such as, wheel rotation speed or airflow rate. Nonetheless, if a study wants to target another energy recovery wheel with different parameters, the model needs to be recalculated and validated under the new conditions. For parametric studies on energy recovery wheels with dif-

ferent geometries or operating settings, the work of training and validating the models for all the possible wheels will consume a tremendous amount of time. If another approach can accurately and quickly predict the performance of energy recovery wheels with different geometries or operating conditions, it will be beneficial for academic studies as well as research and development activities in the industry.

The physical processes of heat and mass transfer that occur in an energy recovery wheel involve complex transport phenomena, so using an FDM to simulate energy recovery wheel operation is complicated and time-consuming. To identify an appropriate form for a simple, algebraic mapping model, Buckingham's pi theorem was utilized in a first attempt to formulate a method to predict the wheel's performance, however, the outcome of this work demonstrated that the resulting dimensionless groups were not capable of accurately capturing the correct performance characteristics over a wide range of operating conditions and wheel geometries.

The next approach for identifying a potential model form was to look at basic efficiency and energy balance definitions that are used in current industry standards. Eq. (6) represents the efficiency of an energy recovery wheel as given in AHRI Standard 1060 "Performance Rating of Air-to-Air Exchangers for Energy Recovery Ventilation Equipment" (U.S. Energy Information Administration 2017; Standard, 2013).

$$\varepsilon = \frac{c_{OA}(X_{OA} - X_{RA})}{c_{RA}(X_{OA} - X_{RA})} \quad (6)$$

$$X = T_g \text{ or } W_g$$

$$c = C_p \rho \dot{m}_g$$

This equation was used as a preliminary basis to establish the mapping method. In AHRI 1060, the variable,  $c$ , is used to represent the capacity rate (the product of mass flow rate and specific heat) for each of the airstreams. Thus, the efficiency equation from AHRI 1060 can be written in the following form of Eqs. (7) and (8).

$$T_{g,RA} - T_{g,OA} = \varepsilon \frac{\dot{m}_{RA} C_{p,g}}{\dot{m}_{OA} C_{p,g}} (T_{g,OA} - T_{g,RA}) \quad (7)$$

$$W_{g,RA} - W_{g,OA} = \varepsilon_w \frac{\dot{m}_{RA} \Delta H_{\text{air}}}{\dot{m}_{OA} \Delta H_{\text{air}}} (W_{g,OA} - W_{g,RA}) \quad (8)$$

We can readily note that this form for the efficiency equations is similar to the air temperature and humidity governing equations that are shown in (1) & (3), so we will use this general form as a basis for developing a new mapping method. However, to finalize the form of the equation, the wheel rotational speed and wheel depth also need to be integrated. These two variables are important in developing an energy recovery wheel, because it is common to change the wheel rotational speed and the wheel depth to design a product that fits a specific application's requirements. Therefore, the authors felt it necessary that the effect of these two variables also be captured in the model form. Additionally, the hydraulic diameter of the flutes will influence the convective heat and mass transfer coefficients, so these coefficients will also be characterized in the mapping method by introducing the hydraulic diameter. If the energy wheel efficiency equation is combined in part with the AHRI 1060 efficiency Eqs. (7) and (8), and the governing Eqs. (1) and (3), then Eqs. (9) and (10) become general forms for the semi-empirical mapping method that are obtained.

$$T_{g,RA} - T_{g,OA} = \frac{h}{\rho_g L C_{p,g}} f(\text{SRM}) f(u_{OA}) f(L) \frac{u_{RA}}{u_{OA}} (T_{g,OA} - T_{g,RA}) \quad (9)$$

$$W_{g,RA} - W_{g,OA} = \frac{h_m}{\rho_g} f(\text{SRM}) f(u_{OA}) f(L) \frac{u_{RA}}{u_{OA}} (W_{g,OA} - W_{g,RA}) \quad (10)$$

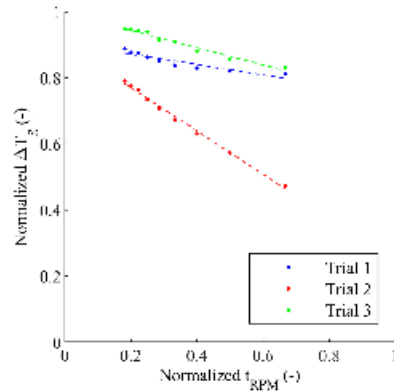


Fig. 4. Effect of the traveling time of a flume in one airstream on wheel performance.

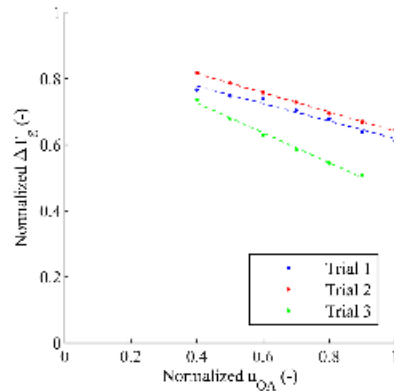


Fig. 5. Effect of the air face velocity on wheel performance.

The functions relating wheel performance to rotational speed,  $f(t_{RPM})$ , airflow rate,  $f(u_{OA})$ , and wheel depth,  $f(L)$ , need to be developed. By running the energy recovery wheel finite difference models, it is possible to isolate each variable and its effect on the performance results. Using this approach, one input variable is changed at a time while all other inputs remain fixed. The trend of influence on the changing variable can be observed and the results are then used to identify the form of an empirical function for that variable.

Figs. 4, 5, and 6 show the results of changing the different variables, including the traveling time of a flume in the airstream (which is a surrogate for wheel rotational speed), outdoor air face velocity, and wheel depth. By observing the resulting patterns, a

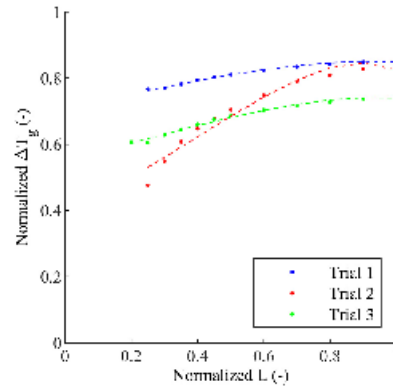


Fig. 6. Effect of the wheel depth on wheel performance.

general function format can be developed. First, the traveling time of a flume in one air stream is isolated. For easier observation, the traveling time of a flume in one air stream is moved to the left-hand side of the equation, and the rest of the terms are moved to the right-hand side. Then, the function is normalized by its maximum. Three trials were conducted. For each trial, all non-isolated variables (e.g.  $T_g$ ,  $W_g$ ,  $u$ ,  $d_g$ , etc.) are held constant, while the isolated variable is allowed to vary across its range. This same variable isolation process is also performed later for the outdoor air face velocity and the wheel depth.

The function that relates the traveling time of a flume in one airstream to the supply air temperature was observed to be substantially linear in each of the trials that were conducted, as clearly seen in Fig. 4, with regression  $R^2$ -values of 0.8607, 0.9951, and 0.9671. Therefore, a decision was made that the functional form relating the traveling time of a flume in the airstream should be represented by a linear function as shown in Eq. (11).

$$\frac{f(t_{RPM})}{f(t_{RPM})_{max}} = \frac{\frac{T_{g,OA} - T_{g,SA}}{T_{g,OA} - T_{g,SA}} \frac{u_{OA}}{u_{SA}} \frac{\rho_g C_p}{h} \frac{1}{f(u_{OA}) f(L)}}{\frac{(T_{g,OA} - T_{g,SA})_{max}}{(T_{g,OA} - T_{g,SA})_{max}} \frac{u_{OA}}{u_{SA}} \frac{\rho_g C_p}{h} \frac{1}{f(u_{OA}) f(L)}} = \frac{T_{g,OA} - T_{g,SA}}{(T_{g,OA} - T_{g,SA})_{max}} \quad (11)$$

Next, the air face velocity was isolated to determine the appropriate form of its function. The effect of the air face velocity on the supply air temperature was also shown in Fig. 5 to be substantially linear, with regression  $R^2$ -values of 0.9757, 0.9985, and 0.9925 for each of the trial cases studied. Therefore, the form of the air face velocity function was also selected to be a linear function as given in Eq. (12).

$$\frac{f(u_{OA})}{f(u_{OA})_{max}} = \frac{\frac{T_{g,OA} - T_{g,SA}}{T_{g,OA} - T_{g,SA}} \frac{u_{OA}}{u_{SA}} \frac{\rho_g C_p}{h} \frac{1}{f(t_{RPM}) f(L)}}{\frac{(T_{g,OA} - T_{g,SA})_{max}}{(T_{g,OA} - T_{g,SA})_{max}} \frac{u_{OA}}{u_{SA}} \frac{\rho_g C_p}{h} \frac{1}{f(t_{RPM}) f(L)}} = \frac{T_{g,OA} - T_{g,SA}}{(T_{g,OA} - T_{g,SA})_{max}} \frac{u_{OA}}{u_{SA}}$$



$$f(u_{OA}) = a_2 u_{OA} + b_2 \quad (12)$$

Finally, the wheel depth influence function was isolated for further investigation. Fig. 6 clearly shows that in each of the trial cases the effect of the wheel depth on the supply air temperature is not linear. Various approaches were investigated to identify an appropriate functional form to capture the relationship between wheel depth and wheel performance, including, polynomial, power, and exponential functions. A two-term exponential regression was found to consistently deliver the best approximation, exhibiting  $R^2$ -values of 0.9956, 0.9990, and 0.9914. Therefore, the appropriate form of the wheel depth influence function is shown in Eq. (13).

$$\frac{f(L)}{f(L)_{max}} = \frac{\frac{T_{E,OA} - T_{E,SA}}{(T_{E,OA} - T_{E,SA})_{max}} \frac{u_{OA}}{u_{RA}} \frac{\rho_R C_P}{h} \frac{1}{f(u_{OA}) f(t_{RM})}}{\frac{(T_{E,OA} - T_{E,SA})_{max}}{(T_{E,OA} - T_{E,SA})_{max}} \frac{u_{OA}}{u_{RA}} \frac{\rho_R C_P}{h} \frac{1}{(u_{OA}) f(t_{RM})}} = \frac{T_{E,OA} - T_{E,SA}}{(T_{E,OA} - T_{E,SA})_{max}} \quad (13)$$

The convective heat transfer coefficient for air flowing within a flute of the energy recovery wheel can be calculated, as shown in Eq. (14), using an integrated Nusselt number correlation, and a characteristic length (e.g. the flute hydraulic diameter). Since all the selected regressions in the previous trials (illustrated in Figs. 4–6) have a high indicated  $R^2$  value, it is assumed that the employed approaches capture the relationships well. In the mapping equations for both air temperature and humidity ratio prediction, the influence functions of wheel rotational speed, airflow rate, and wheel depth are identical. This is because the heat and mass transfer processes of an energy recovery wheel are linear processes on a psychrometric chart. Hence, the form of the temperature and humidity ratio mapping methods share the same equation format, although they may have different constants. Finally, the format of the mapping method for supply air temperature Eq. (15), and the supply air humidity ratio Eq. (16) can be identified.

$$h = \frac{Nu \cdot k_g}{d_h} = \frac{0.59L^{0.624}}{d_h} \quad (14)$$

$$T_{E,SA} - T_{E,OA} = \frac{0.59L^{0.624}}{d_h \rho_R C_P} (a_1 t_{RM} + b_1) (a_2 u_{OA} + b_2) (a_3 e^{b_3 L} + c_3 e^{d_3 L}) \times \frac{u_{RA}}{u_{OA}} (T_{E,OA} - T_{E,SA}) \quad (15)$$

$$W_{E,SA} - W_{E,OA} = \frac{0.59L^{0.624}}{d_h \rho_R} (a_1 t_{RM} + b_1) (a_2 u_{OA} + b_2) \times (a_3 e^{b_3 L} + c_3 e^{d_3 L}) \times \frac{u_{RA}}{u_{OA}} (W_{E,OA} - W_{E,SA}) \quad (16)$$

#### Mapping method training and validation

The proposed mapping method was primarily developed based on the definition of efficiency employed by AHRI 1060, and the governing equations for energy recovery wheel heat and mass transfer. This approach allows the mapping method to be considered as a semi-empirical relationship. The ANN approach proposed by Jani et al. (2016) requires a minimum of 10 data points for training, while the mapping method proposed in the current

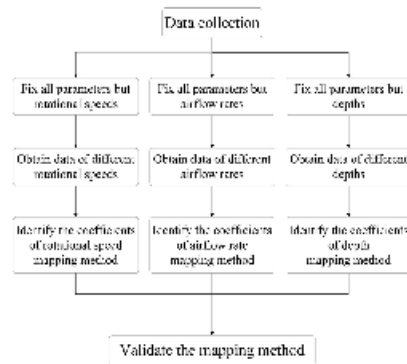


Fig. 7. Semi-empirical performance mapping method configuring process.

work requires a minimum of only 8 data points for training, so the work of generating data points by experimental testing to train the model is further reduced. Additionally, the model form proposed in this work involves simple algebraic equations that are easily implemented on nearly all computational platforms.

Solving for all of the unknown constants simultaneously in the equations of the mapping method can be challenging; however, a feasible approach is to determine the coefficients for the functions of each influence variable separately. To achieve that, it is necessary to generate data points that only change one variable while fixing all other variables. For instance, if the function of the air face velocity is selected, boundary conditions for the FDM simulation (or for experimental tests) should be all the same other than the air face velocity. The parameters for the influence equation associated with the airflow rate can then be trained. The same procedure will be repeated for determining constants of the wheel rotation speed function, and the wheel depth function. The functions of wheel rotation speed and airflow rate are linear. It is easier to solve these two functions first. The function of wheel depth is more complex to solve, thus, it is generally better to solve for the constants of this function after finding those that correspond to the functions of the air face velocity and wheel depth. Fig. 7 is a flow chart that outlines the approach for training the mapping method.

Based on the range of experimental test data that was used in developing and validating the finite difference energy wheel model for this study, it is possible to identify the acceptable application range of the mapping method that has been developed. The extreme cases employed in this study are representative of typical application ranges for energy wheels in the industry. These extreme cases were input into the FDM model, and the results were compared against those generated by the mapping method with the same inputs. If the results agree with each other to within less than 10%, then the application range of the mapping method was considered valid. The overall application range of the mapping method is given in Table 3.

To visualize a comparison between the predicted performance of the mapping method and the values available in the data sets, parity plots are shown for the supply air temperature in Fig. 8 and the humidity ratio in Fig. 9. The validation study for the wheels produced by manufacturer A consist of a total of 140 data

Table 3.	
Operating range of the mapping method.	
Variables	Value
Temperature (°C)	–10 to 60
Humidity ratio (kg/kg <sup>–1</sup> )	0.001 to 0.03
Airflow face speed (m/s <sup>–1</sup> )	1.5–6
Rotation speed (RPM)	15–60
Wheel depth (m)	0.1–0.5

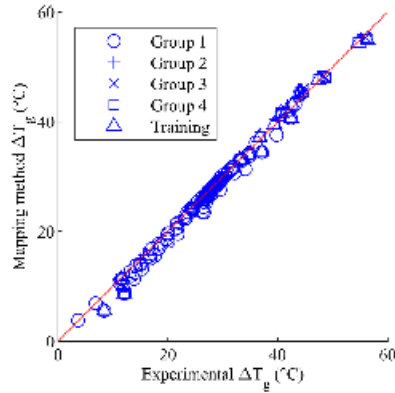


Fig. 8. Temperature  $\Delta T_{g,sa}$  between data sets and mapping method prediction, MAPE = 6.37%.

points from two independent laboratories; a total of 20 data points for manufacturer B; and 10 data points from De Antonellis et al. (2014). As Figs. 8 and 9 show, the results of prediction from the mapping method and data sets agree very well with each other, and the mean absolute prediction errors (MAPE) are under 10%. The parameters of the mapping method for each data group in these plots were determined through an optimization routine. In using the optimization approach to train the coefficients, the authors noted that the algorithm could become trapped in a local minimum when the starting guess values were distant from the true value. Therefore, locating initial values for the parameters by isolating variables as mentioned previously is a preferable approach.

During this research, the mapping method was trained and validated using four separate sets of experimental data to identify the universality of the proposed approach. The first and second data sets represent test data from two independent laboratories who tested three different sizes of energy wheels, which are produced by manufacturer A. The energy wheels from this data set all employ identical desiccant material and flute geometry. The third data

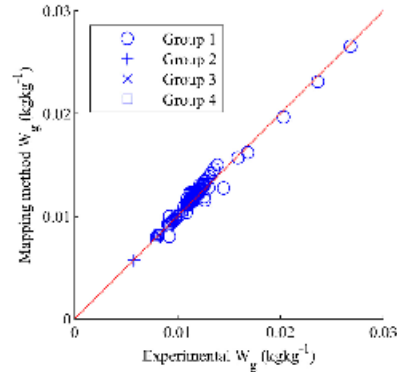


Fig. 9.  $W_{g,sa}$  between data sets and mapping method prediction, MAPE = 2.62%.

set was generated by a selection tool provided by manufacturer B, who produces energy recovery wheels that embed different desiccant materials, and utilize different flute geometries than manufacturer A. The last data set comes from the published work of De Antonellis et al. (2014), who studied energy recovery wheel performance.

One characteristic of the mapping method that was observed during this procedure is that the trained mapping method is valid for wheels with very different physical geometries and operating conditions provided that the desiccant material is identical through all the case studies. In other words, the mapping method doesn't need to be retrained even if the physical geometries, operating conditions, or dimensions of a wheel change. This unique characteristic gives the proposed mapping method a great advantage for conducting parametric or optimization studies on energy recovery wheels. Furthermore, the application of the mapping method is not limited to one specific type of energy recovery wheel. The mapping method applies to different wheels from different manufacturers as long as the desiccant is the same.

Before concluding a discussion on the mapping method, there is one characteristic that needs to be clarified, which is the independence of the mapping method results to the training data points. Theoretically, even if the training data sets are different, they should lead to similar constants for the mapping method and should not significantly affect its performance prediction. Therefore, several different sets of training data points were applied to train the mapping method to evaluate its applicability and robustness. The predictions of the mapping method are compared with the FDM model simulation result. As Table 4 shows, the mean absolute percentage errors of the difference between the mapping

Table 4.  
Study for the effect of training data sets selection to prediction.

Iteration	a1	b1	a2	b2	a3	b3	c3	d3	$\Delta T$ MAPE (%)
1	-2.28	10.93	-0.76	11.77	0.16	-1.25	-0.62	-38.13	5.17
2	-2.84	11.53	-1.35	13.65	0.15	-1.25	-0.6	-38.13	6.71
3	-2.72	11.53	-0.94	11.91	0.15	-1.25	-0.6	-38.13	5.46
4	-2.9	11.6	-0.89	11.92	0.15	-1.25	-0.6	-38.13	9.83
5	-2.64	11.47	-1.73	13.89	0.17	-1.25	-0.68	-38.13	8.86

method and the FDM simulation are all under 10% among different training data sets. Hence, with random training data points, the mapping method still delivers precise and accurate predictions; however, it is always good practice to select training data points that are separated by some distance from one another to ensure that artifacts such as measurement error and uncertainty don't have a significant impact on the final results.

### Conclusion

In this research, a detailed finite difference numerical model for an energy recovery wheel was developed and validated, and subsequently utilized for developing a semi-empirical performance mapping method. Validation of the numerical model was carried out using experimental results from different manufacturers, and from two different laboratories who follow the AHRI 1060 standard test procedures. Additionally, the mapping method results are validated against data published in the available literature. The applicable range of the mapping method is defined, and the process of configuring and training model coefficients for the mapping method is outlined in the flow chart of Fig. 7. The characteristics and benefits of the proposed semi-empirical performance mapping method are as follows:

- The mapping method is very broad in its derivation and, as such, can account for most of the important design parameters of an energy recovery wheel. This feature of incorporating additional flexibility into the model inputs makes the mapping method ideal for commercial usage (e.g., as a product selection tool), and in academic research (e.g., optimization analysis). The flexible input boundary conditions include the following: outdoor/return air conditions (air temperature and humidity ratio), geometric parameters of an energy recovery wheel (wheel diameter, depth and flute dimensions), and operating conditions (wheel rotational speed and airflow rate).
- The proposed mapping method is more efficient in predicting the performance characteristics of different energy recovery wheel models that are available in the open literature. In addition, this new model can be trained with as few as 8 data points, which reduces the time and cost associated with obtaining sufficient data to train the model.

The proposed mapping method for energy recovery wheel performance prediction contributes to the establishment of an economical and user-friendly tool for design, analysis, and optimization of HVAC systems with integrated energy recovery wheels.

### Declaration of Competing Interest

None.

### Supplementary materials

Supplementary material associated with this article can be found, in the online version, at doi:10.1016/j.jirefr.2020.10.018.

### Reference

- Antonellis, S.D., Intini, M., Joppolo, C.M., 2015. Desiccant wheels effectiveness parameters: correlations based on experimental data. *Energy Build.* 103, 296–306. doi:10.1016/j.enbuild.2015.06.041.
- ANSI/ASHRAE/IES Standard (2016), 90.1-2016 energy standard for buildings: except low-rise residential buildings, 101–103.
- AHRI Standard (2013), AHRI Standard 1060 performance rating of air-to-air exchangers for energy recovery ventilation equipment, 1–3, 9.
- Beccali, M., Butera, F., Giannelis, R., Adhikari, R.S., 2002. Simplified models for the performance evaluation of desiccant wheel dehumidification. *Int. J. Energy Res.* 27 (1), 17–28. doi:10.1002/er.856.
- Chung, J.D., Lee, D.-Y., 2009. Effect of desiccant isotherm on the performance of desiccant wheel. *Int. J. Refrigeration* 32 (4), 720–726. doi:10.1016/j.jirefr.2009.01.003.
- Comino, F., Gujo-Rubio, D., Adana, M.R.D., Hervás-Martínez, C., 2019. Validation of multilayer artificial neural networks to model desiccant wheels activated at low temperature. *Int. J. Refrigeration* 100, 434–442. doi:10.1016/j.jirefr.2019.02.002.
- De Amone, S., Intini, M., Joppolo, C., Leone, C., 2014. Design optimization of heat wheels for energy recovery in HVAC systems. *Energies* 7 (11), 7348–7367. doi:10.3390/en7117348.
- De Amone, S., Joppolo, C.M., Molinaroli, L., 2010. Simulation, performance analysis and optimization of desiccant wheels. *Energy Build.* 42 (9), 1386–1393. doi:10.1016/j.enbuild.2010.03.007.
- Estandari Nia, F., van Paassen, D., 2006. Application of desiccant adsorption for air-conditioning cycle. In: *Proceedings of the 4th International Energy Conversion Engineering Conference and Exhibition (IECECE)* doi:10.2514/6.2006-4150.
- Ge, T.S., Li, Y., Wang, R.Z., Dai, Y.J., 2008. A review of the mathematical models for predicting rotary desiccant wheel. *Renew. Sustain. Energy Rev.* 12 (6), 1485–1528. doi:10.1016/j.rser.2007.01.012.
- Jain, D., Mishra, M., Sahoo, P., 2016. Performance prediction of rotary solid desiccant dehumidifier in hybrid air-conditioning system using artificial neural network. *Appl. Therm. Eng.* 98, 1091–1103. doi:10.1016/j.applthermaleng.2015.12.112.
- Koronaki, I., Rogdaki, E., Kakasliou, T., 2012. Thermodynamic analysis of an open cycle solid desiccant cooling system using Artificial Neural Network. *Energy Conv. Manag.* 60, 152–160. doi:10.1016/j.enconman.2012.01.022.
- Lakshminarayana, R., Haji-Sheikh, A., 1992. Entrance heat transfer in isosceles and right triangular ducts. *J. Thermophys. Heat Transf.* 6 (1), 167–171. doi:10.2514/3.336.
- Narayanan, R., Saman, W.Y., White, S.D., 2013. A non-adiabatic desiccant wheel: modeling and experimental validation. *Appl. Therm. Eng.* 61 (2), 178–185. doi:10.1016/j.applthermaleng.2013.07.007.
- Parmar, H., Hindiyeh, D., 2011. Artificial neural network based modelling of desiccant wheel. *Energy Build.* 43 (12), 3505–3513. doi:10.1016/j.enbuild.2011.09.016.
- Panaras, G., Maziouliakis, E., Belesiotis, V., Nyrakis, N., 2010. Experimental validation of a simplified approach for a desiccant wheel model. *Energy Build.* 42 (10), 1719–1725. doi:10.1016/j.enbuild.2010.05.006.
- Simonsen, C.J., Besant, R.W., 1998. Heat and moisture transfer in energy wheels during sorption, condensation, and frosting conditions. *J. Heat Transf.* 120 (3), 699–708. doi:10.1115/1.2824330.
- U.S. Energy Information Administration (2017), *Annual Energy Outlook 2017*, 101–114.
- Van Den Hulik, E., Mitchell, J.W., Klein, S.A., 1985. Design theory for rotary heat and mass exchangers—I. Wave analysis of rotary heat and mass exchangers with infinite transfer coefficients. *Int. J. Heat Mass Transf.* 28 (8), 1575–1586. doi:10.1016/0017-9310(85)90250-5.
- Yadav, L., Yadav, A., 2016. Mathematical investigation of purge sector angle for clockwise and anticlockwise rotation of desiccant wheel. *Appl. Therm. Eng.* 93, 830–848. doi:10.1016/j.applthermaleng.2015.10.062.
- Zendehboudi, A., 2016. Implementation of GA-LSSVM modelling approach for estimating the performance of solid desiccant wheels. *Energy Conv. Manag.* 127, 245–255. doi:10.1016/j.enconman.2016.08.070.
- Zendehboudi, A., Li, X., 2018. Desiccant-wheel optimization via response surface methodology and multi-objective genetic algorithm. *Energy Conv. Manag.* 174, 640–660. doi:10.1016/j.enconman.2018.07.078.
- Zhai, C., Archer, D.H., Fischer, J.C., 2008. Performance modeling of desiccant wheels: 1 – model development. In: *Proceedings of the 2nd International Conference on Energy Sustainability*, pp. 18–53. doi:10.1115/es.2008-54185.

Re: Obtain permission request - Journal (1175177) [210612-012649]

Rights and Permissions (ELS) <Permissions@elsevier.com>

Mon 6/14/2021 5:17 PM

To: Yu-Wei Hung <hung13@purdue.edu>

Dear Mr. Yu-Wei Hung,

We hereby grant you permission to reprint the material below at no charge in your thesis subject to the following conditions:

1. If any part of the material to be used (for example, figures) has appeared in our publication with credit or acknowledgement to another source, permission must also be sought from that source. If such permission is not obtained then that material may not be included in your publication/copies.
2. Suitable acknowledgment to the source must be made, either as a footnote or in a reference list at the end of your publication, as follows:  
  
"This article was published in Publication title, Vol number, Author(s), Title of article, Page Nos, Copyright Elsevier (or appropriate Society name) (Year)."
3. Your thesis may be submitted to your institution in either print or electronic form.
4. Reproduction of this material is confined to the purpose for which permission is hereby given.
5. This permission is granted for non-exclusive world English rights only. For other languages please reapply separately for each one required. Permission excludes use in an electronic form other than submission. Should you have a specific electronic project in mind please reapply for permission.
6. As long as the article is embedded in your thesis, you can post/share your thesis in the University repository.
7. Should your thesis be published commercially, please reapply for permission.

This includes permission for the Library and Archives of Canada to supply single copies, on demand, of the complete thesis. Should your thesis be published commercially, please reapply for permission.

This includes permission for UMI to supply single copies, on demand, of the complete thesis. Should your thesis be published commercially, please reapply for permission.

8. Posting of the full article/ chapter online is not permitted. You may post an abstract with a link to the Elsevier website [www.elsevier.com](http://www.elsevier.com), or to the article on ScienceDirect if it is available on that platform.

Regards,

Kaveri  
ELSEVIER | Permissions Granting Team

---

**From:** Administrator  
**Date:** Saturday, June 12, 2021 03:42 PM GMT

Dear Yu-wei Hung,

Thank you for contacting the Permissions Granting Team.

We acknowledge the receipt of your request and we aim to respond within seven business days. Your unique reference number is 210612-012649.

Please avoid changing the subject line of this email when replying to avoid delay with your query.

Regards,  
Permission Granting Team

---

**From:** Yu-wei Hung  
**Date:** Saturday, June 12, 2021 03:42 PM GMT

**Submission ID:** 1175177  
**Date:** 12 Jun 2021 4:42pm

**Name:** Mr. Yu-Wei Hung  
**Institute/company:** Purdue University  
**Address:** 177 S Russell St  
**Post/Zip Code:** 47907  
**City:** West Lafayette  
**State/Territory:** Indiana  
**Country:** United States  
**Telephone:** 7657756832  
**Email:** [hung13@purdue.edu](mailto:hung13@purdue.edu)

**Type of Publication:** Journal

**Title:** International Journal of Refrigeration  
**Authors:** Yu-Wei Hung, W. Travis Horton  
**Year:** 2021  
**From page:** 102  
**To page:** 110  
**ISSN:** 0140-7007  
**Volume:** 123  
**Article title:** Semi-empirical mapping method for energy recovery wheel performance simulation

**I would like to use:** Full article / chapter

**I am the author of the Elsevier material:** Yes

7/14/2021

Mail - Yu-Wei Hung - Outlook

In what format will you use the material: Print and Electronic

Translation: No

Proposed use: Reuse in a thesis/dissertation

Material can be extracted: No

Additional Comments / Information:

---

This email is for use by the intended recipient and contains information that may be confidential. If you are not the intended recipient, please notify the sender by return email and delete this email from your inbox. Any unauthorized use or distribution of this email, in whole or in part, is strictly prohibited and may be unlawful. Any price quotes contained in this email are merely indicative and will not result in any legally binding or enforceable obligation. Unless explicitly designated as an intended e-contract, this email does not constitute a contract offer, a contract amendment, or an acceptance of a contract offer.

Elsevier Limited. Registered Office: The Boulevard, Langford Lane, Kidlington, Oxford, OX5 1GB, United Kingdom, Registration No. 1982084, Registered in England and Wales. [Privacy Policy](#)

---

<https://outlook.office.com/mail/id/AAQkAGVjZWY5MDU1LWF1ZTt1NGE0ZS05YWU1LTE4NTEyYzhIMzU2ZQAQALqpySssvltXGjnvTeil%2BBug%3D>

3/3